Using spins in diamond for quantum technologies

Important note
To cite this publication, please use the final published version (if applicable).
Please check the document version above.

USING SPINS IN DIAMOND FOR QUANTUM TECHNOLOGIES

USING SPINS IN DIAMOND FOR QUANTUM TECHNOLOGIES

Dissertation

for the purpose of obtaining the degree of doctor
at Delft University of Technology,
by the authority of the Rector Magnificus prof. dr. ir. T.H.J.J. van der Hagen,
Chair of the Board for Doctorates,
to be defended publicly on
Tuesday 19 September 2023 at 15:00 o'clock

by

Yang WANG

Master of Science in Physics,
RWTH Aachen University, Aachen, Germany,
born in Wanzhou, China.

This dissertation has been approved by the promotor:

Promotor: Prof. dr. B. M. Terhal
Copromotor: Dr. ir. T. H. Taminiau

Composition of the doctoral committee:

Rector Magnificus,	chairperson
Prof. dr. B. M. Terhal	Delft University of Technology
Dr. ir. T. H. Taminiau	Delft University of Technology

Independent members:

Prof. dr. A. F. Otte	Delft University of Technology
Dr. J. Borregaard	Delft University of Technology
Prof. dr. D. P. DiVincenzo	RWTH-Aachen University, Germany
Prof. dr. S. E. Economou	Virginia Tech University, USA

Reserve member:

Prof. dr. Y. M. Blanter	Delft University of Technology
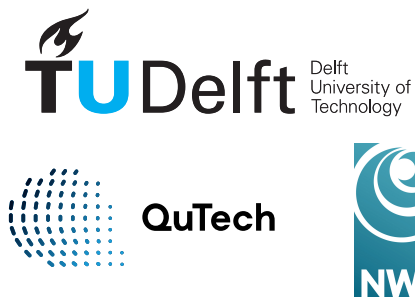
An electronic version of this dissertation is available at
`http://repository.tudelft.nl/`.

CONTENTS

SUMMARY

Solid-state defect centers, such as the nitrogen-vacancy (NV) centers in diamond, represent a promising and versatile platform for quantum technologies. The attractiveness stems from their extended coherence time and the provision of an optical interface. Of particular note is the ability to use the electronic spin associated with a single NV center to construct a multi-qubit register, achieved through its magnetic interactions with adjacent nuclear spins in the host material.

Recent advances in experimental efforts have underscored the potential utility of NV centers in quantum technologies. This includes areas such as quantum sensing, quantum network, quantum simulation, and fault-tolerant quantum computation. The focus of this thesis is on overcoming noise-related challenges to facilitate the practical realization of these applications.

One of the main goals of this work is to develop fault-tolerant quantum error correction (QEC) protocols that specifically take into account the physical limitations of NV centers, thereby reducing the high fidelity requirements of fault-tolerant QEC and increasing its practical feasibility. The ultimate goal is to realize other quantum technology applications using NV centers under the protection of fault-tolerant QEC. Towards this goal, this thesis presents experimental proof-of-concept demonstrations of fault-tolerance and proposes protocols that are feasible for further experimental validation.

In addition, this thesis explores noise mitigation techniques that require less demanding operations, compared to QEC, on the spin qubits associated with the NV centers. One such proposed technique involves only single-qubit initialization and measurements, which could significantly improve the nuclear spin coherence time when creating remote entanglement between NV centers. This technique expands the toolbox for scaling up to large networks using NV centers.

Another research direction explored in this thesis is the use of hybrid diamond devices. Some hybrid devices consider NV centers as memory for other systems with better control fidelity, taking advantage of the remarkably long coherence time of NV centers and bypassing the need to perform complex gate operations directly on them. Other hybrid devices aim to develop innovative methods to control NV centers, which could lead to new applications.

This thesis examine the latter possibility and proposes an efficient method to generate a highly entangled state in a spin ensemble with potential applications in magnetic sensing. In particular, this thesis considers the use of global control over an ensemble of NV centers, which can be realized in a hybrid device consisting of an NV center ensemble and a superconducting flux qubit.

SAMENVATTING

Defect centers in vaste stoffen, zoals het nitrogen-vancancy (NV) center in diamant, zijn een veelbelovend en veelzijdig platform voor kwantumtechnologieën. Deze aantrekkingskracht komt voort uit hun lange coherentietijd en de aanwezigheid van een optisch interface. Van bijzonder belang is de mogelijkheid om de elektronische spin geassocieerd met een enkel NV-centrum te gebruiken om een multi-qubit register te construeren, bereikt door magnetische interacties met aangrenzende kernspins in het diamant. Recente vooruitgang in experimenteel onderzoek heeft het potentiële nut van NV-centers in kwantumtechnologieën benadrukt. Dit omvat gebieden zoals kwantumsensing, kwantumnetwerken, kwantumsimulaties en fouttolerante kwantumberekeningen. De focus van dit proefschrift ligt op het overwinnen van uitdagingen met betrekking tot ruis, om de praktische realisatie van deze toepassingen te vergemakkelijken. Een van de belangrijkste doelen van dit werk is het ontwikkelen van fouttolerante kwantum-foutcorrectie protocollen (QEC) die specifiek rekening houden met de fysieke beperkingen van NV-centers, waardoor de hoge getrouwheidseisen van fouttolerante QEC worden verlaagd en de praktische haalbaarheid ervan wordt verhoogd. Het uiteindelijke doel is om andere kwantumtechnologische toepassingen te realiseren met NV centers via de bescherming van fouttolerante QEC. Om dit doel te bereiken, presenteert dit proefschrift experimentele proof-of-principle demonstraties van fouttolerantie en stelt protocollen voor die haalbaar zijn voor verdere experimentele validatie. Daarnaast verkent dit proefschrift technieken om ruis te onderdrukken. In vergelijking met QEC zijn voor deze technieken minder veeleisende operaties nodig op de spin qubits die geassocieerd zijn met de NV centers. Eén zo'n voorgestelde techniek omvat alleen single-qubit initialisatie en metingen, wat de nucleaire spin coherentietijd aanzienlijk zou kunnen verbeteren bij het creëren van verstrengeling op afstand tussen NV centers. Deze techniek breidt de gereedschapskist voor het opschalen naar grote netwerken met NV centers uit. Een andere onderzoeksrichting in dit proefschrift is het gebruik van NV centers voor hybride technologieën. Sommige hybride technologieën beschouwen NV centers als geheugen voor andere systemen met een betere controlegetrouwheid, waarbij gebruik wordt gemaakt van de opmerkelijk lange coherentietijd van NV centers en de noodzaak om complexe operaties direct op hen uit te voeren wordt omzeild. Andere hybride technologieën richten zich op het ontwikkelen van innovatieve methoden om NV centers te besturen, wat zou kunnen leiden tot nieuwe toepassingen. Deze thesis onderzoekt deze laatste mogelijkheid en stelt een efficiënte methode voor om een sterk verstrengelde toestand te genereren in een spin ensemble met potentiële toepassingen in magnetische detectie. In het bijzonder beschouwt dit proefschrift het gebruik van globale controle over een ensemble van NV centers, wat gerealiseerd kan worden in een hybride technologie bestaande uit een NV centrum ensemble en een supergeleidende flux qubit.

1

OVERVIEW

Nitrogen-vacancy (NV) centers in diamond are point defects that arise when a nitrogen atom replaces a carbon atom and an adjacent carbon atom is missing, creating a vacancy [12]. Each NV center possesses an electronic spin that exhibits a long coherence time and can be initialized and read out using optical methods [5, 12]. Such defect centers also provide a spin-photon interface that enables the creation of remote entanglement between separated NV centers through the use of optical links [9, 31]. Additionally, the NV centers' sensitivity to magnetic and electric fields makes them attractive for quantum sensing applications [6]. Furthermore, the magnetic interaction between the electronic spin and neighboring nuclear spins allows for the indirect manipulation of these nuclear spins, resulting in a controllable multi-qubit register in each NV center [7, 26, 27].

Thanks to these favorable spin and optical properties, NV centers in diamond have become a promising and versatile platform for quantum technologies [5, 12] since the detection of individual NV centers in 1997 [16]. Recent experimental studies have highlighted its potential in various quantum technologies, such as quantum sensing [1, 4], quantum networking [17, 22], quantum simulation [23], and quantum computation [7, 26, 27]. Despite these significant advancements, the practical utilization of current NV setups is still hampered due to the presence of noise.

Quantum Error Correction (QEC) is expected to be a key technique to manage noise perturbations in quantum systems [28]. Central to QEC protocols is the encoding of multiple physical qubits onto a logical qubit, followed by specific operations designed to remove accumulated noise [8, 11]. The fault-tolerance threshold theorem states that if the error rates associated with the physical qubits remain below a certain threshold, the use of fault-tolerant QEC protocols can significantly reduce the error rates of the logical qubits [3, 8]. This theorem guarantees the theoretical possibility of performing arbitrary quantum computation even in the presence of noise [3, 28].

Accurate control of the physical qubits is thus critical for the use of QEC protocols, [3, 8, 11, 28], otherwise the additional noise removal operations can easily introduce more errors than they correct. Unfortunately, keeping the noise level of the physical qubits below the required threshold is a challenging task for most of today's experimen-

1

tal platforms [10, 15, 18, 21, 24, 30]. To this end, considerable effort has been devoted to tailoring fault-tolerant protocols to the constraints of the underlying physical platforms, with the goal of minimizing the demanding high-fidelity requirements as much as possible. As illustrated in Chap 4, selecting an 8-qubit code designed to take advantage of the all-to-all connectivity between physical qubits can significantly reduce the number of gate operations required. The fault-tolerant protocol we have developed can result in relatively high thresholds for certain quantum computing tasks, making it particularly suitable for systems with all-to-all connectivity, such as trapped-ion qubits and NV-based networks.

Furthermore, we experimentally realize for the first time the essential building blocks for the realization of fault-tolerant QEC protocols using a single NV center (Chap 5). Our fault-tolerant protocol is highly optimized for the spin register in a single NV center by avoiding relatively more costly nuclear-nuclear entangling gates and minimizing the total number of operations involved. The key of this work is the experimental demonstration of the concept that introducing additional operations can further suppress the error rate of a logical qubit. However, the error rate of the logical qubit is still much higher than that of its constituent physical qubits, meaning that fault-tolerant QEC remains insufficient to facilitate other applications using current setups, such as building an NV-based quantum network.

An important question then arises: since QEC remains infeasible for today's setups, what strategies might we employ to manage noise and thereby advance other applications? To address this issue, one direction we have explored is to develop alternative noise mitigation techniques that rely on more rudimentary operations. In Chap 6, we present an error mitigation strategy in which additional "spectator" qubits are measured to directly assess the noise affecting the data qubits.

The effectiveness of this spectator approach is supported by the observation that the noise on the nuclear spins within an NV center manifests itself as random phases, and that these phases exhibit spatial correlation across different nuclear spins. The phase correlation enables the probing of the noise on data qubits simply by measuring spectator qubits, requiring only single-qubit measurement and initialization of these spectators. The use of spectator qubits highlights the importance of a deep understanding of the physical systems at hand.

In addition, we investigate the hybridization of NV centers with alternative systems to avoid the complicated operations required for direct implementation of QEC protocols using NV centers. The basic idea is to exploit NV centers by exploiting their extended coherence time and using them as memory for other systems with better control fidelity [19, 32]. This specialized use of NV centers as memory promises to simplify the manipulation of its spin qubits, eliminating the need for complex gate sequences required to execute fault-tolerant protocols directly on NV centers.

In parallel, hybridized devices can offer new possibilities for controlling defect centers [2, 13, 14, 20, 25, 29]. For example, coupling an ensemble of NV centers to a superconducting flux qubit facilitates global control over the NV centers [20, 33]. Building on such global control, a much more efficient strategy for the preparation of highly entangled Dicke states has been proposed in Chap 7. Furthermore, the coupling of NV centers to phonon modes provides another example, offering the potential for efficient

entanglement generation between two spatially separated NV centers [2, 13, 14, 29]. The prospect of combining the strengths of different systems represents a vibrant area of ongoing research that warrants thorough exploration and analysis [2, 13, 14, 19, 29, 32].

Thesis outline

The main body of this thesis is divided into the following chapters:

Chapter 2: Properties of nitrogen-vacancy centers in diamond

This chapter aims to provide a comprehensive overview of the fundamental properties of NV centers in diamond. The presentation combines standard group theory with simple physical models to provide a qualitative understanding of the underlying physics. The primary objective is to establish a solid foundation for understanding the techniques used to exploit NV centers for quantum information processing applications in subsequent chapters. Additionally, this chapter explains some key terminologies and notations that are commonly used in the NV center literature, with the intention of assisting beginners of this field in bridging their knowledge gap.

The primary reference for this chapter is Maze et al., Properties of nitrogen-vacancy centers in diamond: the group theoretic approach, New J. Phys. 13.2 (2011): 025025.

Chapter 3: Multi-qubit register in diamond

This chapter provides a comprehensive theoretical survey of the methods employed to utilize NV centers as quantum processors. In addition to the optical addressing methods that enable the initialization and readout of the NV centers, the main focus is on illuminating the principles behind the dynamical decoupling technique.

First, the coherence time of spin qubits can be significantly prolonged through the application of dynamical decoupling sequences. Moreover, an understanding of dynamical decoupling is a prerequisite for comprehending how neighboring nuclear spins could be manipulated as qubits indirectly through the electronic spin. The dynamical decoupling technique serves as the cornerstone for using NV centers in quantum technologies.

Chapter 4: Basics of quantum error correction

This chapter provides an introductory overview of QEC. We elucidate fundamental concepts that are crucial for understanding various QEC-related experiments nowadays, including stabilizer, fault-tolerance, threshold, pseudo-threshold, and universality.

As a concrete example of fault-tolerant universal quantum computation, we have developed a novel fault-tolerant protocol to implement a simple quantum algorithm, one-bit addition. By exploiting the all-to-all connectivity of physical qubits in platforms such as trapped ions and NV-based networks, we achieve a relatively better threshold for this particular computational task, which would be more feasible for experimental setups in the near future.

Chapter 5: Fault-tolerant operation of a logical qubit in a diamond quantum processor

This chapter presents a demonstration of essential building blocks of fault-tolerant quantum error correction using spin qubits associated with a single NV center in diamond.

1

The approach is based on the 5-qubit code, with a recently discovered flag protocol that enables fault-tolerance using a total of seven qubits. The central aspect of this work involves encoding the logical qubit by repeatedly measuring multi-qubit operators.

CHAPTER 6: ROBUST QUANTUM-NETWORK NODES THROUGH REAL-TIME NOISE MITIGATION USING SPECTATOR QUBITS

In this chapter, we present an error mitigation technique to facilitate building a large-scale network using NV centers. When entangling two spatially separated NV centers, the dominant noise source is expected to be correlated dephasing on nuclear spins. The proposed method mitigates this correlated dephasing noise by implementing a phase estimation protocol, involving only single-qubit initialization and measurement.

CHAPTER 7: PREPARING DICKE STATES IN A SPIN ENSEMBLE USING PHASE ESTIMATION

This chapter presents an efficient scheme for preparing Dicke states, a class of highly entangled states, using a hybrid system consisting of an ensemble of NV centers and a superconducting flux qubit. Our proposed preparation scheme involves global control over the NV center ensemble through the manipulation of a superconducting flux qubit, and is exponentially efficient in the number of operations required compared to previous proposals.

REFERENCES

[1] M. H. Abobeih, J. Randall, C. E. Bradley, H. P. Bartling, M. A. Bakker, M. J. Degen, M. Markham, D. J. Twitchen, and T. H. Taminiau. Atomic-scale imaging of a 27-nuclear-spin cluster using a quantum sensor. *Nature*, 576(7787):411–415, 2019.

[2] A. Albrecht, A. Retzker, F. Jelezko, and M. B. Plenio. Coupling of nitrogen vacancy centres in nanodiamonds by means of phonons. *New J. Phys.*, 15(8):083014, 2013.

[3] P. Aliferis, D. Gottesman, and J. Preskill. Quantum accuracy threshold for concatenated distance-3 codes. *Quantum Inf. Comput.*, 6(97), 2006.

[4] N. Aslam, M. Pfender, P. Neumann, R. Reuter, A. Zappe, F. F. de Oliveira, A. Denisenko, H. Sumiya, S. Onoda, J. Isoya, and J. Wrachtrup. Nanoscale nuclear magnetic resonance with chemical resolution. *Science*, 357(6346):67–71, 2017.

[5] D. D. Awschalom, R. Hanson, J. Wrachtrup, and B. B. Zhou. Quantum technologies with optically interfaced solid-state spins. *Nat. Photonics*, 12(9):516–527, 2018.

[6] J. F. Barry, J. M. Schloss, E. Bauch, M. J. Turner, C. A. Hart, L. M. Pham, and R. L. Walsworth. Sensitivity optimization for nv-diamond magnetometry. *Rev. Mod. Phys.*, 92:015004, 2020.

[7] C. E. Bradley, J. Randall, M. H. Abobeih, R. C. Berrevoets, M. J. Degen, M. A. Bakker, M. Markham, D. J. Twitchen, and T. H. Taminiau. A Ten-Qubit Solid-State spin register with quantum memory up to one minute. *Phys. Rev. X*, 9(3):031045, 2019.

[8] C. Chamberland and M. E. Beverland. Flag fault-tolerant error correction with arbitrary distance codes. *Quantum*, 2(53):53, 2018.

[9] Y. Chu and M. D. Lukin. 229Quantum optics with nitrogen-vacancy centres in diamond. In *Quantum Optics and Nanophotonics*. Oxford University Press, 2017.

[10] J. Cramer, N. Kalb, M. A. Rol, B. Hensen, M. S. Blok, M. Markham, D. J. Twitchen, R. Hanson, and T. H. Taminiau. Repeated quantum error correction on a continuously encoded qubit by real-time feedback. *Nat. Commun.*, 7:11526, 2016.

[11] S. J. Devitt, W. J. Munro, and K. Nemoto. Quantum error correction for beginners. *Rep. Prog. Phys.*, 76(7):076001, 2013.

[12] M. W. Doherty, N. B. Manson, P. Delaney, F. Jelezko, J. Wrachtrup, and L. C. L. Hollenberg. The nitrogen-vacancy colour centre in diamond. *Phys. Rep.*, 528(1):1–45, 2013.

[13] M. Fukami, D. R. Candido, D. D. Awschalom, and M. E. Flatté. Opportunities for long-range magnon-mediated entanglement of spin qubits via on- and off-resonant coupling. *PRX Quantum*, 2:040314, 2021.

[14] D. A. Golter, T. Oo, M. Amezcua, I. Lekavicius, K. A. Stewart, and H. Wang. Coupling a surface acoustic wave to an electron spin in diamond via a dark state. *Phys. Rev. X*, 6(4):041060, 2016.

[15] Google Quantum AI. Suppressing quantum errors by scaling a surface code logical qubit. *Nature*, 614(7949):676–681, 2023.

[16] A. Gruber, A. Dräbenstedt, C. Tietz, L. Fleury, J. Wrachtrup, and C. von Borczyskowski. Scanning confocal optical microscopy and magnetic resonance on single defect centers. *Science*, 276(5321):2012–2014, 1997.

[17] S. L. N. Hermans, M. Pompili, H. K. C. Beukers, S. Baier, J. Borregaard, and R. Hanson. Qubit teleportation between non-neighbouring nodes in a quantum network. *Nature*, 605(7911):663–668, 2022.

[18] S. Krinner, N. Lacroix, A. Remm, A. Di Paolo, E. Genois, C. Leroux, C. Hellings, S. Lazar, F. Swiadek, J. Herrmann, G. J. Norris, C. K. Andersen, M. Müller, A. Blais, C. Eichler, and A. Wallraff. Realizing repeated quantum error correction in a distance-three surface code. *Nature*, 605(7911):669–674, 2022.

[19] G. Kurizki, P. Bertet, Y. Kubo, K. Mølmer, D. Petrosyan, P. Rabl, and J. Schmiedmayer. Quantum technologies with hybrid systems. *Proc. Natl. Acad. Sci. U. S. A.*, 112(13):3866–3873, 2015.

[20] D. Marcos, M. Wubs, J. M. Taylor, R. Aguado, M. D. Lukin, and A. S. Sørensen. Coupling nitrogen-vacancy centers in diamond to superconducting flux qubits. *Phys. Rev. Lett.*, 105:210501, 2010.

[21] Z. Ni, S. Li, X. Deng, Y. Cai, L. Zhang, W. Wang, Z.-B. Yang, H. Yu, F. Yan, S. Liu, C.-L. Zou, L. Sun, S.-B. Zheng, Y. Xu, and D. Yu. Beating the break-even point with a discrete-variable-encoded logical qubit. *Nature*, 2023.

1

[22] M. Pompili, S. L. N. Hermans, S. Baier, H. K. C. Beukers, P. C. Humphreys, R. N. Schouten, R. F. L. Vermeulen, M. J. Tiggelman, L. Dos Santos Martins, B. Dirkse, S. Wehner, and R. Hanson. Realization of a multinode quantum network of remote solid-state qubits. *Science*, 372(6539):259–264, 2021.

[23] J. Randall, C. E. Bradley, F. V. van der Gronden, A. Galicia, M. H. Abobeih, M. Markham, D. J. Twitchen, F. Machado, N. Y. Yao, and T. H. Taminiau. Many-body-localized discrete time crystal with a programmable spin-based quantum simulator. *Science*, 374(6574):1474–1478, 2021.

[24] C. Ryan-Anderson, J. G. Bohnet, K. Lee, D. Gresh, A. Hankin, J. P. Gaebler, D. Francois, A. Chernoguzov, D. Lucchetti, N. C. Brown, T. M. Gatterman, S. K. Halit, K. Gilmore, J. A. Gerber, B. Neyenhuis, D. Hayes, and R. P. Stutz. Realization of real-time fault-tolerant quantum error correction. *Phys. Rev. X*, 11:041058, 2021.

[25] P. K. Shandilya, D. P. Lake, M. J. Mitchell, D. D. Sukachev, and P. E. Barclay. Optomechanical interface between telecom photons and spin quantum memory. *Nat. Phys.*, 17(12):1420–1425, 2021.

[26] T. H. Taminiau, J. Cramer, T. van der Sar, V. V. Dobrovitski, and R. Hanson. Universal control and error correction in multi-qubit spin registers in diamond. *Nat. Nanotechnol.*, 9(3):171–176, 2014.

[27] T. H. Taminiau, J. J. T. Wagenaar, T. van der Sar, F. Jelezko, V. V. Dobrovitski, and R. Hanson. Detection and control of individual nuclear spins using a weakly coupled electron spin. *Phys. Rev. Lett.*, 109:137602, 2012.

[28] B. M. Terhal. Quantum error correction for quantum memories. *Rev. Mod. Phys.*, 87:307–346, 2015.

[29] L. Trifunovic, F. L. Pedrocchi, and D. Loss. Long-distance entanglement of spin qubits via ferromagnet. *Phys. Rev. X*, 3:041023, 2013.

[30] G. Waldherr, Y. Wang, S. Zaiser, M. Jamali, T. Schulte-Herbrüggen, H. Abe, T. Ohshima, J. Isoya, J. F. Du, P. Neumann, and J. Wrachtrup. Quantum error correction in a solid-state hybrid spin register. *Nature*, 506(7487):204–207, feb 2014.

[31] S. Wehner, D. Elkouss, and R. Hanson. Quantum internet: A vision for the road ahead. *Science*, 362(6412), 2018.

[32] Z.-L. Xiang, S. Ashhab, J. Q. You, and F. Nori. Hybrid quantum circuits: Superconducting circuits interacting with other quantum systems. *Rev. Mod. Phys.*, 85:623–653, 2013.

[33] X. Zhu, S. Saito, A. Kemp, K. Kakuyanagi, S. I. Karimoto, H. Nakano, W. J. Munro, Y. Tokura, M. S. Everitt, K. Nemoto, M. Kasu, N. Mizuochi, and K. Semba. Coherent coupling of a superconducting flux qubit to an electron spin ensemble in diamond. *Nature*, 478(7368):221–224, 2011.

2

PROPERTIES OF NITROGEN-VACANCY CENTERS IN DIAMOND

This chapter provides a comprehensive review of the fundamental properties of nitrogen-vacancy centers in diamond. It combines standard group theory with straightforward physical models to provide a qualitative understanding of the physics. The objective is to establish a foundation for comprehending the techniques of using NV centers for quantum information processing applications in subsequent chapters.
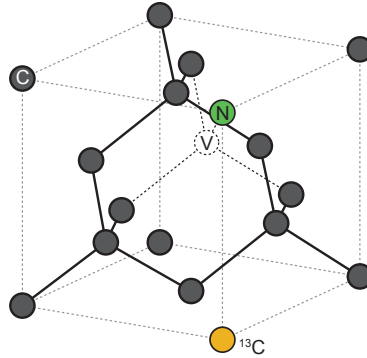
Figure 2.1: The lattice structure of a diamond. The nitrogen-vacancy (NV) center is formed by a substitutional nitrogen atom with nuclear spin-1 next to a vacant lattice side. About 1.1% of the carbon atoms in the diamond lattice are ^{13}C isotopes with nuclear spin-1/2 (yellow). Figure taken from Ref. [1]

The nitrogen-vacancy (NV) center is a point defect in the diamond lattice, where a nitrogen atom and a vacant lattice site replace two neighboring carbon atoms [12, 17, 18, 36]. This results in the breaking of covalent bonds between the carbon atoms, each of which then provides an outer electron, also known as a dangling bond [12, 17, 18, 36]. In addition, the replacement of a carbon atom by a nitrogen atom introduces an extra electron, resulting in a 5-electron state that is neutral and denoted as NV^0. The capture of an additional electron from the environment leads to a negatively charged state, denoted as NV$^-$. Importantly, the NV center is unchanged under the exchange of the nitrogen atom with one of the three adjacent carbons. This results in four unique types of NV centers, each characterized by the axis from the nitrogen to the vacancy, which is called the NV axis [18, 33].

Single NV centers were first detected in 1997 [25] and have since become a promising and versatile platform for quantum technologies [8]. Much of the research focuses on negatively charged NV centers (NV$^-$) due to their advantageous properties over their neutral counterparts (NV^0) [18, 35], such as long-lasting electronic spin coherence, zero-phonon line luminescence (see Chap 2.4.2), and the intersystem crossing mechanism for spin reset (see Chap 2.5). These properties are essential for various applications including sensing [2, 6, 15, 45], information processing [3, 44, 50], networking and communication [30, 39, 47], and fundamental tests [26]. This thesis will focus specifically on NV$^-$, and refer to it as NV for simplicity.

Note that this chapter is a summary of the existing literature, see Refs. [16–18] for a more complete overview.

2.1. REDUCED SYMMETRY

The presence of a defect center in a lattice breaks its translational symmetry, resulting in symmetry only with respect to specific rotations and reflections [36]. To separate the dynamics of the slower-moving nuclei from the electrons, the Born-Oppenheimer approximation is typically used [36], treating the nuclei as stationary. This leads to the symmetry

(a) E

(b) C^+

(c) C^-

(d) σ_v

(e) σ'_v

(f) σ''_v
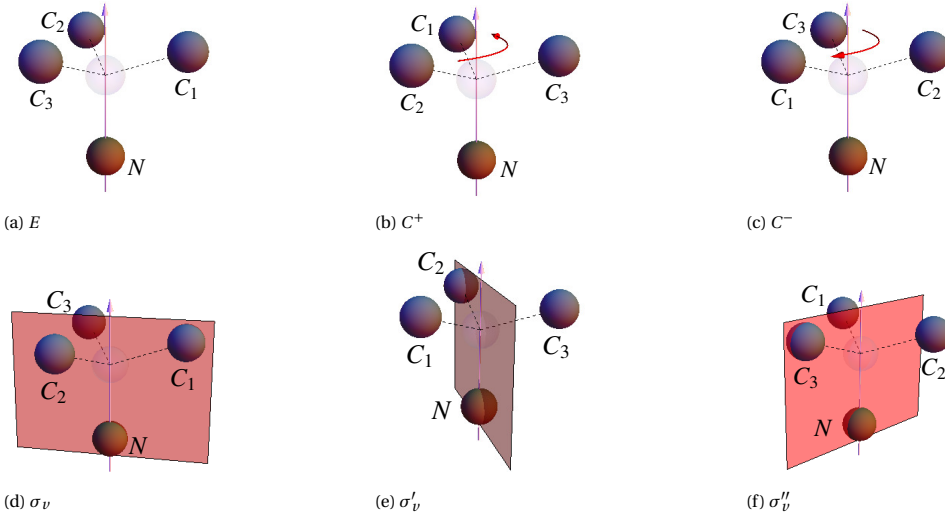
Figure 2.2: The symmetry operations of the C_{3v} group on the structure of the NV center. The nitrogen (brown) and nearest carbon (gray) atoms adjacent to the vacancy (transparent) are as shown. The operations of the group elements result in all permutations of the carbon atom labels. Figure taken from Ref. [18].

of the resulting system being described by the C_{3v} point group, which includes the identity, rotations about the NV axis by $\pm 2\pi/3$, and three reflection operations in the planes containing the vacancy, the nitrogen, and one of the adjacent carbons [31, 36]. Fig 2.2 depicts the symmetry operations on the NV center structure, where E, C^+/C^- and σ_vs represent the identity, rotations about the NV-axis, and the reflections, respectively.

MOTIVATION FOR ANALYZING THE SYMMETRY

The outer electrons are predominantly described by the electron-nuclei (see Chap 2.2.2), spin-spin (see Chap 2.3.3), and spin-orbit interactions (see Chap 2.3.2) [18, 36], which form the unperturbed Hamiltonian. Other weaker effects, such as lattice strain (see Chap 2.3.4) and lattice vibrations (see Chap 2.4.2 and Chap 2.5), can be treated as perturbations.

Analyzing the symmetry of NV centers is motivated by the fact that the unperturbed Hamiltonian is invariant under all C_{3v} symmetry operations, implying that the energy eigenstates should have certain symmetries. For example, consider an energy eigenstate $|\psi\rangle$ of the unperturbed Hamiltonian. By applying the C_{3v} symmetry operations, we obtain a set of degenerate energy eigenstates,

$$\left\{ |\psi\rangle, \quad U(C^+)|\psi\rangle, \quad U(C^-)|\psi\rangle, \quad U(\sigma_v)|\psi\rangle, \quad U(\sigma'_v)|\psi\rangle, \quad U(\sigma''_v)|\psi\rangle \right\}. \tag{2.1}$$

where the unitary operator U describes the effect of the corresponding symmetry operation. In the simplest case, the energy eigenstate $|\psi\rangle$ is unchanged by all symmetry operations, it then forms a 1-dimensional invariant subspace consisting only of that state. Restricted to this invariant subspace, all symmetry operations are represented by the

1×1 identity matrix, forming the simplest 1-dimensional irreducible representation (IR) of the C_{3v} group.

If n orthogonal degenerate eigenstates can be constructed by taking proper linear combinations of the eigenstates in the set in Eq (2.1), then we say that this set forms a n-dimensional invariant subspace associated. Similarly, this invariant subspace is associated with a n-dimensional IR. Such a representation is said to be irreducible because it can only be associated with an invariant subspace containing only degenerate and orthogonal eigenstates. The concept of irreducibility will be further explained in the following sections, and the basics of group representation can be found in standard group theory textbooks.

Group theory is a powerful tool for describing and studying NV centers [18, 34, 36] as well as other defect centers [28, 43] . The main task of this chapter is to construct a set of basis states, each of which lives in an invariant subspace associated with an IR. These basis states facilitate the qualitative analysis of the effects of the relevant interactions. Such a qualitative picture of the physics is essential for understanding the techniques of using NV centers for quantum technologies, which are discussed in other chapters of this thesis. Furthermore, the group-theoretic analysis reduces the computational cost of ab initio calculations and facilitates a detailed study of point defects [36, 43].

2.2. MOLECULAR ORBITALS

Each atom in the NV center structure has 4 sp^3 hybridized orbitals [7, 18]. To simplify the analysis, only one orbital from each atom is considered, since the others interact primarily with carbon atoms outside the NV structure [20, 36]. These considered orbitals are labeled $\sigma_N, \sigma_1, \sigma_2$ and σ_3, where σ_N belongs to the nitrogen atom and the others belong to the neighboring carbon atoms. Furthermore, these atomic orbitals are assumed to have negligible overlap and are treated as a set of orthonormal basis vectors, such as $\sigma_N = (1, 0, 0, 0)^T$, $\sigma_1 = (0, 1, 0, 0)^T$, and so on.

For pedagogical reasons, we study the case of a single outer electron using explicit 4×4 matrices, with the 4 atomic orbitals as the basis. The C_{3v} symmetry operations are represented by the matrices,

$$\Gamma(E) = \begin{pmatrix} 1 & 0 & 0 & 0 \\ 0 & 1 & 0 & 0 \\ 0 & 0 & 1 & 0 \\ 0 & 0 & 0 & 1 \end{pmatrix}, \quad \Gamma(C^+) = \begin{pmatrix} 1 & 0 & 0 & 0 \\ 0 & 0 & 0 & 1 \\ 0 & 1 & 0 & 0 \\ 0 & 0 & 1 & 0 \end{pmatrix}, \quad \Gamma(C^-) = \begin{pmatrix} 1 & 0 & 0 & 0 \\ 0 & 0 & 1 & 0 \\ 0 & 0 & 0 & 1 \\ 0 & 1 & 0 & 0 \end{pmatrix},$$

$$\tag{2.2}$$

$$\Gamma(\sigma_v) = \begin{pmatrix} 1 & 0 & 0 & 0 \\ 0 & 1 & 0 & 0 \\ 0 & 0 & 0 & 1 \\ 0 & 0 & 1 & 0 \end{pmatrix}, \quad \Gamma(\sigma_v') = \begin{pmatrix} 1 & 0 & 0 & 0 \\ 0 & 0 & 0 & 1 \\ 0 & 0 & 1 & 0 \\ 0 & 1 & 0 & 0 \end{pmatrix}, \quad \Gamma(\sigma_v'') = \begin{pmatrix} 1 & 0 & 0 & 0 \\ 0 & 0 & 1 & 0 \\ 0 & 1 & 0 & 0 \\ 0 & 0 & 0 & 1 \end{pmatrix},$$

which form a 4-dimensional matrix representation for the C_{3v} group [13, 31]. This representation, denoted as Γ, is made up of a 1-dimensional representation acting on the nitrogen atom and a 3-dimensional representation acting on the carbon atoms.

This representation Γ is considered reducible [13, 31], as the three carbon atomic orbitals can be further separated into a 1-dimensional and a 2-dimensional invariant subspace. This is achieved by taking proper linear combinations of the carbon atomic orbitals, which are referred to as the symmetry adapted linear combinations [28].

2.2.1. Symmetry adapted linear combinations

For a finite group, two representations are said to be equivalent if they differ only by a similarity transformation, which is a change of basis using a non-singular matrix R such that $\Gamma' = R\Gamma R^{-1}$ [13, 31]. The 3-dimensional representation of carbons can also be reduced, shown by transforming it into an equivalent representation Γ', which can be written as the direct sum of two smaller representations. For educational purposes, the transformation matrix R is explicitly written down,

$$
R = \begin{pmatrix}
1 & 0 & 0 & 0 \\
0 & -\sqrt{\frac{2}{3}} & \sqrt{\frac{1}{6}} & \sqrt{\frac{1}{6}} \\
0 & 0 & -\sqrt{\frac{1}{2}} & \sqrt{\frac{1}{2}} \\
0 & -\sqrt{\frac{1}{3}} & -\sqrt{\frac{1}{3}} & -\sqrt{\frac{1}{3}}
\end{pmatrix}.
\tag{2.3}
$$

This similarity transformation yields a set of orthonormal molecular orbitals,

$$
(a_N, e_x, e_y, a_C)^T = R\,(\sigma_N, \sigma_1, \sigma_2, \sigma_3)^T
\tag{2.4}
$$

which are explicitly written in the form,

$$
a_N = \sigma_N, \quad e_x = \frac{2\sigma_1 - \sigma_2 - \sigma_3}{\sqrt{6}}, \quad e_y = \frac{\sigma_2 - \sigma_3}{\sqrt{2}}, \quad a_c = \frac{\sigma_1 + \sigma_2 + \sigma_3}{\sqrt{3}}.
\tag{2.5}
$$

The matrices of the equivalent representation $\Gamma' = R\Gamma R^{-1}$ are expressed using these newly constructed molecular orbitals as the basis, i.e.,

$$
\Gamma'(E) = \begin{pmatrix} 1 & 0 & 0 & 0 \\ 0 & 1 & 0 & 0 \\ 0 & 0 & 1 & 0 \\ 0 & 0 & 0 & 1 \end{pmatrix} \quad
\Gamma'(C^+) = \begin{pmatrix} 1 & 0 & 0 & 0 \\ 0 & -\frac{1}{2} & -\frac{\sqrt{3}}{2} & 0 \\ 0 & \frac{\sqrt{3}}{2} & -\frac{1}{2} & 0 \\ 0 & 0 & 0 & 1 \end{pmatrix} \quad
\Gamma'(C^-) = \begin{pmatrix} 1 & 0 & 0 & 0 \\ 0 & -\frac{1}{2} & \frac{\sqrt{3}}{2} & 0 \\ 0 & -\frac{\sqrt{3}}{2} & -\frac{1}{2} & 0 \\ 0 & 0 & 0 & 1 \end{pmatrix}
$$

$$
\Gamma'(\sigma_v) = \begin{pmatrix} 1 & 0 & 0 & 0 \\ 0 & 1 & 0 & 0 \\ 0 & 0 & -1 & 0 \\ 0 & 0 & 0 & 1 \end{pmatrix} \quad
\Gamma'(\sigma_v') = \begin{pmatrix} 1 & 0 & 0 & 0 \\ 0 & -\frac{1}{2} & -\frac{\sqrt{3}}{2} & 0 \\ 0 & -\frac{\sqrt{3}}{2} & \frac{1}{2} & 0 \\ 0 & 0 & 0 & 1 \end{pmatrix} \quad
\Gamma'(\sigma_v'') = \begin{pmatrix} 1 & 0 & 0 & 0 \\ 0 & -\frac{1}{2} & \frac{\sqrt{3}}{2} & 0 \\ 0 & \frac{\sqrt{3}}{2} & \frac{1}{2} & 0 \\ 0 & 0 & 0 & 1 \end{pmatrix}.
\tag{2.6}
$$

The representation Γ' consists of two irreducible representations (IR), a 2-dimensional one and a 1-dimensional one that appears twice. These representations cannot be decomposed into smaller representations by any similarity transformation. Due to their symmetry, the two inequivalent IRs are identified by the Mulliken symbols E and A_1, respectively. More information about these symbols can be found in Tab 2.1.

Symbol	Property
A	symmetric with respect to rotations around the principal axis (1-dimensional)
E	degenerate (2-dimensional)
Subscript 1	symmetric w.r.t rotations about a C_2 axis perpendicular to the principle axis or symmetric to the reflection about the principle plane
Subscript 2	antisymmetric w.r.t rotations about a C_2 axis perpendicular to the principle axis or antisymmetric to the reflection about the principle plane

Table 2.1: Mulliken symbols for irreducible representations. The standard convention takes the Z-axis as the principal axis of the system (i.e., the NV axis) and the XZ-plane as the principal plane (i.e., σ_v in Fig 2.2(d)). A symmetry axis is said to be a C_2 axis for an object, when this object remains unchanged after rotating it around the axis by the angle π. See more about the Mulliken symbols in Chap 4.5 of Ref. [31]

It is easy to verify that both a_N and a_c are unchanged by all symmetry operations. They are therefore said to transform as IR A_1, or to have A_1 symmetry. Similarly, e_x and e_y live in a 2-dimensional invariant subspace associated with the IR E. These e orbitals are therefore said to transform as the IR E and have the E symmetry. Note also that e_x is symmetric and e_y is antisymmetric with respect to the reflection in the XZ plane (the principal plane), as shown in Fig 2.2(d). These two orbitals are said to have E_1 and E_2 symmetry, respectively. The subscripts 1 and 2 are also taken from the Mulliken symbols in Tab 2.1.

2.2.2. ELECTRON-NUCLEI INTERACTION

In this section, we will study the effect of the electron-nucleus Coulomb interaction on the symmetry-adapted molecular orbitals given in Eq (2.5). The goal is to determine the energy eigenstates and their energy order.

The electron-nucleus interaction can be expressed in terms of the atomic dangling orbitals as follows:

$$V = v_n |\sigma_N\rangle\langle\sigma_N| + \sum_i v_c |\sigma_i\rangle\langle\sigma_i| + h_c \sum_{i\neq j} |\sigma_i\rangle\langle\sigma_j| + h_n \sum_i \left(|\sigma_i\rangle\langle\sigma_N| + h.c.\right), \qquad (2.7)$$

where v_n and v_c are the Coulomb interactions of the dangling nitrogen and carbon orbitals, h_c is the interaction strength between two carbons, and h_n is the interaction strength between a carbon and the nitrogen. Note that $|h| \ll |v_n| \ll |v_c|$ [36].

It's easy to check that the a_N and a_C orbitals are mixed by the Coulomb interaction, which can be seen by a straightforward calculation, i.e.,

$$\langle a_N| V |a_C\rangle = \sqrt{3}h_n, \quad \langle a_N|V|e_{x/y}\rangle = \langle a_C|V|e_{x/y}\rangle = \langle e_x|V|e_y\rangle = 0. \qquad (2.8)$$

The e_x and e_y orbitals, however, are the eigenstates with energy $E_{e_{x/y}} = \langle e_{x/y}|V|e_{x/y}\rangle = v_c - h_c$. Then, for simplicity, we look at the subspace of a_N and a_C only, within which the Coulomb interaction reads

$$V = v_n |a_N\rangle\langle a_N| + (v_c + 2h_c) |a_C\rangle\langle a_C| + \sqrt{3}h_n(|a_N\rangle\langle a_C| + |a_C\rangle\langle a_N|). \qquad (2.9)$$
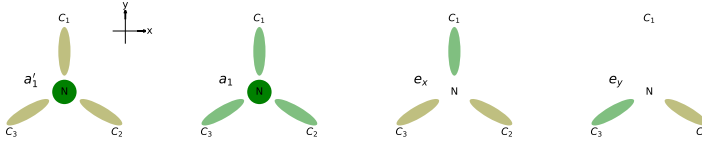
Figure 2.3: NV molecular orbitals that transform as the IRs of the C_{3v} point group. The nitrogen (labeled N) and three carbons (labeled C) are shown, where the perspective is along the NV-axis or the z-axis. The x-axis is defined to go through C_1 and the nitrogen projection point on the carbon plane, which is in the σ_v plane in Fig 2.2. Each orbital is a linear combination of the dangling bonds from the nitrogen and the three carbons. The color scale roughly represents the sign and occupation of each orbital. Note that the blob containing the nitrogen represents its dangling orbital σ_N, while other blobs represent the dangling orbitals (σ_1, σ_2 and σ_3) from the carbons. Figure adapted from Ref. [12].

The eigenvalues and eigenvectors in this subspace are given by

$$
\begin{aligned}
|a_1\rangle = \alpha |a_N\rangle + \sqrt{1-\alpha^2}\,|a_C\rangle, \quad & E_{a_1} = \frac{1}{2}(\nu_n + \nu_c + 2h_c) + \frac{1}{2}\Delta, \\
\left|a_1'\right\rangle = \alpha |a_C\rangle - \sqrt{1-\alpha^2}\,|a_N\rangle, \quad & E_{a_1'} = \frac{1}{2}(\nu_n + \nu_c + 2h_c) - \frac{1}{2}\Delta,
\end{aligned}
\tag{2.10}
$$

where $\alpha^2 = 12h_n^2 / \left[(\nu_n - \nu_c - \Delta)^2 + 12h_n^2\right]$ and $\Delta^2 = (\nu_c + 2h_c - \nu_n)^2 + 12h_n^2$. This set of molecular orbitals $\{a_1', a_1, e_x, e_y\}$ have been extensively used to describe NV centers in diamond [18, 36]. To get an idea about the symmetries, these orbitals are schematically illustrated in Fig 2.3.

By simply including the Coulomb interaction in Eq (2.7), group theory qualitatively predicts that a_1' has lower energy than a_1, which in turn has lower energy than the degenerate e orbitals [36]. This group theory prediction is in agreement with ab initio calculations [20, 24]. Furthermore, ab initio calculations also found that the orbital a_1' lies within the valence band, while other orbitals lie within the band gap [20, 24]. The energy ordering is shown schematically in Fig 2.4.

It is important to note that these orthogonal dangling atomic orbitals used here form only a limited basis set; hence, their linear combinations only approximately describe the molecular orbitals of the NV center. However, when the additional contribution from the rest of the crystal is included, most ab initio calculations find molecular orbitals that resemble these highly localized orbitals predicted by group theory [17, 20].

2.3. ELECTRONIC STRUCTURE

In this section, we construct a set of basis states for the six electrons in the NV structure. These constructed basis states transform as the IRs of the C_{3v} group, making it easier to analyze other weaker effects such as spin-spin interaction, spin-orbit interaction, and lattice strain. The objective of this section is to establish a qualitative understanding of the fine structure of the energy levels shown in Fig 2.5.
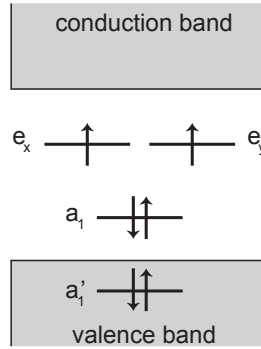
Figure 2.4: The energy ordering of the NV molecular orbitals with respect to the diamond band gap and their occupation for the ground-state spin-triplets. The relevant molecular orbitals are presented in Eq (2.5), and the spin-triplet states are given in Eq (2.12). Figure taken from Ref. [1]

2.3.1. SYMMETRY ADAPTED BASIS STATES

Considering the spin states of the six electrons, the four molecular orbitals in Eq (2.5) provide eight modes in total that can be occupied by the 6 outer electrons. If two more electrons were added in any of these electron configurations, all eight electrons would form a singlet and the associated spatial wave function would be totally symmetric, which is equivalent to the state of an atom whose shells are fully filled [17, 18, 36]. The NV center is thus often modeled as a two-hole system for simplicity [17, 36].

GROUND STATES

In the ground-state configuration, as demonstrated in Fig 2.4, the two lower energy a orbitals are filled with four electrons, and the two higher energy e orbitals are half-filled with the remaining two, as shown in Fig 2.1(b). The corresponding hole-configuration is labeled as e^2, indicating that two holes are present in the e orbitals, with one in e_x and one in e_y.

To determine the lowest energy state, it is assumed that the Coulomb repulsion between the outer shell electrons is stronger than the spin-orbit coupling, which is in turn stronger than all other interactions [18, 36]. Based on the first Hund's rule, this results in the ground state energy being associated with a spatial wave function that is antisymmetric upon particle exchange [7]. For the e^2 hole-configuration, such antisymmetric spatial wave function is unique and expressed as

$$\left| e_x e_y - e_y e_x \right\rangle = \frac{e_x \otimes e_y - e_y \otimes e_x}{\sqrt{2}}, \tag{2.11}$$

which is coincidently symmetric with respect to the identity and the two rotational operations, but antisymmetric with respect to the three reflection operations. In the language of group theory, this spatial wave function transforms as the IR A_2, which is the third IR of the C_{3v} group. More information on the IR A_2 can be found in Appendix 2.6.1.
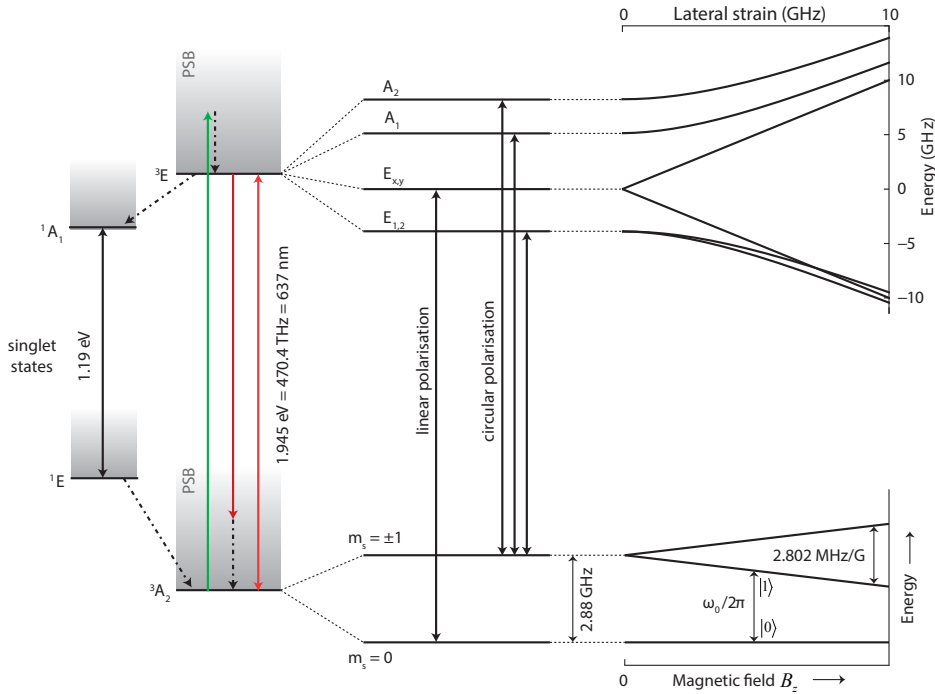
Figure 2.5: Energy level diagram of the negatively charged NV center. **Bottom center**: The NV ground-state spin-triplets ($S = 1$) are denoted as $^3A_2$ in Eq (2.12). The zero field splitting ($\Delta_{\mathrm{ZFS}} \approx 2.88$ GHz) is mainly due to the spin-spin interaction (Chap 2.3.3), which separates the $m_s = 0$ state and the two degenerate states $m_s = \pm 1$. Resonant optical transitions are called the zero phonon line (ZPL), and off-resonant transitions are said to be in the phonon side band (PSB) (Chap 2.4.2). **Bottom right**: An external magnetic field (along the NV axis or z-axis) lifts the degeneracy within the $^3A_2$ manifold by Zeeman splitting and allows the definition of a qubit (Chap 3.1). **Top center**: The manifold of the first-excited states are labeled as ^3E, see Eq (2.14). The ^3E states get split by the spin-spin (Chap 2.3.3) and the spin-orbit (Chap 2.3.2) interaction, even at zero strain. Excitation of the NV from the ground state to one of the six ^3E states can occur by optical excitations with the selection rules discussed in Chap 2.4.1. **Left**: The electronic state can decay from ^3E to $^3A_2$ indirectly through the ground-state singlets, $^1A_1$ and ^1E. This is the so-called intersystem crossing (Chap 2.5), during which the spin multiplicity is changed. **Top right**: To the first order, the lateral strain (in the XY-plane) does not affect the $^3A_2$ states, but changes the energies of the ^3E states (Chap 2.3.4). Figure adapted from Pfaff [38], Bernien [10], and Hensen [27].

2

Furthermore, according to the Pauli exclusion principle, the associated spin wave function should be triplet, the total wave functions are hence given by

$$^3A_2: \quad \begin{array}{lcl} |m_s = +1\rangle & = \\ |m_s = \ 0\rangle & = |e_x e_y - e_y e_x\rangle \otimes \\ |m_s = -1\rangle & = \end{array} \begin{cases} |\uparrow\uparrow\rangle \\ |\uparrow\downarrow + \downarrow\uparrow\rangle \\ |\downarrow\downarrow\rangle \end{cases} \quad (2.12)$$

where m_s is the magnetic quantum number and represents the spin angular momentum component along the NV-axis. The symbols $|\uparrow\rangle$ and $|\downarrow\rangle$ represent the "spin up" and "spin down" states, respectively. These three states make up the $^3A_2$ manifold, where the Mulliken symbol A_2 indicates the spatial symmetry and the superscript $2S+1$ on the left represents the spin multiplicity. The symmetry of the total wave functions can be easily determined: $|m_s = \pm 1\rangle$ transform as the IR E, while $|m_s = 0\rangle$ transforms as the IR A_1.

Finding symmetry-adapted basis states in the e^2 hole configuration with a singlet spin wave function is however more difficult, as the spatial wave function must be symmetric upon particle exchange, and the total wave function must transform as IRs of the C_{3v} group. This difficulty is even greater when trying to find basis states to describe the first-excited states, as given in Eq (2.14).

Fortunately, group theory provides a powerful tool, the projection operators for each IR [13, 31]. By applying these projection operators on the combinations of spatial and spin wave functions, the desired basis states can be obtained [36]. The use of projection operators is detailed in Appendix 2.6.1. Here, we directly write down the three spin singlets (S=0) within the e^2 hole-configuration, i.e.,

$$^1E: \quad \begin{array}{lcl} |^1E_1\rangle & = & |e_x e_x - e_y e_y\rangle \otimes |\uparrow\downarrow - \downarrow\uparrow\rangle \\ |^1E_2\rangle & = & |e_x e_y + e_y e_x\rangle \otimes |\uparrow\downarrow - \downarrow\uparrow\rangle \end{array} \quad (2.13)$$
$$^1A_1: \quad |^1A_1\rangle = |e_x e_x + e_y e_y\rangle \otimes |\uparrow\downarrow - \downarrow\uparrow\rangle$$

The states $|^1E_1\rangle$ and $|^1E_2\rangle$ belong to the ^1E manifold and both transform as the IR E. It is noteworthy to explain the symbols inside the kets. The superscript on the left signifying the spin multiplicity, which allows differentiation from the optically excited states that share the same symmetry, as given in Eq (2.14). Additional subscripts are used to distinguish the degenerate eigenstates transforming as the 2-dimensional IR E.

In accordance with the symmetry, the Coulomb interaction does not alter the degeneracy of the two ^1E states, as explained in detail in Appendix E.2 of Ref. [41]. Furthermore, due to the highest symmetry of its spatial wave function, the Coulomb interaction of the state $|^1A_1\rangle$ is stronger than that of the other states in the e^2 configuration. Moreover, ab initio calculations also indicate that the $|^1A_1\rangle$ state has lower energy compared to the optically excited states discussed below [18, 36].

FIRST-EXCITED STATES

The hole-configuration ae has a higher energy and is achieved through the use of optical pulses that promote an electron from a_1 to e_x or e_y. Due to the negligible spin-orbit coupling, the optical transitions are spin-conserving, resulting in the creation of spin-triplet orbital-doublet states with the ae hole-configuration, known as the first-excited

states [11, 18]. The spin-conserving nature of the optical transitions is further discussed in Chapter 2.3.2.

It's worth noting that both the ground and first-excited states of the NV center are characterized by the half-filled molecular orbitals, which lie within the diamond band gap, as depicted in Fig 2.4. The optical transitions hence do not alter its charge state, making the optical properties similar to those of a single ion trapped in the lattice [11].

The presence of one of the holes in e_x, e_y or their superposition greatly complicates the total wave functions of the states transforming as the IRs. Nonetheless, similar to the spin-singlets in the ae configuration, these basis states can be efficiently constructed using projection operators of the IRs, as discussed in Appendix 2.6.1. The expression for these basis states are given below [18, 36],

$$^3\text{E}: \quad \begin{aligned} |A_1\rangle &= |E_-\rangle \otimes |\uparrow\uparrow\rangle - |E_+\rangle \otimes |\downarrow\downarrow\rangle \\ |A_2\rangle &= |E_-\rangle \otimes |\uparrow\uparrow\rangle + |E_+\rangle \otimes |\downarrow\downarrow\rangle \\ |E_y\rangle &= |Y\rangle \otimes |\uparrow\downarrow + \downarrow\uparrow\rangle \\ |E_x\rangle &= |X\rangle \otimes |\uparrow\downarrow + \downarrow\uparrow\rangle \\ |E_1\rangle &= |E_-\rangle \otimes |\downarrow\downarrow\rangle - |E_+\rangle \otimes |\uparrow\uparrow\rangle \\ |E_2\rangle &= |E_-\rangle \otimes |\downarrow\downarrow\rangle + |E_+\rangle \otimes |\uparrow\uparrow\rangle \end{aligned} \quad , \tag{2.14}$$

where the antisymmetric spatial wave functions $|E_\pm\rangle = |a_1 e_\pm - e_\pm a_1\rangle$ with $|e_\pm\rangle = \mp(e_x \pm i e_y)$, $|X\rangle = (|E_+\rangle - |E_-\rangle)/\sqrt{2}$ and $|Y\rangle = i(|E_+\rangle + |E_-\rangle)/\sqrt{2}$ all transform as the IR E. The manifold containing these first-excited states is hence denoted as ^{3}E. It is important to emphasize that $|E_y\rangle$, $|E_1\rangle$, and $|^1E_1\rangle$ are completely identical in terms of their symmetry, and are symmetric under the reflection in the principal plane (Fig 2.2(d)). Similarly, $|E_x\rangle$, $|E_2\rangle$, and $|^1E_2\rangle$ have the same symmetry, but are antisymmetric under the same reflection in the principal plane. Note that two objects with the same symmetry means that any of the C_{3v} symmetry operations has the same effect on both objects.

Even under low strain, $|A_1\rangle$, $|A_2\rangle$, and $\{|E_1\rangle, |E_2\rangle\}$, as well as $\{|E_x\rangle, |E_y\rangle\}$ are split by spin-orbit and spin-spin interactions. Furthermore, since these interactions transform as the IR A_1, they only couple states with the same symmetry, as shown by Eq (2.19) and Eq (2.21). As will become clear in the following sections, these basis states greatly simplify the analysis of spin-spin and spin-orbit interactions.

2.3.2. SPIN-ORBIT INTERACTION

In the reference frame of an electron, the nucleus is seen orbiting it. The nuclear potential thus produces a magnetic field that is felt by the electron. The interaction between the electron orbital angular momentum and the electron spin angular momentum is known as the spin-orbit interaction, which is written as (using the SI units) [34, 37]

$$H_{\text{SO}} = \frac{1}{n_{\text{so}}} \sum_k \left[(\nabla_k V) \times \vec{p}_k \right] \cdot \vec{s}_k, \tag{2.15}$$

where V is the nuclear potential, $\vec{p}_k$ ($\vec{s}_k$) is the momentum (spin-1/2) operator of the electron labeled as k, and $n_{\text{so}} = 2m_e^2 c^2$ with m_e the electron mass, c the speed of light. To qualitatively understand how the spin-orbit interaction acts on the system, we can

find all the non-zero matrix elements of the orbital operator $\vec{O} = (\nabla V) \times \vec{P}$ in the basis of $|e_x\rangle$, $|e_y\rangle$ and $|a_1\rangle$. Note that $|a_1'\rangle$ is ignored, as it is fully filled in both the ground and first-excited states.

We determine all non-zero matrix elements by examining the symmetry. The full analysis can be found in Chapter 2.6.2. Here, we write down the non-zero matrix elements,

$$\langle e_y | O_x | a_1 \rangle = -\langle e_x | O_y | a_1 \rangle = i n_{\text{so}} \lambda_\perp, \quad \langle e_x | O_z | e_y \rangle = i n_{\text{so}} \lambda_\parallel \qquad (2.16)$$

where $\lambda_\parallel$ ($\lambda_\perp$) represents the strength for the parallel (perpendicular) part of the spin-orbit interaction. Based on experimental data, it has been estimated that $\lambda_\parallel = 5.3$ GHz and $\lambda_\perp = 0.2$ GHz [9]. For convenience, we define a set of operators that are analogous to the angular momentum operators, i.e.,

$$l^x = i\left(|e_y\rangle\langle a_1| - |a_1\rangle\langle e_y|\right), \quad l^y = i\left(|a_1\rangle\langle e_x| - |e_x\rangle\langle a_1|\right), \quad l^z = i\left(|e_x\rangle\langle e_y| - |e_y\rangle\langle e_x|\right), \qquad (2.17)$$

which enables us to write down the spin-orbit interaction in a simpler form,

$$H_{\text{SO}} = \lambda_\perp \underbrace{\sum_k \left(l_k^x s_k^x + l_k^y s_k^y\right)}_{H_{\text{SO},\perp}} + \lambda_\parallel \underbrace{\sum_k l_k^z s_k^z}_{H_{\text{SO},\parallel}}. \qquad (2.18)$$

It is straightforward to check that, the spin-orbit interaction does not appear in the basis of the $^3A_2$ ground-states, where matrix elements of H_{SO} are all zero. On the contrary, in the basis of the ^1E, ^1A and ^3E states, the spin-orbit interaction is written in the form [22, 36]

$$H_{\text{SO},\parallel} = \lambda_\parallel \left(|A_1\rangle\langle A_1| + |A_2\rangle\langle A_2| - |E_1\rangle\langle E_1| - |E_2\rangle\langle E_2|\right)$$
$$H_{\text{SO},\perp} = \sqrt{2}\lambda_\perp \left(|A_1\rangle\langle{}^1A_1| + |E_1\rangle\langle{}^1E_1| + i|E_2\rangle\langle{}^1E_2|\right) + H.c. \qquad (2.19)$$

Note that the effect of $H_{\text{SO},\perp}$ cannot be observed within the ^3E manifold, but it mixes the spin-triplet ^3E states with the spin-singlet ground-states. This leads to the change in the spin state, which is known as the intersystem crossing, see discussion in Chap 2.5.

Note that $|A_1\rangle$ and $|{}^1A_1\rangle$ are coupled because they have the same symmetry. In addition, $|E_1\rangle$ ($|E_2\rangle$) and $|{}^1E_1\rangle$ ($|E_2\rangle$) also possess the same symmetry so that they are also coupled.

2.3.3. Spin-spin interaction

The Hamiltonian governing the spin-spin interactions may be written in the form [34]

$$H_{\text{SS}} = -\frac{\mu_0}{4\pi} \frac{g^2 \beta^2}{r^3} \left(3(\vec{s}_1 \cdot \vec{r})(\vec{s}_2 \cdot \vec{r}) - \vec{s}_1 \cdot \vec{s}_2\right), \qquad (2.20)$$

where $\vec{r}$ is the spatial vector between two electrons, β is the Bohr magneton, g is the electron spin g-factor and μ_0 is the magnetic permeability in free space.

The spin-spin interaction not only changes the energy of the ^3E states, but also mixes them. Inside the ^3E manifold, the spin-spin interaction is calculated to be [36]

$$H_{\text{SS}} = \Delta\left(|A_1\rangle\langle A_1| + |A_2\rangle\langle A_2| + |E_1\rangle\langle E_1| + |E_2\rangle\langle E_2|\right) - 2\Delta\left(|E_x\rangle\langle E_x| + |E_y\rangle\langle E_y|\right)$$
$$+ 2\Delta'\left(|A_1\rangle\langle A_1| - |A_2\rangle\langle A_2|\right) + \Delta''\left(|E_1\rangle\langle E_y| + |E_y\rangle\langle E_1| - i|E_2\rangle\langle E_x| + i|E_x\rangle\langle E_2|\right), \qquad (2.21)$$

where $3\Delta \approx 1.42$ GHz and $\Delta' \approx 1.55$ GHz characterize the spin-spin induced zero-field splittings [34, 36, 42]. The terms with Δ'' represent the transitions that are not spin-conserving, and inside the ^3E manifold. They are typically negligible, especially for low strain [36].

In the basis of the $^3A_2$ ground-states, the spin-spin interaction is calculated to be in the form [17]

$$H_{SS} = -\frac{2\Delta_{ZFS}}{3}|m_s = 0\rangle\langle m_s = 0| + \frac{\Delta_{ZFS}}{3}\Big(|m_s = -1\rangle\langle m_s = -1| + |m_s = +1\rangle\langle m_s = +1|\Big),$$
(2.22)

where the so-called zero field energy splitting (ZFS) Δ_{ZFS} is calculated to be around 2.88 GHz [17, 36]. This theoretical prediction agrees with the experimental measurements [16, 18]. An external magnetic field along the NV-axis can further split the $m_s = \pm 1$ states, which allows using the subspace of states with $m_s = 0, -1$ as a qubit, see discussion in Chap 3.1.

2.3.4. Lattice strain

Strain describes change of the atomic positions when the lattice is stretched, which can be produced by temperature, stress (forces applied to the solid structure), or electric field (via piezoelectric effect) [36]. In the 3-dimensional Euclidean space, strain is represented by the tensor ϵ_{ij} that acts on the infinitesimal vector $\vec{R} = (R_1, R_2, R_3)$ connecting two atoms. The change in the components of $\vec{R}$ can be expressed as,

$$\delta R_i = R'_i - R_i = \sum_j \epsilon_{ij} R_j,$$
(2.23)

Note that strain also induces rotations of the whole system, which do not alter the NV structure's symmetry and are therefore disregarded [36, 48]. For more information about strain, we recommend the online course on Structural Mechanics [48].

The primary effect of strain is to modify the electron-nuclei Coulomb interaction given in Eq (2.7). This modification is due to the alteration in relative atomic positions induced by the strain. According to the Born–Oppenheimer approximation, the relative position of an electron orbital does not change with respect to its associated nuclei, so the self-interactions remain unchanged. Moreover, we also assume that the interaction strength between two atomic orbitals depends solely on the distance between their associated nuclei [36].

The effect of strain can then be easily calculated with these simplifications. The Coulomb interaction is first expanded into a Taylor series based on the changes in relative positions. Then, the change in the Coulomb interaction can be written as a function of the strain tensor using Eq (2.23), as detailed in Appendix 2.6.3.

The most important effect of strain is to remove the degeneracy of the electron orbitals (e_x, e_y) and mix them. This arises from the leading-order term in the Taylor expansion of the change in Coulomb interaction, which gives the strain Hamiltonian,

$$H_{strain} = \delta_{E_1}\underbrace{\Big(|e_x\rangle\langle e_x| - |e_y\rangle\langle e_y|\Big)}_{V_{E_1}} + \delta_{E_2}\underbrace{\Big(|e_x\rangle\langle e_y| + |e_y\rangle\langle e_x|\Big)}_{V_{E_2}}.$$
(2.24)

The strain-induced mixing between the a_1 and the e orbitals is neglected due to the large energy gap between them [18, 36].

The strain Hamiltonian represents the lateral strain that is in the XY-plane, which transforms as the IR E. It consists of two terms, V_{E_1} and V_{E_2}, which which are symmetric and antisymmetric, respectively, with respect to reflection in the principal plane, as depicted in Fig 2.2(d). They are hence said to have E_1- and E_2-symmetries, respectively. Note that the strain Hamiltonian that transforms as the IR A_1 only induces contraction or expansion of the system and does not change the relative energies, which is hence neglected [36].

The antisymmetric spatial wave function $|e_x e_y - e_y e_x\rangle$ is an eigenstate of the strain Hamiltonian, resulting in the $^3A_2$ ground-states remaining unchanged by strain to the first order. However, strain greatly affects the ground-state singlets and excited-state triplets, leading to their energies being changed and these states being mixed. This is described by the interaction terms given in the form [22, 36],

$$
\begin{aligned}
V_{E_1} &= |E_x\rangle\langle E_x| - |E_y\rangle\langle E_y| + \left(|E_1\rangle\langle A_1| - |E_2\rangle\langle A_2| + 2\left|^1E_1\right\rangle\left\langle^1A_1\right| + H.c.\right), \\
V_{E_2} &= |E_x\rangle\langle E_y| + i|E_2\rangle\langle A_1| - i|E_1\rangle\langle A_2| + 2\left|^1E_2\right\rangle\left\langle^1A_1\right| + H.c..
\end{aligned}
\tag{2.25}
$$

The energy splittings of the mixed excited triplet states ^3E are schematically demonstrated as functions of δ_{E_1} on the top right of Fig 2.5 [36].

2.4. OPTICAL PROPERTIES

NV centers in diamond have unique optical properties that are favorable for numerous applications. Optical excitation enables transitions from the $^3A_2$ ground states to the ^3E excited states. At cryogenic temperatures (<10 K), energy separations between the ^3E states, typically few-GHz, are large compared to their lifetime-limited line widths of about 13 MHz. These optical transitions can thus be individually resolved [11].

2.4.1. SELECTION RULES FOR OPTICAL TRANSITIONS

For the state $|\psi_i\rangle$ in the $^3A_2$ manifold and the state $|\psi_f\rangle$ in the ^3E manifold, an optical transition is allowed only if the corresponding electric dipole matrix element is non-zero [12], i.e.,

$$
\langle\psi_f|\vec{d}\cdot\vec{E}|\psi_i\rangle \neq 0
\tag{2.26}
$$

where $\vec{d}$ and $\vec{E}$ are the electric dipole moment and electric field, respectively. The selection rules for the transitions between $^3A_2$ and ^3E states are given in Tab 2.2 [12].

The spin-orbit interaction is so weak (≈ 5.3 GHz, see Chap 2.3.2) that it is neglected for optical transitions, and the electronic spin states are thus preserved [18, 35]. Therefore, by examining the symmetry of their spatial wave functions, one can determine the polarization axes for allowed optical transitions. This is the same as the symmetry analysis for the spin-orbit interaction (see Chap 2.3.2).

To give an example, we consider the optical transition between $\left|^3A_2\right\rangle$ and $|E_x\rangle$. First, the spatial wave function of $\left|^3A_2\right\rangle$ is antisymmetric with respect to the reflection in the XZ-plane, i.e., σ_v, see Eq (2.6). However, the $\hat{z}$-polarized electric field and the spatial

Polarization	$|A_1\rangle$	$|A_2\rangle$	$|E_1\rangle$	$|E_2\rangle$	$|E_x\rangle$	$|E_y\rangle$
$|^3A_{2,-1}\rangle$	$\hat{\sigma}_+$	$\hat{\sigma}_+$	$\hat{\sigma}_-$	$\hat{\sigma}_-$		
$|^3A_{2,0}\rangle$					$\hat{x}$	$\hat{y}$
$|^3A_{2,+1}\rangle$	$\hat{\sigma}_-$	$\hat{\sigma}_-$	$\hat{\sigma}_+$	$\hat{\sigma}_+$		

Table 2.2: Selection rules for optical transitions between the $^3A_2$ ground-states and the ^3E excited-states. The linear polarization is represented by $\hat{x}$ and $\hat{y}$, while $\hat{\sigma}_\pm = \hat{x} \pm i\hat{y}$ denote the circular polarization.

wave function of $|E_x\rangle$ both stay invariant under this reflection. As a result, the corresponding matrix element is antisymmetric with respect to σ_v. However, a matrix element is also a scalar, which should not be changed by any symmetry operations. Therefore, this matrix element representing this particular optical transition should vanish.

2.4.2. Phonon side band transitions

The transitions between $^3A_2$ and ^3E can be excited resonantly at 637 nm (red), but it turns out that it is more efficient to excite the transitions using green light at high temperature [4]. Moreover, when the electronic spin decays from ^3E excited states, the emitted photons are often with longer wave length so that its energy is lower than the resonant energy. The main reason for this is that both photon absorption and emission processes can create lattice vibration, meaning that phonons are emitted. The optical transition without emitting phonons is called the zero-phonon line (ZPL), which is otherwise said to be in the phonon-side band (PSB).

Modelling the lattice vibration as a single Harmonic oscillator suffices for a qualitative understanding of the PSB emissions. However, a more in-depth model is needed to accurately describe the luminescence spectra [5, 21]. Furthermore, the consideration of the symmetries of multiple phonon modes is essential for understanding the change in spin multiplicity during the optical transitions (see Chap. 2.5).

Each electronic state is associated with a set of lattice vibrational modes that is quasi-continuous [18]. In addition, the lattice vibration is assumed to be decoupled from the electronic state, which is based on the separation of the electronic and nuclear wave functions, according to the Born-Oppenheimer approximation [7]. Due to Coulomb repulsion, the electronic state determines a common equilibrium configuration of the nuclear spins for the vibrational levels.

The Franck-Condon principle states that the rate of an optical transition is largely influenced by the vibrational levels associated with the ground and first-excited states [7]. From a semi-classical viewpoint, the optical transitions of the electronic spin occur much faster than the motions of the nucleus. Thus, during an optical excitation, when the system transitions to a new vibrational level, the nuclear configuration should remain unchanged. This means that the optical transition rate increases as the overlap between the old and new vibrational levels gets larger.

Huang-Rhys model
The Huang-Rhys model is commonly used to interpret the experimental spectra [49]. This model replaces the quasi-continuous lattice vibrational modes with a single har-
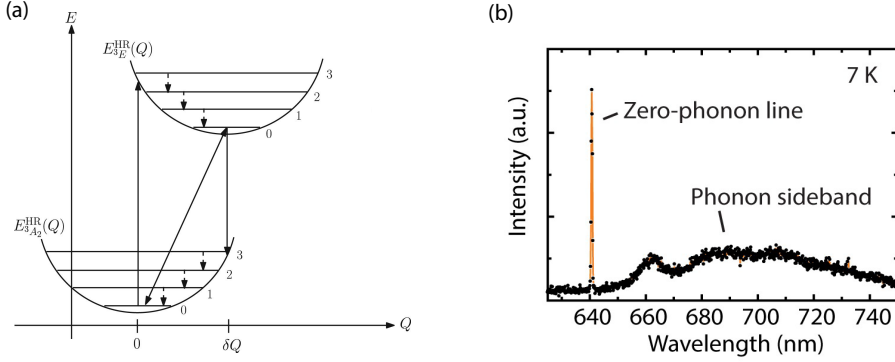
Figure 2.6: (a) The Huang-Rhys model in the Franck-Condon picture with a single harmonic vibrational mode. The potential energies $E^{HR}_{3A_2}(Q)$ and $E^{HR}_{3E}(Q)$ (curved lines) are approximated as harmonic functions of the nuclear displacement coordinate Q. δQ is the equilibrium nuclear coordinate associated with the ^{3}E states. The horizontal lines represent the vibrational levels associated with each electronic state. The diagonal transition (solid arrow) between the lowest vibrational levels of two electronic states corresponds to the ZPL emission. The non-radiative transitions are denoted as dashed arrows, where phonons are lost into the environment. (b) The emission spectrum at cryogenic temperature, which consists of a sharp ZPL and a broad PSB. Due to the involvement of lattice vibration or phonons, when the electronic state decays from the ^{3}E excited states to the ^{3}A$_2$ ground states, most of the emitted photons are red-shifted ($\approx$ 97% at cryogenic temperature) and go into the PSB. Figure (a) adapted from Ref. [18], and Figure (b) taken from Ref. [29].

monic oscillator and represents the nuclear configuration with a single 1-dimensional coordinate, denoted as Q [5, 18]. The potential energies of the ^{3}A$_2$ and ^{3}E states are then approximated as quadratic functions of Q [18], i.e.,

$$E^{HR}_{3A_2}(Q) = \frac{1}{2}\omega^2 Q^2$$
$$E^{HR}_{3E}(Q) = E_{3E} + aQ + \frac{1}{2}bQ^2 + \frac{1}{2}\omega^2 Q^2, \tag{2.27}$$

where E_{3E} is the electronic energy of the excited state at equilibrium nuclear coordinate of the ground state ($Q = 0$), a and b are the linear and quadratic electron–vibration coupling parameters of the excited state, ω is the frequency of the lattice vibration associated with the ^{3}A$_2$ ground states.

In the Huang-Rhys model, the Franck-Condon principle simply says that the most probable transition is "vertical", during which the nuclear coordinate Q is unchanged. As shown in Fig 2.6(a), after optically exciting a ^{3}A$_2$ state with $Q = 0$ (i.e., no vibration) to a ^{3}E state, the nuclear coordinate will be quickly shifted to its equilibrium δQ. This is due to the electron-vibration coupling redistributing the electrons, which is a non-radiative process with the relaxation energy [18]

$$E_R = E^{HR}_{3E}(\delta Q) - E^{HR}_{3E}(0) = a\,\delta Q. \tag{2.28}$$

where the second-order term of δQ is ignored as we assume that it is small. Furthermore,

it is easy to find out that $\delta Q \approx -a/(b+\omega^2)$ by rewriting the potential energy in the form

$$E_{3_E}^{\text{HR}}(Q) = E_{3_E} + \underbrace{aQ + (\omega^2 + b)Q\,\delta Q - \frac{1}{2}(\omega^2 + b)\delta Q^2}_{E_R} + \frac{1}{2}(\omega^2 + b)(Q - \delta Q)^2. \quad (2.29)$$

The process of redistributing electrons can then be described as the vibrational excitations or phonons with frequency $\sqrt{\omega^2 + b}$ being dissipated into propagating phonon modes, i.e., vibrations of the whole lattice. This relaxation process is mediated by the phonon-phonon interaction [22].

Due to the displacement δQ in the equilibrium coordinates, a $^3A_2$ ground-state without lattice vibration has non-zero overlaps with ^3E excited-states that contain vibrational excitations. Note that the change in the phonon frequency also contributes to such non-zero overlaps, which is yet secondary [18]. Experimentally, a wide PSB absorption spectrum with a peak around 570 nm has been observed [4]. It is important to emphasize again that it is an oversimplification to consider only a single vibrational mode. By including multiple phonon modes, first-principle calculations can yield an accurate description of the luminescence spectra [5, 21].

The emission process can also involve phonons. From the lowest vibrational level of the excited state, the system radiatively decays to all the vibrational levels of the ground state randomly. If the photon is not emitted at the ZPL, the phonon-phonon mediated decay will follow, leaving the system finally in the lowest vibrational level of the ground state. In this case, the emitted light is red-shifted, which leads to a wide PSB emission spectrum around 650-800 nm as well as a narrow ZPL [18]. Because the lattice vibration is frozen at cryogenic temperature, the ZPL is well separated from the PSB emission, as shown in Fig 2.6(b). Note that the PSB emission obscures the ZPL at room temperature [4].

The probability of emitting a ZPL photon is very low even at cryogenic temperature, which has been experimentally determined to be only about 3% [14, 19, 40]. This sets a limit on the rate of generating remote entanglement between NV centers [30, 39], see discussion in Chap 3.1.3.

2.5. INTERSYSTEM CROSSING

In the previous section, it was assumed that optical transitions conserve the spin state, meaning that the spin-orbit interaction was neglected. However, this is not accurate when considering the process of the electronic spin decaying back to the $^3A_2$ ground-states. This is because the spin-orbit interaction can couple an excited-state triplet (i.e., ^3E) with a ground-state singlet (i.e., $^1A_1$ and ^1E), when they share the same symmetry. That is to say, the electronic spin does not necessarily decay back to its original spin state. Moreover, for a ^3E triplet state that does not share the same symmetry with the ground-state singlets, the spin-phonon interaction in conjunction with the spin-orbit interaction can result in indirect coupling between a ^3E triplet state and a ground-state singlet, even if they possess different symmetries.

This leads to an important mechanism in NV centers and other solid-state atom-like impurities, which is known as the intersystem crossing (ISC). These non-radiative transitions between states with different spin multiplicity [18] allow for optical initialization
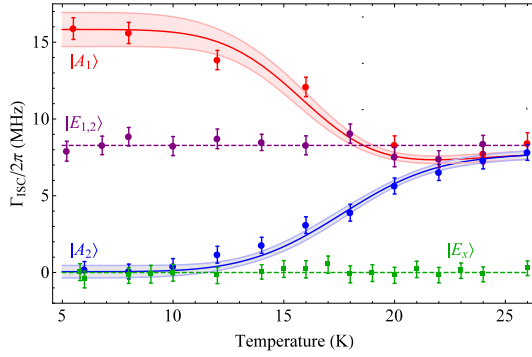
Figure 2.7: ISC rates from the ^{3}E states, which are extracted from the measurements of fluorescence decay times at $T \sim 5$ K. The blue and red bands are fits with 95% confidence intervals to the phonon-induced mixing model described in the text, and the purple and green lines are placed at the mean values of the corresponding data sets. Because $|A_2\rangle$ is not directly coupled to $|A_1\rangle$, so its ISC rates largely depends on the temperature. For the same reason, the ISC rate for $|E_{x,y}\rangle$ remains almost zero even at higher temperature, as the spin-phonon interaction does not couple them to other ^{3}E states at all. Figure adapted from Ref. [23].

of the electronic spin, but reduce the readout fidelity, as will be discussed in Chap 3.1.2. The ISC rates are experimentally determined for different ^{3}E states through indirect measurements, such as measurements of spin-resolved fluorescence lifetimes [23, 46]. To illustrate by example, see a recent measurement at cryogenic temperature in Fig 2.7 [23].

The experimental results have provided a comprehensive picture of the ISC mechanism [23, 32, 46]. To understand these experimental observations, we discuss the theoretical model developed in Ref. [22], as schematically depicted in Fig 2.8. The model first considers the perpendicular part of the spin-orbit interaction in Eq (2.19). For convenience, we replicate the equation here,

$$H_{\mathrm{SO},\perp} = \sqrt{2}\lambda_\perp \left(|A_1\rangle \left\langle {}^1A_1 \right| + |E_1\rangle \left\langle {}^1E_1 \right| + i\, |E_2\rangle \left\langle {}^1E_2 \right| \right) + H.c.$$

It is important to note that, to make the ISC transition energy-conserving, the lattice vibrational states need to be considered. That is to say, this perpendicular spin-orbit interaction couples the excited-state triplets $|A_1\rangle$ and $|E_{1,2}\rangle$ with no vibrational excitation to the resonant excited vibrational states associated with the ground-state singlets $|{}^1A_1\rangle$ and $|{}^1E_{1,2}\rangle$, respectively. However, as illustrated in Fig 2.5, the energy of $|{}^1E_{1,2}\rangle$ is much lower, the direct transition from $|E_{1,2}\rangle$ to $|{}^1E_{1,2}\rangle$ is hence negligible [22, 23]. Subsequently, the vibrational excitations of $|{}^1A_1\rangle$ are dissipated into propagating phonon modes through the phonon-phonon interaction. Such non-radiative relaxation process is as fast as about a few picoseconds [18, 22].

To explain the finite ISC rates of $|E_{1,2}\rangle$ and $|A_2\rangle$, we need to consider the spin-phonon interaction. The basic idea is to interpret the effect of phonon modes as inducing strain on the lattice [22]. Moreover, only phonon modes transforming as the IR E can induce lateral strain in the XY-plane, which couples different electronic orbital states, as discussed in Chap 2.3.4. The corresponding spin-phonon interaction is then given by [22]

$$H_{\mathrm{spin, phonon}} = \sum_{i,k} \lambda_{i,k} V_{E_i} (\hat{a}^\dagger_{i,k} + \hat{a}_{i,k}), \tag{2.30}$$
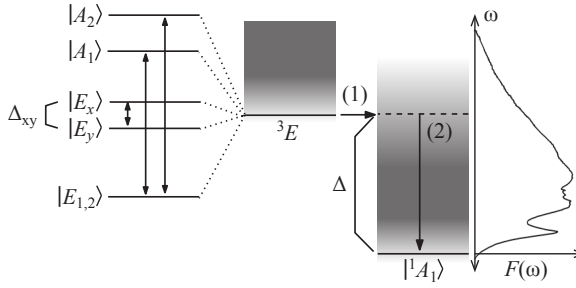
Figure 2.8: Schematic of phonon induced mixing inside the ^{3}E manifold, and the ISC process. The phonon-induced transitions are represented by solid arrows on the left, see the interaction in Eq (2.25). Note that this interaction also induces a mixing between $|E_{x,y}\rangle$ states and an energy separation Δ_{xy} between the new states. The quasi-continuum of the vibrational levels are represented by the shaded regions. The excited triplets without vibration are first coupled $|^1A_1\rangle$ with vibrational excitations, which is driven by the spin-orbit coupling in Eq (2.19). The vibrational excitations associated with $|^1A_1\rangle$ are quickly lost through a non-radiative decay process that is mediated by the phonon-phonon interaction. Figure adapted from Ref. [22].

where $\hat{a}^{\dagger}_{i,k}$ and $\hat{a}_{i,k}$ are the creation and annihilation operators for the phonon modes with wave vector k and E_i-symmetric polarization ($i = 1, 2$). The spin-strain interaction terms V_{E_i} are given in Eq (2.25) and $\lambda_{i,k}$ are the associated coupling strengths. For convenience, we replicate the strain interaction terms here,

$$V_{E_1} = |E_x\rangle\langle E_x| - |E_y\rangle\langle E_y| + \left(|E_1\rangle\langle A_1| - |E_2\rangle\langle A_2| + 2|^1E_1\rangle\langle^1A_1| + H.c.\right),$$

$$V_{E_2} = |E_x\rangle\langle E_y| + i|E_2\rangle\langle A_1| - i|E_1\rangle\langle A_2| + 2|^1E_2\rangle\langle^1A_1| + H.c.$$

This spin-phonon interaction couples $|E_{1,2}\rangle$ to $|A_1\rangle$. However, instead of being coupled to $|A_1\rangle$ directly, $|A_2\rangle$ is only coupled to $|E_{1,2}\rangle$ through the spin-phonon interaction. As a consequence, the ISC rate for $|A_2\rangle$ is much lower than that of $|E_{1,2}\rangle$ at low temperature, as shown on the left of Fig 2.7. However, as we can expect because higher temperatures lead to the lattice more likely to vibrate, which means faster transition rates within the ^{3}E states. As a result, ISC rates of these states converge at high temperature, as shown on the right of Fig 2.7.

Moreover, $|E_{x,y}\rangle$ are not coupled to other ^{3}E states, and maintain a near-zero irrespective of the temperature, making them ideal for reading out the spin state and generating remote entanglement. These applications favor the spin state being invariant during optical transitions, as discussed in Chap 3.1.2.

Beyond the qualitative explanation given above, the ISC rates can be explicitly calculated for different ^{3}E states by treating the spin-orbit and the spin-phonon interactions as perturbations [22].

2.6. APPENDIX

2.6.1. GROUP THEORY: CHARACTERS AND PROJECTION OPERATORS
Determining all the inequivalent IRs of a group can be challenging when working with explicit matrices, as it requires expressing the symmetry operations in a proper basis.

For instance, only two inequivalent IRs are found in the matrix representation in Eq (2.6) because none of the dangling atomic orbitals transform as IR A_2.

Instead of explicitly writing down the matrices of a representation, it is much more convenient to focus on their traces. This is because the trace of a matrix is unchanged by similarity transformations. These traces are hence called characters of a representation, determining the representations up to equivalence [13, 31]. The character table of the C_{3v} group is given in Tab 2.3.

The orthogonality theorem of characters predicts the existence of the IR A_2, which involves only very basic arithmetic calculations [13, 31]. Using characters, one can also construct a projection operator for each inequivalent IR, which eliminates the need to write out matrices explicitly in constructing symmetry-adapted basis states. This is especially important when the basis states have many degrees of freedom, such as those in Eq (2.14) used to describe the first-excited states of NV centers. Each of these basis states consists of the spatial and spin wave functions of two particles, making it cumbersome to explicitly write down the matrices due to their large size.

The projection operator of an IR labeled as r is constructed using its characters, which is given by [13, 31]

$$P_r = \frac{l_r}{h} \sum_e \chi_e^r R_e, \tag{2.31}$$

where l_r is the dimension of the IR, h is the number of group elements R_e, and χ_e^r is the character of R_e in the IR.

In the following, by using concrete examples, we demonstrate how to use these projection operators for constructing the desired basis states.

MOLECULAR ORBITALS

First, we use the projection operators to reproduce the molecular orbitals in Eq (2.5). To this end, we first need to determine how the C_{3v} symmetry operations act on the atomic orbitals. This can be easily seen by looking at the matrix representation in Eq (2.2), which is expressed in the basis of the atomic orbitals. Then it is easy to write down the actions of these symmetry operations on $\sigma_1 = (0, 1, 0, 0)^T$, e.g.,

$$\Gamma(E)\sigma_1 = \sigma_1, \quad \Gamma(C^+)\sigma_1 = \sigma_2, \quad \Gamma(C^-)\sigma_1 = \sigma_3,$$
$$\Gamma(\sigma_v)\sigma_1 = \sigma_1, \quad \Gamma(\sigma_v')\sigma_1 = \sigma_3, \quad \Gamma(\sigma_v'')\sigma_1 = \sigma_2 \tag{2.32}$$

Now we can evaluate the projection operators of the IR A_1 and E acting on σ_1, i.e.,

$$P_{A_1}\sigma_1 = \frac{1}{6}\left(\Gamma(E) + \Gamma(C^+) + \Gamma(C^-) + \Gamma(\sigma_v) + \Gamma(\sigma_v') + \Gamma(\sigma_v'')\right)\sigma_1 = \frac{\sigma_1 + \sigma_2 + \sigma_3}{3},$$
$$P_E\sigma_1 = \frac{2}{6}\left(2\Gamma(E) - \Gamma(C^+) - \Gamma(C^-)\right)\sigma_1 = \frac{2\sigma_1 - \sigma_2 - \sigma_3}{3}, \tag{2.33}$$

which are the a_c and e_x molecular orbitals (up to normalization), respectively. Following a general procedure (see details in Ref. [28]), one can use these projection operators to

C_{3v}	E	$2C_3$	$3\sigma_v$
A_1	1	1	1
A_2	1	1	-1
E	2	-1	0

Table 2.3: Character table for the point group C_{3v}. The first column gives Mulliken symbols for each irreducible representation, and the first row contains all operations of the group, which are sorted in the three equivalent classes. The characters of the IRs A_1 and E can be easily obtained by looking at the matrices in Eq (2.6). The orthogonality theorem predicts the existence of the 1-dimensional IR A_2, and gives its characters, see details in Ref. [13, 31]. Note that any rotation around the Z-axis transforms as the IR A_2. Such rotations are symmetric with respect to the identity (E) and the two rotation operations ($2C_3$), but are antisymmetric with respect to the three reflection operations ($3\sigma_v$).

construct an orthonormal set of molecular orbitals, i.e.,

$$
\begin{aligned}
a_N &= P_{A_1}\,\sigma_N = \sigma_N, \\
e_x &= \sqrt{\frac{3}{2}}\,P_E\,\sigma_1 = \frac{2\sigma_1 - \sigma_2 - \sigma_3}{\sqrt{6}}, \\
e_y &= P_E\,\frac{\sigma_2 - \sigma_3}{\sqrt{2}} = \frac{\sigma_2 - \sigma_3}{\sqrt{2}}, \\
a_c &= \sqrt{3}\,P_{A_1}\,\sigma_{i=1,2,3} = \frac{\sigma_1 + \sigma_2 + \sigma_3}{\sqrt{3}},
\end{aligned}
\tag{2.34}
$$

The constant numbers before the projectors are normalization factors.

$^3A_2$ SPATIAL WAVE FUNCTION

Now we consider the spatial wave function of the $^3A_2$ ground-state triplet. As there are two particles, the projection operator of an IR is now written as

$$
P_r = \frac{l_r}{h}\sum_e \chi^r_e R_e \otimes R_e.
\tag{2.35}
$$

The spatial wave function is obtained by applying the projection operator of the IR A_2 to the basis function $e_x \otimes e_y$. Similarly, we now express the symmetry operations in the basis of the molecular orbitals above with $e_x = (0,1,0,0)^T$ and $e_y = (0,0,1,0)^T$. The application of P_{A_2} is then written as

$$
\begin{aligned}
P_{A_2}\left(e_x \otimes e_y\right) &= \frac{1}{6}\Big(\Gamma'(E)\otimes\Gamma'(E) + \Gamma'(C^+)\otimes\Gamma'(C^+) + \Gamma'(C^-)\otimes\Gamma'(C^-) \\
&\quad - \Gamma'(\sigma_v)\otimes\Gamma'(\sigma_v) - \Gamma'(\sigma_v')\otimes\Gamma'(\sigma_v') - \Gamma'(\sigma_v'')\otimes\Gamma'(\sigma_v'')\Big)\left(e_x \otimes e_y\right) \\
&= \frac{e_x \otimes e_y - e_y \otimes e_x}{2}.
\end{aligned}
\tag{2.36}
$$

SPIN WAVE FUNCTIONS

We need to include the spin wave functions while applying the projections operators to construct the basis states. The application of the projection operator is similar. We need

to determine how the spin states transform under the symmetry operations. In the basis of a single spin, $|\uparrow\rangle = (1,0)^T$ and $|\downarrow\rangle = (0,1)^T$. The effects of these symmetry operations can be represented as unitary operations:

$$U(E) = 1, \qquad U(C^+) = e^{i\frac{2\pi}{3}S_z}, \qquad U(C^-) = e^{-i\frac{2\pi}{3}S_z},$$
$$U(\sigma_v) = e^{-i\pi S_x}, \quad U(\sigma'_v) = e^{-i\pi S_{\sigma'_v}}, \quad U(\sigma'_v) = e^{-i\pi S_{\sigma''_v}}, \tag{2.37}$$

where $S_{\sigma'_v} = \frac{1}{2}S_x - \frac{\sqrt{3}}{2}S_y$ and $S_{\sigma''_v} = \frac{1}{2}S_x + \frac{\sqrt{3}}{2}S_y$ with S_x, S_y, S_z the spin-1/2 operators. One can then easily check that the spin singlet transform as the IR A_1, the triplet with $m_s = 0$ transforms as the IR A_2, and the triplet state with $m_s = \pm 1$ transform as the IR E.

2.6.2. NON-ZERO MATRIX ELEMENTS OF SPIN-ORBIT INTERACTION

Because the orbital operator is purely imaginary, diagonal terms should vanish so that the Hamiltonian is hermitian [34]. In addition, a matrix element is a scalar, hence should be unchanged by any of the symmetry operations in the C_{3v} group. Therefore, a matrix element **M** being antisymmetric w.r.t a symmetry operation must vanish, i.e., **M** = −**M** = 0. Only when such a symmetry does not exist, this matrix element **M** can possibly be non-zero.

The spin-orbit interaction energy should not be changed by any of the symmetry operations in the C_{3v} group, meaning that it transforms as the totally symmetric IR A_1. Because of this, in the basis of $|a_1\rangle$, $|e_x\rangle$ and $|e_y\rangle$, a matrix element $\langle\phi_1| O_{i=x,y,z} |\phi_2\rangle$ should vanish if it does not transform as the IR A_1, where **O** = $\nabla V \times$ **P** is called the orbital operator. In addition, another restriction is set by the fact that the spatial wave functions are real, while the orbital operator **O** is purely imaginary [34]. That is to say, all the diagonal terms should vanish to ensure hermicity of the Hamiltonian.

To find out the non-zero matrix elements, we need to determine the symmetry for the components of the orbital operator. First, the x, y components of the momentum operator **P** transform as the IR E, while the z component transforms as the IR A_1. In addition, as the nuclear potential V transforms as the IR A_1, the components of $\nabla V = (V_x, V_y, V_z)$ with $V_i = \partial V/\partial x_i$ transform as the same set of IRs. Consequently, one can verify that the components of the orbital operator **O** = $(V_y P_z - V_z P_y, V_z P_x - V_x P_z, V_x P_y - V_y P_x)$ transform as the IRs E, E and A_2, respectively.

The orbital operator O_x (O_y) is antisymmetric (symmetric) with respect to σ_v, i.e., the reflection about the x-z plane. As a consequence, we can directly conclude that the matrix elements $\langle e_x| O_x |a_1\rangle^{(\dagger)}$ and $\langle e_y| O_y |a_1\rangle^{(\dagger)}$ are antisymmetric with respect to σ_v, hence do not transform as the IR A_1. These four matrix elements thus should all vanish.

Furthermore, one can calculate the direct product of two IRs by first multiplying the characters of each IR, and then finding out the linear combination of IRs that generates the product, see details in Ref [31]. Here we write down the rules that are useful for the C_{3v} group, i.e.,

$$A_1 \otimes A_1 = A_1, \quad A_1 \otimes A_2 = A_2, \quad A_2 \otimes A_2 = A_1,$$
$$A_1 \otimes E = E, \quad A_2 \otimes E = E, \quad E \otimes E = A_1 \oplus A_2 \oplus E. \tag{2.38}$$

The matrix elements $\langle e_{\{x,y\}}| O_z |a_1\rangle^{(\dagger)}$ are all equal to zero, as they transform as the IR $E \otimes A_2 \otimes A_1 = E$.

O_x	$|e_x\rangle$	$|e_y\rangle$	$|a_1\rangle$
$\langle e_x|$	0	0	0
$\langle e_y|$	0	0	$i\alpha$
$\langle a_1|$	0	$-i\alpha$	0

O_y	$|e_x\rangle$	$|e_y\rangle$	$|a_1\rangle$
$\langle e_x|$	0	0	$-i\alpha$
$\langle e_y|$	0	0	0
$\langle a_1|$	$i\alpha$	0	0

O_z	$|e_x\rangle$	$|e_y\rangle$	$|a_1\rangle$
$\langle e_x|$	0	$i\beta$	0
$\langle e_y|$	$-i\beta$	0	0
$\langle a_1|$	0	0	0

Table 2.4: Matrix elements of the orbital operator $\mathbf{O} = \nabla V \times \mathbf{P}$ in the basis of the orbitals $|e_x\rangle$, $|e_y\rangle$ and $|a_1\rangle$.

2

The symmetry allows the matrix elements $\langle e_x| O_x |e_y\rangle^{(\dagger)}$ and $\langle e_y| O_y |e_x\rangle^{(\dagger)}$ to be non-zero; however, they mush vanish to ensure the hermicity of the interaction. This is a consequence of the Wigner-Eckart theorem [17, 34], which states that these matrix elements are proportional to the zero diagonal terms like $\langle e_x| O_x |e_x\rangle$.

Now we find all the non-zero matrix elements, i.e.,

$$
\begin{aligned}
\langle e_y| O_x |a_1\rangle = - \langle e_x| O_y |a_1\rangle = i\alpha \\
\langle e_x| O_z |x_y\rangle = i\beta,
\end{aligned}
\tag{2.39}
$$

where α and β are real. Hermitian conjugates of these matrix elements are also non-zero. See the matrix elements in Tab 2.4.

2.6.3. CALCULATION OF THE EFFECT OF STRAIN

The electron-nuclei Coulomb interaction given in Eq (2.7) is modified by strain-induced changes in relative atom positions. Assuming the relative position of an electron orbital remains unchanged with respect to its associated nuclei through the Born–Oppenheimer approximation, the self-interaction terms remain constant. However, strain can reduce the system's symmetry, leading to the matrix element $h_{n,m} = \langle \sigma_m| V |\sigma_n\rangle$ not necessarily equal the constants v_c or v_n in Eq (2.7), where $\sigma_n, \sigma_m \in \{\sigma_N, \sigma_{i=1,2,3}\}$ denote two different orbitals. For simplicity, the matrix element $h_{n,m}$ is assumed to depend solely on the distance $R_{n,m}$ between the associated nucleus.

Now we consider the case where two atoms are connected by the vector

$$
\mathbf{R} = (R_x, R_y, R_z).
\tag{2.40}
$$

When the change δR in the distance $R = (R_x^2 + R_y^2 + R_z^2)^{1/2}$ is small, the induced change δh in the matrix element of the Coulomb interaction can be approximated by the first-order term of its Taylor expansion,

$$
\begin{aligned}
\delta h = h(R) - h(R^0) &\approx \left(\frac{\mathrm{d}h}{\mathrm{d}R} \right)_{R^0} \delta R \\
&= \left(\frac{\mathrm{d}h}{\mathrm{d}R} \right)_{R^0} \left(\frac{\partial R}{\partial R_x} \delta R_x + \frac{\partial R}{\partial R_y} \delta R_y + \frac{\partial R}{\partial R_z} \delta R_z \right) \\
&= \frac{1}{r} \left(\frac{\mathrm{d}h}{\mathrm{d}R} \right)_{R^0} \left(R_x \, \delta R_x + R_y \, \delta R_y + R_z \, \delta R_z \right),
\end{aligned}
\tag{2.41}
$$

where R^0 is the distance in the absence of strain. Using the expression for the strain

tensor in Eq (2.23), we have

$$
\delta h = \frac{1}{R}\left(\frac{\mathrm{d}h}{\mathrm{d}R}\right)_{R^0}\Big[\ \epsilon_{xx}R_x^2 + \epsilon_{xy}R_xR_y + \epsilon_{xz}R_xR_z
$$
$$
+\ \epsilon_{yx}R_yR_x + \epsilon_{yy}R_y^2 + \epsilon_{yz}R_yR_z
$$
$$
+\ \epsilon_{zx}R_zR_x + \epsilon_{zy}R_zR_y + \epsilon_{zz}R_z^2\ \Big].
$$
(2.42)

The strain Hamiltonian is then given in the form

$$
H_{\mathrm{strain}} = \delta V = \sum_{i\neq j}\delta h_{i,j}\,|\sigma_i\rangle\langle\sigma_j| + \delta h_{i,N}\sum_i\big(|\sigma_i\rangle\langle\sigma_N| + h.c.\big),
$$
(2.43)

where $i, j = 1, 2, 3$. Determining the matrix elements is now simple. As depicted in Fig 2.3, the carbons associated with the carbon dangling orbitals σ_2 and σ_3 lie along the Y-axis, resulting in a vector connecting them given by

$$
\mathbf{R}_{2,3} = (0,\ l_c,\ 0),
$$
(2.44)

where l_c is the distance between the two carbon atoms. The change in the corresponding matrix element can be easily calculated,

$$
\delta h_{2,3} = g\epsilon_{yy}, \qquad g = l_c\,(\frac{\mathrm{d}h_c}{\mathrm{d}R})_{R_0}.
$$
(2.45)

The parameter g has been estimated to be of the order of 10^{15} Hz using ab initio calculations [36]. The rest of the terms in the strain Hamiltonian can also be determined similarly.

Due to the significant energy gap between the a_1 and $e_{x,y}$ orbitals, the mixing between them due to strain can be ignored [36]. We concentrate on determining the matrix elements of the strain Hamiltonian in the basis of e_x and e_y. These matrix elements are written as

$$
\langle e_x|\,H_{\mathrm{strain}}\,|e_x\rangle = g(3\epsilon_{xx}-\epsilon_{yy})/2, \quad \langle e_x|\,H_{\mathrm{strain}}\,|e_y\rangle = 3g\epsilon_{xy}/2,
$$
$$
\langle e_y|\,H_{\mathrm{strain}}\,|e_x\rangle = 3g\epsilon_{xy}/2, \quad \langle e_y|\,H_{\mathrm{strain}}\,|e_y\rangle = g\epsilon_{xy}.
$$
(2.46)

The strain Hamiltonian in Eq (2.24) is obtained by shifting the reference energy.

REFERENCES

[1] M. H. Abobeih. *From atomic-scale imaging to quantum fault-tolerance with spins in diamond.* PhD thesis, Delft University of Technology, 2021.

[2] M. H. Abobeih, J. Randall, C. E. Bradley, H. P. Bartling, M. A. Bakker, M. J. Degen, M. Markham, D. J. Twitchen, and T. H. Taminiau. Atomic-scale imaging of a 27-nuclear-spin cluster using a quantum sensor. *Nature*, 576(7787):411–415, 2019.

[3] M. H. Abobeih, Y. Wang, J. Randall, S. J. H. Loenen, C. E. Bradley, M. Markham, D. J. Twitchen, B. M. Terhal, and T. H. Taminiau. Fault-tolerant operation of a logical qubit in a diamond quantum processor. *Nature*, 606(7916):884–889, 2022.

[4] V. M. Acosta. *Optical Magnetometry with Nitrogen-Vacancy Centers in Diamond.* PhD thesis, University of California, Berkeley, 2011.

[5] A. Alkauskas, B. B. Buckley, D. D. Awschalom, and C. G. Van de Walle. First-principles theory of the luminescence lineshape for the triplet transition in diamond NV centres. *New J. Phys.*, 16(7):073026, 2014.

[6] N. Aslam, M. Pfender, P. Neumann, R. Reuter, A. Zappe, F. Fávaro de Oliveira, A. Denisenko, H. Sumiya, S. Onoda, J. Isoya, and J. Wrachtrup. Nanoscale nuclear magnetic resonance with chemical resolution. *Science*, 357(6346):67–71, 2017.

[7] P. Atkins and R. Friedman. *Molecular Quantum Mechanics.* Oxford university press, 2011.

[8] D. D. Awschalom, R. Hanson, J. Wrachtrup, and B. B. Zhou. Quantum technologies with optically interfaced solid-state spins. *Nat. Photonics*, 12(9):516–527, 2018.

[9] A. Batalov, V. Jacques, F. Kaiser, P. Siyushev, P. Neumann, L. J. Rogers, R. L. McMurtrie, N. B. Manson, F. Jelezko, and J. Wrachtrup. Low temperature studies of the excited-state structure of negatively charged Nitrogen-vacancy color centers in diamond. *Phys. Rev. Lett.*, 102:195506, 2009.

[10] H. Bernien. *Control, measurement and entanglement of remote quantum spin registers in diamond.* PhD thesis, Delft University of Technology, 2014.

[11] C. E. Bradley. *Order from disorder: Control of multi-qubit spin registers in Diamond.* PhD thesis, Delft University of Technology, 2021.

[12] Y. Chu and M. D. Lukin. Quantum optics with nitrogen-vacancy centers in diamond. *Quantum Optics and Nanophotonics*, pages 229–270, 2015.

[13] J. Cornwell. *Group Theory in Physics.* Group Theory in Physics. Academic Press, 1984.

[14] G. Davies. The Jahn-Teller effect and vibronic coupling at deep levels in diamond. *Rep. Prog. Phys.*, 44(7):787, 1981.

2

[15] C. L. Degen, F. Reinhard, and P. Cappellaro. Quantum sensing. *Rev. Mod. Phys.*, 89:035002, 2017.

[16] M. W. Doherty, F. Dolde, H. Fedder, F. Jelezko, J. Wrachtrup, N. B. Manson, and L. C. L. Hollenberg. Theory of the ground-state spin of the NV⁻ center in diamond. *Phys. Rev. B*, 85:205203, 2012.

[17] M. W. Doherty, N. B. Manson, P. Delaney, and L. C. L. Hollenberg. The negatively charged nitrogen-vacancy centre in diamond: the electronic solution. *New J. Phys.*, 13(2):025019, 2011.

[18] M. W. Doherty, N. B. Manson, P. Delaney, F. Jelezko, J. Wrachtrup, and L. C. L. Hollenberg. The nitrogen-vacancy colour centre in diamond. *Phys. Rep.*, 528(1):1–45, 2013.

[19] A. Faraon, C. Santori, Z. Huang, V. M. Acosta, and R. G. Beausoleil. Coupling of nitrogen-vacancy centers to photonic crystal cavities in monocrystalline diamond. *Phys. Rev. Lett.*, 109:033604, 2012.

[20] A. Gali, M. Fyta, and E. Kaxiras. Ab initio supercell calculations on nitrogen-vacancy center in diamond: Electronic structure and hyperfine tensors. *Phys. Rev. B*, 77:155206, 2008.

[21] A. Gali, T. Simon, and J. E. Lowther. An ab initio study of local vibration modes of the nitrogen-vacancy center in diamond. *New J. Phys.*, 13(2):025016, 2011.

[22] M. L. Goldman, M. W. Doherty, A. Sipahigil, N. Y. Yao, S. D. Bennett, N. B. Manson, A. Kubanek, and M. D. Lukin. State-selective intersystem crossing in nitrogen-vacancy centers. *Phys. Rev. B*, 91:165201, 2015.

[23] M. L. Goldman, A. Sipahigil, M. W. Doherty, N. Y. Yao, S. D. Bennett, M. Markham, D. J. Twitchen, N. B. Manson, A. Kubanek, and M. D. Lukin. Phonon-induced population dynamics and intersystem crossing in nitrogen-vacancy centers. *Phys. Rev. Lett.*, 114:145502, 2015.

[24] J. P. Goss, R. Jones, S. J. Breuer, P. R. Briddon, and S. Öberg. The twelve-line 1.682 ev luminescence center in diamond and the vacancy-silicon complex. *Phys. Rev. Lett.*, 77:3041–3044, 1996.

[25] A. Gruber, A. Dräbenstedt, C. Tietz, L. Fleury, J. Wrachtrup, and C. von Borczyskowski. Scanning confocal optical microscopy and magnetic resonance on single defect centers. *Science*, 276(5321):2012–2014, 1997.

[26] B. Hensen, H. Bernien, A. E. Dréau, A. Reiserer, N. Kalb, M. S. Blok, J. Ruitenberg, R. F. L. Vermeulen, R. N. Schouten, C. Abellán, W. Amaya, V. Pruneri, M. W. Mitchell, M. Markham, D. J. Twitchen, D. Elkouss, S. Wehner, T. H. Taminiau, and R. Hanson. Loophole-free Bell inequality violation using electron spins separated by 1.3 kilometres. *Nature*, 526(7575):682–686, 2015.

[27] B. J. Hensen. *Quantum Nonlocality with Spins in Diamond*. PhD thesis, Delft University of Technology, 2016.

[28] C. J. Hepp. *Electronic Structure of the Silicon Vacancy Color Center in Diamond*. PhD thesis, Saarland University, 2014.

[29] S. L. N. Hermans. *Quantum networks using spins in diamond*. PhD thesis, Delft University of Technology, 2022.

[30] S. L. N. Hermans, M. Pompili, H. K. C. Beukers, S. Baier, J. Borregaard, and R. Hanson. Qubit teleportation between non-neighbouring nodes in a quantum network. *Nature*, 605(7911):663–668, 2022.

[31] P. Jacobs. *Group Theory with Applications in Chemical Physics*. Cambridge University Press, 2005.

[32] N. Kalb, P. C. Humphreys, J. J. Slim, and R. Hanson. Dephasing mechanisms of diamond-based nuclear-spin memories for quantum networks. *Phys. Rev. A*, 97:062330, 2018.

[33] S. Kitazawa, Y. Matsuzaki, S. Saijo, K. Kakuyanagi, S. Saito, and J. Ishi-Hayase. Vector-magnetic-field sensing via multifrequency control of nitrogen-vacancy centers in diamond. *Phys. Rev. A*, 96:042115, 2017.

[34] A. Lenef and S. C. Rand. Electronic structure of the N-V center in diamond: Theory. *Phys. Rev. B*, 53:13441–13455, 1996.

[35] R. Löfgren, S. Öberg, and J. Larsson. A theoretical study of de-charging excitations of the NV-center in diamond involving a nitrogen donor. *New J. Phys.*, 22(12):123042, 2020.

[36] J. R. Maze, A. Gali, E. Togan, Y. Chu, A. Trifonov, E. Kaxiras, and M. D. Lukin. Properties of nitrogen-vacancy centers in diamond: the group theoretic approach. *New J. Phys.*, 13(2):025025, 2011.

[37] M. A. Nielsen and I. L. Chuang. *Quantum Computation and Quantum Information*. Cambridge University Press, 2000.

[38] W. Pfaff. *Quantum measurement and entanglement of spin quantum bits in diamond*. PhD thesis, Delft University of Technology, 2013.

[39] M. Pompili, S. L. N. Hermans, S. Baier, H. K. C. Beukers, P. C. Humphreys, R. N. Schouten, R. F. L. Vermeulen, M. J. Tiggelman, L. Dos Santos Martins, B. Dirkse, S. Wehner, and R. Hanson. Realization of a multinode quantum network of remote solid-state qubits. *Science*, 372(6539):259–264, 2021.

[40] D. Riedel, I. Söllner, B. J. Shields, S. Starosielec, P. Appel, E. Neu, P. Maletinsky, and R. J. Warburton. Deterministic enhancement of coherent photon generation from a nitrogen-vacancy center in ultrapure diamond. *Phys. Rev. X*, 7:031040, 2017.

2

[41] J. M. Rios. *Quantum manipulation of nitrogen-vacancy centers in diamond: from basic properties to applications*. PhD thesis, Harvard University, 2010.

[42] L. J. Rogers, R. L. McMurtrie, M. J. Sellars, and N. B. Manson. Time-averaging within the excited state of the nitrogen-vacancy centre in diamond. *New J. Phys.*, 11(6):063007, 2009.

[43] O. O. Soykal, P. Dev, and S. E. Economou. Silicon vacancy center in $4h$-sic: Electronic structure and spin-photon interfaces. *Phys. Rev. B*, 93:081207, 2016.

[44] T. H. Taminiau, J. Cramer, T. van der Sar, V. V. Dobrovitski, and R. Hanson. Universal control and error correction in multi-qubit spin registers in diamond. *Nat. Nanotechnol.*, 9(3):171–176, 2014.

[45] J. M. Taylor, P. Cappellaro, L. Childress, L. Jiang, D. Budker, P. R. Hemmer, A. Yacoby, R. Walsworth, and M. D. Lukin. High-sensitivity diamond magnetometer with nanoscale resolution. *Nat. Phys.*, 4(10):810–816, 2008.

[46] D. M. Toyli, D. J. Christle, A. Alkauskas, B. B. Buckley, C. G. Van de Walle, and D. D. Awschalom. Measurement and control of single nitrogen-vacancy center spins above 600 k. *Phys. Rev. X*, 2:031001, 2012.

[47] S. Wehner, D. Elkouss, and R. Hanson. Quantum internet: A vision for the road ahead. *Science*, 362(6412), 2018.

[48] T. Wierzbicki. *MIT OpenCourseWare: Structural Mechanics*. Massachusetts Institute of Technology, 2013.

[49] G. Wolfowicz, F. J. Heremans, C. P. Anderson, S. Kanai, H. Seo, A. Gali, G. Galli, and D. D. Awschalom. Quantum guidelines for solid-state spin defects. *Nature Reviews Materials*, 6(10):906–925, 2021.

[50] J. Wrachtrup and F. Jelezko. Processing quantum information in diamond. *J. Phys. Condens. Matter*, 18(21):S807, 2006.

3

MULTI-QUBIT REGISTER IN DIAMOND

Each NV center contains an electronic spin qubit defined by two sublevels of its energy ground state triplet. This qubit is initialized and read out by optical methods, while single qubit manipulation is achieved by resonant microwave pulses. In addition, dynamical decoupling techniques allow the selective control of surrounding nuclear spins as qubits by exploiting the electron-nuclear interaction. These features make NV centers in diamond a promising platform for the development of quantum technologies.

In this chapter, we present the techniques for controlling NV centers as quantum processors. The electronic spin qubit is defined using two sublevels of the $^3A_2$ ground-state triplet, and the methods for manipulating the qubit are described. The main source of decoherence for the electronic spin qubit is also analyzed, which is crucial for understanding the techniques of dynamical decoupling. This technique not only extends the coherence time of the electronic spin, but also allows for the indirect control of nearby nuclear spins through the electronic spin. This indirect control of nuclear spins offers numerous opportunities for quantum technology applications.

3.1. ELECTRONIC SPIN QUBIT

As we discussed in Chap 2.3.3, when there is no external magnetic field, the spin-spin interaction induces a large zero field energy splitting $\Delta_{\text{ZFS}} \approx 2.88$ GHz between $|m_s = 0\rangle$ and $|m_s = \pm 1\rangle$ in the $^3A_2$ manifold. By applying an external magnetic field, the $|m_s = \pm 1\rangle$ states can be further split due to the Zeeman term with the electric gyromagnetic ratio $\gamma_e \approx 2.8$ MHz/G. The Hamiltonian describing the $^3A_2$ ground-state triplet is then written in the form,

$$H_e = \Delta_{\text{ZFS}} S_z^2 + \gamma_e (\mathbf{B} \cdot \mathbf{S}), \tag{3.1}$$

where $\mathbf{S} = (S_x, S_y, S_z)$ represents the spin-1 operators, and $\mathbf{B} = (B_x, B_y, B_z)$ is the applied external magnetic field vector with the Z-axis set to be along the NV-axis.

Typically, a large external magnetic field around 400 Gauss is applied along the NV-axis (i.e., $B_{x,y} = 0$), so that the $m_s = \pm 1$ states are well separated [1, 9]. As is fairly standard, an electronic spin qubit is defined using the states with $m_s = 0$ and $m_s = -1$. Throughout this chapter, we simplify the spin-1 operators as (ignoring the state $|m_s = +1\rangle$)

$$\begin{aligned}
S_x &= \frac{1}{2}\Big(|m_s = 0\rangle\langle m_s = -1| + |m_s = -1\rangle\langle m_s = 0|\Big), \\
S_y &= \frac{i}{2}\Big(|m_s = -1\rangle\langle m_s = 0| - |m_s = 0\rangle\langle m_s = -1|\Big), \\
S_z &= \frac{1}{2}\Big(|m_s = -1\rangle\langle m_s = -1| - |m_s = 0\rangle\langle m_s = 0|\Big).
\end{aligned} \tag{3.2}$$

3.1.1. MICROWAVE CONTROL

The Larmor frequency ω_e of the qubit system is around 2 GHz, allowing for single-qubit manipulation through the use of resonant Rabi oscillations driven by microwave (MW) pulses. To understand this, we consider an oscillating magnetic field applied along the x-axis. This applied field leads to a driving term with amplitude $2h$, frequency ω, and initial phase α, resulting in the Hamiltonian,

$$H_{q,\text{drive}} = \omega_e S_z + 2h \cos(\omega t + \alpha) S_x. \tag{3.3}$$

Magnetic resonance control requires $|\omega - \omega_e| \ll \omega$, thus the applied field must be in the MW regime. To clarify it, we go into the rotating frame of the MW field through the transformation operator,

$$W = \exp(-i\omega t S_z). \tag{3.4}$$

For an arbitrary qubit state $|\psi_R\rangle = W|\psi\rangle$ in the rotating frame, the Schrödinger equation reads

$$
\begin{aligned}
i\partial_t |\psi_R\rangle &= (W H_{q,\text{drive}} W^\dagger - \omega S_z)|\psi_R\rangle \\
&= \left[(\omega_e - \omega) S_z + 2h\cos(\omega t + \alpha) W S_x W^\dagger \right] |\psi_R\rangle \\
&= \Big[\underbrace{(\omega_e - \omega) S_z + h\left(\cos(\alpha) S_x + \sin(\alpha) S_y\right)}_{\text{secular}} \\
&\qquad + \underbrace{h\left(\cos(2\omega t + \alpha) S_x + \sin(2\omega t + \alpha) S_y\right)}_{\text{non-secular}} \Big] |\psi_R\rangle,
\end{aligned}
\tag{3.5}
$$

When the MW field is close to resonance, i.e. $|\omega - \omega_e| \ll \omega$, the fast-oscillating terms in the Hamiltonian average out and do not accumulate over time. In the secular approximation, these terms are said to be non-secular and are neglected, resulting in an approximate Hamiltonian

$$
H_{R,\text{drive}} = (\omega_e - \omega) S_z + h\left(\cos(\alpha) S_x + \sin(\alpha) S_y\right),
\tag{3.6}
$$

where $\sqrt{(\omega_e - \omega)^2 + h^2}$ is the Rabi frequency. By adjusting the parameters of the driving MW field, it is possible to perform arbitrary single-qubit rotations around any axis in the XY-plane on the electronic spin qubit.

To safely ignore the fast oscillating terms, the driving field must be much weaker than the qubit Larmor frequency [62]. If not, a more detailed treatment beyond the secular approximation is required. For example, if the amplitude $2h$ is comparable to the frequency ω, the fast oscillating terms can cause a noticeable shift in the resonance frequency [18]. Strictly speaking, the term "non-secular" actually refers to terms that are not only small, but also do not build up over time.

Typically, experiments use MW pulses with Rabi frequencies of about 10-25 MHz, resulting in single-qubit gate durations on the order of tens of nanoseconds [4, 10]. The finite pulse duration limits gate fidelity due to electronic qubit decoherence, as discussed in Chap 3.2. To partially suppress noise during single-qubit gates, a composite pulse technique has been developed, resulting in an average fidelity of 99.9952% [47]. In this thesis, we consider the direct Rabi oscillations described by Eq (3.6), so the single-qubit gate fidelity is expected to be slightly lower.

3.1.2. OPTICAL ADDRESSING

In addition to MW control, the electronic spin qubit can be manipulated through appropriate optical transitions between the $^3A_2$ and ^3E states, followed by the detection of emitted photons. The qubit is initialized through spin-flipping induced by intersystem crossing (ISC), while reading the qubit state requires optical transitions with reduced ISC rates. The optical transitions and the ISC mechanism are summarized in Fig 2.5.

QUBIT READOUT

To measure the state of the qubit, the electronic spin in the state $|m_s = 0\rangle$ is optically excited to the excited states $|E_{x,y}\rangle$ as shown in Fig 2.5. When the electron decays back to the ground state, it emits a photon, which can be detected by a photodetector. This
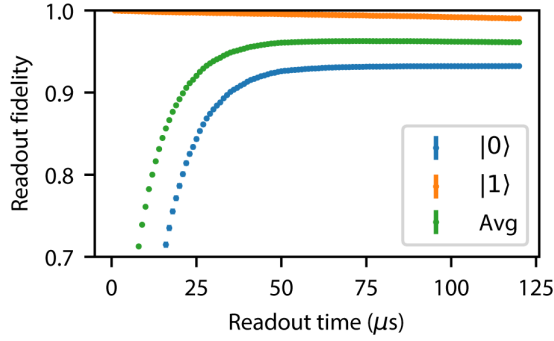
Figure 3.1: The relationship between readout duration and fidelity. Here $|0\rangle$ and $|1\rangle$ represent the electronic spin states with $m_s = 0$ and $m_s = -1$, respectively. The optimal readout duration is the duration that maximizes the average readout fidelity. This optimal duration can be determined by varying the readout duration, during which the optical laser is continuously applied, and measuring the resulting average readout fidelity F_{avg} in Eq (3.7). Figure taken from Ref. [22]

process is called an optical cycle. If a photon is detected, the measurement outcome is assigned as $|m_s = 0\rangle$; otherwise, it is assigned as $|m_s = -1\rangle$. However, because photons are emitted randomly in all directions, only a small fraction (typically around 10-14%) of them can be detected, leading to a low signal-to-noise ratio in the readout signal [22]. Therefore, the readout process requires continuously exciting the electronic spin , so that the optical cycles can be repeated many times to increase the photon number contrast and improve the readout fidelity.

The quality of the readout process is typically characterized by the average readout fidelity, which is the average probability of correctly reading out the spin states:

$$F_{\text{avg}} = \frac{1}{2}\big(P(0|0) + P(-1|-1)\big). \tag{3.7}$$

Here, $P(i|j)$ is the probability of assigning the measurement outcome to be the state $|m_s = i\rangle$ when the electronic spin is indeed in the state $\big|m_s = j\big\rangle$. The average readout fidelity typically falls between 94%-98% with a minimum total readout duration of a few μs [21], Specifically, in Fig 3.1, an average fidelity of 94.5% can be realized with a duration of 38 μs [1, 9, 22].

However, when the optical cycles are repeated, the ISC-induced spin flipping is detrimental. The spin state may have changed before a photon is detected, leading to an incorrect measurement of the qubit state. To mitigate this detrimental effect, we choose to excite the optical transitions between $|m_s = 0\rangle$ and the excited states $\big|E_{x,y}\big\rangle$. These two states have much lower ISC transition rates compared to other ^{3}E states, as shown in Fig 2.7. However, the ISC-induced spin flipping still occurs on average every $\sim$ 100 optical cycles, limiting the readout fidelity [26]. It is worth noting that, depending on other conditions such as strain and external electric field, the optical transition to $|E_x\rangle$ is typically preferred [35].

An important aspect of the readout process is its asymmetry. When photons are detected, it is certain that the spin is in the state $|m_s = 0\rangle$, because the state $|m_s = -1\rangle$ is

hardly excited at all. This means that $P(0|-1)$ is much smaller than $P(0|0)$. As a result, the readout fidelity conditioned on the detection of a photon can be much higher. This conditional fidelity is given by the expression

$$F_{\text{CRO}} = \frac{P(0|0)}{P(0|0) + P(0|-1)},\tag{3.8}$$

which can be as high as 99.1% [1, 9]. This is particularly useful when post-selection or heralding is involved. For instance, in Chap 5, the fidelity for preparing an entangled state can be improved by post-selecting on all measurement outcomes being $|m_s = 0\rangle$ (i.e., photons are detected in each readout).

On the contrary, if no photons are detected, the spin state can be either $|m_s = -1\rangle$ with no photons emitted, or $|m_s = 0\rangle$ with the emitted photons lost. To be sure which is the case, we have to repeat the optical cycles many times, which increases the risk of ISC-induced spin flipping.

It is also important to improve the so-called "projectivity", which refers to the probability that the spin state does not change after being read out [9, 22]. This is because the post-measurement states must be available for further processing in applications such as quantum error correction. For this purpose, it is preferable to stop the readout process immediately after the detection of a single photon, which can suppress the ISC-induced spin flip. In addition, since the hardware requires some response time to completely turn off the laser, the ISC-induced flip probability can be further reduced during this period if low optical power is used [22].

QUBIT INITIALIZATION
The electronic spin reset is performed by exciting the ground states $|m_s = \pm 1\rangle$ to the excited states $|E_{1,2}\rangle$. This is because these excited states are likely to transfer to the singlet state $|^1A_1\rangle$ due to their high ISC rates, as shown in Fig. 2.7, resulting in a significant spin flipping probability of more than 40% per cycle at 4 K [19, 26].

The spin in $|^1A_1\rangle$ then radiatively decays to another ground state singlet $|^1E_1\rangle$, and finally returns to the ground state triplet through another non-radiative decay process. For strain fields of 2-5 GHz and a temperature of 4 K, the spin in the ground state singlet $|^1E_1\rangle$ returns to $|m_s = 0\rangle$ with a probability of about 75% [26]. Therefore, continuous excitation of the electronic spin in $|m_s = \pm 1\rangle$ to the $|E_{1,2}\rangle$ states can initialize it to $|m_s = 0\rangle$. This spin reset or spin pumping process is shown schematically on the left side of Fig 2.5. Note that the reset fidelity exceeds 99.8% with a time duration of only about 3 μs.[26, 46].

3.1.3. REMOTE ENTANGLEMENT
An important application of NV centers in diamond is the establishment of remote entanglement. The electronic spins provide a spin-photon interface and facilitate remote entanglement through the integration of MW control and optical addressing techniques [6, 12]. This was demonstrated by entangling two NV centers 1.3 km apart and performing a loophole-free Bell test [21]. In addition, the surrounding nuclear spins can act as quantum memories to store the already generated entangled states, as will be discussed in chapter 3.4. These nuclear quantum memories are essential for the entanglement of multiple NV centers. Recently, a three-node quantum network based on NV centers

in diamond has been built [23, 43, 44]. NV centers in diamond are currently a leading platform for large-scale quantum networks and related applications [27, 58].

The entanglement of the NV nodes is achieved by exploiting the electronic spins and photons emitted during the optical cycles. In the experimental setup, two distant NV nodes are connected by optical fibers to a beam splitter, with each output port associated with a photon detector. The emitted photons are directed into the beam splitter to interfere with each other. The measurement of the photons then results in a probabilistic projection of the electronic spins into an entangled state. More details on the entangling protocols can be found in the chapter 6.

Building a large-scale network using NV centers is a challenging task. First, the low photon detection efficiency of only about 10-14% is due to the fact that photons are emitted in all directions. Second, about 97% of the emitted photons are in the broad phonon sideband (PSB), where phonon loss destroys the spin-photon entanglement, as discussed in Chap. 2.4.2. Consequently, entanglement protocols must be repeated many times to generate entanglement, and this becomes increasingly difficult when scaling beyond a two-node network. This is because the stored entanglement between the first two nodes tends to be lost before the second and third nodes are successfully entangled [23, 43, 44]. To address this issue, we present in Chap 6 a real-time error mitigation method that can extend the coherence time of the nuclear spins that serve as memory during the entanglement protocols. A comprehensive study of the entanglement protocols and their experimental implementations in diamond can be found in Refs. [22, 24].

3.2. ELECTRONIC SPIN DECOHERENCE

In this section, we will study the effect of the nuclear spins ($S = 1/2$) associated with the naturally abundant (1.1%) ^{13}C atoms in diamond, which are the main source of noise degrading the electronic spin coherence. The primary mechanism for the interaction between the electronic spin and the neighboring nuclear spins is the dipole-dipole interaction, with a secondary contribution from the Fermi contact interaction [9, 13].

Understanding the underlying mechanism of the noise induced by the nuclear spin bath is essential for understanding the widely used dynamical decoupling techniques.

3.2.1. SECULAR BATH HAMILTONIAN

The Hamiltonian of the electronic spin together with the nuclear bath is given in the form,

$$H_{q,\text{bath}} = \omega_e S_z + \omega_c \sum_i I_z^i + \sum_i \mathbf{S} \cdot \mathbf{A}^i \cdot \mathbf{I}^i, \tag{3.9}$$

where $\omega_c = \gamma_c B_z$ is the carbon-spin Larmor frequency with $\gamma_c = 1.0705$ kHz/G the gyromagnetic ratio, $\mathbf{I} = (I_x, I_y, I_z)$ is the spin-1/2 operator, and the tensor $\mathbf{A}$ describes the electron-nuclear interaction. Note that for simplicity, the coupled nuclear spin pairs are neglected in the Hamiltonian.

To study the noise induced by the nuclear spin bath, we transform the Hamiltonian into the joint rotating frame through the operator

$$W_{ec} = e^{-i\omega_e S_z t} \prod_i e^{-i\omega_c I_z^i t}. \tag{3.10}$$

3

(a)

(b)
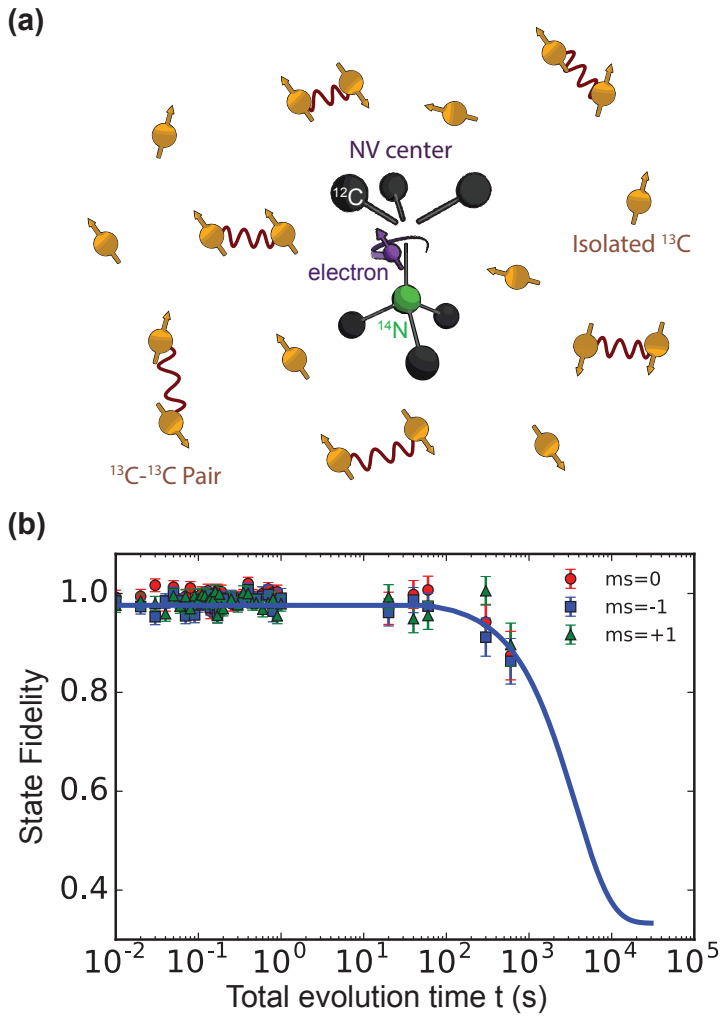
Figure 3.2: (a) A single NV center in diamond surrounded by a bath of ^{13}C atoms (1.1% abundance), each contains a nuclear spin-1/2. The bath also contains strongly coupled spin pairs, which can form long-lived qubits [7]. (b) Longitudinal relaxation of the electronic spin. The spin is prepared in $m_s = 0, +1, -1$ states and the fidelity with the initial state is measured after time t. By fitting the experimental data to Eq (3.15), a relaxation time $T_1 = 3.6(3) \times 10^3$ s is extracted. Figure adapted from Ref. [2].

Remember that we typically work with a large external magnetic field so that $\omega_e \gg \omega_c \gg A$, where A denotes the electron-nuclear interaction strength. It is simple to verify that only the $S_z I_z$ terms are secular, while all other off-resonant terms become fast-oscillating. Under the secular approximation, the Hamiltonian in the rotating frame is written in the form,

$$H_{R,\text{bath}} = \sum_i A_\parallel^i \, S_z I_z^i. \tag{3.11}$$

The energy exchange terms are worthy of special attention, as a significant energy difference between the electronic and nuclear spins (i.e., $\omega_e \gg \omega_c$) is vital for them to be non-secular. This is clearly evident upon explicitly writing down these terms in the joint rotating frame,

$$W_{ec} S_+ I_- W_{ec}^\dagger = e^{-i(\omega_e - \omega_c)t} S_+ I_- \qquad W_{ec} S_- I_+ W_{ec}^\dagger = e^{i(\omega_e - \omega_c)t} S_- I_+, \tag{3.12}$$

where $S_\pm = S_x \pm i S_y$ and $I_\pm = I_x \pm i I_y$ are the ladder operators. To put it simpler, fluctuations in the nuclear spins primarily cause the electronic spin qubit to acquire random phase shifts, rather than flipping it.

The rate of the bath-induced dephasing process is quantified by the dephasing time, or T_2. This parameter is defined as the characteristic time at which the expectation value of the spin operator S_x decreases to $1/e$ of its initial value. To measure this, a qubit is initially prepared in an equal superposition state, which acquires a random phase $\phi(t)$ at the time t. The expectation value of S_x is then measured as a function of time,

$$f(t) = \text{Tr}\big(S_x \, \rho(t)\big) = \frac{1}{2} + \frac{1}{2} \big\langle \cos\big(\phi(t)\big)\big\rangle, \tag{3.13}$$

which is the weighted average of all possible values of the acquired random phase. This experiment for determining the dephasing time T_2 is commonly known as the free induction decay (FID), a term borrowed from nuclear magnetic resonance [40].

It is worth noting that in FID experiments, the dephasing time is usually denoted as T_2^*, while T_2 is typically used when implementing dynamical decoupling protocols, as discussed in Chap 3.3.

3.2.2. LONGITUDINAL RELAXATION

Before delving into the details of bath-induced dephasing, it would be beneficial to gain an understanding of the (longitudinal) relaxation process that occurs due to energy exchanges between the electronic spin and its environment. This relaxation process is primarily driven by spin-phonon interactions [41], as the electron-nuclear dipolar coupling is far too weak to flip the electronic spin. In other words, the vibration of the entire lattice, including all possible phonon modes, is responsible for the longitudinal relaxation process [41].

It's worth noting that in Chap 2, we focused primarily on the vibrations or phonon modes that are localized in the NV structure. These localized phonon modes are modeled as inducing strain on the lattice, causing changes in the positions of atoms associated with the NV structure. These phonon modes are responsible for the ISC mechanism, as discussed in detail in Chap 2.5.

In the limit of weak electron-phonon coupling [41], the relaxation process can be modeled using the generalized amplitude damping channel as described in Ref. [40]. This phenomenological model assumes that the correlation time of the induced noise is much shorter than the typical timescale of the system [11, 59]. Note that the concept of noise correlation time will be further clarified when discussing the bath-induced dephasing. The effect of this channel can be equivalently expressed as a transformation on the density matrix,

$$\rho(0) = \begin{pmatrix} a & b \\ b^* & 1-a \end{pmatrix} \quad \longrightarrow \quad \rho(t) = \begin{pmatrix} (a-a_0)e^{-t/T_1} + a_0 & be^{-t/(2T_1)} \\ b^*e^{-t/(2T_1)} & (a_0-a)e^{-t/T_1} + 1 - a_0 \end{pmatrix},$$

(3.14)

where the constant a_0 corresponds to the population at thermal equilibrium, and the parameter T_1 is referred to as the relaxation time.

To measure the relaxation time, the electronic spin is first set to one of the three possible spin states, and the state fidelity is then tracked over time. Note that the spin state with $m_s = +1$ cannot be ignored when considering the thermal equilibrium state with $k_b T \gg \hbar\omega_e$. In a recent experiment at 3.7 Kelvin [2], the relaxation time was found to be $T_1 = 3.6(3) \times 10^3$ s, as shown in Fig 3.2(b). This value was determined by fitting the experimental data to the equation,

$$F(t) = 2/3e^{-t/T_1} + 1/3.$$

(3.15)

Furthermore, the measured T_1 is more likely to be limited by drifts in the optical and microwave setups, rather than by spin-phonon relaxation [2, 9]. It is worth noting that the measured relaxation time is already one order of magnitude longer than the theoretical prediction based on single-phonon processes in Ref. [41]. This indicates that the spin-phonon relaxation mechanism is not fully understood yet.

It should be noted that the relaxation process also causes the off-diagonal terms of the density matrix to decay. The off-diagonal terms vanish when the qubit reaches its thermal equilibrium, which is a mixed state. This effect can be quantified by measuring the FID decay function, which gives the T_1-limited dephasing time, i.e.,

$$f(t) = \text{Tr}(S_x\rho(t)) = \frac{1}{2}(b+b^*)e^{-\frac{t}{2T_1}}.$$

(3.16)

3.2.3. BATH-INDUCED DEPHASING

At cryogenic temperatures, the relaxation time T_1 is too long to be a limiting factor for electronic spin coherence [1], the much shorter dephasing time (T_2 or T_2^*) is therefore often referred to as the decoherence time for simplicity. We now analyze the dynamics of the nuclear spin bath with the aim of understanding the bath-induced dephasing mechanism.

An important consideration is that the dynamics of the nuclear spins in the bath is significantly slower than that of the electronic spin. This is because the interaction between the electronic spin and any single nuclear spin is negligible for the bath, and only the cumulative coupling to all bath spins has a finite effect. The bath dynamics is therefore primarily determined by the intrabath dipolar coupling [15], which is usually only a few Hertz [3]. However, for nuclei located near the defect center, the electron-nuclear

coupling strengths ($A_\parallel$) can be tens of kHz [3], setting the timescale of the electronic spin dynamics.

To begin with the simplest case, we model the effect of the nuclear spin bath as a quasi-static magnetic field that acts on the electronic spin. This is represented by the Hamiltonian as an approximation of Eq (3.9),

$$H_{\text{bath}} = \beta\, S_z, \qquad \beta = \sum_i^n A_\parallel^i\, p_i, \tag{3.17}$$

where n is the number of nuclear spins in the bath, and $p_i = \pm 1/2$ corresponds to the nuclear spin labeled i being in the $m_s = \pm 1/2$ states. In this approximation, the bath is described by a single variable β, which randomly takes one of the 2^n possible values in each experimental round and remains constant.

The FID decay function in Eq (3.13) and the associated noise spectrum $P_\beta(\omega)$ are both approximately Gaussian,

$$f_\beta(t) \approx \left\langle S_x(t) \right\rangle_\beta \approx \frac{1}{2} e^{-\frac{1}{2} b^2 t^2}, \qquad P_\beta(\omega) = \int e^{-i\omega t} f_\beta(t)\mathrm{d}t \approx \frac{1}{b} e^{-\frac{\omega^2}{2b^2}}, \tag{3.18}$$

where $b = \sqrt{\sum_i \left(A_\parallel^i\right)^2}$ measures the coupling strength between the electronic spin and the nuclear spin bath; the subscript β indicates that the expectation value is calculated based on the probability distribution of the 2^n possible values of β. For the detailed derivation of $f_\beta(t)$, $P_\beta(\omega)$ and b, we refer the readers to the chapter 2.4 of Ref. [63]. The prediction of the Gaussian decay shape has been experimentally observed, and the dephasing time $T_2^* = (b/\sqrt{2})^{-1}$ is typically around 5 μs [2, 15].

The noise spectrum $P_\beta(\omega)$ in Eq (3.18) is the probability distribution of the values taken by β in each experimental round. This is because β determines the Larmor frequency of the electronic spin qubit in the joint rotating frame, as shown in Eq (3.17). To gain more intuition, it is useful to note that this Gaussian shape assumes that each nuclear spin serves as an independent noise source and that the interactions between any pair of nuclear spins, occurring at a few Hertz [3], are ignored. This is reflected in the Hamiltonian given in Eq (3.9) by the absence of nuclear-nuclear interactions. As a result, $p_i = \pm 1/2$ in Eq (3.17) are all independent random variables, and thus β is expected to be a Gaussian random variable according to the central limit theorem.

3.2.4. BATH DYNAMICS

Modeling the noise field as a quasi-static magnetic field and ignoring its dynamics in each experimental round is useful for understanding FID experiments. However, when dynamical decoupling techniques such as spin echo are considered, this assumption becomes too simplistic. This is because, in reality, the noise fluctuates over time and cannot be eliminated by dynamical decoupling sequences that are designed to cancel out static noise.

For example, the spin echo pulse sequence consists of two inversion π pulses separated by a delay time τ, i.e., $\tau - \pi - \tau - \pi$, where the qubit evolution operator is given by

$$\exp(-i\pi s_x)\exp\left(-i\beta\tau s_z\right)\exp(-i\pi s_x)\exp\left(-i\beta\tau s_z\right) = 1. \tag{3.19}$$

Note that the second inversion pulse is often neglected in experiments. Detailed discussions on dynamical decoupling can be found in Chap 3.3.

To accurately understand the effect of the dynamical decoupling sequences for a NV center electronic spin in reality, the dynamics of the nuclear bath must be considered in each single experimental round. The noise field thus needs to be modeled as a classical random process $\beta(t)$, leading to a time-dependent Hamiltonian,

$$H_{\text{bath}}(t) = \beta(t)\, S_z. \tag{3.20}$$

For the electronic spin qubit initialized in the equal superposition state, its density matrix at the time t is now given by

$$\begin{aligned}
\rho(t) &= \exp\left(-i\int_0^t H_{\text{bath}}(t')\mathrm{d}t'\right)\left(\frac{I}{2} + S_x\right)\exp\left(i\int_0^t H_{\text{bath}}(t')\mathrm{d}t'\right) \\
&= \frac{I}{2} + \cos\left(\int_0^t \beta(t')\mathrm{d}t'\right)S_x + \sin\left(\int_0^t \beta(t')\mathrm{d}t'\right)S_y,
\end{aligned} \tag{3.21}$$

where we have

$$I = |m_s = 0\rangle\langle m_s = 0| + |m_s = -1\rangle\langle m_s = -1|. \tag{3.22}$$

The decay function in the FID experiment is then calculated as,

$$f(t) = \langle\, \text{Tr}(S_x\,\rho(t))\,\rangle_{\beta(t)} \propto \text{Re}\left\langle \exp\left\{-i\int_0^t \beta(t)\mathrm{d}t\right\}\right\rangle_{\beta_t}, \tag{3.23}$$

where the subscript β_t denotes that the expectation value is taken over all possible realizations of the random process $\beta(t)$. Explicitly determining the decay shape requires a more detailed model of the classical random process $\beta(t)$ to capture the properties of the nuclear spin bath.

Similar as in the previous section, we assume that each nuclear spin in the bath is only affected by the cumulative field generated by all other nuclear spins. This assumption allows us to approximate the nuclear spins as independent noise sources at all times. This results in the probability distribution of $\beta(t)$ being always Gaussian, classifying it as a Gaussian random process. The formal definition of this type of random process can be found in Ref. [42].

The noise field is then fully characterized by its mean value and correlation function [30, 42, 55],

$$\langle\beta(t)\rangle = m(t), \qquad C(t,t') = \left\langle\big(\beta(t) - m(t)\big)\big(\beta(t') - m(t')\big)\right\rangle, \tag{3.24}$$

which further lead to the characteristic functional [30, 55],

$$\begin{aligned}
\Phi[\xi(t)] &= \left\langle \exp\left(-i\int_0^t \xi(t')\beta(t')\mathrm{d}t'\right)\right\rangle_\beta \\
&= \exp\left\{-i\int_0^t \xi(t')m(t')\mathrm{d}t'\right\}\exp\left\{-\frac{1}{2}\int_0^t \mathrm{d}t'\int_0^t \mathrm{d}t''\,C(t',t'')\xi(t')\xi(t'')\right\}.
\end{aligned} \tag{3.25}$$

In the context of dynamical decoupling (Chap 3.3), the function $\xi(t)$ is referred to as the filter function because it can be used to remove fast changing noise [15, 52, 57] and fast oscillating signals [16]. The FID decay in Eq (3.23) can be replicated by setting the filter function $\xi(t) = 1$.

ORSTEIN-UHLENBECK PROCESS

Another crucial assumption is to ignore the electronic spin's impact on the nuclear spin bath, as its interaction with any individual nuclear spin in the bath is negligible. This results in the random process $\beta(t)$ being stationary and Markovian, in addition to being Gaussian. Such a random process is known as the Orstein-Uhlenbeck (OU) process [30, 55]. In the following, we will examine the implications of the random process being stationary and Markovian.

By disregarding the influence of the electronic spin on the bath, the flip-flops of the bath nuclear spins are determined solely by the intrabath dipolar coupling [15]. As a result, the bath dynamics remain unchanged over time, leading to the random process $\beta(t)$ being stationary. This means that the mean value of the process remain constant over time, and the correlation between values of the process is dependent solely on the time difference between them, not the specific time at which they were measured. The mean value and the correlation function of a stationary process are expressed as

$$\langle \beta(t) \rangle = 0, \qquad C(s) = \langle \beta(t)\beta(t+s) \rangle = \langle \beta(0)\beta(s) \rangle. \tag{3.26}$$

It is worth noting that we set the mean value to be zero, as we typically work in the regime of $k_B T \gg \hbar\omega_c$ so that the probabilities of a nuclear spin being in $m_s = \pm 1/2$ can be deemed to be equal.

Another ramification of the intrabath dipolar coupling determining the nuclear flip-flop rates is that the future dynamics of the nuclear spin bath are entirely determined by its current state. This results in the classical random process $\beta(t)$ being Markovian, which is mathematically described by a correlation function that decreases exponentially over the time difference [30, 55]. In the context of describing the noise field induced by the nuclear bath, the correlation function can be further specified as [15]

$$C(s) = b^2 \exp\left\{ -\frac{|s|}{t_c} \right\}, \tag{3.27}$$

where the correlation time t_c quantifies the flip-flop rates of the nuclear spins, and the parameter b is the electron-bath coupling strength in Eq (3.18), as will be made clear in the following discussion.

The classical OU process is a simple yet effective model for describing the spin bath in situations where the exact dynamics of individual bath spins are irrelevant [15, 17]. The focus is on the electronic spin dynamics obtained by tracing out all bath spins. This model has been shown to be quantitatively accurate in describing the decay of Rabi oscillations on the electronic spin in direct numerical simulations, as seen in Ref. [17]. Furthermore, as we will see below, this model predicts a Gaussian decay shape of the electronic spin coherence, which is in good agreement with recent measurements.[2].

See Ref. [55] (Chapter 4) and Ref. [30] (Chapter 1 and Chapter 2) for more information on the OU process. For situations where the OU process is not sufficient, the reader can look at Ref. [17] and references therein.

DECAY SHAPES

Having obtained the explicit form of the correlation function, we can now use Eq (3.25) with $\xi(t) = 1$ to compute the FID decay function, which is given by (neglecting the con-
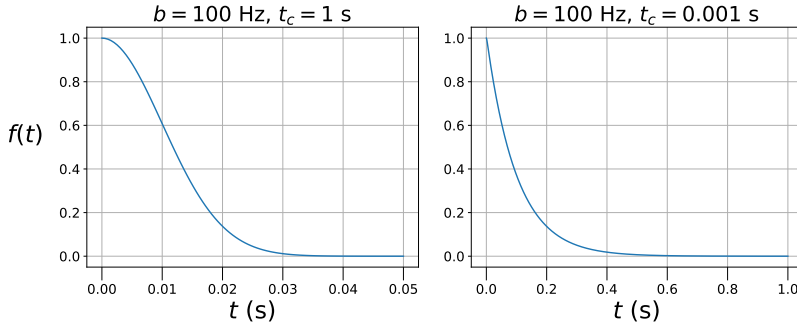
Figure 3.3: The FID decay functions (Eq (3.28)) under two types of noise, fixing b of 100 Hz for clarity. However, in NV centers, b can be much higher and up to 10^5 Hz [3]. (a) When the noise is strong and slow (i.e., $b \gg 1/t_c$) the decay follows a Gaussian shape with coherence loss occurring around 0.03 seconds, which is shorter than the noise correlation time of 1 second. (b) In contrast, weak and fast noise (i.e., $b \ll 1/t_c$) shows that most decoherence occurs at around 0.5 seconds, which is far longer than the noise correlation time of 0.001 s.

stant factor)

$$f(t) = \exp\left(-b^2 t_c^2 \left[\frac{t}{t_c} + e^{-\frac{t}{t_c}} - 1\right]\right). \tag{3.28}$$

The shape of the decay function depends on the ratio of the electronic spin evolution time t and the bath correlation time t_c. For example, if $t \ll t_c$, the decay function is approximately a Gaussian decay as given by Eq (3.18). On the other hand, for $t \gg t_c$, the decay function is better described by an exponential decay with a dephasing time $T_2^* = (b^2 t_c/2)^{-1}$. The noise spectrum $P_\beta(\omega)$ in this case is Lorentzian with a line width of $b^2 t_c/2$.

The electron-bath coupling for NV centers in diamond is significantly stronger than the intrabath dipolar coupling, with values of ~ kHz and ~ Hz, respectively. This results in the bath-induced noise being strong and slow (i.e., $b \gg 1/t_c$), leading to almost complete decoherence of the electronic spin when $t \ll t_c$, as seen in the Gaussian decay shape of its coherence. If the noise is weak and fast (i.e., $b \ll 1/t_c$), most of the decoherence occurs at $t \gg t_c$, resulting in an exponential decay. To make this clearer, we sketch the decay functions for these two types of noise in Fig 3.3.

However, it is important to note that for other physical systems, decay functions may be a combination of exponential and Gaussian, or even more complex. For more information on general types of noise, detailed discussions can be found in Refs. [8, 28], which are about superconducting qubits.

3.3. DYNAMICAL DECOUPLING

With a deeper understanding of bath dynamics, we are ready to explore how dynamic decoupling (DD) protocols address bath-induced dephasing that fluctuates over time [2]. DD works by applying repeated inversion π pulses to the electronic spin, effectively isolating it from the bath and extending the coherence time. In addition, advances in quantum control have made it possible to selectively detect and control individual carbon

nuclear spins [10, 53, 54], making them useful for quantum information processing [4] and nanoscale magnetic sensing [3]. DD pulse sequences are designed to selectively enhance perpendicular electron-nuclear coupling terms [10, 53, 54], whereas these terms were previously neglected in Eq (3.11).

3.3.1. PERIODIC PROTOCOL

We have noticed that static noise can be eliminated by the spin echo sequence in Eq (3.19). Now we reexamine the effect of the spin echo pulse sequence in the presence of bath dynamics. The filter function for the spin echo sequence is given by

$$\xi_{\text{echo}}(t) = \begin{cases} +1, & t \in [0, \tau] \\ -1, & t \in [\tau, 2\tau]. \end{cases} \tag{3.29}$$

By inserting this filter function into Eq (3.25), we can easily calculate the decay function under a spin echo,

$$
\begin{aligned}
f(t = 2\tau) &= \text{Re} \left\langle \exp\left(-i \int_0^{2\tau} \xi_{\text{echo}}(t')\beta(t')\mathrm{d}t'\right) \right\rangle \\
&= \exp\left(-b^2 t_c^2 \left[\frac{2\tau}{t_c} + 4e^{-\frac{\tau}{t_c}} - e^{-\frac{2\tau}{t_c}} - 3\right]\right).
\end{aligned}
\tag{3.30}
$$

For noise that is slow compared to the pulse delay time (i.e., $\tau \ll t_c$), the corresponding decay function with spin echo can be approximated as

$$f(t) \approx \exp\left(-\left(\frac{t}{T_2}\right)^3\right), \qquad T_2 = \sqrt[3]{\frac{b^2}{12 t_c}}. \tag{3.31}$$

The decoherence time T_2 under a spin echo becomes much longer than $T_2^* = (b/\sqrt{2})^{-1}$ as indicated in Eq (3.18). However, if the noise correlation time t_c is negligible compared to the pulse delay time τ, the echoed decay function will revert to an exponential decay. This means that spin echo cannot cancel out noise that changes fast with respect to the pulse delay time τ.

It's crucial to emphasize that the effectiveness of the spin echo is not determined by the total duration of the experiment, but by the slow change of noise during the pulse delay time τ. Therefore, for a given total evolution time t, the spin echo can be repeated to reduce the pulse delay time τ in each repetition so that fast noise can be handled. To illustrate this, we now discuss the widely used Carr-Purcell-Meiboom-Gill (CPMG) protocol, which is realized by repeating the spin echo sequence in a symmetrized manner. The pulse sequence of a period is written as $\tau - \pi - 2\tau - \pi - \tau$ [57]. The CPMG filter function can be easily written, and the resulting decay function can be calculated as [57]

$$f(t) = \exp\left[-\frac{1}{N_c^2}\left(\frac{t}{T_2}\right)^3\right], \tag{3.32}$$

where $t = 4N_c\tau$ is the total evolution time with N_c as the repetition number of periods. Increasing N_c reduces the pulse delay time τ in a given total evolution time t. The effective decoherence time is correspondingly extended by $(N_c)^{2/3}$.

However, N_c cannot be arbitrarily large to completely eliminate the noise, since the finite pulse duration cannot be ignored when it becomes comparable to the pulse delay time τ [32, 63]. Moreover, N_c should also be chosen to avoid the Larmor periods of nearby nuclear spins so that they are not resonantly driven [2], see discussion in Chap 3.3.3. Using more than ten thousand inversion pulses, the electronic spin state can be protected with a fidelity better than 2/3 for more than one second [2].

3.3.2. XY protocol with pulse errors

The axis for inversion pulses has not been considered yet, as we have assumed the absence of pulse errors. However, due to pulse errors caused by inevitable inaccuracies in gate calibration, using π pulses alternately along the X- and Y-axis has been shown to result in improved performance. Such DD sequences are referred to as the XY protocols [15, 57].

To understand the XY protocols, we model control pulses with infinitesimal duration and incorporate their imperfections by considering small deviations in rotation angles and a slight deviation of the rotation axis. A noisy inversion pulse along the X-axis is then expressed as

$$\tilde{\pi}_x = \exp\left[-i(\pi + \epsilon_x)(n_x S_x + n_y S_y + n_z S_z)\right], \tag{3.33}$$

where ϵ_x, n_y and n_z are all small with $n_x = \sqrt{1 - (n_y^2 + n_z^2)}$. The noisy pulse can be written as $\tilde{\pi}_x = \pi_x \delta \pi_x$, i.e., a small random rotation is applied first, followed by the ideal pulse $\pi_x = e^{-i\pi S_x}$. Using the BCH formula, this additional random rotation is approximately given by

$$\delta \pi_x \approx \exp\left(-i(n_x - 1)\pi S_x - i(n_y \pi - n_z \pi^2/2)S_y - i(n_z \pi - n_y \pi^2)S_z\right), \tag{3.34}$$

Because of the excellent stability of the pulse-generating hardware, the pulse error parameters can be assumed constant [4, 15]. As a result, we can incorporate the effect of $\delta \pi_x$ into the qubit evolution governed by the bath Hamiltonian in Eq (3.20). During the pulse delay time τ, the bath dynamics is then governed by an effective Hamiltonian in the form,

$$\tilde{H}_{\text{bath}}(t) \approx H_{\text{bath}}(t) + \frac{(n_x - 1)\pi}{\tau} S_x + \frac{n_y \pi - n_z \pi^2/2}{\tau} S_y + \frac{n_z \pi - n_y \pi^2/2}{\tau} S_z. \tag{3.35}$$

That is to say, using noisy π_x echo pulses to reduce noise from the bath Hamiltonian, $H_{\text{bath}}(t)$, is equivalent to using ideal pulses to reduce noise from this effective bath Hamiltonian, $\tilde{H}_{\text{bath}}(t)$.

The presence of S_x terms in the effective bath Hamiltonian cannot be countered by ideal π_x pulses, causing degradation of fidelity when the qubit is initially in the S_y eigenstate [57]. To handle both S_x and S_y terms that arise from pulse errors, π pulses along X- and Y-axis are alternated. As an example, the widely used XY8 protocol alternates X- and Y-pulses and has a symmetrical period,

$$\tau - \pi_x - 2\tau - \pi_y - 2\tau - \pi_x - 2\tau - \pi_y - \tau - \tau - \pi_y - 2\tau - \pi_x - 2\tau - \pi_y - 2\tau - \pi_x - \tau. \tag{3.36}$$

It is easy to check that this period has the same filter function as the CPMG sequence, making both protocols equivalent in the absence of pulse errors.
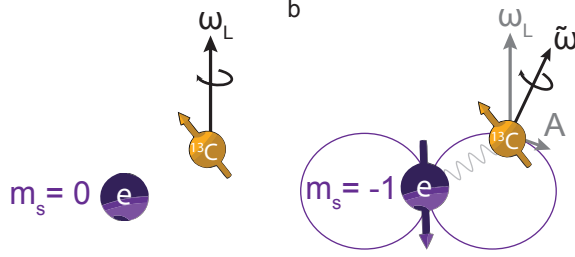
Figure 3.4: Distinct rotation axes of ^{13}C nuclear spin conditioned on the electronic spin state. a) With $m_s = 0$, the ^{13}C nuclear spin rotates at bare Larmor frequency $\omega_0 = \gamma_c B_z$ along an axis parallel to the external magnetic field. b) With $m_s = -1$ and non-zero $A_\perp$, the rotation axis tilts and the frequency becomes $\tilde{\omega} = \sqrt{(\omega_0 - A_\parallel)^2 + A_\perp^2}$. Figure adapted from Ref. [13].

The XY8 protocol is a popular choice due to its simplicity in programming and its second-order insensitivity to pulse errors [57]. To observe the second-order pulse error sensitivity, we must include the pulse error of the π pulses along the Y-axis. Similar to Eq (3.37), a noisy inversion pulse along the Y-axis can be modeled as:

$$\tilde{\pi}_y = \exp\left[-i(\pi + \epsilon_y)(m_x S_x + m_y S_y + m_z S_z)\right], \tag{3.37}$$

where ϵ_y, m_x and m_z are all small with $m_y = \sqrt{1 - (m_x^2 + m_z^2)}$. The qubit evolution operator during the XY8 period is calculated as [57],

$$
\begin{aligned}
U^{XY8} \approx \mathbf{1} &+ 2i(m_x + n_y)\big(\epsilon_y \cos(\phi_\tau) + 2m_z \sin(\phi_\tau)\big)S_x \\
&+ 2i(m_x + n_y)\big(\epsilon_x \cos(\phi_\tau) + 2n_z \sin(\phi_\tau)\big)S_y,
\end{aligned} \tag{3.38}
$$

where the phase ϕ_τ is accumulated during an interpulse delay. For many other DD protocols and comparison between them, we refer the readers to Ref. [57] and references therein.

3.3.3. NUCLEAR MAGNETIC RESONANCE

Instead of isolating the electronic spin from the bath, we now concentrate on specific cases where DD protocols have been designed to significantly enhance the contribution of previously disregarded perpendicular electron-nuclear coupling terms. To assess the impact of these terms, we will enter the rotating frame of the electronic spin only, which can be accomplished through the transformation operator $W_e = \exp(-i\omega t S_z)$.

For simplicity, we first consider only one nuclear spin. The resulting secular Hamiltonian in the electronic rotating frame is expressed as follows:

$$H = \omega_c I_z + A_\parallel S_z I_z + A_\perp S_z I_x. \tag{3.39}$$

The X-axis is defined as the direction of the electron-nuclear interaction component that is perpendicular to the NV-axis ($A_\perp$), leading to no $S_z I_y$ term. As a result, each nuclear spin is likely to possess a unique spatial coordinate system due to the dipolar coupling significantly contributing to the electron-nuclear interaction [10].

3

The behavior of the nuclear spin depends on the state of the electronic spin, as illustrated in Fig. 3.4. When the electronic spin is in $|m_s = 0\rangle$, the nuclear spin rotates around the Z-axis with the Larmor frequency ω_c. On the other hand, when the electronic spin is in $|m_s = -1\rangle$, the rotation axis is slightly tilted, and the frequency becomes

$$\tilde{\omega}_c = \sqrt{(\omega_c - A_\parallel)^2 + A_\perp^2}. \tag{3.40}$$

For convenience, we rewrite the Hamiltonian as

$$H = |m_s = 0\rangle \langle m_s = 0| \otimes H_0 + |m_s = -1\rangle \langle m_s = -1| \otimes H_1, \tag{3.41}$$

$$H_0 = \omega_c I_z, \quad H_1 = (\omega_0 - A_\parallel) I_z + A_\perp I_x. \tag{3.42}$$

By switching between the electronic spin states using DD sequences, we can control the average Hamiltonian and realize desired rotations. For instance, we consider the basic CMPG sequence with a period $\tau - \pi - 2\tau - \pi - \tau$. The corresponding nuclear evolution operators are given by

$$
\begin{aligned}
V_0 &= \exp[-iH_0\tau]\exp[-iH_1 2\tau]\exp[-iH_0\tau] = \exp[-i\phi(\mathbf{I} \cdot \hat{\mathbf{n}}_0)], \\
V_1 &= \exp[-iH_1\tau]\exp[-iH_0 2\tau]\exp[-iH_1\tau] = \exp[-i\phi(\mathbf{I} \cdot \hat{\mathbf{n}}_{-1})],
\end{aligned}
\tag{3.43}
$$

where $\hat{\mathbf{n}}_0$ ($\hat{\mathbf{n}}_{-1}$) is the rotation axis for the electronic spin initially in the $m_s = 0$ ($m_s = -1$) state, and the rotation angle ϕ is independent of the initial electronic spin state, as $\cos(\phi) = \text{Tr}V_0 = \text{Tr}V_1$ [54]. It is important to note that, in reality, the XY8 protocol is typically used to suppress pulse errors [2, 4].

The two rotation axes of the nuclear spin become antiparallel when the pulse delay time τ is at the magnetic resonance given by (integer $k > 0$)

$$\tau_k = \frac{(2k-1)\pi}{2\omega_c - A_\parallel} \tag{3.44}$$

This non-trivial conditional rotation of the nuclear spin can be detected by first initializing the electronic spin into the state $(|m_s = 0\rangle + |m_s = -1\rangle)/\sqrt{2}$, and then measuring the decay of its fidelity. The electronic spin fidelity is given by $P_x = (1 + M)/2$, where M is calculated from the trace of two unitary matrices, and is described by the equation [54],

$$M = \text{Tr}\left(U_0 U_1^\dagger\right) = 1 - \left(1 - \hat{\mathbf{n}}_0 \cdot \hat{\mathbf{n}}_{-1}\right) \sin^2\left(\frac{N\phi}{2}\right) \tag{3.45}$$

with $U_0 = (V_0)^{N/2}$, $U_1 = (V_1)^{N/2}$ and N the total number of inversion pulses. For most other values of τ, the two rotation axes are parallel (i.e., $\hat{\mathbf{n}}_0 \cdot \hat{\mathbf{n}}_{-1} = 1$), causing the $A_\perp$ term to have minimal impact. This means the DD sequence effectively decouples the electronic spin from the bath.

The strength of the signal M at resonances is proportional to the rotation angle ϕ, which is of the order of $A_\perp/\tilde{\omega}_c$. Note that increasing the number of repetitions N amplifies the small rotation angle, which allows for the detection of nuclear spins that are only weakly coupled to the electronic spin. See Ref. [57] for further details.

The total signal M from multiple nuclear spins, neglecting the few-Hertz nuclear-nuclear interactions, has the following form,

$$M = \prod_{i=1}^{n} M_i, \tag{3.46}$$

where the subscript i labels the nuclear spins. In the cases of strong nuclear-nuclear interactions, detailed analysis can be found in Refs. [2, 51, 64].

By varying N and τ, the hyperfine parameters $A_\parallel$ and $A_\perp$ can be estimated by comparing simulated signals with experimental data [2, 54]. The measured spectra can be used to identify single spins that are suitable for selective control. A drop in the signal M indicates that the electronic spin becomes entangled with the nuclear spins, e.g., the maximally entangling gate is implemented when $M = 0$. Broad or overlapping resonances indicate that the electronic spin is entangled with multiple nuclear spins simultaneously, making them unsuitable for selective control. Nuclear spins with isolated and narrow resonances are more promising candidates for use as nuclear spin qubits. Methods for manipulating these nuclear spin qubits will be discussed in the following section.

This method of sweeping τ and N is cumbersome and the estimate is not accurate. A more advanced method is developed in Ref. [3], which enables the precise characterization of 27 ^{13}C nuclear spins associated with a NV center. For a more detailed discussion, see Refs. [3, 9] and references therein.

3.4. Nuclear spin qubits

In this section, we will briefly outline the techniques for realizing universal control over nuclear spins that are weakly coupled to the electronic spin. These nuclear spins were previously regarded as a source of decoherence. However, some nuclear spins are suitable to be controlled as qubits. Precise characterization of such nuclear spins enables two-qubit gates through DD pulse sequences and single-qubit gates using resonant RF pulses. In addition, nuclear spin readout and initialization are performed indirectly through optical addressing of the electronic spin. Moreover, nuclear spins have exceptionally long dephasing time $T_2^* \approx 0.5\,\text{s}$ [3], which can serve as long-lived quantum memories.

These nuclear spins are used to enhance the performance of electronic spins as sensors [56, 61] and are also a necessity for creating long-distance entanglement of multiple nodes using NV centers [23, 43, 44]. Furthermore, the control of the nuclear spins opens up opportunities for basic quantum simulation [45], and prototypes of quantum error correction (Chapter 5).

For conciseness, we use simpler notations for the electronic spin states in this section,

$$|0\rangle = |m_s = 0\rangle, \qquad |1\rangle = |m_s = -1\rangle. \tag{3.47}$$

3.4.1. Electron-nuclear gates

To control a particular nuclear spin, we choose the value of τ to be at one of its magnetic resonances, as given in Eq (3.44). Other nuclear spins should be far from their magnetic resonances so that they are decoupled from the electronic and the target nuclear spin,
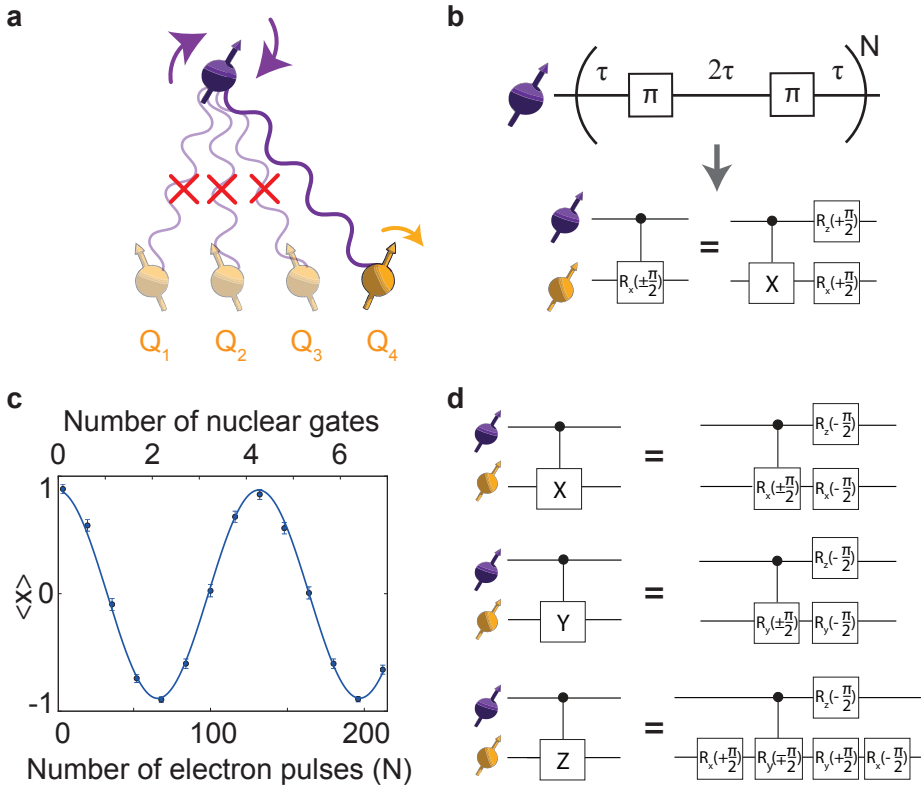
Figure 3.5: Selective control of individual nuclear spins through resonant DD sequences. a) Under DD sequences, carbons whose Larmor frequencies are not at the magnetic resonance are decoupled from the electronic spin. b) By selecting appropriate pulse delay time τ and pulse number N, DD sequences realize maximally entangling gates between the electronic spin and the targeted nuclear spin. This entangling gate is equivalent to a standard CNOT gate up to single qubit rotations. c) Sweeping the number of pulses N leads to the expectation value of $X = 2S_x$ oscillating. d) Controlled nuclear rotations around other axes can be realized by adding additional single-qubit nuclear rotations. Figure taken from Ref. [1].

as depicted in Fig 3.5(a). This enables selective controlled rotation of the target nuclear spin using the DD sequence in Fig 3.5(b),

$$U_x\left(\pm\frac{\theta}{2}\right) = |0\rangle\langle0| \otimes R_x\left(+\frac{\theta}{2}\right) + |1\rangle\langle1| \otimes R_x\left(-\frac{\theta}{2}\right),\tag{3.48}$$

where $R_x(\theta)$ is the rotation around the X-axis by the angle θ. From Eq (3.43), it's easy to see that the total rotation angle of the nuclear spin is proportional to the number of pulses N. This leads to a coherent oscillation in the electronic spin coherence when sweeping N. In Fig 3.5(c), this oscillation is seen by measuring the expectation value of the operator $X = 2S_x$. Particularly, when $\theta = \pi/2$, the DD sequence in Fig 3.5(b) implements the standard CNOT gate up to some single-qubit gates, i.e.,

$$\begin{aligned}U_x(\pm\pi/2) &= |0\rangle\langle0| \otimes R_x(+\pi/2) + |1\rangle\langle1| \otimes R_x(-\pi/2),\\ &= \left[R_z(+\pi/2) \otimes R_x(+\pi/2)\right] \cdot \underbrace{\left[|0\rangle\langle0| \otimes I + |1\rangle\langle1| \otimes 2I_x\right]}_{\text{CNOT}}\end{aligned}\tag{3.49}$$

where I denotes the identity operation. Controlled-rotation around other axes can also be realized with appropriate single-qubit rotations, as shown in Fig 3.5(d).

It is important to emphasize that the achievable rotation angles for a given τ are discretized, with the number of pulses N being limited to integers. This discretization error can be largely mitigated by choosing a slightly detuned τ while retaining gate fidelity. This gives some space for gate optimization, where the two-qubit gates can be optimized by testing a set of values for N and τ, and finding out the combination that gives the highest gate fidelity. Theoretical calculation predicts that such discretization error reduces the fidelity of CNOT, as given in Eq (3.49), only by about 0.5% [53]. Details about the gate optimization can be found in Refs. [1, 9].

However, experimentally, fidelities for electron-nuclear two-qubit gates range from 90-99% for different nuclear spins [10]. The drops from the predicted 99.5% are attributed to residual electronic spin decoherence, nuclear spin decoherence, and imperfect decoupling of non-targeted nuclear spins [10]. Moreover, a smaller value of $A_\perp$ results in a longer gate duration, exacerbating the reduction in gate fidelity. Note that the gate duration of an electron-nuclear entangling gate is typically of the order of 1 ms [4, 10]. For more information on the gate infidelities, we refer the readers to Ref. [9] and references therein.

To manipulate nuclear spins with weak $A_\perp$, a novel two-qubit gate scheme has been proposed, which interleaves resonant radio-frequency (RF) driving on the nuclear spin with a DD sequence on the electronic spin. This new gate scheme enabled the control of a 10-qubit register in NV centers [10] and the demonstration of prototypes for quantum error correction, as discussed in Chapter 5.

3.4.2. SINGLE-QUBIT GATES
One way to implement single-qubit gates on a nuclear spin is by using resonant RF pulses to drive Rabi oscillations, as discussed in Chapter 3.1.1. To selectively control a specific nuclear spin, the electronic spin is prepared in the $m_s = -1$ state, which alters the resonant frequencies of the nuclear spins. In the rotating frame of the nuclear spin,
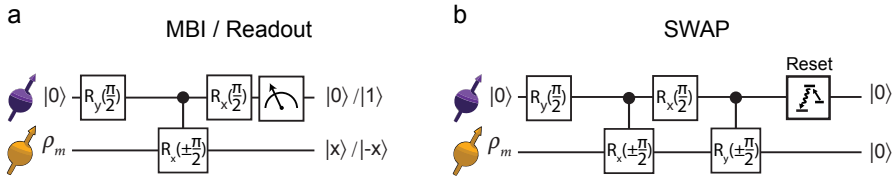
Figure 3.6: Reading out and Initializing weakly coupled nuclear spins. (a) Readout and measurement-based initialization (MBI). The electronic spin is initially set to the state $|0\rangle$, followed by a $\pi/2$ pulse along the Y-axis. A resonant DD sequence is then applied to implement a controlled-rotation. Before measuring the electronic spin, another $\pi/2$ pulse along the X-axis is applied. Depending on the measurement outcome, the nuclear spin is projected into one of the eigenstates of the nuclear spin operator I_x, denoted as $|\pm x\rangle$. (b) SWAP initialization. The electronic spin state $|0\rangle$ is deterministically transferred to the nuclear spin ($m_s = -1/2$). The electronic spin can then be reset to $|0\rangle$ after the state transfer. Figure adapted from Ref. [1].

the nonsecular $A_\perp$ term can be neglected, and the nuclear spin is effectively rotating around the Z-axis at a frequency of $\omega_c - A_\parallel$. Because the nuclear Larmor frequency is much smaller than that of the electronic spin, the gate duration is significantly longer, approximately 1 ms [9].

An alternative method of rotating the nuclear spin around the X-axis is to set $\theta = \pi$ in Eq (3.48) by choosing appropriate values of τ and N. Instead of entangling the electronic and nuclear spins, the DD sequence effectively performs a single-qubit rotation around the X-axis by an angle of π on the target nuclear spin. To rotate a single-qubit around the Z-axis, we can set τ to be off-resonant so that the electronic and nuclear spins are decoupled, making the nuclear spin to rotate around the Z-axis.

3.4.3. READOUT AND INITIALIZATION
Reading out the state of a nuclear spin is done indirectly through the electronic spin. The electronic spin is optically initialized to the $m_s = 0$ state, then a $\pi/2$ pulse on the Y-axis prepares it into an equal superposition state $|x_e\rangle = (|m_s = 0\rangle + |m_s = -1\rangle)/\sqrt{2}$. Subsequently, a DD pulse sequence resonant to the target nuclear spin is applied, using appropriate values of τ and N to apply the maximally entangling gate, i.e., controlled-$R_x(\pm\pi/2)$. Before the final measurement of the electronic spin, another $\pi/2$ pulse on the X-axis is applied to it. The pulse sequence is shown in Fig 3.6(a).

It is straightforward to check that, if the electronic spin should be measured to be in the $m_s = 0$ ($m_s = -1$) state, the nuclear spin is left in the $+1$ (-1) eigenstate of the spin-1/2 operator I_x. See details about the electronic spin readout in Chap 3.1.2.

This readout process of the nuclear spins can also be used to initialize them, which is known as measurement-based initialization (MBI). Remember that we typically work in the regime where the temperature is so high that nuclear spins can be regarded to be in the completely mixed state. As a result, MBI stochastically initializes the target nuclear spin into the ± 1 eigenstate of the nuclear spin operator I_x with equal chance. Note that the readout or MBI fidelity can be improved by repeating the whole process [4].

MBI initializes the nuclear spin with high fidelity, albeit lower than that of the electronic spin. The method is probabilistic, as the output state of the nuclear spin depends

on the measurement outcome of the electronic spin. MBI requires real-time processing of the electronic spin measurement result and application of appropriate single-qubit gates on the target nuclear spin, which may pose experimental challenges when dealing with many nuclear spins [4, 9]. An alternative is the deterministic SWAP method that swaps the state of the electronic spin with the target nuclear spin, as shown in Fig 3.6(b). SWAP is achieved by replacing the electronic spin readout in MBI with a controlled nuclear rotation around the Y-axis, followed by a final electronic spin reset.

The choice of initialization method for different weakly coupled nuclear spins can vary. While SWAP includes an extra controlled nuclear rotation, it saves the use of electronic spin readout used in MBI. The decision between these two methods depends on which operation results in higher fidelity on the targeted nuclear spin. For example, in Chap 4, we prepare a complicated entangled state into 5 weakly coupled nuclear spins, which are all initialized using SWAP.

It is important to note that the strong electron-nitrogen coupling in NV centers enables a unique MBI method for the nitrogen nuclear spin, where the nitrogen nuclear spin acts as control and the electronic spin is the target of a controlled rotation [46]. This is because the strong electron-nitrogen coupling can significantly change the resonant frequency of the electronic spin qubit. To initialize the nitrogen spin, the electronic spin is first initialized, then a resonant weak MW pulse is applied, and finally the electronic spin state is read out. This initialization method is preferred for the nitrogen spin in NV centers (Chap 5) due to the much higher fidelity of MW pulses applied to the electronic spin.

3.5. Hybrid device of diamond

The precise control of nuclear spins is desired for utilizing diamond spins in quantum technologies. Each NV center can also act as a multi-qubit quantum computer, demonstrating elementary simulation algorithms [45] and building blocks for quantum error correction [53] (Chap 5) through the control of its nuclear spins as qubits. Besides the limited number of nuclear spin qubits within a single NV center, the demanding high-fidelity requirements for practical large-scale quantum computing make NV centers a less favorable option, particularly in comparison to platforms like trapped ions [48] and superconducting qubits [29, 65]. Moreover, the low fidelity and slow rate of connecting multiple NV centers presents further challenges for distributed quantum computation with an NV-based network [14, 39].

However, NV centers and many other defect centers have unique advantages, such as the long coherence time of the electronic spin [2], and the potential to use surrounding nuclear spins as additional long-lived memories. NV centers also have favorable optical properties, allowing for photon-mediated entanglement between nodes over 1.3 km, which has been used for loop-hole free Bell tests [21] and three-node network demonstrations [23, 43, 44]. These properties have driven research into hybridizing NV centers with systems such as superconducting (SC) qubits [25, 33, 34, 36–38, 49]. While SC qubits can be controlled with exceedingly high fidelity [29, 65], they do not couple to optical photons and suffer from relatively short coherence times, typically around 100 μs at most [28]. Hybridized quantum devices have the potential to combine the best of both types of systems, with different natures [5, 31, 50, 60].
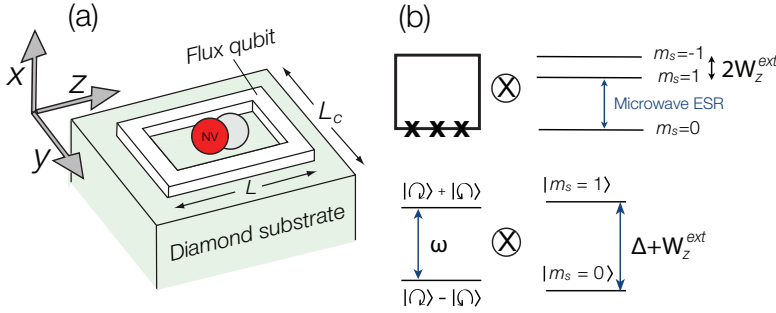
Figure 3.7: (a) Schematic of a hybrid system combining a flux qubit and NV centers. The flux qubit is $L \times L$ in size and has two persistent-current quantum states, each with a unique magnetic field that interacts with NV electronic spins. (b) The eigenstates of the flux qubit are superpositions of currents circulating in opposite directions. An external magnetic field splits the NV center into a two-level system with a transition near the resonance frequency of the flux qubit. Figure adapted from Ref. [38]

To illustrate this, we discuss a NV-SC hybrid system proposed in Ref. [38], where a SC flux qubit is directly coupled to an ensemble of NV centers, as sketched in Fig 3.7(a). The coupling between the flux qubit and the NV centers is magnetic, i.e., the two persistent current states of the flux qubit generate opposite magnetic fields which enter the Zeeman term in the NV center electronic spin Hamiltonian. These eigenstates are equal superpositions of currents circulating in opposite directions, as depicted in Fig 3.7(b). By applying a suitable external magnetic field, the transition frequency between the $m_s = 0$ and $m_s = -1$ states of the NV electronic spins is set close to the resonant frequency of these flux qubit eigenstates.

In the rotating frame, fast-oscillating terms can be neglected, leading to the collective coupling Hamiltonian [38],

$$H_{\text{int}} = \sqrt{N} g \left(\sigma_+ J_- + \sigma_- J_+ \right), \tag{3.50}$$

where g is the coupling strength between the flux qubit and an individual electronic spin; N is the number of NV centers; $\sigma_\pm$ are the ladder operators acting on the flux qubit and $J_\pm = (J_x \pm i J_y)/2$ are the collective ladder operators acting on the ensemble. Note that $J_\alpha = \frac{1}{\sqrt{N}} \sum_i^N S_\alpha$ with $\alpha = X, Y, Z$.

While the interaction between the flux qubit and a single NV center is weak, however, the collective coupling between the flux qubit and the ensemble of NV electronic spins is enhanced by a factor of $\sqrt{N}$. In Ref. [66], a flux qubit was successfully coupled to approximately $N \sim 10^7$ NV centers, with a coupling strength estimated to be around 70 MHz [66]. This strong coupling enables the demonstration of transferring a flux qubit excitation to a collective spin excitation. It should be noted that while uniform coupling between the flux qubit and individual NV electronic spins is assumed for simplicity, this is not a requirement for the excitation transfer [38, 66].

This hybrid system not only allows for efficient transfer and storage of quantum information, but also can make NV centers an interface between SC qubits and light. Furthermore, it enables global control of an ensemble of NV centers through a SC qubit

[20]. In Chapter 6, we present an efficient method for preparing Dicke states, a class of highly entangled states with applications in magnetic sensing. Our Dicke state preparation method is based on global control of an ensemble of spin qubits, and could potentially be implemented using the hybrid system of a flux qubit and NV centers.

REFERENCES

[1] M. H. Abobeih. *From atomic-scale imaging to quantum fault-tolerance with spins in diamond*. PhD thesis, Delft University of Technology, 2021.

[2] M. H. Abobeih, J. Cramer, M. A. Bakker, N. Kalb, M. Markham, D. J. Twitchen, and T. H. Taminiau. One-second coherence for a single electron spin coupled to a multi-qubit nuclear-spin environment. *Nat. Commun.*, 9(1):2552, 2018.

[3] M. H. Abobeih, J. Randall, C. E. Bradley, H. P. Bartling, M. A. Bakker, M. J. Degen, M. Markham, D. J. Twitchen, and T. H. Taminiau. Atomic-scale imaging of a 27-nuclear-spin cluster using a quantum sensor. *Nature*, 576(7787):411–415, 2019.

[4] M. H. Abobeih, Y. Wang, J. Randall, S. J. H. Loenen, C. E. Bradley, M. Markham, D. J. Twitchen, B. M. Terhal, and T. H. Taminiau. Fault-tolerant operation of a logical qubit in a diamond quantum processor. *Nature*, 606(7916):884–889, 2022.

[5] M. Aspelmeyer, T. J. Kippenberg, and F. Marquardt. Cavity optomechanics. *Rev. Mod. Phys.*, 86:1391–1452, 2014.

[6] S. D. Barrett and P. Kok. Efficient high-fidelity quantum computation using matter qubits and linear optics. *Phys. Rev. A*, 71:060310, 2005.

[7] H. P. Bartling, M. H. Abobeih, B. Pingault, M. J. Degen, S. J. H. Loenen, C. E. Bradley, J. Randall, M. Markham, D. J. Twitchen, and T. H. Taminiau. Entanglement of spin-pair qubits with intrinsic dephasing times exceeding a minute. *Phys. Rev. X*, 12:011048, 2022.

[8] F. Battistel. *Mitigating Leakage and Noise in Superconducting Quantum Computing*. PhD thesis, Delft University of Technology, 2022.

[9] C. E. Bradley. *Order from disorder: Control of multi-qubit spin registers in Diamond*. PhD thesis, Delft University of Technology, 2021.

[10] C. E. Bradley, J. Randall, M. H. Abobeih, R. C. Berrevoets, M. J. Degen, M. A. Bakker, M. Markham, D. J. Twitchen, and T. H. Taminiau. A Ten-Qubit Solid-State spin register with quantum memory up to one minute. *Phys. Rev. X*, 9(3):031045, 2019.

[11] H. Breuer, F. Petruccione, and S. Petruccione. *The Theory of Open Quantum Systems*. Oxford University Press, 2002.

[12] C. Cabrillo, J. I. Cirac, P. García-Fernández, and P. Zoller. Creation of entangled states of distant atoms by interference. *Phys. Rev. A*, 59:1025–1033, 1999.

[13] J. Cramer. *Quantum error correction with spins in diamond*. PhD thesis, Delft University of Technology, 2016.

[14] S. de Bone, R. Ouyang, K. Goodenough, and D. Elkouss. Protocols for creating and distilling multipartite GHZ states with bell pairs. *IEEE trans. quantum eng*, 1:1–10, 2020.

3

[15] G. de Lange, Z. H. Wang, D. Ristè, V. V. Dobrovitski, and R. Hanson. Universal dynamical decoupling of a single solid-state spin from a spin bath. *Science*, 330(6000):60–63, 2010.

[16] C. L. Degen, F. Reinhard, and P. Cappellaro. Quantum sensing. *Rev. Mod. Phys.*, 89:035002, 2017.

[17] V. V. Dobrovitski, A. E. Feiguin, R. Hanson, and D. D. Awschalom. Decay of rabi oscillations by dipolar-coupled dynamical spin environments. *Phys. Rev. Lett.*, 102:237601, 2009.

[18] P. Forn-Díaz, J. Lisenfeld, D. Marcos, J. J. García-Ripoll, E. Solano, C. J. P. M. Harmans, and J. E. Mooij. Observation of the bloch-siegert shift in a qubit-oscillator system in the ultrastrong coupling regime. *Phys. Rev. Lett.*, 105:237001, 2010.

[19] M. L. Goldman, A. Sipahigil, M. W. Doherty, N. Y. Yao, S. D. Bennett, M. Markham, D. J. Twitchen, N. B. Manson, A. Kubanek, and M. D. Lukin. Phonon-induced population dynamics and intersystem crossing in nitrogen-vacancy centers. *Phys. Rev. Lett.*, 114:145502, 2015.

[20] H. Hakoshima and Y. Matsuzaki. Efficient detection of inhomogeneous magnetic fields from a single spin with Dicke states. *Phys. Rev. A*, 102:042610, 2020.

[21] B. Hensen, H. Bernien, A. E. Dréau, A. Reiserer, N. Kalb, M. S. Blok, J. Ruitenberg, R. F. L. Vermeulen, R. N. Schouten, C. Abellán, W. Amaya, V. Pruneri, M. W. Mitchell, M. Markham, D. J. Twitchen, D. Elkouss, S. Wehner, T. H. Taminiau, and R. Hanson. Loophole-free Bell inequality violation using electron spins separated by 1.3 kilometres. *Nature*, 526(7575):682–686, 2015.

[22] S. L. N. Hermans. *Quantum networks using spins in Diamond*. PhD thesis, Delft University of Technology, 2022.

[23] S. L. N. Hermans, M. Pompili, H. K. C. Beukers, S. Baier, J. Borregaard, and R. Hanson. Qubit teleportation between non-neighbouring nodes in a quantum network. *Nature*, 605(7911):663–668, 2022.

[24] S. L. N. Hermans, M. Pompili, L. Dos Santos Martins, A. R-P Montblanch, H. K. C. Beukers, S. Baier, J. Borregaard, and R. Hanson. Entangling remote qubits using the single-photon protocol: an in-depth theoretical and experimental study. *New J. Phys.*, 25(1):013011, 2023.

[25] Y. Hu, Y. Song, and L. Duan. Quantum interface between a transmon qubit and spins of nitrogen-vacancy centers. *Phys. Rev. A*, 96:062301, 2017.

[26] N. Kalb, P. C. Humphreys, J. J. Slim, and R. Hanson. Dephasing mechanisms of diamond-based nuclear-spin memories for quantum networks. *Phys. Rev. A*, 97:062330, 2018.

[27] H. J. Kimble. The quantum internet. *Nature*, 453(7198):1023–1030, 2008.

[28] P. Krantz, M. Kjaergaard, F. Yan, T. P. Orlando, S. Gustavsson, and W. D. Oliver. A quantum engineer's guide to superconducting qubits. *Appl. Phys. Rev.*, 6(2):021318, 2019.

[29] S. Krinner, N. Lacroix, A. Remm, A. Di Paolo, E. Genois, C. Leroux, C. Hellings, S. Lazar, F. Swiadek, J. Herrmann, G. J. Norris, C. K. Andersen, M. Müller, A. Blais, C. Eichler, and A. Wallraff. Realizing repeated quantum error correction in a distance-three surface code. *Nature*, 605(7911):669–674, 2022.

[30] R. Kubo, M. Toda, and N. Hashitsume. *Statistical Physics II: Nonequilibrium Statistical Mechanics*. Springer Series in Solid-state Sciences. Springer Berlin Heidelberg, 2012.

[31] G. Kurizki, P. Bertet, Y. Kubo, K. Mølmer, D. Petrosyan, P. Rabl, and J. Schmiedmayer. Quantum technologies with hybrid systems. *Proc. Natl. Acad. Sci. U. S. A.*, 112(13):3866–3873, 2015.

[32] D. Li, Y. Dong, R. G. Ramos, J. D. Murray, K. MacLean, A. E. Dementyev, and S. E. Barrett. Intrinsic origin of spin echoes in dipolar solids generated by strong π pulses. *Phys. Rev. B*, 77:214306, 2008.

[33] X.-K. Li, S.-L. Ma, Y.-L. Ren, J.-K. Xie, and F.-L. Li. Coupling a single NV center to a superconducting flux qubit via a nanomechanical resonator. *J. Opt. Soc. Am. B*, 39(1):69, 2022.

[34] Q. Liao, L. Chen, X. Liu, and N. Zhou. Properties of hybrid entanglement among two flux qubits and a nitrogen-vacancy-center ensemble. *Laser Phys.*, 28(8):085204, 2018.

[35] S. J. H. Loenen. Improving single-shot readout for diamond quantum processors. Master's thesis, Eindhoven University of Technology, 2019.

[36] X.-Y. Lü, Z.-L. Xiang, W. Cui, J. Q. You, and F. Nori. Quantum memory using a hybrid circuit with flux qubits and nitrogen-vacancy centers. *Phys. Rev. A*, 88:012329, 2013.

[37] Y. Maleki and A. M. Zheltikov. Witnessing quantum entanglement in ensembles of nitrogen-vacancy centers coupled to a superconducting resonator. *Opt. Express*, 26(14):17849–17858, 2018.

[38] D. Marcos, M. Wubs, J. M. Taylor, R. Aguado, M. D. Lukin, and A. S. Sørensen. Coupling nitrogen-vacancy centers in diamond to superconducting flux qubits. *Phys. Rev. Lett.*, 105:210501, 2010.

[39] N. H. Nickerson, J. F. Fitzsimons, and S. C. Benjamin. Freely scalable quantum technologies using cells of 5-to-50 qubits with very lossy and noisy photonic links. *Phys. Rev. X*, 4:041041, 2014.

[40] M. A. Nielsen and I. L. Chuang. *Quantum Computation and Quantum Information*. Cambridge University Press, 2000.

3

[41] A. Norambuena, E. Muñoz, H. T. Dinani, A. Jarmola, P. Maletinsky, D. Budker, and J. R. Maze. Spin-lattice relaxation of individual solid-state spins. *Phys. Rev. B*, 97:094304, 2018.

[42] H. Pishro-Nik. *Introduction to Probability, Statistics, and Random Processes.* Kappa Research, LLC, 2014.

[43] M. Pompili, C. Delle Donne, I. te Raa, B. van der Vecht, M. Skrzypczyk, G. Ferreira, L. de Kluijver, A. J. Stolk, S. L. N. Hermans, P. Pawełczak, W. Kozlowski, R. Hanson, and S. Wehner. Experimental demonstration of entanglement delivery using a quantum network stack. *NPJ Quantum Inf.*, 8(1):1–10, 2022.

[44] M. Pompili, S. L. N. Hermans, S. Baier, H. K. C. Beukers, P. C. Humphreys, R. N. Schouten, R. F. L. Vermeulen, M. J. Tiggelman, L. Dos Santos Martins, B. Dirkse, S. Wehner, and R. Hanson. Realization of a multinode quantum network of remote solid-state qubits. *Science*, 372(6539):259–264, 2021.

[45] J. Randall, C. E. Bradley, F. V. van der Gronden, A. Galicia, M. H. Abobeih, M. Markham, D. J. Twitchen, F. Machado, N. Y. Yao, and T. H. Taminiau. Many-body-localized discrete time crystal with a programmable spin-based quantum simulator. *Science*, 374(6574):1474–1478, 2021.

[46] L. Robledo, L. Childress, H. Bernien, B. Hensen, P. F. A. Alkemade, and R. Hanson. High-fidelity projective read-out of a solid-state spin quantum register. *Nature*, 477(7366):574–578, 2011.

[47] X. Rong, J. Geng, F. Shi, Y. Liu, K. Xu, W. Ma, F. Kong, Z. Jiang, Y. Wu, and J. Du. Experimental fault-tolerant universal quantum gates with solid-state spins under ambient conditions. *Nat. Commun.*, 6:8748, 2015.

[48] C. Ryan-Anderson, J. G. Bohnet, K. Lee, D. Gresh, A. Hankin, J. P. Gaebler, D. Francois, A. Chernoguzov, D. Lucchetti, N. C. Brown, T. M. Gatterman, S. K. Halit, K. Gilmore, J. A. Gerber, B. Neyenhuis, D. Hayes, and R. P. Stutz. Realization of real-time fault-tolerant quantum error correction. *Phys. Rev. X*, 11:041058, 2021.

[49] S. Saito, X. Zhu, R. Amsüss, Y. Matsuzaki, K. Kakuyanagi, T. Shimo-Oka, N. Mizuochi, K. Nemoto, W. J. Munro, and K. Semba. Towards realizing a quantum memory for a superconducting qubit: storage and retrieval of quantum states. *Phys. Rev. Lett.*, 111(10):107008, 2013.

[50] P. K. Shandilya, D. P. Lake, M. J. Mitchell, D. D. Sukachev, and P. E. Barclay. Optomechanical interface between telecom photons and spin quantum memory. *Nat. Phys.*, 17(12):1420–1425, 2021.

[51] F. Shi, X. Kong, P. Wang, F. Kong, N. Zhao, R.-B. Liu, and J. Du. Sensing and atomic-scale structure analysis of single nuclear-spin clusters in diamond. *Nat. Phys.*, 10(1):21–25, 2013.

[52] P. Szańkowski, G. Ramon, J. Krzywda, D. Kwiatkowski, and Ł. Cywiński. Environmental noise spectroscopy with qubits subjected to dynamical decoupling. *J. Phys. Condens. Matter*, 29(33):333001, 2017.

[53] T. H. Taminiau, J. Cramer, T. van der Sar, V. V. Dobrovitski, and R. Hanson. Universal control and error correction in multi-qubit spin registers in diamond. *Nat. Nanotechnol.*, 9(3):171–176, 2014.

[54] T. H. Taminiau, J. J. T. Wagenaar, T. van der Sar, F. Jelezko, V. V. Dobrovitski, and R. Hanson. Detection and control of individual nuclear spins using a weakly coupled electron spin. *Phys. Rev. Lett.*, 109:137602, 2012.

[55] N. Van Kampen. *Stochastic Processes in Physics and Chemistry*. North-Holland Personal Library. Elsevier Science, 2011.

[56] V. Vorobyov, S. Zaiser, N. Abt, J. Meinel, D. Dasari, P. Neumann, and J. Wrachtrup. Quantum fourier transform for nanoscale quantum sensing. *NPJ Quantum Inf.*, 7(1):1–8, 2021.

[57] Z.-H. Wang, G. de Lange, D. Ristè, R. Hanson, and V. V. Dobrovitski. Comparison of dynamical decoupling protocols for a nitrogen-vacancy center in diamond. *Phys. Rev. B*, 85:155204, 2012.

[58] S. Wehner, D. Elkouss, and R. Hanson. Quantum internet: A vision for the road ahead. *Science*, 362(6412), 2018.

[59] H. Wiseman and G. Milburn. *Quantum Measurement and Control*. Cambridge University Press, 2010.

[60] Z.-L. Xiang, S. Ashhab, J. Q. You, and F. Nori. Hybrid quantum circuits: Superconducting circuits interacting with other quantum systems. *Rev. Mod. Phys.*, 85:623–653, 2013.

[61] S. Zaiser, T. Rendler, I. Jakobi, T. Wolf, S.-Y. Lee, S. Wagner, V. Bergholm, T. Schulte-Herbrüggen, P. Neumann, and J. Wrachtrup. Enhancing quantum sensing sensitivity by a quantum memory. *Nat. Commun.*, 7:12279, 2016.

[62] D. Zeuch, F. Hassler, J. J. Slim, and D. P. DiVincenzo. Exact rotating wave approximation. *Ann. Phys.*, 423:168327, 2020.

[63] Y. Zhang. Quantum control of interacting spins. Master's thesis, Delft University of Technology, 2022.

[64] N. Zhao, J.-L. Hu, S.-W. Ho, J. T. K. Wan, and R. B. Liu. Atomic-scale magnetometry of distant nuclear spin clusters via nitrogen-vacancy spin in diamond. *Nat. Nanotechnol.*, 6(4):242–246, 2011.

[65] Y. Zhao, Y. Ye, H.-L. Huang, Y. Zhang, D. Wu, H. Guan, Q. Zhu, Z. Wei, T. He, S. Cao, F. Chen, T.-H. Chung, H. Deng, D. Fan, M. Gong, C. Guo, S. Guo, L. Han, N. Li, S. Li, Y. Li, F. Liang, J. Lin, H. Qian, H. Rong, H. Su, L. Sun, S. Wang, Y. Wu, Y. Xu, C. Ying,

J. Yu, C. Zha, K. Zhang, Y.-H. Huo, C.-Y. Lu, C.-Z. Peng, X. Zhu, and J.-W. Pan. Realization of an error-correcting surface code with superconducting qubits. *Phys. Rev. Lett.,* 129:030501, 2022.

[66] X. Zhu, S. Saito, A. Kemp, K. Kakuyanagi, S. I. Karimoto, H. Nakano, W. J. Munro, Y. Tokura, M. S. Everitt, K. Nemoto, M. Kasu, N. Mizuochi, and K. Semba. Coherent coupling of a superconducting flux qubit to an electron spin ensemble in diamond. *Nature*, 478(7368):221–224, 2011.

3

4

BASICS OF QUANTUM ERROR CORRECTION

Quantum error correction (QEC) is essential for realizing practical large-scale quantum computing. This is guaranteed by the fault-tolerance threshold theorem, which states that once the error rates of controlling the physical qubits are below a certain threshold, an arbitrarily long quantum computation can be achieved using QEC. However, these error thresholds can be daunting for most current experimental setups, making the practical application of QEC challenging. Designing efficient protocols tailored to the noise mechanism and hardware constraints to implement QEC-related experiments is an interesting area of research.

XXI	IXX	Single-qubit Error	Multi-qubit Error
+1	+1	I	ZZZ
+1	-1	IIZ	ZZI
-1	+1	ZII	IZZ
-1	-1	IZI	ZIZ

Table 4.1: The syndrome table for the 3-qubit phase-flip code. A set of stabilizer measurement outcomes is known as a syndrome, and each syndrome corresponds to a unique single-qubit phase-flip error. However, it is possible for a syndrome to also correspond to a multi-qubit error. In most cases, we aim to operate in a regime where multi-qubit errors are unlikely to occur, and therefore the optimal strategy is to perform single-qubit correction based on the obtained syndrome. Note that if a multi-qubit error happens by chance, the single-qubit correction will lead to a logical X error, ZZZ. The stabilizers can be measured using an additional qubit, referred to as an ancilla qubit, which is illustrated in Figure 4.1.

In this chapter, we will introduce the concept of active QEC using stabilizer codes through practical examples, including the key terms such as stabilizer, fault-tolerance, threshold, and universality. For the general framework of stabilizer codes, we refer the readers to Ref. [55] and references therein. More elementary introductions can be found in Refs. [8, 12, 58]. Furthermore, we present a proposal to use a small code to demonstrate the one-bit addition algorithm, serving as a simple illustration of fault-tolerant universal quantum computation. Our proposed protocol takes advantage of the all-to-all connectivity of the qubits, resulting in a less demanding requirement for qubit control fidelity. This example emphasizes the importance of customizing quantum computing protocols to suit hardware constraints, such as qubit connectivity, in experimental setups.

4.1. STABILIZER CODES
Stabilizer codes have been studied extensively, where the logical states are defined as the simultaneous +1 eigenstates of stabilizer operators. Each stabilizer operator is a tensor product of several Pauli operators acting on physical qubits. All stabilizers commute with each other and are also known as parity check operators. Daniel Gottesman proposed the general framework of stabilizer codes in his Ph.D. thesis [18]. In this section, we will give an informal introduction with explicit examples of the bit-flip and phase-flip codes.

4.1.1. BIT-FLIP AND PHASE-FLIP CODES
We start with the simplest 3-qubit phase-flip code, where the logical states are defined as:

$$|0_L\rangle = |+++\rangle, \qquad |1_L\rangle = |---\rangle. \tag{4.1}$$

These two logical states are orthogonal and are eigenstates of the two stabilizers with eigenvalue +1:

$$\text{XXI}, \quad \text{IXX}. \tag{4.2}$$

These operators can detect any single-qubit phase flip (Pauli Z) error, since such errors will anti-commute with one or both of these two stabilizers. By measuring the stabilizers, it is possible to determine if a phase flip error has occurred and then correct it. The

results of these measurements are called syndromes, and each syndrome corresponds to a specific single-qubit phase-flip error, as shown in the table 4.1.

The eigenvalues of the stabilizers can be measured through an ancilla qubit, which interacts with the physical qubits where the logical information is stored. The process of measuring the stabilizers and performing subsequent correction for the 3-qubit phase-flip code is illustrated in Fig 4.1. The use of ancilla qubits allows for the determination of the stabilizer eigenvalues without disrupting the logical states.

In some cases, such as when measuring the stabilizers at the end of a quantum computation, the stabilizer eigenvalues can be obtained by measuring each physical qubit in the appropriate basis. The eigenvalues of the stabilizers can then be calculated by multiplying the individual measurement outcomes. This approach destroys the logical information, but has the advantage of being less prone to errors, as single-qubit measurements typically have a higher fidelity compared to implementing two-qubit entangling gates.

The bit-flip code has a similar structure, with the ability to correct any single-qubit bit-flip (Pauli X) errors. For the simplest 3-qubit code, the stabilizers are $Z_1 Z_2, Z_2 Z_3$, and the logical states are given by

$$|0_L\rangle = |000\rangle, \qquad |1_L\rangle = |111\rangle. \tag{4.3}$$

To correct multi-qubit errors, we can extend the phase-flip or bit-flip codes to include more qubits. For instance, the 5-qubit bit-flip code is defined by four stabilizers: $Z_1 Z_2$, $Z_2 Z_3$, $Z_3 Z_4$, and $Z_4 Z_5$. By repeating this process, we can add more qubits and create a larger bit-flip code. The phase-flip codes follow a similar pattern, and both are referred to as repetition codes.

The bit-flip and phase-flip codes can only correct one type of error, either Pauli X or Pauli Z errors. To correct both types of errors, Shor proposed a solution by replacing each physical qubit in the 3-qubit phase-flip code (Eq (4.1)) with a logical qubit from the 3-qubit bit-flip code (Eq (4.3)) [53]. This encodes quantum information in the entanglement of 9 qubits, allowing correction of any single-qubit error on them. This process of replacing physical qubits with logical qubits is known as code concatenation [12, 55]. By repeating code concatenation to combine smaller codes, larger codes that can tolerate more errors can be created [2].

4.1.2. THE FIVE-QUBIT CODE

In this section, we discuss the smallest code that can correct both bit-flip and phase-flip errors, known as the 5-qubit code [26, 28]. Due to its compact resource requirements, this code is often chosen for proof-of-principle experiments in platforms with a limited number of physical qubits. For example, in Chapter 4, we demonstrate some building blocks of fault-tolerant QEC using this 5-qubit code with only 7 spins in a single diamond NV center.

The 5-qubit code is defined by 4 stabilizers with a cyclic structure:

$$S_1 = XXYIY, S_2 = YXXYI, S_3 = IYXXY, S_4 = YIYXX, \tag{4.4}$$

The logical operators are $X_L = X_1 X_2 X_3 X_4 X_5$ and $Z_L = Z_1 Z_2 Z_3 Z_4 Z_5$. It is easy to check that each syndrome corresponds to a unique single-qubit error. For instance, if all stabilizer
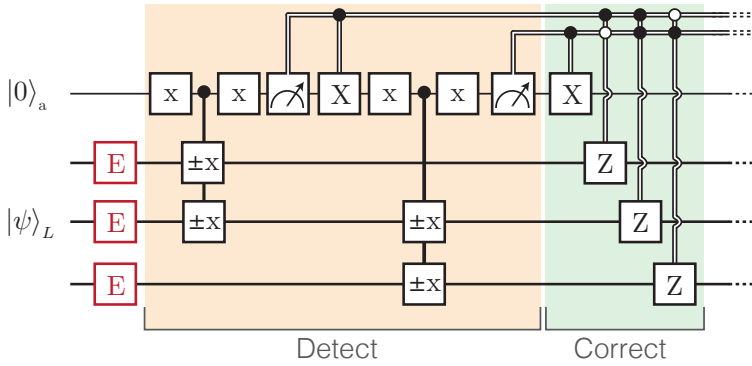
Figure 4.1: Circuit for measuring the $X_1 X_2$ and $X_2 X_3$ stabilizers and performing corrections depending on their measurement outcomes. The subscript a denotes the ancilla qubit and $|\psi\rangle_L$ denotes the state of a logical qubit. The symbol E in a red square represents a single-qubit error. The $\pm x$ (lowercase) gates are $\pm\pi/2$ rotations around the X-axis, where the sign is controlled by the ancilla qubit. The capital X denotes a Pauli X gate on the qubit. Depending on the measurement outcomes of the stabilizers, Pauli Z correction is applied to the appropriate physical qubit. Solid double lines represent classical control wires. Figure taken from Ref. [11].

eigenvalues are -1, it indicates a Z error on the third physical qubit, since this error anti-commutes with all stabilizers simultaneously.

Due to its ability to correct arbitrary single-qubit Pauli errors, this code is often referred to as

$$[[n = 5, k = 1, d = 3]], \tag{4.5}$$

where n is the number of physical qubits, k is the number of encoded qubits, and $d = 2t + 1$ is the code distance with t the maximum weight of correctable errors. In this case, $d = 3$ indicates that the code can only correct a single-qubit error, i.e., $t = 1$.

LOGICAL STATES

The 5-qubit code is the smallest code that can correct both types of errors, yet its logical states are already complex enough to highlight the usefulness of the stabilizer formalism. The logical states of this code can be expressed as a combination of the 32 possible tensor product states of five qubits [37],

$$
\begin{aligned}
|0_L\rangle = \frac{1}{4}\Big[&|00000\rangle + |10010\rangle + |01001\rangle + |10100\rangle \\
&+ |01010\rangle - |11011\rangle - |00110\rangle - |11000\rangle \\
&- |11101\rangle - |00011\rangle - |11110\rangle - |01111\rangle \\
&- |10001\rangle - |01100\rangle - |10111\rangle + |00101\rangle \Big] \\
|1_L\rangle = \frac{1}{4}\Big[&|11111\rangle + |01101\rangle + |10110\rangle + |01011\rangle \\
&+ |10101\rangle - |00100\rangle - |11001\rangle - |00111\rangle \\
&- |00010\rangle - |11100\rangle - |00001\rangle - |10000\rangle \\
&- |01110\rangle - |10011\rangle - |01000\rangle + |11010\rangle \Big].
\end{aligned}
\tag{4.6}
$$

It is easy to verify that these two states are simultaneous +1 eigenstates of all the stabilizers in Eq (4.4).

Instead of dealing with these complicated logical states, it is much simpler to track the eigenvalues of their stabilizers. This simplification facilitates the analysis of the performance of a QEC code and the design of fault-tolerant protocols. For instance, in Chapter 5, by monitoring the changes in the eigenvalues of the stabilizers to track the propagation of errors, we have designed a highly optimized logical state preparation circuit for the spins in a single NV center.

4.1.3. DISCRETIZATION OF ERRORS

So far, we have discussed only Pauli errors, but physical qubits usually undergo continuous changes in their encoded information, such as fluctuations in amplitude and phase. Nevertheless, ideal stabilizer measurements can convert these continuous changes into a set of discretized errors by projecting the qubit state into either a +1 or -1 eigenstate. This discretization of errors enables simplified error models, where only Pauli X, Y, and Z errors are probabilistically assigned to physical qubits.

To demonstrate this, we examine a 3-qubit phase-flip code with the logical state expressed as:

$$|\psi\rangle_L = \alpha |+++\rangle + \sqrt{1-\alpha^2} e^{i\phi} |---\rangle, \tag{4.7}$$

where α and ϕ are arbitrary real constants. We consider the scenario where each physical qubit is subject to dephasing, similar to that observed in the NV electronic spin caused by the nuclear bath (see Chap 3.2). This dephasing leads to a random Z-axis rotation for each qubit, which can be expressed in the following form:

$$e^{i\frac{\theta}{2}Z} = \cos(\theta) + i\sin(\theta)Z \approx 1 + i\theta Z, \tag{4.8}$$

where θ is the rotation angle assigned according to some probability distribution. For simplicity, it is assumed that θ is small and higher-order terms are neglected. It is then straightforward to write the logical state after dephasing:

$$\begin{aligned}|\psi\rangle_L \rightarrow{}& \exp(i\theta_1 Z_1/2 + i\theta_2 Z_2/2 + i\theta_3 Z_3/2)|\psi\rangle_L \\ \approx{}& |\psi\rangle_L + i\theta_1 Z_1 |\psi\rangle_L + i\theta_2 Z_2 |\psi\rangle_L + i\theta_3 Z_3 |\psi\rangle_L \\ &- \theta_1\theta_2 Z_1 Z_2 |\psi\rangle_L - \theta_1\theta_3 Z_1 Z_3 |\psi\rangle_L - \theta_2\theta_3 Z_2 Z_3 |\psi\rangle_L \\ &- i\theta_1\theta_2\theta_3 Z_1 Z_2 Z_3 |\psi\rangle_L. \end{aligned} \tag{4.9}$$

After the dephasing error, the logical state becomes a superposition of eight states, each of which is the original state with some Pauli Z errors on the physical qubits. Measuring the two stabilizers will collapse the logical qubit into one of four possible syndromes, each of which corresponds to a specific combination of Pauli Z errors. The syndrome measurement outcome determines the correction operation that needs to be applied to the logical qubit to recover the initial state.

We consider a specific case where the measurement outcomes of $X_1 X_2$ and $X_2 X_3$ are both -1. The logical state is projected onto the following state (up to normalization):

$$i\theta_2 Z_2 |\psi\rangle_L - \theta_1\theta_3 Z_1 Z_3 |\psi\rangle_L. \tag{4.10}$$

Since θ is small, the optimal strategy is to perform the single-qubit correction based on the syndrome table provided in Tab 4.1. The optimal correction in this case is to apply a Pauli-Z correction on the second qubit, resulting in the corrected state (up to normalization),

$$i\theta_2 \left|\psi\right\rangle_L - \theta_1\theta_3 Z_1 Z_2 Z_3 \left|\psi\right\rangle_L. \tag{4.11}$$

It is important to note that for the 3-qubit phase-flip code, the logical X operator is represented by $Z_1 Z_2 Z_3$, which is not correctable as it commutes with both stabilizers. However, as the random rotation angles are assumed to be small, the original logical state can be restored with high fidelity, since the second-order term $\theta_1\theta_3$ is small.

To avoid noise accumulation, it is crucial to repeat the stabilizer measurements and ensure that the random rotation angles do not become large enough to make second-order terms, such as $\theta_1\theta_3$, significant.

4.2. FAULT TOLERANCE

In the process of encoding quantum information in a QEC code, a tradeoff exists between the level of protection against errors and the additional resources required. Specifically, the use of a QEC code results in an increase in qubit overhead, which represents the additional number of qubits needed to encode the quantum state with error correction as compared to without it. Furthermore, performing stabilizer measurements during the QEC process necessitates the use of ancilla qubits and supplementary operations, which can be very noisy in practice. As a result, these additional requirements can significantly increase the likelihood of errors, which can significantly impact the overall effectiveness of the QEC code.

To enable the practical application of QEC, the development of fault-tolerant (FT) protocols that remain effective even when their components are noisy is essential. In this section, we focus our discussion on distance-3 codes for the sake of simplicity. We do not consider QEC codes with larger distances, but readers interested in such discussions can look at Refs. [8, 55].

FT protocols for distance-3 codes are designed to ensure that at most one single-qubit error occurs in any of the encoded qubits due to a single fault, which can refer to a faulty gate on the physical qubits or a single-qubit error in the initial state. These codes are capable of correcting any single-qubit error on the constituent physical qubits, ensuring that single-qubit errors cannot corrupt the logical information. In principle, restoring a logical state with such errors can be achieved by applying a noiseless QEC round. If a noiseless QEC round results in a logical error, the encoded qubits are considered to have logical errors.

Despite the increased qubit overhead and number of operations required to implement FT protocols, the logical error probability of an encoded qubit can be lower than the error rate for controlling the constituent physical qubits, provided that this physical error rate is below a certain threshold [2, 55]. Roughly speaking, this is because, when the physical error rate is sufficiently low, the occurrence of two faults simultaneously is highly unlikely.

4.2.1. INDEPENDENT NOISE

Before discussing the fault-tolerance error threshold, we need to clarify the types of errors we will be addressing. Fault tolerance is commonly studied under the assumption that errors occur independently on physical qubits [2, 8, 55]. One widely used error model is the depolarizing noise model, which basically assumes Pauli errors occur on the involved physical qubits with equal probability after a faulty operation. Specifically, this model can be defined as follows [8]:

1. With probability p, each single-qubit gate is followed by a single-qubit Pauli error drawn uniformly from $\{X, Y, Z\}$.

2. With probability p, each two-qubit gate is followed by a two-qubit Pauli error, drawn uniformly from $\{I, X, Y, Z\}^{\otimes 2} \setminus \{I \otimes I\}$. There are 15 possible errors in total.

3. With probability p, a single-qubit Pauli error drawn uniformly from $\{X, Y, Z\}$ is applied to a prepared state. Specifically, the preparation of $|0\rangle$ has a probability of $\frac{2p}{3}$ of being replaced by $|1\rangle = X|0\rangle$, and the preparation of $|+\rangle$ has the same probability of being replaced by $|-\rangle = Z|0\rangle$.

4. With probability $\frac{2p}{3}$, the outcome of a single-qubit measurement is flipped.

Each of the cases mentioned above refers to a fault, which includes the two-qubit Pauli errors that occur after a two-qubit gate. It is worth noting that a qubit undergoing a random Pauli error with a probability of p can be expressed as the depolarizing channel [37]:

$$\rho \to \xi(\rho) = (1-p)\rho + \frac{p}{3}\left(X\rho X + Y\rho Y + Z\rho Z\right)$$
$$= p\frac{I}{2} + (1-p)\rho. \tag{4.12}$$

Here, ρ is the initial density matrix of the qubit. If this channel is applied to a qubit, the qubit is depolarized and goes into a completely mixed state $I/2$ with a probability of p. Conversely, the qubit remains in its initial state with a probability of $1 - p$.

It is essential to note that reported threshold values in various publications must be interpreted with care since the noise model, designated codes, and implemented FT protocols can all affect the results. For instance, when the noise on the constituent physical qubits is correlated, the performance of a QEC code can be significantly compromised, as we discuss briefly below.

CORRELATED NOISE

The assumption of independent errors is not always valid, especially when qubits are in proximity and share a common environment. Correlated errors can simultaneously affect multiple, or even all physical qubits in the system, and have been observed in many experimental implementations, such as trapped-ion qubits [46, 51], NV centers in diamond [48, 54], superconducting qubits [20, 22], and quantum dots [4]. Numerous studies have explored the effects of correlated errors on the performance of QEC codes [25, 39, 42, 52]. The presence of noise correlation can significantly compromise the performance of QEC codes that are designed to correct independent errors [23, 25].

However, knowledge of noise correlation can be leveraged to design more effective protocols [10, 13, 29, 33, 38]. For instance, if the error model is known, optimization of the encoding or recovery of a QEC protocol can be formulated as a convex optimization problem [13]. Another example is a noise-tailored code that is efficient with respect to global dephasing caused by a common fluctuator [29]. Compared to the n-qubit phase-flip code discussed in Chap 4.1.1, this code reduces the qubit overhead exponentially. In more general scenarios where the underlying error model is unknown, machine learning can be a powerful tool for finding noise-tailored codes [33]. Machine learning can also be used to develop better decoders [3, 35].

Another interesting approach is to concatenate QEC codes with decoherence-free subspaces in the presence of correlated errors [10, 30]. Logical qubits encoded within decoherence-free subspaces are effectively decoupled from the environment. The idea of decoherence-free subspaces has been experimentally realized in trapped-ion qubits [24] and NV centers in diamond [48]. Note that the existence of decoherence-free subspaces is due to the symmetry of correlated errors, and Ref. [30] presents a rigorous and comprehensive criterion for constructing such subspaces.

Recent studies by Majumder et al. [31] and Orrell et al. [41] have proposed using spectator qubits to directly probe noise sources, leading to a direct reduction in the error rate of the physical data qubits. Unlike the ancilla qubits used for stabilizer measurements, spectator qubits do not directly interact with the data qubits but are utilized because their noise is correlated with that of the data qubits. For example, in typical trapped-ion systems, global dephasing is an important noise source because the system size is often much smaller than the scale of the fluctuating external magnetic field [31, 46, 51]. In Chapter 6, we utilize such spectator qubits to create robust quantum memories that are valuable for constructing a large quantum network based on NV centers in diamond.

4.2.2. THRESHOLD

In this section, we discuss the concept of the fault-tolerance threshold, with the assumption of depolarizing noise that is characterized by a single parameter, the error rate p. The threshold theorem guarantees that if the error rate is below a certain critical value, the logical error rate can be suppressed to arbitrarily low levels using fault-tolerant QEC. Consequently, arbitrary long quantum computations can be executed [2, 12, 55]. The specific critical value, referred to as the error threshold, is dependent on the details of the error model and how FT protocols are designed. A rigorous derivation of the theorem can be found in Ref. [2].

Although some platforms, such as superconducting qubits and trapped-ion qubits, have high control fidelity (with 2-qubit gate fidelities of around 0.995 to 0.999) [17, 50], this is still insufficient to get below the error threshold below which meaningful quantum algorithms can be practically run. Therefore, even in these platforms, most experiments focus on implementing multiple rounds of stabilizer measurements to preserve the coherence of an encoded qubit, without actually performing any computations [17, 49, 50].

Instead of focusing on the threshold in experiments, the primary concern at present is the critical error rate for each specific quantum computation task, below which fault-tolerant protocols can outperform implementations using physical qubits directly. Such

critical error rates are known as the pseudo-threshold and pertain to designated computation tasks, such as the one-bit addition (i.e., calculating 1+1=2) in Chapter 4.3, which uses specific codes and computational protocols.

Unlike the threshold, being below the pseudo-threshold only indicates that using the fault-tolerant protocol may be advantageous for that particular task, but it does not guarantee the ability to perform arbitrarily long quantum computations.

PSEUDO-THRESHOLD

We will now take a closer look at the pseudo-threshold. When performing a quantum computation task directly at the physical qubit level, the error rate is given by Cp, where C is a constant that primarily depends on the number of operations required to complete the task. However, by using fault-tolerant protocols, the logical error rate of an encoded qubit of a distance-3 code scales as p^2. This means that the logical error rate can be expressed as $C'p^2$, where C' is a constant that mainly depends on the number of operations needed to complete the same task, but using encoded qubits and fault-tolerant protocols. It's important to note that C' is typically much larger than C, and one of the primary objectives of designing FT protocols is to minimize C'.

For fault-tolerant protocols to be practically useful, they must satisfy the following condition: $C'p^2 < Cp$. This leads to the pseudo-threshold being given by:

$$p'_c = \frac{C}{C'} < 1. \tag{4.13}$$

In other words, if the physical error rate is below the pseudo-threshold, the likelihood of an incorrect computation occurring while using encoded qubits can be lower than the likelihood of such an error when using physical qubits directly.

Typically, being below the pseudo-threshold is much easier than being below the threshold. In Chapter 4.3, we examine the one-bit addition algorithm as an example of a specific computation task. Despite being a trivial quantum algorithm, it involves both Clifford and non-Clifford gates, and therefore serves as an instance of universal quantum computation. Implementing the algorithm directly at the physical qubit level necessitates 3 physical qubits and 5 2-qubit gates. We have proposed a fault-tolerant protocol that uses an 8-qubit error detecting code, and restart the entire computation once an error is detected. The protocol necessitates 10 physical qubits (including 2 ancilla qubits) and 24 2-qubit gates.

Consequently, our proposed FT protocol for this particular computation task has a pseudo-threshold of approximately

$$\frac{5}{\binom{24}{2}} \approx 1.8\% \tag{4.14}$$

Note that, for simplicity, we have assumed that the error rates of single-qubit operations are insignificant compared to those of the 2-qubit gates. This relatively high pseudo-threshold makes it feasible to observe the benefits of employing fault-tolerant protocols in various physical platforms. For example, the 2-qubit gate error rate of trapped-ion qubits is significantly lower than this pseudo-threshold, on the order of 2×10^{-3} [49, 50].
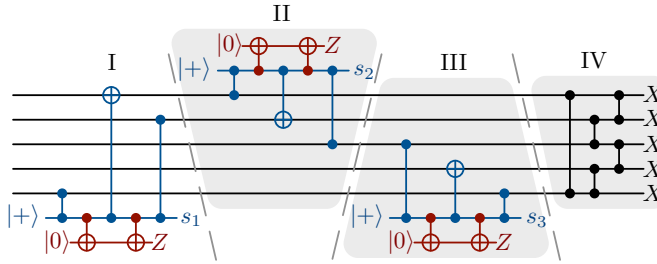
Figure 4.2: Circuit used to measure the logical X operator $X_1X_2X_3X_4X_5$ on a logical qubit of the 5-qubit code. The circuit is divided into four labeled portions. Depending on the results of previous measurements, the last three portions may be skipped. The stabilizer measured here s_1, s_2, s_3 (lowercase) are all weight-3 logical X operators of the 5-qubit code. Additionally, the circuit includes an extra ancilla qubit in red known as the flag qubit, which is crucial for ensuring fault-tolerance. Figure taken from Ref. [9]

However, it is crucial to reiterate that crossing the pseudo-threshold for this specific task of one-bit addition does not ensure that fault-tolerant protocols using encoded qubits will be beneficial for longer and more complex quantum computation tasks. Other tasks may require additional techniques and resources beyond those used for one-bit addition. That is, the pseudo-threshold for each computational task must be evaluated independently, taking into account the intended codes, protocol optimizations, and properties of the physical qubits employed.

4.2.3. CONSIDERATIONS FOR CHOOSING CODES

The 5-qubit code is highly suitable for proof-of-principle experiments using small quantum processors due to its minimal qubit resource requirement. Recent works have used this code to demonstrate building blocks for realizing fault-tolerant quantum computation using superconducting qubits [16] and NV centers in diamond (see Chapter 5). However, it is important to note that the 5-qubit code may not be an optimal choice for practical quantum computation, since certain logical operations in this code can be challenging to implement in the presence of gate errors.

For example, imagine a scenario where there is a single-qubit Pauli Z error occurring on one of the physical qubits, and the objective is to read out the logical X operator. To obtain the correct measurement outcome, using stabilizer measurements to correct this potential Pauli Z error is necessary, as it anti-commutes with the logical X operator and leads to a measurement error. However, the problem is that the gate operations performed during stabilizer measurements for QEC can introduce additional errors and result in a wrong measurement outcome. To address this issue, it is crucial to design fault-tolerant protocols that can extract the measurement outcome correctly even in the presence of gate errors. Fig 4.2 depicts such a FT readout protocol for the logical X operator of the 5-qubit code, which involves many 2-qubit gates and is therefore challenging to implement.

In contrast to the 5-qubit code, fault-tolerant readout for other codes can be much easier. For example, another widely studied type is the CSS codes, which are named after their inventors, Calderbank, Shor, and Steane. The construction of CSS codes is

described in Ref. [37]. One notable feature of CSS codes is that their stabilizers are either entirely made up of Pauli Z operators or entirely made up of Pauli X operators. The most well-known CSS code is the 7-qubit Steane code, which is defined by the stabilizers, $Z_4 Z_5 Z_6 Z_7$, $Z_2 Z_3 Z_6 Z_7$, $Z_1 Z_3 Z_5 Z_7$, and $X_4 X_5 X_6 X_7$, $X_2 X_3 X_6 X_7$, $X_1 X_3 X_5 X_7$ [12, 37]. This code can correct an arbitrary single-qubit Pauli error, and is hence denoted as $[[n = 7, k = 1, d = 3]]$.

For these codes, to measure the logical X operator, $X_1 X_2 X_3 X_4 X_5 X_6 X_7$, one only needs to measure each physical qubit in the Pauli X basis, and then calculate the eigenvalues of the X-type stabilizers from these single-qubit measurements. This enables correction of any single-qubit Pauli Z error, allowing for the correct calculation of the eigenvalue of logical X. This method of measuring logical X is fault-tolerant and only requires single-qubit measurements, rather than the many 2-qubit gates involved in the fault-tolerant readout protocol of the 5-qubit code. Similarly, fault-tolerant measurement of the logical Z operator only requires single-qubit measurements in the Pauli Z basis.

Another advantage of any CSS code is that the logical CNOT gates can be implemented using transversal CNOT operations between the paired physical qubits in each encoded qubit simultaneously [55], which is inherently fault-tolerant. However, for a fault-tolerant logical CNOT gate between two logical qubits of the 5-qubit code, a pieceable fault-tolerant technique is required [60]. This approach involves breaking non-fault tolerant logical CNOT gates into two pieces, each of which is individually fault-tolerant. An additional round of QEC is required between the two fault-tolerant pieces, making it a much more expensive than the transversal implementations.

For more information on the 5-qubit code and the 7-qubit Steane codes, we refer the reader to Ref. [50], which has experimentally implemented fault-tolerant logical gates using both codes and compared their performance on trapped-ion systems. Note that experimental demonstrations of multiple rounds of fault-tolerant QEC with a single logical qubit of the 7-qubit code have also been reported in Ref. [49].

4.2.4. FLAG FAULT-TOLERANCE

In this section, we use the example of flag ancilla qubits to show how fault-tolerant protocols are designed. Flag ancilla qubits provide additional information to capture errors that occur during stabilizer measurements, ensuring that a single fault can only result in a correctable error after the QEC is completed [8, 9]. The concept of flag fault tolerance is critical to our demonstration of fault-tolerant universal quantum computation using an 8-qubit error detection code in Chap 4.3, as well as the fault-tolerant state preparation experiment in Chap 5.

The QEC code we consider is the 5-qubit code with a total of 7 qubits, as defined in Eq. 4.4. Each single-qubit error corresponds to a unique 4-bit syndrome, given as the eigenvalues of the stabilizers. However, the ability of this 5-qubit code to correct arbitrary single-qubit errors is based on the assumption that syndrome extraction is realized by ideal stabilizer measurements. In practice, fault-tolerant error syndrome extraction protocols must be designed to work when the operations involved are noisy.

For distance-3 codes, a unit of fault-tolerant quantum error correction or syndrome extraction satisfies the following criteria [2, 8]: (1) If the logical input state has a single qubit error and the syndrome extraction unit is noise-free, the output state is the logical
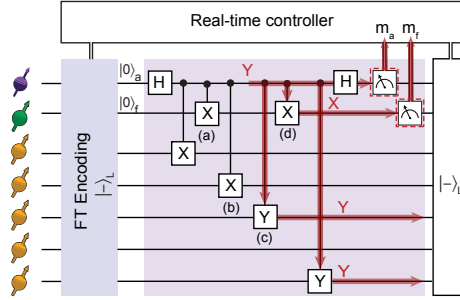
Figure 4.3: The circuit for measuring the stabilizer $s_1 = XXYIY$ with flag on the encoded state. Given this specific order of gates, the Y error on the auxiliary qubit is a malicious fault for the logical state $|-\rangle_L$, as it will propagate to the data qubits to become $Y_3 X_5 = -Z_4 \cdot \overline{Z} \cdot s_1 \cdot s_3 \cdot s_4$. This 2-qubit error $Y_3 Y_5$ will lead to a logical Z error after a round of noiseless error correction. However, this Y error will also propagate to the flag auxiliary qubit and flip its measurement outcome, which provides additional information: a flipped flag measurement heralds the possibility of such a malicious fault.

input state with its error removed; (2) If the logical input state is noise-free and there is a single fault in the syndrome extraction unit, the output state has at most a single-qubit error on top of the given input state; (3) If the input state is an arbitrary state, and there is at most one single fault in the syndrome extraction unit, then the output state is any encoded state with at most a single-qubit error. For the 5-qubit code, the last requirement is automatically fulfilled. For details about fault-tolerance, we refer the reader to Refs. [2, 8].

The circuit for measuring the stabilizer $s_1 = XXYIY$ is shown in Fig. The basic idea of using a flag ancilla qubit is to use the additional information provided by the flag qubit measurements to correct certain two-qubit errors [8]. For example, consider first preparing the logical state $|-\rangle_L$ and then measuring $s_1 = XXYIY$ using the circuit in Fig. 4.3. We assume that the logical preparation is noise free and that there is a single error in the measurement of s_1. It can then be shown that if the flag qubit is not flipped, there is at most a single qubit error in the output state. On the other hand, if the flag qubit measurement is flipped, errors on the data qubits can only be X_1, $X_1 Z_2$, $X_3 Y_5$, $Y_3 Y_5$, $Z_3 Y_5$, $X_1 Y_2$, and Y_5 (see Tab 4.2 for details). Each of these possible errors corresponds to a unique syndrome, so if we were to perform a round of noiseless error correction on the output state, i.e., measure all four stabilizers without flag qubits, these errors can be identified and corrected since they have distinguishable syndromes.

It is important to note that the noisy measurement of stabilizer s_1 combined with this round of noiseless stabilizer measurements consists of a complete fault-tolerant QEC cycle with flag. In general, to implement a complete flag QEC cycle, one repeatedly measures stabilizers (with and without flag) in a conditional form until the error on the logical qubit can be unambiguously identified [8, 9]. We summarize the protocol proposed by Chao and Reichardt [9] as a flowchart in Fig. 4.4. A similar version of the flag-FT error correction protocol can be found in Ref. [8].

gate (b): fault	data qubit error	gate (c): fault	data qubit error
XI (YI)	$Y_3 Y_5$	XI (YI)	Y_5
XX (YX)	$X_2 Y_3 Y_5 \equiv X_1$	XX (YX)	$X_3 Y_5$
XY (YY)	$Y_2 Y_3 Y_5 \equiv X_1 Z_2$	XY (YY)	$Y_3 Y_5$
XZ (YZ)	$Z_2 Y_3 Y_5 \equiv X_1 Y_2$	XZ (YZ)	$Z_3 Y_5$
gate (a): fault	data qubit error	gate (d): fault	data qubit error
XZ (YZ)	$X_2 Y_3 Y_5 \equiv X_1$	XX (XY)	Y_5
XI (YI)	$X_2 Y_3 Y_5 \equiv X_1$	YX (YY)	Y_5
IX (IY)	I	IX (IY)	I
ZX (ZY)	I	ZX (ZY)	I

Table 4.2: Single faults that can flip the flag qubit measurement in the stabilizer $s_1 = XXYIY$ measurement circuit (Fig. 4.3). Such a fault is either induced by a faulty two-qubit gate or a single-qubit idling error after the gate. A readout error of the flag qubit can lead a different correction but does not induce an error on the output state directly. These 2-qubit Pauli errors are arranged in the order of control and target qubit respectively and they result in certain data qubit errors on the output state (errors in parentheses lead to the same data qubit errors). Syndromes of these resulting data qubit errors remain distinguishable, hence a perfect round of stabilizer measurements would identify and correct them. Note that here we assume only one fault during the circuit of measuring s_1 and the state preparation is noiseless.
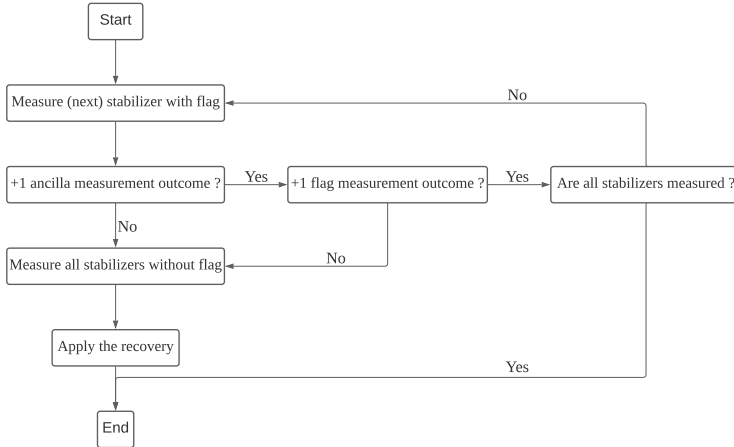
Figure 4.4: The flowchart of a full flag error correction cycle proposed by Chao and Reichardt [9]. For the 5-qubit code, the stabilizers are $s_1 = XXYIY, s_2 = YXXYI, s_3 = IYXXY$ and $s_4 = YIYXX$. The stabilizer measurements without flag give a 4-bit error syndrome, which determines the recovery operation. Note that the error syndrome is interpreted differently depending on whether there is a raised flag. In the experiments presented in this work, we apply one stabilizer measurement of this error correction cycle and characterize the resulting post-measurement state.

4.3. UNIVERSAL QUANTUM COMPUTATION USING AN 8-QUBIT CODE

Fault-tolerant quantum computation protocols often rely on QEC codes, such as the CSS codes mentioned earlier, to enable the implementation of logical Clifford gates, including the logical CNOT gate. However, the Gottesman-Knill theorem [19] shows that quantum circuits consisting solely of Clifford gates can be efficiently simulated by classical computers. This is because Clifford gates merely conjugate tensor products of Pauli matrices into other tensor products of Pauli matrices, a process that can be tracked easily by a classical computer.

To attain universal quantum computation that cannot be efficiently simulated by a classical computer, it is necessary to incorporate non-Clifford gates, like the Toffoli (also called CCNOT) gate or the T gate. A few examples of universal gate sets include $\{H, T, \text{CNOT}\}$ and $\{H, \text{Toffoli}\}$ [55], with the Hadamard gate H being a Clifford gate. Non-Clifford gates are typically implemented using gate teleportation, which requires consuming encoded magic states. These states can be prepared with high fidelity through a process called magic state distillation [6]. However, the qubit and gate overhead for implementing a non-Clifford through magic state can be demanding [6, 40, 55]. For a pedagogical introduction to gate teleportation, the use of magical states, and magical state distillation, readers may wish to consult Ref. [58].

To avoid the challenging task of magic state distillation, one alternative approach is to use stabilizer codes that support transversal non-Clifford gates [7, 56]. While some Clifford gates may require gate teleportation using encoded Pauli eigenstates, the benefit is that preparing encoded Pauli eigenstates fault-tolerantly may be much simpler than preparing high-fidelity encoded magic states through distillation.

To investigate this alternative approach for achieving fault-tolerant universal quantum computation, we focus on an 8-qubit error-detecting code, known as the "smallest interesting color code" [1, 15]. In addition to supporting the transversal CCZ gate, we chose this code for its high encoding rate, with 3 logical qubits encoded into 8 physical qubits. This is particularly beneficial for experimental platforms with a limited number of qubits.

It is important to note that this is an error-detecting code, meaning that it can only detect, but not correct, arbitrary single-qubit errors. Therefore, implementing quantum computation using this code requires post-selection, with the entire computation restarted from the beginning if an error is detected. This code is represented as $[[n = 8, k = 3, d = 2]]$.

4.3.1. FAULT-TOLERANT LOGICAL GATES OF THE 8-QUBIT CODE

In the following, we present the fault-tolerant implementations of several logical Clifford and non-Clifford gates for this code. We use Q to label the encoded qubits and q to label physical qubits. The stabilizers and logical operators of the 8-qubit code are displayed in

$$S$$

$$\mathsf{S_3} = Z_{1,2,3,4} \qquad \mathsf{S_4} = Z_{1,2,5,6} \qquad \mathsf{S_5} = Z_{1,3,5,7}$$

$$\mathsf{S_2} = Z_{1,2,3,4,5,6,7,8} \qquad \mathsf{S_1} = X_{1,2,3,4,5,6,7,8}$$

$$L$$

$$\mathsf{Q_1} : \begin{array}{l} X_{1,2,3,4} = \mathsf{X_{L1}} \\ Z_{1,5} = \mathsf{Z_{L1}} \end{array} \qquad \mathsf{Q_2} : \begin{array}{l} X_{1,2,5,6} = \mathsf{X_{L2}} \\ Z_{1,3} = \mathsf{Z_{L2}} \end{array} \qquad \mathsf{Q_3} : \begin{array}{l} X_{1,3,5,7} = \mathsf{X_{L3}} \\ Z_{1,2} = \mathsf{Z_{L3}} \end{array}$$
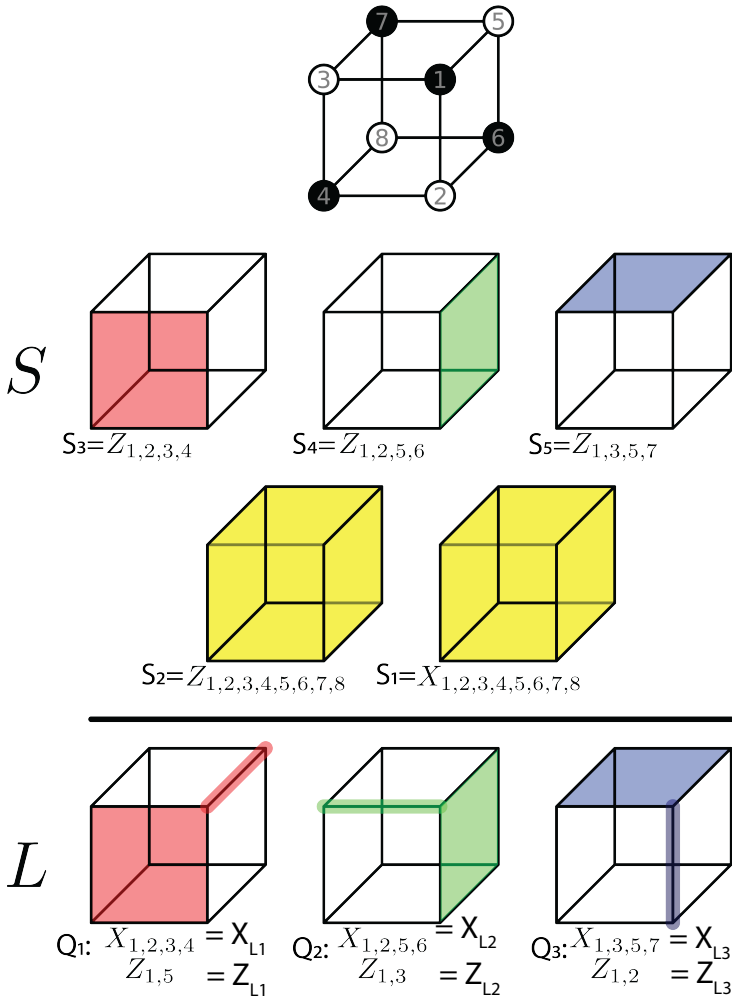
Figure 4.5: Stabilizers and logical operators of the 8-qubit error-detecting code. The numbering scheme of the physical qubits at the top follows Earl Campbell's blog post. The encoded qubits are labeled as Q.

Fig 4.5, along with the specific physical qubit numbering scheme from Earl Campbell's blog post [1].

CCZ GATE

For the purpose of achieving universal quantum computation, a key property is that the logical 3-qubit CCZ gate is transversal; it is implemented using the single-qubit non-Clifford T gate, i.e.,
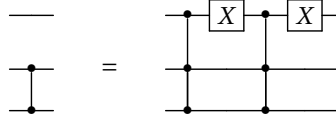
$$CCZ_L = T \otimes T^\dagger \otimes T^\dagger \otimes T \otimes T^\dagger \otimes T \otimes T \otimes T^\dagger \tag{4.15}$$

where the T gate is written as

$$T = \begin{pmatrix} 1 & 0 \\ 0 & e^{-i\pi/4} \end{pmatrix}. \tag{4.16}$$

CZ GATE

The CZ gate can be decomposed into two CCZ gates and two Pauli X gates, as shown in the following circuit:

 (4.17)
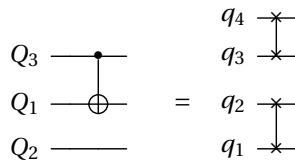
It's worth noting that $TXTX = TT^\dagger = I$. Therefore, the logical CZ gates can be obtained in terms of the physical gates as follows

$$CZ_{L_{1,2}} = S_2^\dagger S_4 S_6 S_8^\dagger, \quad CZ_{L_{1,3}} = S_3^\dagger S_4 S_7 S_8^\dagger, \quad CZ_{L_{2,3}} = S_5^\dagger S_6 S_7 S_8^\dagger \tag{4.18}$$

where $S = T^2$ represents the S gate, not to be confused with the stabilizers. The notation $CZ_{L_{i,j}}$ refers to the logical CZ gate between the encoded qubits Q_i and Q_j.

CNOT GATE

The logical CNOT gate for the 8-qubit code can be easily implemented with two swap gates between physical qubits. For instance, if we want to implement the logical CNOT with Q_3 as the control qubit and Q_1, we first swap q_1 and q_2, and then swap q_3 and q_4. This is illustrated in the circuits below:

 (4.19)

These SWAP gates can be executed in hardware by simply relabeling the physical qubits. See the detailed proof in Appendix 4.4.1.

HADAMARD GATE

Implementing a logical Hadamard gate on a single logical qubit poses a significant challenge for the 8-qubit code. However, we have developed a fault-tolerant scheme that uses gate teleportation and involves consuming a Pauli eigenstate of the 4-qubit error-detecting code. This gate scheme requires a total of 32 2-qubit gates, and more information can be found in Appendix 4.4.2.

4.3.2. EXAMPLE COMPUTATION: ONE-BIT ADDITION

This section explores an example of using the 8-qubit code to achieve fault-tolerant universal quantum computation: the one-bit addition algorithm. Even though this is a trivial quantum algorithm, it involves both Clifford (CNOT) and non-Clifford (Toffoli) gates. The circuit for this algorithm is shown below:

$$\begin{array}{ll}
|a_0\rangle \quad & |a_0\rangle \\
|a_1\rangle \quad & |b_0\rangle \\
|0\rangle \quad & |b_1\rangle
\end{array} \qquad (4.20)$$
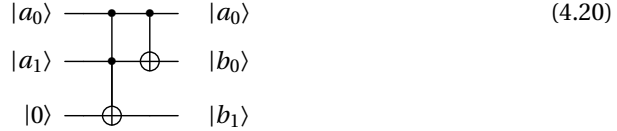
It is straightforward to confirm that this circuit performs one-bit addition of two one-bit numbers (a_0 and a_1) and stores their sum in two bits (b_0 and b_1), such that $a_0 + a_1 = b_0 + 2b_1$. Additionally, the circuit preserves the initial summand a_0 to ensure its reversibility. As the Toffoli gate can be decomposed into 6 CNOT gates and some single-qubit gates [37], this circuit can be implemented using only three physical qubits and a minimum of 5 elementary CNOT gates.

If both summand qubits are initially in the computational basis (eigenstates of Pauli Z), the algorithm can be implemented solely with Pauli X gates. For instance, when the three qubits are initially in the state $|000\rangle$, both the Toffoli and CNOT gates become equivalent to identity gates, and the calculation of 0+0=0 can be performed without any qubits. To make the implementation slightly more interesting, we can initialize the circuit with both summand qubits in the +1 eigenstate of Pauli X.

CIRCUIT AT THE LOGICAL LEVEL
The circuit below depicts the logical level implementation of the one-bit addition algorithm using the 8-qubit code:

$$\begin{array}{ll}
Q_3 : |+\rangle \quad & \boxed{Z} \\
Q_1 : |+\rangle \quad & \boxed{Z} \\
Q_2 : |+\rangle \quad & \boxed{X}
\end{array} \qquad (4.21)$$

It is important to note that we have replaced the logical Toffoli gate with the logical CCZ gate, which is obtained by sandwiching the former Toffoli gate with two Hadamard gates on the encoded qubit Q_2. To avoid the costly implementation of these two logical Hadamard gates, one is absorbed by preparing Q_2 in the eigenstate of logical Pauli X, and the other is absorbed by measuring Q_2 in the X basis.

CIRCUIT AT THE PHYSICAL LEVEL
We have developed a fault-tolerant circuit to implement the algorithm, as shown in Fig 4.6. By using the 8-qubit code, we can almost eliminate the cost of implementing logical CCZ and CNOT gates, as they do not require additional 2-qubit gates. This has enabled us to significantly optimize the circuit, reducing the number of 2-qubit gates to only 24, which are used solely for the logical state preparation and readout.

The fault-tolerant readout of the encoded qubits is complicated because they are measured in different bases. Specifically, Q_1 and Q_3 are measured in the Z-basis, while
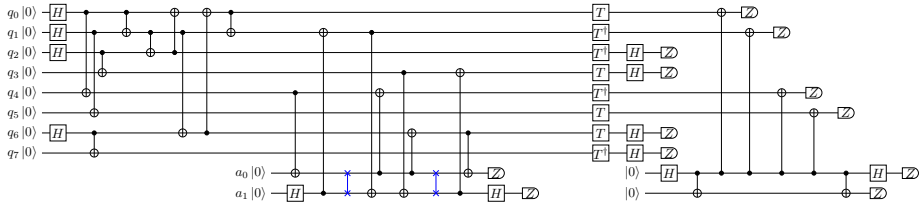
Figure 4.6: The circuit for implementing the one-bit addition algorithm fault-tolerantly using the 8-qubit code. The first 10 CNOT gates prepare the three encoded qubits into the +1 eigenstates of their logical Pauli X operators non-fault-tolerantly. Then two stabilizers are measured simultaneously to ensure the output state has at most a single-qubit detectable error. The transversal T gates implement the logical CCZ gate; the logical CNOT is realized by relabeling the physical qubits.

Q_2 is measured in the X-basis. To read out Q_2 in the X-basis, we measure $X_1 X_2 X_5 X_6$ and $X_3 X_4 X_7 X_8$, both of which are logical X operators of Q_2. Because they differ by the X-stabilizer, their measurement outcomes should be equal; otherwise, an error is detected, and the computation must be restarted. The eigenvalue of $X_3 X_4 X_7 X_8$ can be extracted through single-qubit measurements, as it commutes with the logical Z operators of Q_1 and Q_3. However, the eigenvalue of $X_1 X_2 X_5 X_6$ must be extracted through stabilizer measurements, which requires an additional flag ancilla qubit to ensure fault-tolerance, resulting in 6 CNOT gates. Finally, the logical Z operators of Q_1 and Q_3 are measured through single-qubit measurements on the physical qubits q_1, q_2, q_5, q_6 in the Z-basis. The product of the four single-qubit measurement outcomes is the eigenvalue of the Z-type stabilizer $S_5 = Z_1 Z_2 Z_5 Z_6$, which should be +1; otherwise, an error is detected, and the computation should restarted.

The most expensive part is preparing the three encoded qubits into the +1 eigenstates of logical Pauli X operators. This is done by first preparing the desired state using 10 CNOT gates, as depicted on the left-hand side of the circuit in Fig 4.6. This preparation is generated automatically by a search algorithm on a graph. The basic idea is to treat each stabilizer state, which is a simultaneous +1 eigenstate of some tensor product of Pauli operators, as a node in a graph. If one state can be generated by applying a CNOT gate to another state, the two nodes in the graph representing these two states are connected by an edge. Then, a breadth-first search on the graph can automatically find the shortest path to the desired state. This gives us the preparation circuit that is optimized in terms of the minimum number of CNOT gates required to prepare the desired state.

This preparation is not fault-tolerant, and a brute-force search using a computer reveals that a single fault can lead to the following errors:

$$< X_1 X_2, Z_1 Z_2, Y_1 X_2, Y_5 Y_6, Z_5 Y_6, X_1 X_7, Y_1 Z_2 X_7, Z_3 X_4, Z_7 X_8, Z_1 Z_7, Y_1 X_2 Z_7 > .$$

To detect all possible errors, we need to measure a logical X operator $X_2 X_3 X_6 X_7$ and a Z-type stabilizer $Z_1 Z_4 Z_5 Z_8$, as each of the possible errors anti-commutes with at least one of these two operators. To ensure fault-tolerance, we use a technique proposed by Ben Reichardt, where the two operators are measured simultaneously and interleaved by two swap gates [47]. This technique allows us to detect any single fault that may have occurred during the stabilizer measurements.

Note that we have verified the fault-tolerance of the designed circuit in Fig 4.6 by brute force using a computer program. Details of the verification are currently being prepared for publication.

CHARACTERIZATION OF THE PERFORMANCE

We have carried out the experiments using a trapped-ion quantum computer from Quantinuum, where the 2-qubit gate error rate is typically around 2×10^{-3} [49, 50]. The error rates of single-qubit operations are negligible compared to the 2-qubit gate error rates. Implementing the algorithm at the physical qubit level requires only 3 qubits and 5 2-qubit gates, resulting in an error rate of approximately $5 \times 2 \times 10^{-3} = 1\%$. However, by using the 8-qubit code and the optimized circuit shown in Fig 4.6, the logical error rate is estimated to be $\binom{24}{2} \times (2 \times 10^{-3})^2 = 0.1104\%$, as there are only 24 2-qubit gates in total. This value is substantially lower than the estimated 1% error rate of the implementation using physical qubits directly.

To assess the performance of the trapped-ion qubits without performing costly 3-qubit process tomography, we use the arithmetic error rate as a metric. An arithmetic error occurs when we can confirm that the classical output is impossible. For instance, in the circuit shown in Eq (4.20), if the final qubit readout yields $b_0 = b_1 = 1$, it indicates an impossible summation of 3, resulting in an arithmetic error event that makes the computation incorrect.

Further optimization of the circuit for the trapped-ion computer reduced the arithmetic error rate to approximately 0.07% using the fault-tolerant protocol, which is considerably lower than the 1% arithmetic error rate observed when using physical qubits directly. We are currently preparing detailed reports on the experimental optimizations and the analysis of the experimental results.

4.3.3. DISCUSSION

Our analysis assumes all-to-all connectivity of physical qubits, but some experimental platforms such as superconducting qubits [17, 27, 32], quantum dots [43, 59], and single NV centers [5, 11] do not have this connectivity, necessitating additional constraints and resources to use this 8-qubit code for quantum computing. For example, implementing the one-bit addition circuit in Fig 4.6 using a single NV center would require replacing the preparation stage with a sequence of stabilizer measurements to use only electron-nuclear entangling gates, resulting in significantly more gate operations. This approach is similar to the preparation scheme in Chap 5 for preparing the logical states of the 5-qubit code with a single NV center.

Moreover, due to nearest-neighbor connectivity limitations, platforms like superconducting qubits [17, 27, 32] and quantum dots [43, 59] commonly prefer the surface code for QEC, as it has a high error threshold and a simple structure that allows physical qubits to interact with only their nearest neighbors [14, 22]. In particular, with a 2-qubit gate fidelity typically higher than 99.5%, the Google AI team has realized a milestone for fault-tolerant quantum computation, namely the logical error rate in a real device is reduced by scaling up the size of the surface code [17].

However, for experimental platforms such as trapped ions [49, 50], neutral atoms [34], and NV-based networks [21, 45], giving up the advantage of their all-to-all qubit

connectivity is not a reasonable option. Taking advantage of the good qubit connectivity in these platforms is another motivation for us to explore this 8-qubit code. Even though a detailed comparison of the required resources of the 8-qubit code and the surface code is necessary, our preliminary findings suggest that investigating more efficient codes beyond the surface code would be an intriguing direction to pursue when the connectivity constraint is removed.

As the thesis focuses on utilizing spins in diamond for quantum technologies, it is crucial to examine NV-based networks in detail. Although entangling NV centers through optical links is a challenging task, as discussed in Chap 3.1.3, for distributed quantum computation, connecting distant NV centers is no more difficult than connecting nearby ones. This is because, in the context of distributed quantum computation, we typically consider multiple NV centers within a small chip, where the differences in distance between any pair of NV centers are negligible. Thus, qubit connectivity is not a limiting factor for distributed quantum computation using an NV-based network, and implementing the surface code would forfeit one of its advantages [36, 57].

Furthermore, the two-qubit gate fidelity between remote NV centers is low, with the best reported number being only around 80% [21, 44, 45]. Therefore, a more realistic goal for NV-based networks is to design experiments that can demonstrate the concept of fault-tolerance with less stringent gate fidelity requirements, instead of aiming to cross the surface code threshold as with superconducting qubits. For instance, the proposed one-bit addition algorithm using the 8-qubit code as an example of fault-tolerant universal quantum computation would be an interesting and feasible experiment for NV-based networks in the near future, as the pseudo-threshold is as high as about 2%. Additionally, other algorithms can be considered, and other codes can also be explored for NV-based networks.

4.4. APPENDIX

Before providing a step-by-step explanation of how the circuits work, it is important to clarify how CNOT gates transform Pauli operators. Specifically, if an X error occurs on the control qubit, it will be copied and propagate to the target qubit, whereas if a Z error occurs on the target qubit, it will be copied and propagate to the control qubit. This can be easily seen by examining the following circuits:

$$X \quad \begin{matrix} \bullet \\ \oplus \end{matrix} \quad \begin{matrix} X \\ X \end{matrix} \qquad Z \quad \begin{matrix} \bullet \\ \oplus \end{matrix} \quad Z \tag{4.22}$$

$$Z \quad \begin{matrix} \bullet \\ \oplus \end{matrix} \quad \begin{matrix} Z \\ Z \end{matrix} \qquad X \quad \begin{matrix} \bullet \\ \oplus \end{matrix} \quad X$$

4.4.1. LOGICAL CNOT GATE OF THE 8-QUBIT CODE

If we want to implement the logical CNOT with Q_3 as the control qubit and Q_1 as the target qubit, we can swap q_1 and q_2, and then swap q_3 and q_4. The swap gates can be implemented by simply relabeling the physical qubits.

By examining the mapping of stabilizers and logical operators as shown in the table below, it is clear that the resulting circuit is indeed the desired logical CNOT gate.
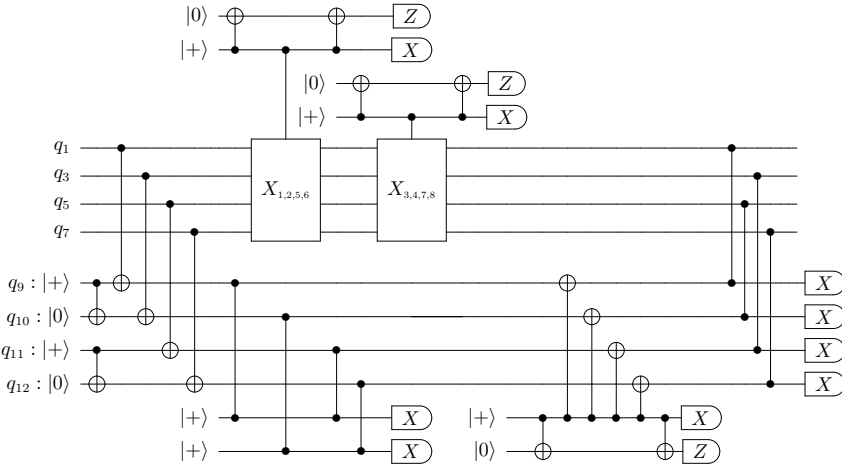
Figure 4.7: This circuit implements a logical Hadamard gate on an encoded qubit of the 8-qubit code (q_1 to q_8) using gate teleportation, which involves consuming a Pauli eigenstate of the 4-qubit error-detecting code (q_9 to q_{12}). For clarity, we do not depict the physical qubits q_2, q_4, q_6, and q_8. The basic idea is to teleport the encoded information from the 8-qubit block to the 4-qubit block, and then teleport the state back to the 8-qubit block. This process can effectively apply a logical Hadamard gate. Error-detection gadgets are incorporated at appropriate locations, and post-selection is performed to restart the entire computation when an error is detected, ensuring that the entire process is fault-tolerant.

S_1	X	X	X	X	X	X	X	X		S_1	X	X	X	X	X	X	X	X
S_2	Z	Z	Z	Z	Z	Z	Z	Z		S_2	Z	Z	Z	Z	Z	Z	Z	Z
S_3	Z	Z	Z	Z	I	I	I	I		S_3	Z	Z	Z	Z	I	I	I	I
S_4	Z	Z	I	I	Z	Z	I	I		S_4	Z	Z	I	I	Z	Z	I	I
S_5	Z	I	Z	I	Z	I	Z	I		$S_3 S_5$	I	Z	I	Z	Z	I	Z	I
X_{L1}	X	X	X	X	I	I	I	I		X_{L1}	X	X	X	X	I	I	I	I
Z_{L1}	Z	I	I	I	Z	I	I	I		$Z_{L1} Z_{L3}$	I	Z	I	I	Z	I	I	I
X_{L2}	X	X	I	I	X	X	I	I		X_{L2}	X	X	I	I	X	X	I	I
Z_{L2}	Z	I	Z	I	I	I	I	I		$S_3 X_{L2}$	I	Z	I	Z	I	I	I	I
X_{L3}	X	I	X	I	X	I	X	I		$X_{L1} X_{L3}$	I	X	I	X	X	I	X	I
Z_{L3}	Z	Z	I	I	I	I	I	I		Z_{L3}	Z	Z	I	I	I	I	I	I

$$\xrightarrow{\text{SWAP}_{1,2}\text{SWAP}_{3,4}}$$

4.4.2. LOGICAL HADAMARD GATE OF THE 8-QUBIT CODE

To apply a logical Hadamard gate on any of the three encoded qubits of the eight-qubit code, gate teleportation is utilized through the four-qubit error-detecting code [[4,2,2]]. The circuit for this process is depicted in Fig.4.7, and involves a total of 32 2-qubit gates.

		q_1	q_2	q_3	q_4	q_5	q_6	q_7	q_8	q_9	q_{10}	q_{11}	q_{12}
		X	X	X	X	X	X	X	X	I	I	I	I
		Z	Z	Z	Z	Z	Z	Z	Z	I	I	I	I
Stabs	[8,3,2]	Z	Z	Z	Z	I	I	I	I	I	I	I	I
		Z	Z	I	I	Z	Z	I	I	I	I	I	I
		Z	I	Z	I	Z	I	Z	I	I	I	I	I
Stabs	[4,2,2]	I	I	I	I	I	I	I	I	X	X	X	X
		I	I	I	I	I	I	I	I	Z	Z	Z	Z
Q_1:	X_{L1}	X	X	X	X	I	I	I	I	I	I	I	I
	Z_{L1}	Z	I	I	I	Z	I	I	I	I	I	I	I
Q_2:	X_{L2}	X	X	I	I	X	X	I	I	I	I	I	I
	Z_{L2}	Z	I	Z	I	I	I	I	I	I	I	I	I
Q_3:	X_{L3}	X	I	X	I	X	I	X	I	I	I	I	I
	Z_{L3}	Z	Z	I	I	I	I	I	I	I	I	I	I
Q_4:	X_{L4}	I	I	I	I	I	I	I	I	X	I	X	I
	Z_{L4}	I	I	I	I	I	I	I	I	Z	Z	I	I
Q_5:	X_{L5}	I	I	I	I	I	I	I	I	X	X	I	I
	Z_{L5}	I	I	I	I	I	I	I	I	Z	I	Z	I

Table 4.3: The physical qubit numbering convention; definitions of stabilizers and logical operators for each logical qubit in the [[4,2,2]] and [[8,3,2]] codes.

The qubit numbering convention, stabilizers, and logical operators are detailed in Table 4.3. Let's proceed with a step-by-step explanation of the circuit in Figure 4.7:

STEP 1: 4-QUBIT CODE PAULI EIGENSTATE PREPARATION
To prepare the encoded qubits Q_4 and Q_5 of the [[4,2,2]] code, we begin by initializing q_9 and q_{11} to the $|+\rangle$ state, and q_{10} and q_{12} to the $|0\rangle$ state. Next, we apply two CNOT gates, one between q_9 and q_{10}, and the other between q_{11} and q_{12}, where q_9 and q_{11} serve as controls. This process creates a tensor product of two Bell pairs, resulting in Q_4 and Q_5 being prepared in the $|0\rangle_L$ and $|+\rangle_L$ states, respectively.

STEP 2: LOGICAL STATE TELEPORTATION
Our next step is to teleport the state of Q_2 to Q_4. We achieve this by applying transversal CNOT gates with q_1, q_3, q_5, and q_7 as the control qubits, and q_9, q_{10}, q_{11}, and q_{12} as the target qubits. These gates realize one logical CNOT between Q_1 and Q_5, and one logical CNOT between Q_2 and Q_4:

- These gates do not change the stabilizers of the two codes. For instance, the X-stabilizer of the 8-qubit code is mapped to its tensor product with the X-stabilizer of the 4-qubit code.

- For Q_2, its logical X operator $X_1 X_2 X_5 X_6$ is mapped to $X_1 X_2 X_5 X_6 \otimes X_9 X_{11}$, and its logical Z operator $Z_1 Z_3$ remains unchanged. For Q_5, its logical X operator is not changed, while its logical Z operator $Z_9 Z_{11}$ is mapped to $Z_1 Z_3 \otimes Z_9 Z_{11}$. This corresponds to a logical CNOT gate with Q_2 as control and Q_4 as target.

- Similarly, another logical CNOT with Q_1 as control and Q_5 as target is applied.

Since we have prepared Q_5 in the state $|+\rangle_L$, the logical CNOT gate between Q_1 and Q_5 is effectively an identity gate. However, Q_4 is initialized in the state $|0\rangle_L$. By measuring Q_2 in its logical X basis, we can teleport its state to Q_4. For simplicity, let's assume that the outcome of the logical X measurement of Q_2 is +1, so that Q_2 is left in the state $|0\rangle_L$.

In order to extract the eigenvalue of the logical X operator of Q_2 in a fault-tolerant manner, we perform measurements on the operators $X_1 X_2 X_5 X_6$ and $X_3 X_4 X_7 X_8$ using a flag ancilla qubit. These two operators differ by the X-stabilizer of the 8-qubit code, so the product of their eigenvalues should always be +1. If the product of eigenvalues is not +1, an error is detected, and the computation should be restarted. In addition, these two operators should be measured with an extra flag ancilla qubit [8, 9] to ensure that any single faulty gate can result in at most a single-qubit error, which remains detectable. The circuit for measuring $X_1 X_2 X_5 X_6$ with the flag is shown in the diagram below:

$$(4.23)$$
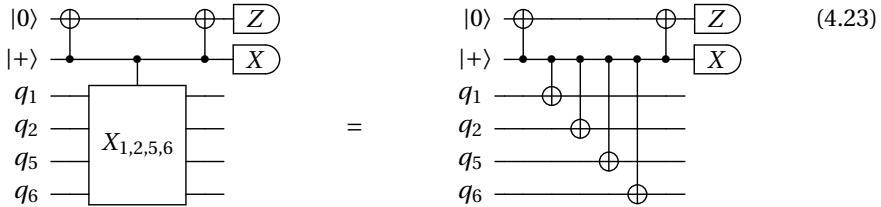
The ancillary qubit that we initialize in the state $|0\rangle$ is referred to as the flag ancilla qubit, which is measured in the Z-basis. We proceed with the circuit only if the flag ancilla qubit is measured to be in the state $|0\rangle$. More information about the use of flag qubits is available in Chapter 4.

After the state teleportation, the encoded qubits Q_1, Q_3 and Q_5 are effectively not touched. For simplicity, we assume the logical X measurement of Q_2 is +1 (up to a Pauli correction) so that it is left in the state $|0\rangle_L$. Q_4 now stores the state that is previously stored in Q_2.

STEP 3: TRANSVERSAL HADAMARD GATES ON THE 8-QUBIT BLOCK
In this step, we apply a transversal Hadamard gates on the 8-qubit block. This changes the definition of the three encoded qubits of the 8-qubit code, we label them using $\tilde{Q}$:

- $\tilde{Q}_1$: $\tilde{X}_{L1} = X_1 X_5$, $\tilde{Z}_{L1} = Z_1 Z_2 Z_3 Z_4$.

- $\tilde{Q}_2$ is now in $|+\rangle_L$ with $\tilde{X}_{L2} = X_1 X_3$, $\tilde{Z}_{L2} = Z_1 Z_3 Z_5 Z_7$.

- $\tilde{Q}_3$: $\tilde{X}_{L3} = X_1 X_2$, $\tilde{Z}_{L3} = Z_1 Z_3 Z_5 Z_7$.

STEP 3: RESET THE ENCODED QUBIT Q_5
To teleport the state stored in Q_4 back to $\tilde{Q}2$ without affecting the other encoded qubits, it's necessary to reset Q_5 to the $|0\rangle_L$ state. This can be achieved by measuring the logical Z operators $Z_9 Z_{11}$ and $Z_{10} Z_{12}$ of Q_5. Similar to the logical X measurement of Q_2, these two operators differ only by the Z-type stabilizer of the 4-qubit code, so their eigenvalues should be identical. If the product of their eigenvalues isn't +1, an error is detected, and

the circuit must be restarted. For simplicity, we assume that the outcome of the logical Z measurement is +1.

It should be noted that measuring the logical Z operators directly is already fault-tolerant because they have a weight of 2. There is no need to use flag qubits, as any single fault can lead to, at most, a single-qubit error on the output state that is detectable.

STEP 4: TELEPORT THE STATE BACK TO THE 8-QUBIT BLOCK

In this step, we can apply transversal CNOT gates with $q_9, q_{10}, q_{11}, q_{12}$ serving as control qubits and q_1, q_5, q_3, q_7 as target qubits, respectively. It is important to note that in this step, q_5 is paired with q_{10} instead of q_{11}, and q_3 is paired with q_{11} instead of q_{10}. Due to this change in qubit pairing, a single fault could lead to undetectable logical errors in the 4-qubit block. For example, an XZ error followed by the CNOT gate between q_3 and q_{10} in Step 2 will result in a two-qubit error, $Z_{10}Z_{11}$. To avoid this, before applying the transversal CNOT gates, we need to measure the stabilizer $X_9 X_{10} X_{11} X_{12}$ on the 4-qubit block with a flag. This measurement can detect any single-qubit Pauli Z error on the 4-qubit block.

As in Step 2, the transversal CNOT gates in this step enable the implementation of one logical CNOT gate with Q_4 as control and $\tilde{Q}_2$ as target, as well as one logical CNOT gate with Q_5 as control and $\tilde{Q}_1$ as target. However, since we have reset Q_5 to $|0\rangle_L$, the latter logical CNOT is equivalent to an identity gate.

At this point, it is no longer necessary to retain the 4-qubit block, so we can destructively measure all four qubits in the X-basis. Consequently, Q_4 is effectively measured in its logical X-basis, and the state can be teleported back to $\tilde{Q}_2$. Furthermore, by calculating the product of the four X-basis measurements, we can determine the eigenvalue of $X_1 X_2 X_3 X_4$ of the 4-qubit code, which enables the detection of a single-qubit Pauli Z error.

STEP 5: TRANSVERSAL HADAMARD GATES ON THE 8-QUBIT BLOCK AGAIN

The final step involves the application of transversal Hadamard gates on the 8-qubit block. It's easy to check that $\tilde{Q}_1$ and $\tilde{Q}_3$ are transformed back to Q_1 and Q_3, respectively, and the states stored in them remain unchanged.

The analysis for the second encoded qubit, Q_2 or $\tilde{Q}_2$, is more subtle. For simplicity, let us assume that Q_2 or $\tilde{Q}_2$ is not entangled with the other two encoded qubits, and its original state is denoted as $|\psi\rangle$. As the previous step teleported the state from Q_4 to $\tilde{Q}_2$, we can express $|\psi\rangle$ as:

$$|\psi\rangle = \alpha |\tilde{0}\rangle_L + \beta |\tilde{1}\rangle_L, \tag{4.24}$$

where $|\tilde{0}\rangle_L$ and $|\tilde{1}\rangle_L$ are eigenstates of the logical Z operator $Z_1 Z_2 Z_5 Z_6$, as discussed in Step 3. Applying the Hadamard gates changes the definitions of the logical operators, i.e., the basis states $|\tilde{0}\rangle_L$ and $|\tilde{1}\rangle_L$ become eigenstates of the logical X operator $Z_1 Z_3$ of Q_2. Thus, we can express the state of Q_2 in the basis of $|0\rangle_L$ and $|1\rangle_L$, which are eigenstates of $Z_1 Z_3$. This clarifies that a logical Hadamard is applied to the original state:

$$|\psi'\rangle = \alpha |+\rangle_L + \beta |-\rangle_L = H_L(\alpha |0\rangle_L + \beta |1\rangle_L). \tag{4.25}$$

This analysis also applies to the cases where Q_2 is entangled with the other two encoded qubits.

REFERENCES

[1] The smallest interesting colour code. `https://earltcampbell.com/2016/09/26/the-smallest-interesting-colour-code/`, 2016.

[2] P. Aliferis, D. Gottesman, and J. Preskill. Quantum accuracy threshold for concatenated distance-3 codes. *Quantum Inf. Comput.*, 6(97), 2006.

[3] P. Baireuther, T. E. O'Brien, B. Tarasinski, and C. W. Beenakker. Machine-learning-assisted correction of correlated qubit errors in a topological code. *Quantum*, 2:48, 2018.

[4] J. M. Boter, X. Xue, T. Krähenmann, T. F. Watson, V. N. Premakumar, D. R. Ward, D. E. Savage, M. G. Lagally, M. Friesen, S. N. Coppersmith, M. A. Eriksson, R. Joynt, and L. M. K. Vandersypen. Spatial noise correlations in a si/sige two-qubit device from bell state coherences. *Phys. Rev. B*, 101:235133, 2020.

[5] C. E. Bradley, J. Randall, M. H. Abobeih, R. C. Berrevoets, M. J. Degen, M. A. Bakker, M. Markham, D. J. Twitchen, and T. H. Taminiau. A Ten-Qubit Solid-State spin register with quantum memory up to one minute. *Phys. Rev. X*, 9(3):031045, 2019.

[6] S. Bravyi and A. Kitaev. Universal quantum computation with ideal clifford gates and noisy ancillas. *Phys. Rev. A*, 71:022316, 2005.

[7] S. Bravyi and A. Kitaev. Universal quantum computation with ideal clifford gates and noisy ancillas. *Phys. Rev. A*, 71:022316, 2005.

[8] C. Chamberland and M. E. Beverland. Flag fault-tolerant error correction with arbitrary distance codes. *Quantum*, 2(53):53, 2018.

[9] R. Chao and B. W. Reichardt. Quantum error correction with only two extra qubits. *Phys. Rev. Lett.*, 121:050502, 2018.

[10] J. P. Clemens, S. Siddiqui, and J. Gea-Banacloche. Quantum error correction against correlated noise. *Phys. Rev. A*, 69:062313, 2004.

[11] J. Cramer, N. Kalb, M. A. Rol, B. Hensen, M. S. Blok, M. Markham, D. J. Twitchen, R. Hanson, and T. H. Taminiau. Repeated quantum error correction on a continuously encoded qubit by real-time feedback. *Nat. Commun.*, 7:11526, 2016.

[12] S. J. Devitt, W. J. Munro, and K. Nemoto. Quantum error correction for beginners. *Rep. Prog. Phys.*, 76(7):076001, 2013.

[13] A. S. Fletcher, P. W. Shor, and M. Z. Win. Structured near-optimal channel-adapted quantum error correction. *Phys. Rev. A*, 77:012320, 2008.

[14] A. G. Fowler, A. C. Whiteside, and L. C. L. Hollenberg. Towards practical classical processing for the surface code. *Phys. Rev. Lett.*, 108:180501, 2012.

[15] L. Garvie and R. Duncan. Verifying the smallest interesting colour code with quantomatic. 2017.

[16] M. Gong, X. Yuan, S. Wang, Y. Wu, Y. Zhao, C. Zha, S. Li, Z. Zhang, Q. Zhao, Y. Liu, F. Liang, J. Lin, Y. Xu, H. Deng, H. Rong, H. Lu, S. C. Benjamin, C.-Z. Peng, X. Ma, Y.-A. Chen, X. Zhu, and J.-W. Pan. Experimental exploration of five-qubit quantum error-correcting code with superconducting qubits. *Natl. Sci. Rev.*, 9(1):nwab011, 2022.

[17] Google Quantum AI. Suppressing quantum errors by scaling a surface code logical qubit. *Nature*, 614(7949):676–681, 2023.

[18] D. Gottesman. *Stabilizer Codes and Quantum Error Correction*. PhD thesis, Caltech, 1997.

[19] D. Gottesman. The heisenberg representation of quantum computers. 1998.

[20] R. Harper, S. T. Flammia, and J. J. Wallman. Efficient learning of quantum noise. *Nat. Phys.*, 16(12):1184–1188, 2020.

[21] S. L. N. Hermans, M. Pompili, H. K. C. Beukers, S. Baier, J. Borregaard, and R. Hanson. Qubit teleportation between non-neighbouring nodes in a quantum network. *Nature*, 605(7911):663–668, 2022.

[22] C. Huang, X. Ni, F. Zhang, M. Newman, D. Ding, X. Gao, T. Wang, H.-H. Zhao, F. Wu, G. Zhang, C. Deng, H.-S. Ku, J. Chen, and Y. Shi. Alibaba cloud quantum development platform: Surface code simulations with crosstalk. 2020.

[23] A. Hutter and D. Loss. Breakdown of surface-code error correction due to coupling to a bosonic bath. *Phys. Rev. A*, 89:042334, 2014.

[24] D. Kielpinski, V. Meyer, M. Rowe, C. A. Sackett, W. M. Itano, C. Monroe, and D. J. Wineland. A decoherence-free quantum memory using trapped ions. *Science*, 291(5506):1013–1015, 2001.

[25] R. Klesse and S. Frank. Quantum error correction in spatially correlated quantum noise. *Phys. Rev. Lett.*, 95:230503, 2005.

[26] E. Knill, R. Laflamme, R. Martinez, and C. Negrevergne. Benchmarking quantum computers: The five-qubit error correcting code. *Phys. Rev. Lett.*, 86:5811–5814, 2001.

[27] S. Krinner, N. Lacroix, A. Remm, A. Di Paolo, E. Genois, C. Leroux, C. Hellings, S. Lazar, F. Swiadek, J. Herrmann, G. J. Norris, C. K. Andersen, M. Müller, A. Blais, C. Eichler, and A. Wallraff. Realizing repeated quantum error correction in a distance-three surface code. *Nature*, 605(7911):669–674, 2022.

[28] R. Laflamme, C. Miquel, J. P. Paz, and W. H. Zurek. Perfect quantum error correcting code. *Phys. Rev. Lett.*, 77:198–201, 1996.

[29] D. Layden, M. Chen, and P. Cappellaro. Efficient quantum error correction of dephasing induced by a common fluctuator. *Phys. Rev. Lett.*, 124:020504, 2020.

[30] D. A. Lidar, I. L. Chuang, and K. B. Whaley. Decoherence-free subspaces for quantum computation. *Phys. Rev. Lett.*, 81:2594–2597, 1998.

[31] S. Majumder, L. Andreta de Castro, and K. R. Brown. Real-time calibration with spectator qubits. *Npj Quantum Inf.*, 6(1):1–9, 2020.

[32] J. F. Marques, B. M. Varbanov, M. S. Moreira, H. Ali, N. Muthusubramanian, C. Zachariadis, F. Battistel, M. Beekman, N. Haider, W. Vlothuizen, A. Bruno, B. M. Terhal, and L. DiCarlo. Logical-qubit operations in an error-detecting surface code. *Nat. Phys.*, 18(1):80–86, 2021.

[33] H. P. Nautrup, N. Delfosse, V. Dunjko, H. J. Briegel, and N. Friis. Optimizing quantum error correction codes with reinforcement learning. *Quantum*, 3:215, 2019.

[34] M.-T. Nguyen, J.-G. Liu, J. Wurtz, M. D. Lukin, S.-T. Wang, and H. Pichler. Quantum optimization with arbitrary connectivity using rydberg atom arrays. *PRX Quantum*, 4:010316, 2023.

[35] N. H. Nickerson and B. J. Brown. Analysing correlated noise on the surface code using adaptive decoding algorithms. *Quantum*, 3:131, 2019.

[36] N. H. Nickerson, J. F. Fitzsimons, and S. C. Benjamin. Freely scalable quantum technologies using cells of 5-to-50 qubits with very lossy and noisy photonic links. *Phys. Rev. X*, 4:041041, 2014.

[37] M. A. Nielsen and I. L. Chuang. *Quantum Computation and Quantum Information*. Cambridge University Press, 2000.

[38] E. Novais and H. U. Baranger. Decoherence by correlated noise and quantum error correction. *Phys. Rev. Lett.*, 97:040501, 2006.

[39] E. Novais, A. J. Stanforth, and E. R. Mucciolo. Surface code fidelity at finite temperatures. *Phys. Rev. A*, 95:042339, 2017.

[40] J. O'Gorman and E. T. Campbell. Quantum computation with realistic magic-state factories. *Phys. Rev. A*, 95:032338, 2017.

[41] J. L. Orrell and B. Loer. Sensor-assisted fault mitigation in quantum computation. *Phys. Rev. Appl.*, 16:024025, 2021.

[42] A. K. Pal, P. Schindler, A. Erhard, Á. Rivas, M.-A. Martin-Delgado, R. Blatt, T. Monz, and M. Müller. Relaxation times do not capture logical qubit dynamics. *Quantum*, 6(632):632, 2022.

[43] S. G. J. Philips, M. T. Mądzik, S. V. Amitonov, S. L. de Snoo, M. Russ, N. Kalhor, C. Volk, W. I. L. Lawrie, D. Brousse, L. Tryputen, B. P. Wuetz, A. Sammak, M. Veldhorst, G. Scappucci, and L. M. K. Vandersypen. Universal control of a six-qubit quantum processor in silicon. *Nature*, 609(7929):919–924, 2022.

[44] M. Pompili, C. Delle Donne, I. te Raa, B. van der Vecht, M. Skrzypczyk, G. Ferreira, L. de Kluijver, A. J. Stolk, S. L. N. Hermans, P. Pawełczak, W. Kozlowski, R. Hanson, and S. Wehner. Experimental demonstration of entanglement delivery using a quantum network stack. *NPJ Quantum Inf.*, 8(1):1–10, 2022.

[45] M. Pompili, S. L. N. Hermans, S. Baier, H. K. C. Beukers, P. C. Humphreys, R. N. Schouten, R. F. L. Vermeulen, M. J. Tiggelman, L. Dos Santos Martins, B. Dirkse, S. Wehner, and R. Hanson. Realization of a multinode quantum network of remote solid-state qubits. *Science*, 372(6539):259–264, 2021.

[46] L. Postler, Á. Rivas, P. Schindler, A. Erhard, R. Stricker, D. Nigg, T. Monz, R. Blatt, and M. Müller. Experimental quantification of spatial correlations in quantum dynamics. *Quantum*, 2:90, 2018.

[47] B. W. Reichardt. Fault-tolerant quantum error correction for steane's seven-qubit color code with few or no extra qubits. *Quantum Sci. Technol.*, 6(1):015007, 2020.

[48] A. Reiserer, N. Kalb, M. S. Blok, and et al. Robust quantum-network memory using decoherence-protected subspaces of nuclear spins. *Phys. Rev. X*, 6:021040, 2016.

[49] C. Ryan-Anderson, J. G. Bohnet, K. Lee, D. Gresh, A. Hankin, J. P. Gaebler, D. Francois, A. Chernoguzov, D. Lucchetti, N. C. Brown, T. M. Gatterman, S. K. Halit, K. Gilmore, J. A. Gerber, B. Neyenhuis, D. Hayes, and R. P. Stutz. Realization of real-time fault-tolerant quantum error correction. *Phys. Rev. X*, 11:041058, 2021.

[50] C. Ryan-Anderson, N. C. Brown, M. S. Allman, B. Arkin, G. Asa-Attuah, C. Baldwin, J. Berg, J. G. Bohnet, S. Braxton, N. Burdick, J. P. Campora, A. Chernoguzov, J. Esposito, B. Evans, D. Francois, J. P. Gaebler, T. M. Gatterman, J. Gerber, K. Gilmore, D. Gresh, A. Hall, A. Hankin, J. Hostetter, D. Lucchetti, K. Mayer, J. Myers, B. Neyenhuis, J. Santiago, J. Sedlacek, T. Skripka, A. Slattery, R. P. Stutz, J. Tait, R. Tobey, G. Vittorini, J. Walker, and D. Hayes. Implementing fault-tolerant entangling gates on the five-qubit code and the color code. 2022.

[51] P. Schindler, J. T. Barreiro, T. Monz, V. Nebendahl, D. Nigg, M. Chwalla, M. Hennrich, and R. Blatt. Experimental repetitive quantum error correction. *Science*, 332(6033):1059–1061, 2011.

[52] A. Shabani. Correlated errors can lead to better performance of quantum codes. *Phys. Rev. A*, 77:022323, 2008.

[53] P. W. Shor. Scheme for reducing decoherence in quantum computer memory. *Phys. Rev. A*, 52:R2493–R2496, 1995.

[54] P. Szańkowski, M. Trippenbach, and L. Cywiński. Spectroscopy of cross correlations of environmental noises with two qubits. *Phys. Rev. A*, 94:012109, 2016.

[55] B. M. Terhal. Quantum error correction for quantum memories. *Rev. Mod. Phys.*, 87:307–346, 2015.

[56] M. Vasmer and D. E. Browne. Three-dimensional surface codes: Transversal gates and fault-tolerant architectures. *Phys. Rev. A*, 100:012312, 2019.

[57] E. Villaseñor. Distributed quantum memory using NV centers. Master's thesis, Delft University of Technology, 2018.

[58] C. Vuillot. *Fault-Tolerant Quantum Computation: Theory and Practice*. PhD thesis, Delft University of Technology, 2019.

[59] X. Xue, M. Russ, N. Samkharadze, B. Undseth, A. Sammak, G. Scappucci, and L. M. K. Vandersypen. Quantum logic with spin qubits crossing the surface code threshold. *Nature*, 601(7893):343–347, 2022.

[60] T. J. Yoder, R. Takagi, and I. L. Chuang. Universal fault-tolerant gates on concatenated stabilizer codes. *Phys. Rev. X*, 6:031039, 2016.

4

5

FAULT-TOLERANT OPERATION OF A LOGICAL QUBIT IN A DIAMOND QUANTUM PROCESSOR

Solid-state spin qubits are a promising platform for quantum computation and quantum networks. Recent experiments have demonstrated high-quality control over multi-qubit systems, elementary quantum algorithms and non-fault-tolerant error correction. Large-scale systems will require using error-corrected logical qubits that are operated fault tolerantly, so that reliable computation becomes possible despite noisy operations. Overcoming imperfections in this way remains a major outstanding challenge for quantum science. Here, we demonstrate fault-tolerant operations on a logical qubit using spin qubits in diamond. Our approach is based on the 5-qubit code with a recently discovered flag protocol that enables fault-tolerance using a total of seven qubits. We encode the logical qubit using a novel protocol based on repeated multi-qubit measurements and show that it outperforms non-fault-tolerant encoding schemes. We then fault-tolerantly manipulate the logical qubit through a complete set of single-qubit Clifford gates. Finally, we demonstrate flagged stabilizer measurements with real-time processing of the outcomes. Such measurements are a primitive for fault-tolerant quantum error correction. While future improvements in fidelity and the number of qubits will be required to suppress logical error rates below the physical error rates, our realization of fault-tolerant protocols on the logical-qubit level is a key step towards quantum information processing based on solid-state spins.

5.1. INTRODUCTION

Large-scale quantum computers and quantum networks will require quantum error correction to overcome inevitable imperfections [3, 17, 26, 29, 36]. The central idea is to encode each logical qubit of information into multiple physical data qubits. Non-destructive multi-qubit measurements, called stabilizer measurements, can then be used to identify and correct errors [3, 17, 29, 36]. If the error rates of all the components are below a certain threshold, it becomes possible to perform arbitrarily large quantum computations by encoding into increasingly more physical qubits [3, 29, 36]. A crucial requirement is that all logical building blocks, including the error-syndrome measurement, must be implemented fault tolerantly. At the lowest level, this implies that any single physical error should not cause a logical error.

Over the last years, steps towards fault-tolerant quantum error correction have been made using spin qubits in silicon [18, 23, 40] and in diamond [12, 38], as well as in various other hardware platforms such as superconducting qubits [7, 11, 24, 32, 33] and trapped-ion qubits [14, 15, 25, 27]. Pioneering experiments have demonstrated codes that can detect but not correct errors [22, 24, 33, 34], quantum error correction protocols that can correct only one type of error [12, 16, 38], as well as non-fault-tolerant quantum error correction protocols [7, 16, 20, 27]. A recent experiment with trapped-ion qubits has demonstrated the fault-tolerant operation of an error correction code, albeit through destructive stabilizer measurements and post-processing [14].

In this work, we realize fault-tolerant encoding, gate operations and non-destructive stabilizer measurements for a logical qubit of a quantum error correction code. Our logical qubit is based on the 5-qubit code, and we use a total of seven spin qubits in a diamond quantum processor (Fig. 5.1). Fault-tolerance is made possible through the recently discovered paradigm of flag qubits [8–10]. First, we demonstrate a novel fault-tolerant encoding protocol based on repeated multi-qubit measurements, which herald the successful preparation of the logical state. Then, we realize the (non-universal) set of transversal single-qubit Clifford gates. Finally, we demonstrate stabilizer measurements on the logical qubit and include a flag qubit to ensure compatibility with fault-tolerance. Our stabilizer measurements are non-destructive, the post measurement state is available in real time, and we use feedforward based on the measurement outcomes. While the logical qubit fidelities do not yet outperform the constituent physical qubits, these results demonstrate the key components of fault-tolerant quantum error correction in a solid-state spin-qubit processor.

5.2. THE LOGICAL QUBIT

Stabilizer error correction codes use auxiliary qubits to perform repeated stabilizer measurements that identify errors. A key requirement for fault-tolerance is to prevent errors on the auxiliary qubits from spreading to the data qubits and causing logical errors (Fig. 5.1b) [36]. The paradigm of flag fault-tolerance provides a solution with minimal qubit overhead [8–10]. Auxiliary qubit errors that would cause logical errors are detected using additional flag qubits, so that they can be subsequently corrected (Fig. 5.1b).

Our logical qubit is based on the 5-qubit code, the smallest distance-3 code which can correct any single-qubit error [20, 21]. Any logical state is a simultaneous +1 eigen-
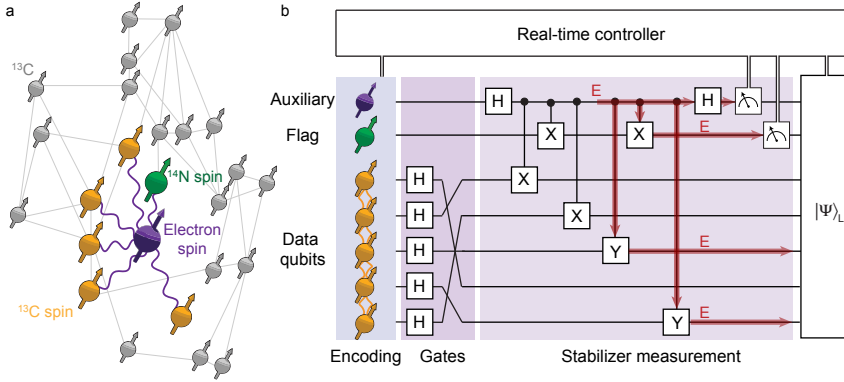
Figure 5.1: Diamond quantum processor, logical qubit and fault-tolerance. a) Our processor consists of a single NV centre and 27 ^{13}C nuclear-spin qubits, for which the lattice sites and qubit-qubit interactions are known [2]. We select 5 ^{13}C qubits as data qubits that encode the logical state (yellow). The other qubits (grey) are not used here. We use the NV electron spin (purple) as an auxiliary qubit for stabilizer measurements, and the NV ^{14}N nuclear spin (green) as a flag qubit to ensure fault-tolerance. Purple lines: electron-nuclear two-qubit gates used here (Methods). Grey lines: dipolar nuclear-nuclear couplings greater than 6 Hz. b) Illustration of the main components of the experiment. We realize fault-tolerant encoding, gates and stabilizer measurements with real-time processing on a logical qubit of the 5-qubit quantum error correction code. To ensure that any single fault does not cause a logical error, an additional flag qubit is used to identify errors that would propagate to multi-qubit errors and corrupt the logical state [9]. An illustration of such an error E is shown in red.

state of the four stabilizers $s_1 = XXYIY$, $s_2 = YXXYI$, $s_3 = IYXXY$, and $s_4 = YIYXX$, and the logical operators are $X_L = XXXXX$ and $Z_L = ZZZZZ$. Because any error on a single data qubit corresponds to a unique 4-bit syndrome, given as the eigenvalues of the stabilizers, arbitrary single-qubit errors can be identified and corrected. Combined with an auxiliary qubit for stabilizer measurements and a flag qubit to capture harmful auxiliary qubit errors, this makes fault-tolerant error correction possible using 7 qubits in total [9].

5.3. SYSTEM: SPIN QUBITS IN DIAMOND

Our processor consists of a single nitrogen-vacancy (NV) centre and its surrounding nuclear spin environment at 4 Kelvin (Fig. 5.1a). These spins are high-quality qubits with coherence times up to seconds for the NV electron spin [1] and minutes for the nuclear spins [6]. The NV electron spin can be read out optically, couples strongly to all other spins, and is used as an auxiliary qubit for stabilizer measurements (Methods) [6, 12]. We use the intrinsic ^{14}N nuclear spin as the flag qubit. Unlike the other qubits, the flag qubit does not need to maintain coherence during the optical readout. In this device, 27 ^{13}C nuclear-spin qubits and their lattice positions have been characterized, so that the 406 qubit-qubit interactions are known [2]. Each ^{13}C qubit can be controlled individually due to their distinct couplings to the NV electron spin (Methods). Here, we use five of the ^{13}C spin qubits as the data qubits to encode the logical qubit.

A challenge for controlling such a quantum processor is that the spins continuously
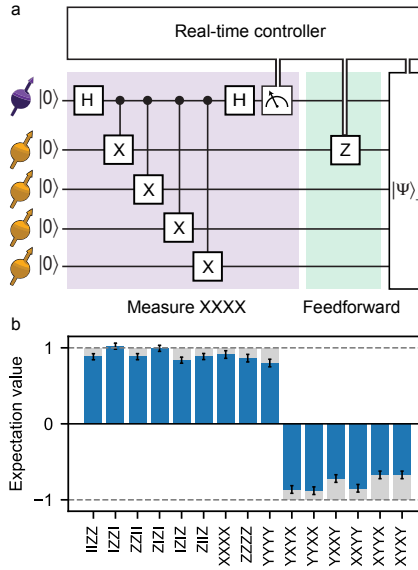
Figure 5.2: Non-destructive stabilizer measurements with real-time feedforward. a) Circuit diagram for the deterministic preparation of a 4-qubit GHZ entangled state ($|\Psi\rangle_+ = (|0000\rangle + |1111\rangle)/\sqrt{2}$) using a measurement of the stabilizer $XXXX$. b) Measured expectation values of the 15 operators that define the ideal state. The obtained fidelity with the target state is 0.86(1), confirming genuine multi-partite entanglement. Grey bars show the ideal expectation values. Error bars are one standard deviation in all figures.

couple to each other. We realize selective control gates through various echo sequences that isolate interactions between the targeted spins, while also protecting them from environmental decoherence. For all 2-qubit gates, we use previously developed electron-nuclear gates, which are based on decoupling sequences on the electron spin (Methods) [6]. Furthermore, we introduce interleaved and asynchronous echo stages that cancel unwanted couplings between the data qubits (Methods). These additional echo stages are essential for the relatively long gate sequences realized here.

5.4. NON-DESTRUCTIVE STABILIZER MEASUREMENTS

We start by demonstrating non-destructive 4-qubit stabilizer measurements with real-time feedforward operations based on the measurement outcomes (Fig. 5.2). Despite the central role of such measurements in many error-correction codes, including the 5-qubit code, the Steane code and the surface code [3, 17, 29, 36], experimental implementations with feedforward have remained an outstanding challenge.

We benchmark the measurement by using it to deterministically create a 4-qubit entangled state. We prepare the state $|0000\rangle$ and measure the operator $XXXX$. This projects the qubits into the GHZ state $|\Psi\rangle_\pm = (|0000\rangle \pm |1111\rangle)/\sqrt{2}$, with the sign determined by the measurement outcome. We process the measurement outcomes in real time using a microprocessor and apply the required correction to deterministically output the state $|\Psi\rangle_+$ with a fidelity of 0.86(1). Because this result is obtained without any post-
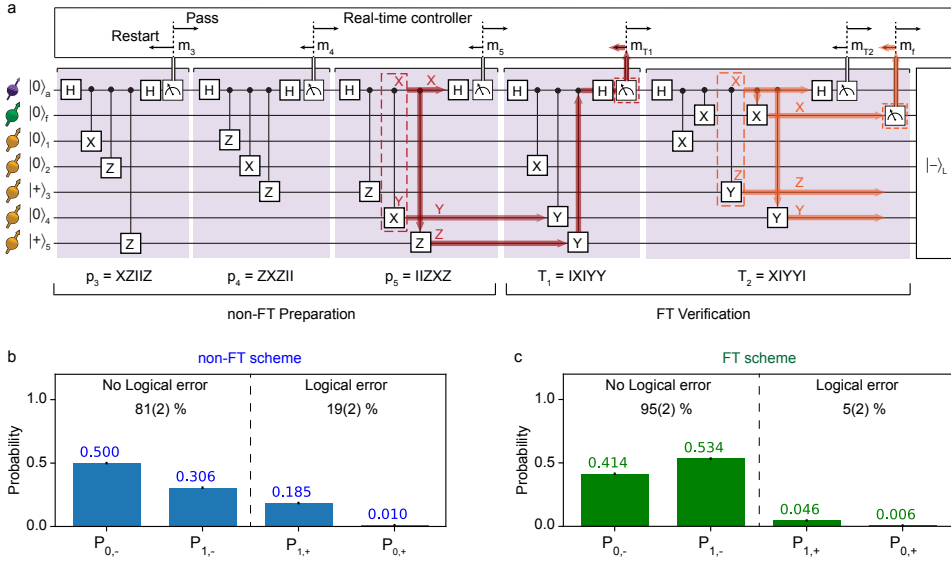
Figure 5.3: Fault-tolerant encoding of the logical qubit. a) Encoding circuit. The first stage prepares $|-\rangle_L$ non-fault-tolerantly ('non-FT preparation') by starting with $|00+0+\rangle$ (an eigenstate of p_1, p_2) and measuring the logical operators p_3, p_4, p_5. The second 'FT verification' stage consists of two stabilizer measurements $T_1 = p_2 p_4 p_5$, $T_2 = p_1 p_3 p_5$ and a flag qubit measurement. Echo sequences are inserted between the measurements to decouple the qubits. Successful preparation is heralded by satisfying a set of conditions for the measurement outcomes (see main text). Red: an example of an auxiliary qubit fault (an XY error in a two-qubit gate) that would propagate to a logical error but is detected by the T_1 verification step. Orange: an example of a single fault in the verification stage that would propagate into a logical error, but is detected by the flag qubit. b,c) Probabilities to obtain the desired logical state $|-\rangle_L$ without error ($P_{0,-}$) or with a single-qubit Pauli error ($P_{1,-}$), and the probabilities to obtain the opposite logical state $|+\rangle_L$ with zero ($P_{0,+}$) or with a single-qubit Pauli error ($P_{1,+}$). Note that $P_{1,\pm}$ are summed over all 15 possible errors. These 32 states are orthogonal and span the full 5-qubit Hilbert space.

selection, it highlights that the post-measurement state is available for all measurement outcomes, satisfying one of the key requirements for error correction.

5.5. FAULT-TOLERANT ENCODING

To prepare the logical qubit, we introduce a novel scheme that uses repeated stabilizer measurements and a flag qubit to herald successful preparation (Fig. 5.3a). In contrast to the scheme introduced by Chao and Reichardt [9], no direct two-qubit gates between the data qubits are required. We demonstrate the preparation of the logical state $|-\rangle_L = \frac{1}{\sqrt{2}}(|0\rangle_L - |1\rangle_L)$. This state is the unique +1 eigenstate of 5 independent weight-3 logical $-X$ operators, namely $p_1 = IZXZI$, $p_2 = ZIIZX$, $p_3 = XZIIZ$, $p_4 = ZXZII$ and $p_5 = IIZXZ$. Therefore, one can prepare $|-\rangle_L$ by initializing the data qubits into the product state $|00+0+\rangle$, which is an eigenstate of p_1 and p_2, and subsequently measuring p_3 to p_5 (Fig. 5.3a). This preparation scheme is not fault-tolerant because faults involving the auxiliary qubit can cause weight-2 errors, which can result in logical errors (Fig. 5.3a). We refer to these steps as the non-FT encoding scheme.

We make the preparation circuit fault-tolerant by adding two stabilizer measurements, $T_1 = p_2 \cdot p_4 \cdot p_5 = IXIYY$ and $T_2 = p_1 \cdot p_3 \cdot p_5 = XIYYI$ with a flag qubit (Fig. 5.3a). Successful preparation is heralded by the following conditions: (1) the measurement outcomes of T_1 and T_2 are compatible with the measurement outcomes m_i of the logical operators p_i, i.e. $m_{T_1} = m_2 \times m_4 \times m_5$ and $m_{T_2} = m_1 \times m_3 \times m_5$; (2) the flag is not raised (i.e., the flag qubit is measured to be in $|0\rangle$). Otherwise the state is rejected. The order of 2-qubit gates is carefully chosen to ensure fault-tolerance while minimizing the number of operations. Further details and a proof of the fault-tolerance of this scheme are given in the Appendix **??**. We refer to this preparation as the FT encoding scheme.

To reduce the impact of auxiliary qubit measurement errors [12, 37], we additionally require all stabilizer measurement outcomes to be +1 (i.e., the NV electron spin is measured to be in $|0\rangle$). These outcomes are more reliable (Methods) [6], increasing the fidelity of the state preparation, at the cost of a lower success probability.

We compare the non-FT and FT encoding schemes. We define the logical state fidelity F_L as (Methods)

$$F_{\mathrm{L}} = \sum_{E \in \mathscr{E}} \mathrm{Tr}\big(E |-\rangle_L \langle -|_L E \cdot \rho\big), \tag{5.1}$$

where ρ is the prepared state, and $\mathscr{E} = \{I, X_i, Y_i, Z_i, i = 1, 2, \cdots, 5\}$ is the set of all single-qubit Pauli errors. The fidelity F_L gives the probability that there is at most a single-qubit error in the prepared state, i.e. there is no logical error. We characterize the prepared state by measuring the 31 operators that define the target state (Methods). We find that the FT encoding scheme ($F_L = 95(2)\%$) outperforms the non-FT scheme ($F_L = 81(2)\%$).

To understand this improvement, we analyze the underlying error probability distributions (Figs. 5.3b,c). For the 5-qubit code, the $|-\rangle_L$ state plus any number of Pauli errors is equivalent to either $|-\rangle_L$ with at most one Pauli error (no logical error), or to $|+\rangle_L$ with at most one Pauli error (a logical error). We calculate the overlaps between the prepared state and those states. The results show that the FT scheme suppresses logical errors, consistent with fault-tolerance preventing single faults propagating to multi-qubit errors. The overall logical state fidelity F_L is improved, despite the higher probability of single-qubit errors due to the increased complexity of the sequence.

5.6. FAULT-TOLERANT LOGICAL GATES

The 5-qubit code supports a complete set of transversal single-qubit Clifford gates, which are naturally fault-tolerant [17, 41]. We apply four transversal logical gates to $|-\rangle_L$ (Fig. 5.4): $X_L = X_1 X_2 X_3 X_4 X_5$, $Y_L = Y_1 Y_2 Y_3 Y_4 Y_5$, the Hadamard gate $H_L = P_\pi H_1 H_2 H_3 H_4 H_5$, and the phase gate $S_L = P_\pi S_1 S_2 S_3 S_4 S_5$, where P_π is a permutation of the data qubits (Fig. 5.4b) [17, 41]. These permutations are fault-tolerant because we realize them by relabelling the qubits rather than by using SWAP gates [41]. For completeness, we note that universal computation requires additional non-transversal gates, constructed for example with auxiliary logical qubits, which are not pursued here [36].

Our control system performs the underlying single-qubit gates by tracking basis rotations and compiling them with subsequent gates or measurements (Methods). In the sequence considered here (Fig. 5.4a), such compilation does not increase the physical operation count, and there is no reduction of fidelity (Fig. 5.4c). For comparison, we also implement the 'worst-case' scenario where the logical gates are applied phys-
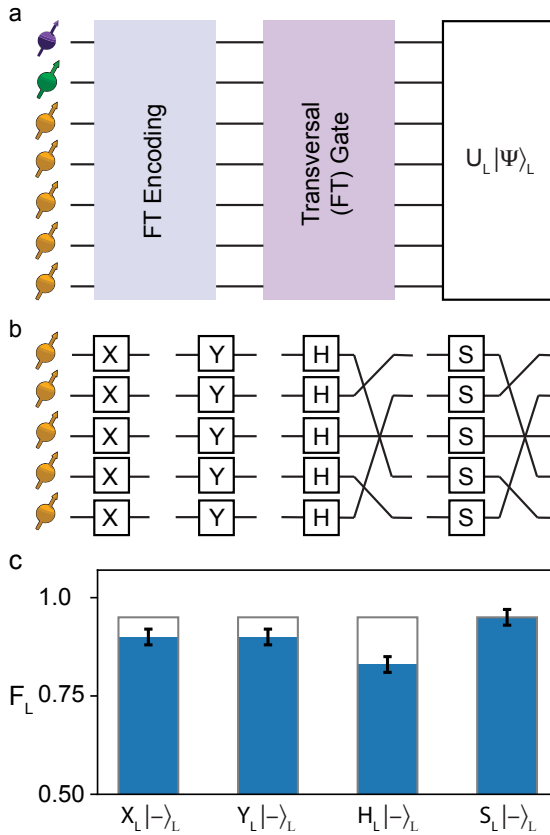
Figure 5.4: Fault-tolerant gates on the logically-encoded qubit. a) We apply transversal logical gates on the encoded state $|-\rangle_L$ and measure the resulting logical state fidelity F_L (Eq. (5.1)) with respect to the targeted state. b) Logical X_L, Y_L, H_L (Hadamard) and S_L ($\pi/2$ rotation around the z-axis) are realized by five single-qubit gates. For H_L and S_L this is followed by a permutation of the qubits by relabelling them. c) Grey bars: logical state fidelity when compiling the logical gates with subsequent operations (0.95(2) for all gates). Blue bars: logical state fidelities after physically applying the transversal logical gates (0.90(2),0.90(2),0.83(2),0.95(2) for X_L, Y_L, H_L, and S_L respectively).

ically (Fig. 5.4c). This includes 5 single-qubit gates and the corresponding additional echo sequences between the state preparation and the measurement stage. Together, the demonstrated transversal logical gates enable the fault-tolerant preparation of all six eigenstates of the logical Pauli operators.

5.7. FAULT-TOLERANT STABILIZER MEASUREMENTS

Finally, we demonstrate and characterize a flagged stabilizer measurement on the encoded state (Fig. 5.5a). Such measurements are a primitive for fault-tolerant quantum error correction protocols [9]. To ensure that the measurement is compatible with fault-tolerance, the two-qubit gates are carefully ordered and a flag qubit is added to capture the auxiliary qubit errors that can propagate to logical errors [9].

We prepare the logical state $|-\rangle_L$ and measure the stabilizer $s_1 = XXYIY$ (Fig. 5.5a). The resulting output consists of the post-measurement state and two classical bits of information from the measurements of the auxiliary and flag qubits (Fig. 5.5b). The logical state fidelity F_L is given by the probability that the logical information can be correctly extracted (no logical error), when taking into account the flag measurement outcome. The interpretation of the error syndrome changes if the flag is raised (Methods). We find $F_L = 0.77(4)$ for the post measurement state without any post-selection. Higher logical state fidelities can be obtained by post-selecting on favourable outcomes, but this is incompatible with error correction.

To illustrate the benefit of the flag qubit we compare the logical state fidelities with and without taking the flag measurement outcome into account. Because auxiliary qubit errors that propagate to logical errors are naturally rare, no significant difference is observed (Fig. 5.5c). Therefore, we introduce a Pauli Y error on the auxiliary qubit (Fig. 5.5a). This error propagates to the 2-qubit error $Y_3 Y_5$. For the case without flag information, this error causes a logical flip Z_L (Methods), and the logical state fidelity drops below 0.5. In contrast, with the flag qubit, this non-trivial error is detected (Fig. 5.5b) and remains correctable, so that the logical state fidelity is partly recovered (Fig. 5.5c).

5.8. CONCLUSION

In conclusion, we have demonstrated encoding, gates and non-destructive stabilizer measurements for a logical qubit of an error correction code in a fault-tolerant way. Our results advance solid-state spin qubits from the physical-qubit level to the logical-qubit level, where fault-tolerant operations become possible. Such fault-tolerance is a necessity for large-scale quantum computation in which error rates ultimately must be suppressed to extremely low levels.

Future challenges are to perform complete quantum error correction cycles, encode multiple logical qubits, realize universal fault-tolerant gates, and ultimately suppress logical error rates exponentially below physical error rates. While the demonstrated operations are of high fidelity—the experiments consist of up to 40 two-qubit gates and 8 mid-circuit auxiliary qubit readouts (Fig. 5.5a)—improvements in both the fidelities and the number of qubits will be required.

Improved gates might be realized through tailored optimal control schemes that leverage the precise knowledge of the system and its environment (Fig. 5.1a) [13]. Coupling
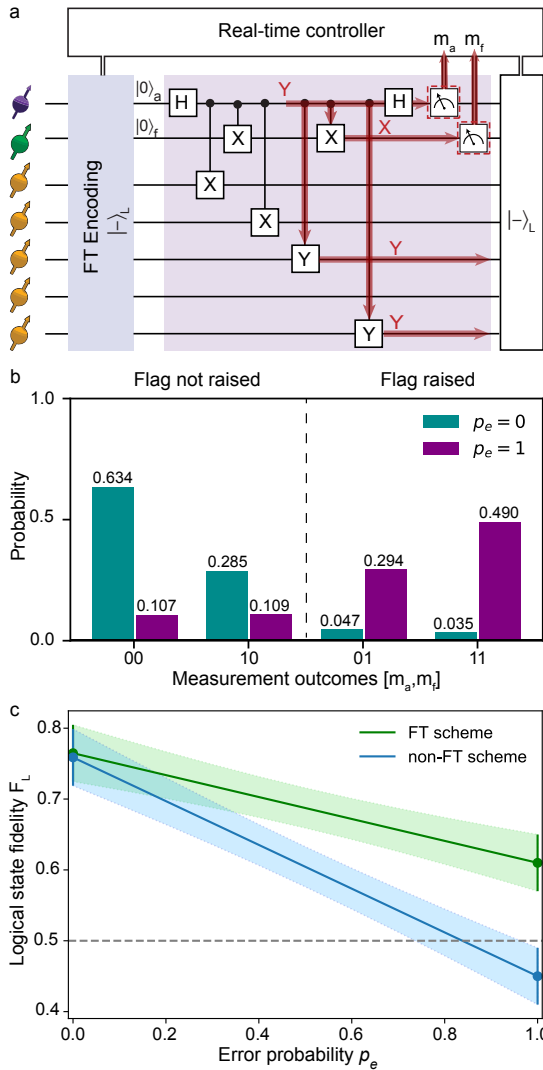
Figure 5.5: Fault-tolerant stabilizer measurement. a) Circuit diagram to measure the stabilizer $XXYIY$ on the encoded state. As an example to illustrate the compatibility with fault-tolerance we insert a Y error on the auxiliary qubit. This error will propagate to the 2-qubit error $Y_3 Y_5$ on the data qubits, which leads to a logical Z error. However, because the error also triggers the flag qubit it can be accounted for (Methods). b) Probability of the measurement outcomes of the auxiliary qubit (m_a) and flag (m_f) qubits when inserting ($p_e = 1$) or not inserting ($p_e = 0$) the Y error on the auxiliary qubit. The results show that the flag qubit successfully detects this error. c) Logical state fidelity F_L after the stabilizer measurement as function of the error probability p_e. The non-FT case does not take the flag outcome into account. Values between $p_e = 0$ and $p_e = 1$ are calculated as weighted sums (Methods).

to optical cavities can further improve readout fidelities [4, 5]. Scaling to large code distances and multiple logical qubits can be realized through already-demonstrated magnetic [13] and optical [28] NV-NV connections that enable modular, distributed, quantum computation based on the surface code and other error correction codes [26]. Therefore, our demonstration of the building blocks of fault-tolerant quantum error correction is a key step towards quantum information processing based on solid-state spin qubits.

5.9. METHODS

5.9.1. THE EXPERIMENTAL SETUP

SAMPLE

We use a naturally occurring NV centre in a homo-epitaxially chemical-vapor-deposition (CVD) grown diamond with a 1.1% natural abundance of ^{13}C and a $\langle 111 \rangle$ crystal orientation (grown by Element Six). A solid-immersion lens is used to enhance the photon-collection efficiency [31]. The NV center has been selected for the absence of ^{13}C spins with hyperfine couplings > 500 kHz. These experiments are performed at a temperature of 4 K where the electron-spin relaxation is negligible ($T_1 = 3.6(3) \times 10^3$ s [1]).

QUBITS AND COHERENCE TIMES.

The NV electron-spin auxiliary qubit is defined between the states $m_s = 0$ ($|0\rangle$) and $m_s = -1$ ($|1\rangle$). The NV electron-spin coherence times are $T_2^* = 4.9(2)\,\mu$s, $T_2 = 1.182(5)$ ms, and up to seconds under dynamical decoupling [1]. The ^{14}N nuclear-spin flag qubit is defined between the states $m_I = 0$ ($|0\rangle$) and $m_I = -1$ ($|1\rangle$). The ^{13}C nuclear-spin data qubits in this device have been characterized in detail in previous work (Fig. 5.1a) [2, 6, 19].

MAGNETIC FIELD.

A magnetic field of ~ 403 G is applied using a room-temperature permanent magnet on a XYZ translation stage. This applied field lifts the degeneracy of the $m_s = \pm 1$ states due to the Zeeman term. We stabilise the magnetic field to < 3 mG using temperature stabilisation and an automatic re-calibration procedure (every few hours). We align the magnetic field along the NV axis using thermal echo sequences with an uncertainty of 0.07 degrees in the alignment [2].

SINGLE- AND TWO-QUBIT GATES.

Single-qubit gates and echo pulses are applied using microwave pulses for the NV electron spin ($m_s = 0 \leftrightarrow m_s = -1$ transition, Hermite pulse shapes [1, 39], Rabi frequency of ~ 15 MHz) and using radio-frequency pulses for the ^{13}C spin qubits (error function pulse shapes [6], typical Rabi frequency of ~ 500 Hz) and the ^{14}N spin qubit (error function pulse shapes, Rabi frequency ~ 2 kHz).

The Hermite pulse envelopes of the microwave pulses are defined as

$$A[1 - c\left(\frac{t-\mu}{T}\right)^2] \cdot \exp[-\left(\frac{t-\mu}{T}\right)^2], \tag{5.2}$$

where $c = 0.956$ for π pulses and $c = 0.667$ for $\pi/2$ pulses, $\mu = 0.5 t_{\text{pulse}}$, $T = 0.1667 t_{\text{pulse}}$, t_{pulse} is the MW pulse length, A is the pulse amplitude which is experimentally calibrated

to achieve a π or $\pi/2$ rotation. For this work we use $t_{\text{pulse}} = 168$ ns for π pulses and $t_{\text{pulse}} = 100$ ns for $\pi/2$ pulses. The envelope of the RF pulses is defined as

$$f(t) = 1 - \frac{1}{2}\,\text{erf}\left(\frac{2(\Delta t - t + t_0)}{\Delta t}\right) - \frac{1}{2}\,\text{erf}\left(\frac{2(\Delta t + t - t_{\text{pulse}})}{\Delta t}\right), \tag{5.3}$$

where Δt is the risetime, t_0 is the start time of the pulse, t_{pulse} is the pulse length and $\text{erf}(x)$ is the error function [6]. We ensure that the RF pulses are comprised of an integer number of periods of the RF waveform, i.e. we ensure that $\omega\, t_{\text{pulse}} = 2\pi n$ for integer n, where t_{pulse} is the RF pulse length. This ensures that any phase picked up on the electron spin due to the RF pulse is cancelled. Note that the ^{13}C spin qubits (data qubits) are distinguishable in frequency due to their hyperfine coupling to the NV electron spin.

Electron-nuclear two-qubit gates are realised using two different gate designs, depending on the properties of the targeted nuclear spin. For data qubits 1,2,4,5, two-qubit gates are realized through dynamical decoupling sequences of N equally spaced π-pulses on the electron spin of the form $(\tau_r - \pi - \tau_r)^N$ [6, 35]. This design requires a significant hyperfine component perpendicular to the applied magnetic field [35]. For data qubit 3 and the flag qubit (the ^{14}N spin) the perpendicular hyperfine coupling is small and we perform two-qubit gates by interleaving the dynamical decoupling sequence with RF pulses [6]. Both gate designs simultaneously decouple the NV electron spin from the other qubits and the environment [6]. Note that direct nuclear-nuclear two-qubit gates can also be constructed [30], but because the natural interaction is much weaker than the electron-nuclear interaction, we don't use such gates here, and designed the FT encoding circuit based on electron-nuclear gates only.

Compilation of gate sequences.
Our native two-qubit gates are electron-controlled nuclear-spin rotations and are equivalent to the CNOT gate up to single-qubit rotations. To implement the sequences shown in the figures, we first translate all gates into these native gates and compile the resulting sequence. Afterwards, the circuit is translated into the actual pulse sequence. At the core of this compilation process is the tracking and synchronization of the qubit phases and the corresponding pulse timings.

Echo sequences for the data qubits.
To mitigate decoherence of the data qubits due to their spin environment, we use echo sequences that are interleaved throughout the experiments. These echo sequences ensure that the data qubits rephase each time they are operated on. Additionally, the sequence design minimizes the time that the auxiliary electron spin qubit is idling in superposition states, which are prone to dephasing. We use two echo stages between stabilizer measurements, as well as before and after the logical gates of Fig. 5.4, which provides a general and scalable solution for the timing of all gates and echoes.

An additional challenge is that, due to the length of the sequences (up to 100 ms), we need to account for the small unwanted interactions between the nuclear-spin data qubits. The measured coupling strengths show that the strongest couplings are between qubits 3 and 2 (16.90(4) Hz, and between qubits 3 and 5 (12.96(4) Hz) [2]). Such interactions can introduce correlated two-qubit errors that are not correctable in the distance-3 code considered here, which can only handle single-qubit errors in the code block.

To mitigate these qubit-qubit couplings, we decouple qubit 3 asynchronously from the other qubits. Ultimately, such local correlated errors can be suppressed entirely by larger distance codes.

REAL-TIME CONTROL AND FEEDFORWARD OPERATIONS.
Real-time control and feedforward operations are implemented through a programmable microprocessor (Jaeger ADwin Pro II) operating on microsecond timescales. The microprocessor detects photon events coming from the detectors, infers the measurement outcomes, and controls both the subsequent sequences in the arbitrary waveform generator (Tektronix AWG 5014c) and the lasers for the auxiliary qubit readout. The precise timing for quantum gates (1 nanosecond precision) is based on the clock of the arbitrary waveform generator. Additionally, the microprocessor operates various control loops that prepare the NV center in the negative charge state, on resonance with the lasers, and in the focus of the laser beam.

READOUT OF THE AUXILIARY QUBIT.
The electron spin (auxiliary qubit) is read out by resonantly exciting the $m_s = 0$ to E_x optical transition [31]. For one or more photons detected we assign the $m_s = 0$ outcome, for zero photons we assign $m_s = \pm 1$. The single-shot readout fidelities are $F_0 = 90.5(2)\%$ and $F_1 = 98.6(2)\%$ for $m_s = 0$ and $m_s = -1$, respectively (average fidelity: 94.6(1)%).

Uncontrolled electron-spin flips in the excited state cause dephasing of the nuclear spins through the hyperfine interaction. To minimize such spin flips we avoid unnecessary excitations by using weak laser pulses, so that a feedback signal can be used to rapidly turn off the laser upon detection of a photon (within 2 μs). The resulting probability that the electron spin is in state $m_s = 0$ after correctly assigning $m_s = 0$ in the measurement is 0.992 [12].

For measurements that are used for heralded state preparation, i.e. where we only continue upon a $m_s = 0$ outcome (see e.g. Fig. 5.3), we use shorter readout pulses. This improves the probability that a $m_s = 0$ outcome correctly heralds the $m_s = 0$ state, at the cost of reduced success probability.

SYSTEM PREPARATION AND QUBIT INITIALIZATION.
At the start of the experiments we first prepare the NV center in its negative charge state and on resonance with the lasers. We then initialize the NV electron spin in the $m_s = 0$ state through a spin pumping process (Fidelity > 99.7%) [31]. We define the electron-spin qubit between the states $m_s = 0(|0\rangle)$ and $m_s = -1(|1\rangle)$. We initialize the data qubits through SWAP sequences into $|0\rangle$, and subsequent optical reset of the auxiliary qubit (initialization fidelities 96.5% − 98.5%). The flag qubit is initialized through a projective measurement that heralds preparation in $|0\rangle$ (initialization fidelity 99.7%). Other product states are prepared by subsequent single qubit gates.

FINAL READOUT OF THE DATA QUBITS.
Measuring single- and multi-qubit operators of the data qubits is performed by mapping the required correlation to the auxiliary qubit (through controlled rotations) and then reading out the auxiliary qubit [12]. In order to provide best estimates for the measurements, we correct the measured expectation values for infidelities in the readout sequence, see Bradley et al. [6] for the correction procedure.

5.9.2. LOGICAL STATE FIDELITY

ASSESSING THE LOGICAL STATE FIDELITY.

The logical state fidelity F_L is defined in Eq. (1) and gives the probability that the state is free of logical errors. Said differently, F_L is the fidelity with respect to the ideal 5-qubit state after a round of perfect error correction, or the probability to obtain the correct outcome in a perfect fault-tolerant logical measurement. While fault-tolerant circuits for logical measurement exist [9], we do not experimentally implement these here. Instead, we extract F_L from a set of measurements, as described in the following using $|-\rangle_L$ as an example.

The logical state $|-\rangle_L$ is the unique simultaneous eigenstate of the 5 weight-3 operators p_i with eigenvalue +1. We can thus describe the state $E|-\rangle_L$ (with E a Pauli error) as the projector

$$E|-\rangle_L \langle -|_L E = \prod_{i=1}^{5} \left(\frac{1 + m_i p_i}{2} \right),$$

where $m_i = \pm 1$ is the measurement outcome of p_i, and $m_i = -1$ when E anti-commutes with p_i. This projector can be expanded as a summation of 31 multi-qubit Pauli operators (including a constant). The logical state fidelity F_L in Eq. (5.1) can then be written as

$$
\begin{aligned}
F_L &= \sum_{E \in \mathscr{E}} \text{Tr}\big(E|-\rangle_L \langle -|_L E \rho\big) \\
&= \frac{1}{2} + \frac{1}{8}(\langle IZXZI \rangle + \langle ZIIZX \rangle + \langle XZIIZ \rangle \\
&\quad + \langle ZXZII \rangle + \langle IIZXZ \rangle + \langle YIXIY \rangle \\
&\quad + \langle IYYIX \rangle + \langle XIYYI \rangle + \langle IXIYY \rangle \\
&\quad + \langle YYIXI \rangle + \langle ZZYXY \rangle + \langle YXYZZ \rangle \\
&\quad + \langle ZYXYZ \rangle + \langle XYZZY \rangle + \langle YZZYX \rangle \\
&\quad + \langle XXXXX \rangle).
\end{aligned}
\tag{5.4}
$$

Here $\mathscr{E} = \{I, X_i, Y_i, Z_i, i = 1, 2, \cdots 5\}$ is the set of correctable errors for the 5-qubit code. To obtain F_L experimentally, we measure this set of expectation values.

LOGICAL STATE FIDELITY WITH FLAG.

If the flag in the circuit in Fig. 5.5a is not raised, then a cycle of error correction would correct any single-qubit error on a logical state. The logical state fidelity is then given by Eq. (5.1), which we now refer to as $F_L^{\text{not raised}}$. A raised flag leads to a different interpretation of the error syndrome (see Tab. **??**) [9].

For example, the Y error on auxiliary qubit in Fig. 5.5a leads to the output state $Y_3 Y_5 |-\rangle_L$, for which the eigenvalues of $s_1 = XXYIY, s_2 = YXXYI, s_3 = IYXXY, s_4 = YIYXX$ give the syndrome $[+1, -1, -1, -1]$. Without flag, the corresponding single-qubit recovery is Z_4, which changes the syndrome back to all +1 (see Tab. **??**). This recovery leads to the remaining error $Y_3 Z_4 Y_5$, which is a logical Z error. However, taking the flag measurement outcome into account, the syndrome is interpreted differently and the recovery is $Y_3 Y_5$ so that no error is left, as shown in Tab. **??**.

For the cases where the flag is raised, the logical state fidelity with respect to $|-\rangle_L$ is now given by:

$$
\begin{aligned}
F_{\mathrm{L}}^{\mathrm{raised}} &= \sum_{E \in \mathscr{E}'} \mathrm{Tr}\big(E |-\rangle_L \langle-|_L E \cdot \rho\big) \\
&= \frac{1}{2} + \frac{1}{32}\big(6\langle IIZXZ\rangle + 6\langle ZXZII\rangle + 6\langle YYIXI\rangle - 2\langle ZIIZX\rangle + 6\langle IXIYY\rangle \\
&\qquad + 2\langle YZZYX\rangle + 2\langle XYZZY\rangle - 2\langle IZXZI\rangle + 2\langle ZYXYZ\rangle + 6\langle XIYYI\rangle \\
&\qquad + 2\langle YXYZZ\rangle + 2\langle ZZYXY\rangle + 6\langle IYYIX\rangle - 2\langle YIXIY\rangle + 2\langle XXXXX\rangle \\
&\qquad - 2\langle XZIIZ\rangle\big)
\end{aligned}
\tag{5.5}
$$

with $\mathscr{E}'$ another set of correctable errors

$$
\mathscr{E}' = \{I, X_1, X_3 Y_5, Z_1, X_2, Y_2, Z_3 Y_5, X_1 Y_2, Y_3, Z_3, X_4, Y_4, Y_3 Y_5, X_5, Y_5, X_1 Z_2\}. \tag{5.6}
$$

A detailed derivation for this set of errors and their corresponding syndromes are given in Appendix 5.10.1.

The logical state fidelity after the stabilizer measurement (Fig. 5.3) is calculated as the weighted sum of the fidelities conditioned on the two flag outcomes:

$$
F_L = p_{\mathrm{f}} F_L^{\mathrm{raised}} + (1 - p_{\mathrm{f}}) F_L^{\mathrm{not\ raised}}, \tag{5.7}
$$

with p_{f} the probability that the flag is raised and F_L^{raised} and $F_L^{\mathrm{not\ raised}}$ are defined above.

Finally, to construct the logical state fidelity as a function of p_e (Fig. 5.3c), we measure F_L with ($p_e = 0$) and without ($p_e = 1$) the auxiliary qubit error and calculate the outcomes for other error probabilities p_e from their weighted sum:

$$
F_L(p_e) = (1 - p_e) F_L(p_e = 0) + p_e F_L(p_e = 1) \tag{5.8}
$$

Error distribution in the prepared state.

The overlaps between the prepared state ρ and the state $E |-\rangle_L$ with E identity or a single-qubit error are written as $P_{0,-}$ and $P_{1,-}$, respectively. These correspond to the cases that there is no logical error. The overlaps between the prepared state ρ and the state $E |+\rangle_L$ with E identity or a single-qubit error are written as $P_{0,+}$ and $P_{1,+}$, respectively. In these cases there is a logical error. These overlaps are shown in Fig. 5.3b,c and calculated as ($\alpha = \pm$)

$$
P_{0,\alpha} = \mathrm{Tr}\big(|\alpha\rangle_L \langle\alpha|_L \cdot \rho\big), \tag{5.9}
$$

$$
P_{1,\alpha} = \sum_{E \in \mathscr{E}} \mathrm{Tr}\big(E |\alpha\rangle_L \langle\alpha|_L E \cdot \rho\big). \tag{5.10}
$$

These overlaps can be explicitly expressed in terms of the measured 31 expectation values (see Appendix 5.10.2).

Error analysis

The uncertainties in the measured fidelities, logical state fidelities, and probabilities ($P_{0/1,\pm}$) are obtained from the uncertainties in the measured expectation values using error propagation. For example the logical state fidelity F_L is calculated as

$$F_L = \frac{1}{2} + \frac{1}{8}(\sum_i A_i), \qquad (5.11)$$

where A_i are the 16 expectation values shown in Eq. (5.4). Assuming that the errors in the measured expectation values are independent, the standard deviation in F_L is:

$$\sigma_{F_L} = \frac{1}{8}(\sum_i \sigma_{A_i}^2)^{\frac{1}{2}}, \qquad (5.12)$$

where σ_{A_i} is the standard deviation of the expectation value A_i, and is given by a binomial distribution [28]. Note that σ_{A_i} is also corrected for the readout correction process described in Bradley et al. [6].

5

5.10. APPENDIX

5.10.1. PROOF OF FAULT-TOLERANCE OF THE PREPARATION SCHEME

In this section, we provide the theoretical proof that a single fault in the encoding circuit (Fig. 5.3a) leads to the correct preparation of $|-\rangle_L$ plus at most a single-qubit error, assuming that the conditions for accepting the state are fulfilled. The conditions are (1) the measurement outcomes of T_1 and T_2 are compatible with the measurement outcomes m_i of the logical operators p_i, i.e. $m_{T_1} = m_2 \times m_4 \times m_5$ and $m_{T_2} = m_1 \times m_3 \times m_5$; (2) the flag is not raised. Otherwise the state is rejected.

The modification of the preparation scheme with additional single-qubit gates does not change the fault-tolerance argument. Therefore, the same derivation applies to preparing other basis states by adding and then compiling transversal logical gates, as well as when we execute echo pulses or use different gate decompositions. In the experimental realization we additionally condition on the preparation runs which give $m_3 = +1, m_4 = +1, m_5 = +1$ since these measurement outcomes ($m_s = 0$ NV electron spin state) are more reliable. Such heralding does not affect the fault-tolerance arguments and we provide the more general proof here. In this section, we denote controlled-NOT and controlled-Y gates as CX and CY.

First, we note that for this 5-qubit code, any state $|-\rangle_L$ with more than 1 Pauli error is equivalent to either a $|+\rangle_L$ with at most 1 Pauli error or a $|-\rangle_L$ state with at most 1 Pauli error. This is due to the code being 'perfect': the states $|\pm\rangle_L$ plus any single-qubit error are all orthogonal and there are $2 \times (1 + 15) = 2^5 = 32$ such states, spanning the full 5-qubit Hilbert space.

Hence we just need to prove that the preparation circuit does not lead to the state $|+\rangle_L$ with at most 1 Pauli error. For this it is useful to tabulate some incarnations of the logical Z and logical Y as these can bring $|-\rangle_L$ to $|+\rangle_L$ up to a global phase, see Tab. 5.1.

$$
\begin{array}{c|c|c|c}
Z_L \equiv & Z_1 Z_2 Z_3 Z_4 Z_5 & -Y_3 Z_4 Y_5 \text{ (cyclic perm.)} & -X_2 X_3 Z_5 \text{ (cyclic perm.)} \\
Y_L \equiv & Y_1 Y_2 Y_3 Y_4 Y_5 & -Z_2 Z_3 Y_5 \text{ (cyclic perm.)} & -X_1 X_4 Y_5 \text{ (cyclic perm.)} \\
X_L \equiv & X_1 X_2 X_3 X_4 X_5 & -X_2 Y_4 Y_5 \text{ (cyclic perm.)} & -Z_1 Z_4 X_5 \text{ (cyclic perm.)}
\end{array}
$$

Table 5.1: Incarnations of the logical operators which can be obtained by multiplying the logical operators by stabilizers (weight-3 incarnations have minus signs). Any cyclic permutation (e.g., $-X_2 X_3 Z_5 \rightarrow -Z_1 X_3 X_4 \rightarrow -Z_2 X_4 X_5$) of a logical operator is an equivalent logical operator.

Throughout this proof, we assume Pauli frame corrections by keeping track of detected errors in classical logic. The classical information changes our interpretation of the final measurement outcome, which can be basically interpreted as applying noiseless recovery according to the measurement outcomes (see Tab. 5.2).

Looking at the circuit in Fig. 5.3a in the main text, we can assume that the fault appears either in the non-FT preparation circuit and the verification circuit is fault-free, or vice versa. So we consider these cases separately as follows.

The complete supplementary information is available online.

m_3	m_4	m_5	correction
+1	+1	+1	I
+1	+1	-1	Z_4
+1	-1	+1	Z_2
+1	-1	-1	X_3
-1	+1	+1	Z_1
-1	+1	-1	X_5
-1	-1	+1	$Z_1 Z_2$
-1	-1	-1	$Z_1 X_3$

Table 5.2: Pauli corrections to bring the prepared state to $|-\rangle_L$ (Fig. 3a in the main text). The correction anti-commutes (resp. commutes) with all p_i with $m_i = -1$ (resp. $m_i = +1$) and commutes with p_1 and p_2. The corrections in the look-up table are not unique as one can apply a stabilizer or any incarnation of a logical X to them which leaves the state $|-\rangle_L$ unchanged (modulo overall phase).

Case A: if the only fault occurs in the verification circuit

Since the only fault occurs in the verification circuit, the preparation circuit prepares the state $|-\rangle_L$ with no errors. We prove that the circuit is fault-tolerant by considering different cases:

- Single-qubit faults on data qubits (in idling or after gates) during the verification. These have the effect of either leading to a single-qubit error on the output state, or leading to a flipped measurement of T_1 or/and T_2 which does not satisfy the consistency check (in which case the output state is not accepted).

- A single measurement fault in the measurement of T_1, T_2 or the flag qubit measurement leads to the state not being accepted.

- A two-qubit fault after one of the two-qubit gates in T_1. If the action of this fault on the auxiliary qubit is Z or Y, then it flips the auxiliary qubit and the state is not accepted. Hence we assume the action on the auxiliary qubit is X. If the error $XP \equiv X \otimes P$, where P is some Pauli I, X, Y, Z acting on a data qubit, occurs after the first CX, it leads to outgoing error $P_2 Y_4 Y_5$ which is equivalent to $(X_2 P_2) X_L$, hence a single-qubit outgoing error. If XP occurs after CY in the middle, it leads to outgoing error $P_4 Y_5$: (1) $Y_4 Y_5$ is equivalent to $X_2 X_L$, (2) $X_4 Y_5$ and $Z_4 Y_5$ lead to the T_2 outcome being flipped and no acceptance, (3) $P = I$ corresponds to the single-qubit error Y_5. If XP occurs after the (last) CY, it leads to a single-qubit outgoing error P_5.

- A two-qubit fault after one of the two-qubit gates in T_2. If the action of this fault on the auxiliary qubit is Z or Y, then it flips the auxiliary qubit and the state is not accepted. Hence we assume that the action on the auxiliary qubit is X.

  Consider first the two-qubit gates between auxiliary and data qubits. If the fault XP occurs after the CX, then it does not flip the flag qubit, and leads to outgoing error $P_1 Y_3 Y_4$ which is equivalent to $(X_1 P_1) X_L$, hence inducing a single-qubit error. If the fault XP occurs after CY in the middle, it flips the flag qubit and the state is

not accepted. If the fault XP occurs after the second CY, it leads to a single qubit error P_4.

Now consider CX gates between auxiliary and flag qubits. Note that an error on the flag qubit cannot propagate to the data qubits, we thus only consider a Pauli X error on the auxiliary qubit. An X error on auxiliary qubit after the first CX leads to $Y_3 Y_4$, which is equivalent to $X_1 X_L$. An X error on the auxiliary qubit after the second CX leads to the single-qubit error Y_4.

	p_1	p_2	p_3	p_4	p_5	$T_1 = p_2 p_4 p_5$	$T_2 = p_1 p_3 p_5$
Y_1		F	F	F			F
X_1		F		F			
Z_1			F				F
Y_2	F		F	F		F	
X_2	F		F				
Z_2				F		F	
Y_3	F			F	F		
X_3				F	F		F
Z_3	F						F
Y_4	F	F			F		
X_4	F	F				F	F
Z_4				F		F	F
Y_5		F	F		F		
X_5			F		F	F	
Z_5		F				F	

Table 5.3: Effect of single qubit errors. F denotes that the eigenvalue is flipped upon application of the error, i.e., the error anti-commutes with the operator. For the logical state $|+\rangle_L$, both measurements of the verification checks T_1 and T_2 should give -1, which fails the verification. However, $|+\rangle_L$ with the errors highlighted in red (X_4 and Z_4) would pass the verification test as both verification checks are flipped.

Case B: if the only fault occurs in the preparation circuit

When the non-FT circuit gives the output $|-\rangle_L$ plus at most a single-qubit error, no matter whether this state passes the verification or not, the final output state can have at most a single-qubit error as the verification circuit is perfect. For output states $|+\rangle_L$ with at most a single-qubit error, we need to argue: (1) either they are caught by the verification circuit (2) or they cannot occur due to a single fault in the non-FT preparation circuit.

Note that the output $|+\rangle_L$ is a -1 eigenstate of p_1, p_2, p_3, p_4 and p_5. If the output state of the non-FT circuit is $|+\rangle_L$ with no error, both T_1 and T_2 should give measurement outcome -1 as they are products of three p_is. Such a state would be rejected by the verification circuit. Now we examine what possible single-qubit errors on $|+\rangle_L$ would lead to passing the verification test. We can see that these are the errors X_4 and Z_4 on top of $|+\rangle_L$, i.e., both anti-commute with the verification checks (see Tab. 5.3).

One can fully characterize these possible bad states $X_4 |+\rangle_L$ and $Z_4 |+\rangle_L$ by their syndromes $M_i = \pm 1$ (eigenvalues of $p_1, \ldots, p_5$ if we were to measure these logical operators

noiselessly). Syndromes of the possible bad states (denoted by capital letters) are given as follows

$$X_4 |+\rangle_L : M_3 = M_4 = M_5 = -1, \qquad\qquad M_1 = M_2 = +1, \qquad (5.13)$$

$$Z_4 |+\rangle_L : M_1 = M_2 = M_3 = M_4 = -1, \qquad\qquad M_5 = +1 \qquad (5.14)$$

Now we argue that no single fault in the preparation circuit can lead to $X_4 |+\rangle_L$ or $Z_4 |+\rangle_L$. We look at various subcases:

1) If the only fault occurs before measuring p_4 and p_5. Then the Pauli corrections correctly fix the eigenvalues of p_4 and p_5 on the output so that $M_4 = M_5 = +1$. Both syndromes in Eq. (5.13) and Eq. (5.14) are therefore excluded.

2) If the only fault occurs in measuring p_4. Similarly, M_5 is fixed to be +1 due to correct Pauli corrections, so that the syndrome in Eq. (5.13) is not possible. Then for the syndrome in Eq. (5.14) we argue as follows:

- In the circuit of measuring p_4, only faults after CX in the middle can lead to non-trivial 2-qubit errors $Z_2 Z_3$ and $Y_2 Z_3$. These errors commute with $p_2 = ZIIZX$, hence M_2 is fixed to be +1. The syndrome in Eq. (5.14) is therefore not possible.

- Up to a stabilizer or a logical X operator, other single faults can only induce single-qubit errors on the data qubits. Because any single-qubit error cannot anti-commute with $p_1 = IZXZI$, $p_2 = ZIIZX$ and $p_3 = XZIIZ$ at the same time, M_1, M_2 and M_3 cannot be -1 at the same time. The syndrome in Eq. (5.14) is therefore not possible.

3) If the only fault occurs in measuring p_5.

- In the circuit of measuring p_5, only faults after CX in the middle can lead to non-trivial 2-qubit errors $Z_4 Z_5$ and $Y_4 Z_5$. These errors both commute with $p_3 = XZIIZ$ and $p_4 = ZXZII$, i.e., both M_3 and M_4 are fixed to be +1. The syndromes in Eq. (5.13) and Eq. (5.14) are thus not possible.

- If the only fault occurs on an idling location of the data qubits C1 or C2, the measurement of p_5 is then correct. Because the induced single-qubit errors commute with $p_5 = IIZXZ$, which means the Pauli correction fixes M_5 to be +1. The syndrome in Eq. (5.13) are therefore not possible. In addition, any single-qubit error on C1 or C2 cannot anti-commute with $p_1 = IZXZI$, $p_2 = ZIIZX$, $p_3 = XZIIZ$ and $p_4 = ZXZII$ at the same time, the syndrome in Eq. (5.14) is also excluded.

- Up to a stabilizer or a logical X operator, other single faults can only induce a single-qubit error on the data qubits C3, C4 or C5. Such single-qubit errors cannot anti-commute with $p_3 = XZIIZ$ and $p_4 = ZXZII$ at the same time, the syndromes in Eq. (5.13) and Eq. (5.14) are therefore not possible.

5.10.2. ERROR DISTRIBUTION IN THE PREPARED STATE

The overlaps between the prepared state ρ and the states $E|-\rangle_L$, $E|+\rangle_L$, with E identity or a single-qubit error ($P_{0,-}$, $P_{1,-}$, $P_{0,+}$, $P_{1,+}$) can be expressed in terms of the measured 31 expectation values as

$$
\begin{aligned}
P_{0,-} =\ & \mathrm{Tr}\big(|-\rangle_L\langle-|_L\,\rho\big) \\
=\ & \frac{1}{32}(1 + \langle IZXZI\rangle + \langle ZIIZX\rangle + \langle XZIIZ\rangle + \langle ZXZII\rangle + \langle IIZXZ\rangle + \langle YIXIY\rangle \\
& + \langle IYYIX\rangle + \langle XIYYI\rangle + \langle IXIYY\rangle + \langle YYIXI\rangle - \langle ZZYXY\rangle - \langle YXYZZ\rangle \\
& - \langle ZYXYZ\rangle - \langle XYZZY\rangle - \langle YZZYX\rangle - \langle XXXXX\rangle + \langle IXZZX\rangle + \langle IYXXY\rangle \\
& + \langle IZYYZ\rangle + \langle XIXZZ\rangle + \langle XXYIY\rangle + \langle XYIYX\rangle + \langle XZZXI\rangle + \langle YIYXX\rangle \\
& + \langle YXXYI\rangle + \langle YYZIZ\rangle + \langle YZIZY\rangle + \langle ZIZYY\rangle + \langle ZXIXZ\rangle + \langle ZYYZI\rangle \\
& + \langle ZZXIX\rangle),
\end{aligned}
\tag{5.15}
$$

$$
\begin{aligned}
P_{1,-} =\ & \sum_{E\in\mathcal{E}} \mathrm{Tr}\big(E|-\rangle_L\langle-|_L\,E\rho\big) \\
=\ & \frac{1}{32}(15 + 3\langle IZXZI\rangle + 3\langle ZIIZX\rangle + 3\langle XZIIZ\rangle + 3\langle ZXZII\rangle + 3\langle IIZXZ\rangle + 3\langle YIXIY\rangle \\
& + 3\langle IYYIX\rangle + 3\langle XIYYI\rangle + 3\langle IXIYY\rangle + 3\langle YYIXI\rangle + 5\langle ZZYXY\rangle + 5\langle YXYZZ\rangle \\
& + 5\langle ZYXYZ\rangle + 5\langle XYZZY\rangle + 5\langle YZZYX\rangle + 5\langle XXXXX\rangle - \langle IXZZX\rangle - \langle IYXXY\rangle \\
& - \langle IZYYZ\rangle - \langle XIXZZ\rangle - \langle XXYIY\rangle - \langle XYIYX\rangle - \langle XZZXI\rangle - \langle YIYXX\rangle \\
& - \langle YXXYI\rangle - \langle YYZIZ\rangle - \langle YZIZY\rangle - \langle ZIZYY\rangle - \langle ZXIXZ\rangle - \langle ZYYZI\rangle \\
& - \langle ZZXIX\rangle),
\end{aligned}
\tag{5.16}
$$

$$
\begin{aligned}
P_{0,+} =\ & \mathrm{Tr}\big(|+\rangle_L\langle+|_L\,\rho\big) \\
=\ & \frac{1}{32}(1 - \langle IZXZI\rangle - \langle ZIIZX\rangle - \langle XZIIZ\rangle - \langle ZXZII\rangle - \langle IIZXZ\rangle - \langle YIXIY\rangle \\
& - \langle IYYIX\rangle - \langle XIYYI\rangle - \langle IXIYY\rangle - \langle YYIXI\rangle + \langle ZZYXY\rangle + \langle YXYZZ\rangle \\
& + \langle ZYXYZ\rangle + \langle XYZZY\rangle + \langle YZZYX\rangle + \langle XXXXX\rangle + \langle IXZZX\rangle + \langle IYXXY\rangle \\
& + \langle IZYYZ\rangle + \langle XIXZZ\rangle + \langle XXYIY\rangle + \langle XYIYX\rangle + \langle XZZXI\rangle + \langle YIYXX\rangle \\
& + \langle YXXYI\rangle + \langle YYZIZ\rangle + \langle YZIZY\rangle + \langle ZIZYY\rangle + \langle ZXIXZ\rangle + \langle ZYYZI\rangle \\
& + \langle ZZXIX\rangle),
\end{aligned}
\tag{5.17}
$$

$$P_{1,+} = \sum_{E \in \mathcal{E}} \mathrm{Tr}\big(E|+\rangle_L \langle+|_L E\rho\big)$$

$$= \frac{1}{32}(15 - 3\langle IZXZI\rangle - 3\langle ZIIZX\rangle - 3\langle XZIIZ\rangle - 3\langle ZXZII\rangle - 3\langle IIZXZ\rangle - 3\langle YIXIY\rangle$$
$$- 3\langle IYYIX\rangle - 3\langle XIYYI\rangle - 3\langle IXIYY\rangle - 3\langle YYIXI\rangle - 5\langle ZZYXY\rangle - 5\langle YXYZZ\rangle$$
$$- 5\langle ZYXYZ\rangle - 5\langle XYZZY\rangle - 5\langle YZZYX\rangle - 5\langle XXXXX\rangle - \langle IXZZZ\rangle - \langle IYXXY\rangle$$
$$- \langle IZYYZ\rangle - \langle XIXZZ\rangle - \langle XXYIY\rangle - \langle XYIYX\rangle - \langle XZZXI\rangle - \langle YIYXX\rangle$$
$$- \langle YXXYI\rangle - \langle YYZIZ\rangle - \langle YZIZY\rangle - \langle ZIZYY\rangle - \langle ZXIXZ\rangle - \langle ZYYZI\rangle$$
$$- \langle ZZXIX\rangle).$$

$$(5.18)$$

REFERENCES

[1] M. H. Abobeih, J. Cramer, M. A. Bakker, N. Kalb, M. Markham, D. J. Twitchen, and T. H. Taminiau. One-second coherence for a single electron spin coupled to a multi-qubit nuclear-spin environment. *Nat. Commun.*, 9(1), 2018.

[2] M. H. Abobeih, J. Randall, C. E. Bradley, H. P. Bartling, M. A. Bakker, M. J. Degen, M. Markham, D. J. Twitchen, and T. H. Taminiau. Atomic-scale imaging of a 27-nuclear-spin cluster using a quantum sensor. *Nature*, 576(7787):411–415, 2019.

[3] P. Aliferis, D. Gottesman, and J. Preskill. Quantum accuracy threshold for concatenated distance-3 codes. *Quantum Inf. Comput.*, 6(2):97–165, 2006.

[4] D. D. Awschalom, R. Hanson, J. Wrachtrup, and B. B. Zhou. Quantum technologies with optically interfaced solid-state spins. *Nat. Photonics*, 12(9):516–527, 2018.

[5] M. K. Bhaskar, R. Riedinger, B. Machielse, D. S. Levonian, C. T. Nguyen, E. N. Knall, H. Park, D. Englund, M. Lončar, D. D. Sukachev, and M. D. Lukin. Experimental demonstration of memory-enhanced quantum communication. *Nature*, 580(7801):60–64, 2020.

[6] C. E. Bradley, J. Randall, M. H. Abobeih, R. C. Berrevoets, M. J. Degen, M. A. Bakker, M. Markham, D. J. Twitchen, and T. H. Taminiau. A ten-qubit solid-state spin register with quantum memory up to one minute. *Phys. Rev. X*, 9:031045, 2019.

[7] P. Campagne-Ibarcq, A. Eickbusch, S. Touzard, E. Zalys-Geller, N. E. Frattini, V. V. Sivak, P. Reinhold, S. Puri, S. Shankar, R. J. Schoelkopf, L. Frunzio, M. Mirrahimi, and M. H. Devoret. Quantum error correction of a qubit encoded in grid states of an oscillator. *Nature*, 584(7821):368–372, 2020.

[8] C. Chamberland and M. E. Beverland. Flag fault-tolerant error correction with arbitrary distance codes. *Quantum*, 2:53, 2018.

[9] R. Chao and B. W. Reichardt. Quantum error correction with only two extra qubits. *Phys. Rev. Lett.*, 121:050502, 2018.

[10] R. Chao and B. W. Reichardt. Flag fault-tolerant error correction for any stabilizer code. *PRX Quantum*, 1:010302, 2020.

[11] Z. Chen, K. J. Satzinger, J. Atalaya, and et al. Exponential suppression of bit or phase errors with cyclic error correction. *Nature*, 595(7867):383–387, 2021.

[12] J. Cramer, N. Kalb, M. A. Rol, B. Hensen, M. S. Blok, M. Markham, D. J. Twitchen, R. Hanson, and T. H. Taminiau. Repeated quantum error correction on a continuously encoded qubit by real-time feedback. *Nat. Commun.*, 7(1):11526, 2016.

[13] F. Dolde, V. Bergholm, Y. Wang, I. Jakobi, B. Naydenov, S. Pezzagna, J. Meijer, F. Jelezko, P. Neumann, T. Schulte-Herbrüggen, J. Biamonte, and J. Wrachtrup. High-fidelity spin entanglement using optimal control. *Nat. Commun.*, 5(1), 2014.

[14] L. Egan, D. M. Debroy, C. Noel, A. Risinger, D. Zhu, D. Biswas, M. Newman, M. Li, K. R. Brown, M. Cetina, and C. Monroe. Fault-tolerant control of an error-corrected qubit. *Nature*, 598(7880):281–286, 2021.

[15] A. Erhard, H. P. Nautrup, M. Meth, L. Postler, R. Stricker, M. Stadler, V. Negnevitsky, M. Ringbauer, P. Schindler, H. J. Briegel, R. Blatt, N. Friis, and T. Monz. Entangling logical qubits with lattice surgery. *Nature*, 589(7841):220–224, 2021.

[16] M. Gong, X. Yuan, S. Wang, Y. Wu, Y. Zhao, C. Zha, S. Li, Z. Zhang, Q. Zhao, Y. Liu, F. Liang, J. Lin, Y. Xu, H. Deng, H. Rong, H. Lu, S. C. Benjamin, C.-Z. Peng, X. Ma, Y.-A. Chen, X. Zhu, and J.-W. Pan. Experimental exploration of five-qubit quantum error-correcting code with superconducting qubits. *Natl Sci. Rev.*, 9(1), 2021.

[17] D. E. Gottesman. *Stabilizer Codes and Quantum Error Correction.* PhD thesis, California Institute of Technology, 1997.

[18] Y. He, S. K. Gorman, D. Keith, L. Kranz, J. G. Keizer, and M. Y. Simmons. A two-qubit gate between phosphorus donor electrons in silicon. *Nature*, 571(7765):371–375, 2019.

[19] K. Jung, M. H. Abobeih, J. Yun, G. Kim, H. Oh, A. Henry, T. H. Taminiau, and D. Kim. Deep learning enhanced individual nuclear-spin detection. *npj Quantum Information*, 7(1), 2021.

[20] E. Knill, R. Laflamme, R. Martinez, and C. Negrevergne. Benchmarking quantum computers: The five-qubit error correcting code. *Phys. Rev. Lett.*, 86:5811–5814, 2001.

[21] R. Laflamme, C. Miquel, J. P. Paz, and W. H. Zurek. Perfect quantum error correcting code. *Phys. Rev. Lett.*, 77:198–201, 1996.

[22] N. M. Linke, M. Gutierrez, K. A. Landsman, C. Figgatt, S. Debnath, K. R. Brown, and C. Monroe. Fault-tolerant quantum error detection. *Sci. Adv.*, 3(10), 2017.

[23] M. T. Mądzik, S. Asaad, A. Youssry, B. Joecker, K. M. Rudinger, E. Nielsen, K. C. Young, T. J. Proctor, A. D. Baczewski, A. Laucht, V. Schmitt, F. E. Hudson, K. M. Itoh, A. M. Jakob, B. C. Johnson, D. N. Jamieson, A. S. Dzurak, C. Ferrie, R. Blume-Kohout, and A. Morello. Precision tomography of a three-qubit donor quantum processor in silicon. *Nature*, 601(7893):348–353, 2022.

[24] J. F. Marques, B. M. Varbanov, M. S. Moreira, H. Ali, N. Muthusubramanian, C. Zachariadis, F. Battistel, M. Beekman, N. Haider, W. Vlothuizen, A. Bruno, B. M. Terhal, and L. DiCarlo. Logical-qubit operations in an error-detecting surface code. *Nat. Phys.*, pages 1–7, 2021.

[25] V. Negnevitsky, M. Marinelli, K. K. Mehta, H.-Y. Lo, C. Flühmann, and J. P. Home. Repeated multi-qubit readout and feedback with a mixed-species trapped-ion register. *Nature*, 563(7732):527–531, 2018.

[26] N. H. Nickerson, Y. Li, and S. C. Benjamin. Topological quantum computing with a very noisy network and local error rates approaching one percent. *Nat. Commun.*, 4:1756, 2013.

[27] D. Nigg, M. Müller, E. A. Martinez, P. Schindler, M. Hennrich, T. Monz, M. A. Martin-Delgado, and R. Blatt. Quantum computations on a topologically encoded qubit. *Science*, 345(6194):302–305, 2014.

[28] M. Pompili, S. L. N. Hermans, S. Baier, H. K. C. Beukers, P. C. Humphreys, R. N. Schouten, R. F. L. Vermeulen, M. J. Tiggelman, L. dos Santos Martins, B. Dirkse, S. Wehner, and R. Hanson. Realization of a multinode quantum network of remote solid-state qubits. *Science*, 372(6539):259–264, 2021.

[29] J. Preskill. Reliable quantum computers. *Proc. R. Soc. A Math. Phys. Eng. Sci.*, 454(1969):385–410, 1998.

[30] J. Randall, C. E. Bradley, F. V. van der Gronden, A. Galicia, M. H. Abobeih, M. Markham, D. J. Twitchen, F. Machado, N. Y. Yao, and T. H. Taminiau. Many-body localized discrete time crystal with a programmable spin-based quantum simulator. *Science*, 374(6574):1474–1478, 2021.

[31] L. Robledo, L. Childress, H. Bernien, B. Hensen, P. F. A. Alkemade, and R. Hanson. High-fidelity projective read-out of a solid-state spin quantum register. *Nature*, 477(7366):574–578, 2011.

[32] S. Rosenblum, P. Reinhold, M. Mirrahimi, L. Jiang, L. Frunzio, and R. J. Schoelkopf. Fault-tolerant detection of a quantum error. *Science*, 361(6399):266–270, 2018.

[33] C. Ryan-Anderson, J. G. Bohnet, K. Lee, D. Gresh, A. Hankin, J. P. Gaebler, D. Francois, A. Chernoguzov, D. Lucchetti, N. C. Brown, T. M. Gatterman, S. K. Halit, K. Gilmore, J. A. Gerber, B. Neyenhuis, D. Hayes, and R. P. Stutz. Realization of real-time fault-tolerant quantum error correction. *Phys. Rev. X*, 11(4):041058, 2021.

[34] M. Takita, A. W. Cross, A. D. Córcoles, J. M. Chow, and J. M. Gambetta. Experimental demonstration of fault-tolerant state preparation with superconducting qubits. *Phys. Rev. Lett*, 119(18):180501, 2017.

[35] T. H. Taminiau, J. Cramer, T. van der Sar, V. V. Dobrovitski, and R. Hanson. Universal control and error correction in multi-qubit spin registers in diamond. *Nat. Nanotechnol.*, 9(3):171–176, 2014.

[36] B. M. Terhal. Quantum error correction for quantum memories. *Rev. Mod. Phys.*, 87:307–346, 2015.

[37] S. B. van Dam, J. Cramer, T. H. Taminiau, and R. Hanson. Multipartite entanglement generation and contextuality tests using nondestructive three-qubit parity measurements. *Phys. Rev. Lett.*, 123:050401, 2019.

[38] G. Waldherr, Y. Wang, S. Zaiser, M. Jamali, T. Schulte-Herbrüggen, H. Abe, T. Ohshima, J. Isoya, J. F. Du, P. Neumann, and J. Wrachtrup. Quantum error correction in a solid-state hybrid spin register. *Nature*, 506(7487):204–207, 2014.

[39] W. S. Warren. Effects of arbitrary laser or NMR pulse shapes on population inversion and coherence. *J. Chem. Phys.*, 81(12):5437–5448, 1984.

[40] X. Xue, M. Russ, N. Samkharadze, B. Undseth, A. Sammak, G. Scappucci, and L. M. K. Vandersypen. Quantum logic with spin qubits crossing the surface code threshold. *Nature*, 601(7893):343–347, 2022.

[41] T. J. Yoder, R. Takagi, and I. L. Chuang. Universal fault-tolerant gates on concatenated stabilizer codes. *Phys. Rev. X*, 6:031039, 2016.

6

ROBUST QUANTUM-NETWORK NODES THROUGH REAL-TIME NOISE MITIGATION

Y. Wang[*], **S. J. H. Loenen**[*], **B. M. Terhal**, **T. H. Taminiau**

The nitrogen-vacancy (NV) center in diamond and other solid-state defect centers hold great potential for constructing quantum networks. NV centers can be remotely connected through entanglement via photonic links. Furthermore, by utilizing the electronic spin of the NV center to control associated nuclear spins, a small multi-qubit register can be formed. However, reliably storing entangled states while generating new entanglement links poses a significant challenge when scaling towards large networks. In this study, we propose a method that utilizes spectator qubits to mitigate noise on stored quantum states in real time. We consider a single NV center with multiple nuclear-spin qubits, and some nuclear spins are selected as spectator qubits that are not entangled with other nuclear spins serving as data qubits. The spectator qubits are initialized in a phase-sensitive state, and measuring them after sequences of optical entanglement attempts allows us to infer the stochastic phases acquired by the data qubits without additional operations on them. The spectator qubit approach is flexible and simple, and our preliminary experiments demonstrate that spectator qubits may be a useful tool for realizing robust quantum-network nodes.

6.1. INTRODUCTION

Large-scale quantum networks are crucial for numerous emerging quantum technologies, including fundamental tests of quantum mechanics [5, 27], timekeeping [34], secure communication [8, 23], metrology [25, 47], and distributed computation [4, 20, 40]. To demonstrate quantum networks with a few nodes, optical links are utilized in various physical systems, such as trapped ions [22, 39, 48], neutral atoms [30, 46], quantum dots [19, 49], and nitrogen-vacancy (NV) centers in diamond [9, 29, 31, 44]. These elementary quantum networks have resulted in experimental demonstrations of various elementary building blocks, such as state teleportation [29], entanglement distillation [33], and the implementation of non-local gates between spatially separated nodes [17].

Among these physical systems, NV centers in diamond is one of the leading platforms for realizing large-scale quantum networks, as evidenced by the recent NV-based 3-node network [29, 44]. Each NV center hosts an electronic spin that provides a spin-photon interface (see Chap 3.1.2) [21] for heralded entanglement generation between spatially separated NV centers [6, 15]. The protocols for generating entanglement rely on applying microwave pulses to the electronic spins and optically exciting them to emit photons. In addition, the electronic spin enables high-fidelity universal control of surrounding nuclear spins [3, 14] that can serve as long-lived memories for storing generated entangled states. Using nuclear spins as quantum memory is crucial for creating networks with more than two nodes and other advanced applications, as the electronic spins need to be freed-up for creating new entanglement links [29, 44].

Although significant progress has been made in extending the coherence time of nuclear spins [1], it continues to be a limiting factor for generating larger networks. The probabilistic nature of entanglement generation protocols leads to uncontrolled electronic spin dynamics, which results in dephasing on the nuclear spins due to the always-on electron-nuclear hyperfine coupling. Since the success rate of entanglement generation is as low as of the order of 10^{-4}, this decoherence mechanism is identified as a significant limiting factor for the nuclear memory lifetime during remote entanglement generation [6, 15, 29, 44]. This issue needs to be addressed to advance the scalability of NV-based quantum networks [11, 13, 29, 32, 45].

Several methods have been proposed to improve the noise resilience of nuclear spins serving as data qubits. One approach is to use isotopically engineered diamond with a greatly reduced ^{13}C concentration, where the electron-nuclear couplings are much weaker [13]. This method reduces the influence of uncontrolled electronic spin dynamics on adjacent nuclear spins, but it compromises the speed of implementing electron-nuclear two-qubit gates. Another method is to reduce the uncertainty in the electronic spin dynamics by optimizing the timing of the microwave pulses used in the entanglement generation protocols [32] or by increasing the external magnetic field strength, which allows to reduce the delay times between consecutive pulses [32, 44].

Additionally, because the electronic spin couples simultaneously to surrounding nuclear spins, the noise induced by entanglement attempts is spatially correlated, leading to the construction of decoherence-protected subspaces [21, 36]. This approach has been experimentally demonstrated in diamond using naturally occurring spin pairs [7], or by encoding two nuclear spins in a Bell state through nuclear-nuclear entangling gates [45]. Furthermore, some efforts are dedicated to designing quantum error correction
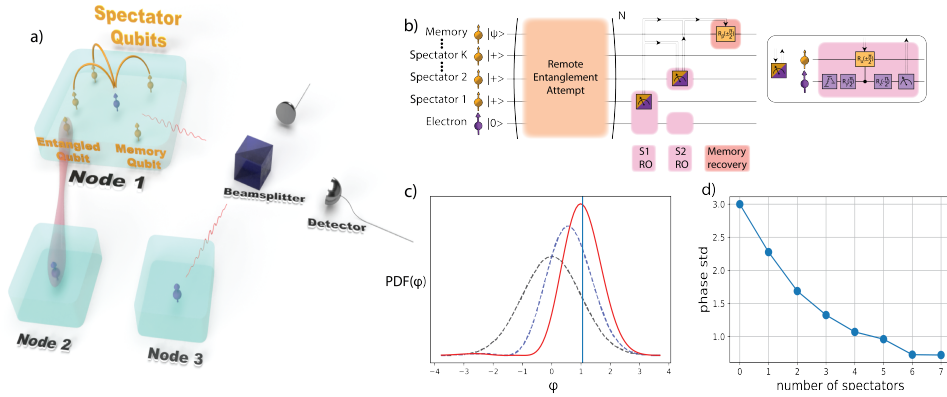
Figure 6.1: Improved memory qubit coherence for generating remote entanglement using spectator qubits. a) The blue blocks in the diagram represent nodes of a quantum network, each containing an NV center with an electronic spin (purple) serving as an optical interface. Additionally, the NV center in a node is surrounded by carbon-13 nuclear spins (orange) that interact with the electronic spin. Note that only the carbon nuclear spins associated with Node 1 are depicted for clarity. Initially, entanglement is successfully achieved between the electronic spins of Node 1 and Node 2. To further entangle Node 1 with Node 3 and build a 3-node network, the electronic spin of Node 1 needs to be freed-up for use in generating the entanglement link between Node 1 and Node 3. This is achieved by transferring the generated entangled state to a surrounding nuclear spin, referred to as the memory qubit. Due to the stochastic evolution of the electronic spin during these attempts to generate entanglement with Node 3, the entangled state stored in the memory qubit of Node 1 will dephase. Other nuclear spins associated with Node 1, referred to as spectator qubits, are responsible for monitoring the electronic spin's evolution to mitigate noise on the memory qubit. b) An example sequence of using spectator qubits, where the inset demonstrates the gate sequence for reading out a nuclear spin via the electronic spin. The pulse sequence for a single entangling attempt is detailed in Fig 6.2. The memory qubit holds an entangled state, and multiple spectator qubits are initialized in a phase-sensitive state. For more details about the sequence of the entanglement generation protocol, see Fig 6.6. After attempting remote entanglement generation N times, the spectators are sequentially measured to gain information about the electronic spin dynamics. The measurement basis of subsequent spectators is adjusted based on previous outcomes to maximize information gain. By measuring all the spectators, we may obtain a more accurate estimate of the phase acquired by the memory qubit and improve its fidelity. c) Example probability distribution functions (PDF) of the memory qubit's acquired phase φ, where the memory and spectator qubits are all assumed to have the same hyperfine interaction strength $A_\parallel$ for simplicity. The black dashed curve represents the phase distribution with no spectator measurements, while the blue dashed and red solid curves show the distributions for specific measurement outcomes of a single spectator and two spectators, respectively. Incorporating the information provided by two spectator measurements results in a sharper posterior PDF, leading to a more precise estimate of the most probable phase φ acquired by the memory qubit, as indicated by the vertical line. d) The standard deviation (std) of the phase acquired by the memory qubit decreases with the addition of more spectator qubits. In this example, we use the nuclear spin C_6 as the memory qubit and seven other nuclear spins as spectator qubits, whose parameters are listed in Tab 6.1. The order in which the spectator qubits are measured is determined by the absolute value of their parallel hyperfine interaction with the electronic spin, with the ones possessing large $|g|$ being measured later. By utilizing the information obtained from earlier spectator measurements, the difficulties associated with distinguishing the large phases accumulated by those spectator qubits with significant $|g|$ are alleviated. The phase uncertainties are obtained numerically using Monte Carlo, see details in Chap 6.4.2. The reduction in the standard deviation of the memory phase signifies a higher fidelity of the memory qubit, as demonstrated in Fig 6.5.

	$A_\parallel/2\pi$ [kHz]	$A_\perp/2\pi$ [kHz]		$A_\parallel/2\pi$ [kHz]	$A_\perp/2\pi$ [kHz]
C_1	-11.346(2)	59.21(3)	C_5	24.399(1)	24.81(4)
C_2	17.643(1)	8.6(2)	C_6	-36.308(1)	26.62(4)
C_3	-19.815(3)	5.3(5)	C_7	-48.58(2)	9(2)
C_4	20.569(1)	41.51(3)	C_8	213.15(4)	3.0(4)

Table 6.1: The parallel ($A_\parallel$) and perpendicular ($A_\perp$) parts of the hyperfine electron-nuclear coupling constants in a NV center are determined using dynamical decoupling spectroscopy [2]. Note that these nuclear spins are ordered by increasing absolute value of $A_\parallel$.

codes that are efficient in dealing with correlated noise [16, 35, 42].

In this chapter, we present an additional, complementary method for mitigating correlated noise using spectator qubits. These spectator qubits are measured in carefully selected bases after noise accumulation, providing direct information about the noise affecting the data qubits. Importantly, this approach only requires single-qubit operations and does not require interaction or entanglement between the data and spectator qubits, reducing the experimental complexity. The concept of spectator qubits has previously been introduced for real-time system calibration in trapped-ion qubits [38] and for monitoring energy injection events in superconducting qubits [41]. Previous research has also explored general techniques for utilizing spectator qubits in various situations [26, 52, 53].

6.2. EXPERIMENTAL SETUP

We demonstrate the proposed error mitigation method using a negatively charged NV center in diamond, which contains a natural abundance of carbon isotopes, including 1.1% ^{13}C. The experiments presented in this chapter are conducted at a temperature of 4 K and an external magnetic field of $B_z \approx 403$ G. The external magnetic field is applied along the NV axis, splitting the $m_s = \pm 1$ levels of the electronic spin, and the lowest two energy levels ($m_s = 0$ and $m_s = -1$) are utilized as the qubit.

In the rotating frame of the electronic spin qubit, and under the secular approximation, the Hamiltonian of the electronic spin and a single ^{13}C nuclear spin is expressed as [21]

$$H = \omega_0 I_z + A_\parallel S_z I_z + A_\perp S_z I_x. \tag{6.1}$$

Here, S and I represent the spin-1 and spin-1/2 operators of the electronic and nuclear spins, respectively. $\omega_0 = \gamma_n B_z$ is the Larmor frequency of the nuclear spin with γ_n the nuclear gyromagnetic ratio. The parallel and perpendicular hyperfine interaction components for the nuclear spins involved here are listed in Table 6.1.

When the electronic spin is in the state $m_s = -1$, the nuclear precession axis gets tilted and the frequency becomes $\omega_{-1} = \sqrt{(\omega_0 - A_\parallel)^2 + A_\perp^2}$. Details about rotating frame and secular approximation can be found in Chap 3. Given a sufficiently large external magnetic field such that $\omega_0 - A_\parallel \gg A_\perp$, the change in the precession axis is substantially suppressed.

However, the effect of $A_\perp$ can accumulate and become significant under specific conditions [12, 50]. For example, applying a sequence of equidistant π pulses on the

electronic spin via a Carr-Purcell sequence can induce a nuclear Rabi rotation if the delay time between consecutive π pulses is given by $t_{delay} \approx \pi/(\omega_0 - A_\parallel/2)$ [50]. This principle serves as the foundation for controlling nuclear spins that are weakly coupled to the electronic spin, and has been further explained in Chapter 3.4.

In the experiments we conducted, the delay times between two consecutive electronic spin flips, induced by either a microwave π pulse or an electronic spin reset process, are far from resonances. Therefore, the perpendicular hyperfine component can be considered non-secular in the rotating frame of the nuclear spin. In the joint rotating frame of the electronic and nuclear spins, we apply the secular approximation to ignore $A_\perp$, and express the Hamiltonian as:

$$H = |0\rangle\langle 0| \otimes I + |1\rangle\langle 1| \otimes A_\parallel I_z, \tag{6.2}$$

where $|0\rangle$ and $|1\rangle$ represent the electronic spin states $m_s = 0$ and $m_s = -1$, respectively.

6.3. REMOTE ENTANGLING PROTOCOLS

We focus on emission-based remote entangling protocols where a spin-selective optical excitation is used to generate spin-photon entanglement [6, 15]. At the heart of the protocols considered here is the optical excitation of the electronic spins, which then quickly decay to the ground state and emit photons. These emitted photons then interfere at a beam splitter, and the resulting interference pattern is detected by photon detectors placed at the output ports of the beam splitter, as schematically illustrated in Fig 6.1(a). The detection of photons heralds the generation of entangled states between the two electronic spins. The pulse sequence considered here to implement such entanglement protocols is schematically shown in Fig 6.2. For a more detailed description of the entangling protocols, see Appendix 6.7.1.

The success rate of generating entangled states through the remote entangling protocols, as heralded by photon detection, is typically low, currently on the order of 10^{-4} for NV centers [29, 44]. This low success rate can be attributed to several factors. Firstly, approximately 97% of the photons are emitted into the phonon sideband, which induces lattice vibrations that can disturb the entangled states between the electronic spins and their emitted photons. In addition, only about 10% of the photons can be collected by the photon detectors [28]. These issues have been discussed in detail in Chap 3.1.3.

6.3.1. DEPHASING MECHANISMS DURING ENTANGLEMENT ATTEMPTS

In order to entangle more than 2 nodes, the generated entangled states must be stored in the respective nuclear spins, thus freeing up the electronic spins for generating new entanglement links with other nodes. With repeated attempts to entangle, it becomes increasingly challenging to determine the duration for which the electronic spin remains in the $m_s = -1$ state and the duration for the $m_s = 0$ state. This can result in a random phase being imparted on the nuclear spins, as can be easily seen from the rotating-frame Hamiltonian in Eq (6.2).

Consequently, the remote entanglement stored in nuclear spins may decay before the new entanglement links can be successfully generated [29, 43, 44]. In the following, we present a detailed discussion of two key factors that contribute to the dephasing of
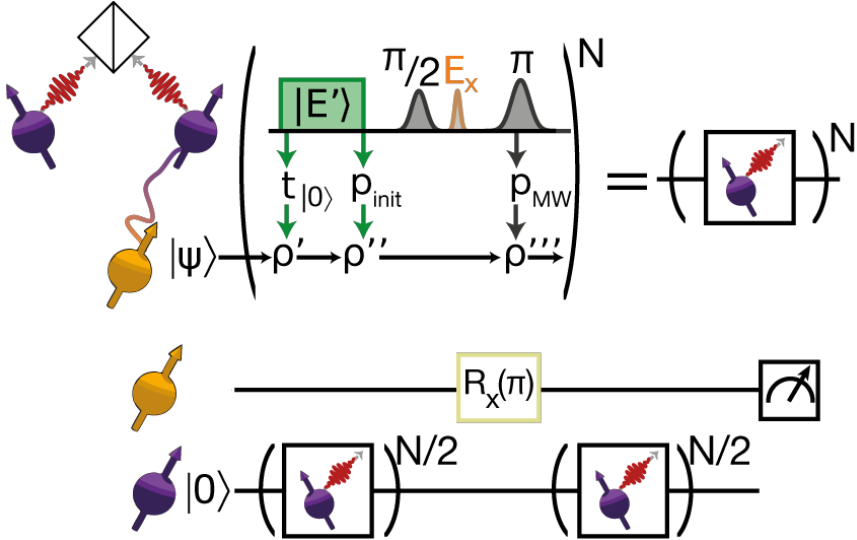
Figure 6.2: Pulse sequence used to entangle two spatially separated NV centers, with one containing a nuclear spin qubit serving as the memory qubit, as shown in Fig 6.1(a). The green box represents the laser used for resetting the electronic spin. The optically excited states $|E_1\rangle$ and $|E_2\rangle$, denoted by $|E'\rangle$, have largely suppressed ISC rates. The parameter $t_{|0\rangle}$ represents the time the electronic spin jumps from the $m_s = \pm 1$ states to the $m_s = 0$ state, and p_{init} represents the probability that the electronic spin reset fails. The laser (in orange) after the $\pi/2$ pulse is used to excite the electronic spin into the excited state $|E_x\rangle$ with a much-reduced ISC rate, which is favorable for generating entangled states between the electronic spins and their emitted photons. The optically excited states and their corresponding optical transitions are summarized in Fig 2.5. Due to the random spin jumping time $t_{|0\rangle}$ and the microwave π pulse errors with an error rate p_{MW}, the nuclear spin in the initial state $|\psi\rangle$ acquires a random phase, leading to a mixed state represented by ρ'''. To preserve nuclear spin coherence, an echo pulse is applied after $N/2$ entangling attempts to cancel quasi-static noise. However, since the entangling protocol is probabilistic, the number of attempts required cannot be determined beforehand. Thus, one may need to wait for some time following the occurrence of heralded entanglement generation to balance the durations before and after the nuclear echo pulse. Additional echo pulses can be used to further protect the nuclear spin coherence in principle. Although we use a $\pi/2$ microwave pulse to prepare the electronic spin in equal superposition of its $m_s = 0$ and $m_s = -1$ states for simplicity, the single-click protocol in practice actually requires it to be initialized in an unbalanced superposition. For the double-click protocol, an additional optical pulse is required to excite the electronic spin after the microwave π pulse. More information regarding the entangling protocols is provided in Appendix 6.7.1. Figure adapted from Ref. [32].

the quantum states during the generation of new entanglement links. First, the stochastic nature of the reset process results in uncontrolled electronic spin dynamics, making it impossible to track its state accurately [11, 45]. Additionally, Ref. [32] has demonstrated that microwave pulse errors can significantly contribute to the randomness of the electronic spin dynamics.

ELECTRONIC SPIN INITIALIZATION

The process of resetting the electronic spin involves the application of a laser to selectively excite the electronic spin in the $m_s = \pm 1$ states into excited states that have high intersystem crossing (ISC) rates. Upon the occurrence of an ISC event, the electronic spin decays to the $m_s = 0$ state instead of its original state. Since the electronic spin remains almost unaffected when it is initially in the $m_s = 0$ state, the electronic spin can be reliably initialized into this state by continuously exciting it for a few microseconds.

To simplify the analysis for the electronic spin reset process, we adopt a model that neglects the complex dynamics of the electronic spin when it is in the optically excited states [11, 45]. In this simplified model, the electronic spin remains in the subspace of $m_s = 0$ and $m_s = -1$ states and undergoes direct transitions from the $m_s = -1$ state to the $m_s = 0$ state at a random spin jumping time $t_{|0\rangle}$ after switching on the laser.

In addition, we make the assumption that the distribution of random spin jumping times $t_{|0\rangle}$ follows an exponential distribution with an average value of τ, commonly known as the characteristic time [11, 45]. Previous research has revealed that this characteristic time is $\tau \approx 0.5\,\mu$s [11, 45] or possibly shorter [32], depending on the laser power used for electronic spin reset. The uncertainty in the spin jumping time introduces only a small random phase each time. However, it is crucial to note that, given the large number of repetitions of the entanglement attempts, these small phases can accumulate into a significant phase when the entanglement link is established.

Let us consider k spin-jumping events. The total duration during which the electronic spin remains in the $m_s = -1$ state is obtained by adding up the individual durations, given as $T'_k = \sum_{i=1}^{k} t_{|0\rangle,i}$. For large values of k, the probability distribution of T'_k can be approximated by a Gaussian distribution [11]. The distribution has a mean value of $\mu = k\tau$ and a standard deviation of $\sigma = \tau\sqrt{k}$, and can be expressed as

$$P(T'_k) = \frac{T_k'^{k-1}}{\tau^k (k-1)!} e^{-T'_k/\tau} \approx \frac{1}{\sigma\sqrt{2\pi}} e^{-\frac{T_k'^2}{2\sigma^2}} \tag{6.3}$$

Moreover, since we use an $\pi/2$ MW pulse to prepare the electronic spin in equal superposition of its $m_s = 0$ and $m_s = -1$ states, the probability of k spin-jumping events occurring after N entanglement attempts is given by the binomial distribution

$$P_k(N) = \frac{1}{2^N} \binom{N}{k}. \tag{6.4}$$

The probability distribution of the total time in which the electronic spin stays in $m_s = -1$ state is then given by

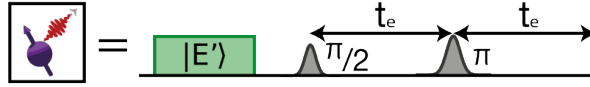$$P(T_N) = \sum_{k=1}^{N} P_k(N) P(T'_k). \tag{6.5}$$

Figure 6.3: Pulse sequence used to simulate entangling attempts using a single NV center. The optical excitation, represented by the orange laser in Fig 6.2, used to generate entangled states between the electronic spins and their emitted photons is omitted, as the probability of electronic spin flipping during this step is considered negligible. The interpulse delay time t_e can be optimized to mitigate the detrimental effects of failed microwave π pulses on the nuclear memory coherence. Figure adapted from Ref. [32].

The mean value and the standard deviation can be easily calculated, which are given by

$$\mu'_N = N\tau/2, \quad \sigma'_N = \sqrt{3}N\tau/2. \tag{6.6}$$

For a nuclear spin with parallel hyperfine interaction strength $A_\parallel$, the acquired phase is written as $\varphi = A_\parallel T_N$, with mean value $\mu_N = A_\parallel \mu'_N$ and standard deviation $\sigma_N = A_\parallel \sigma'_N$

Note that this mean value only introduces a deterministic phase that depends on the number of entanglement attempts. This can be compensated in the control electronics or removed by echo sequences. In contrast, the standard deviation causes a dephasing of the nuclear spins, so we simply assume a zero mean. Furthermore, we approximate the probability distribution of φ as a Gaussian distribution:

$$P_{\text{echo}}(\varphi) \approx \frac{1}{\sigma_N \sqrt{2\pi}} e^{-\frac{\varphi^2}{2\sigma_N^2}}. \tag{6.7}$$

Note that, in Fig 6.2, the probability of the electronic spin state being altered by the laser for generating a spin-photon entangled state is expected to be negligible. This is because this laser selectively excites the electronic spin in the $m_s = 0$ ground state into excited states $|E_x\rangle$ [29, 44], which has substantially reduced ISC rates. This optical transition is exploited to create entangled states between an electronic spin and the emitted photon. A more detailed explanation of the optical addressing methods employed for the electronic spins and the underlying ISC mechanism can be found in Chap 3.1.2 and Chap 2.5, respectively.

MICROWAVE PULSE ERRORS

During each attempt for generating entanglement, a microwave π pulse can be utilized to maintain the coherence of the electronic spin by decoupling it from neighboring nuclear spins and other quasi-static noise sources. Additionally, such π pulses ensure that a neighboring nuclear spin only acquires a global phase $A_\parallel t_e$ in each entangling attempt, where t_e denotes the interpulse delay, as depicted in Fig 6.3.

A noisy π pulse can be modeled as follows: with probability p_{MW}, the pulse fails, and the electronic spin remains untouched. Otherwise, an ideal microwave π pulse is executed [32]. In case of a failed π pulse, the electronic spin becomes entangled with the nuclear spins. By tracing out the electronic spin, a nuclear spin acquires either a phase of $2A_\parallel t_e$ or no phase at all. For the pulse sequence in Fig 6.3, both cases happen with equal probability, as the $\pi/2$ pulse prepares the electronic spin in the equal superposition of its $m_s = 0$ and $m_s = -1$ states. Therefore, failed microwave π pulses effectively increase

the phase uncertainty σ_N in Eq (6.7), which can act as a significant limiting factor on the coherence of the nuclear spin qubit when executing remote entangling protocols [32].

It is worth noting that while a failed electronic spin reset or a failed microwave $\pi/2$ pulse has a negative impact on the creation of remote entanglement between NV centers, it does not directly increase the uncertainty of the phases acquired by the nuclear spins. This is mainly because the π pulse in each entanglement attempt balances the times for the electronic spin to remain in the $m_s = 0, -1$ states during the period of $2t_e$, regardless of its state before this period.

6.4. SPECTATORS FOR NOISE MITIGATION

One important observation is that uncontrolled electronic spin dynamics induces spatially correlated dephasing on neighboring nuclear spins. Extracting information on the phase acquired by one nuclear spin allows us to gain greater insight into the noise affecting all other nuclear spins simultaneously. This is because the random phase acquired by a nuclear spin is proportional to its parallel component $A_\parallel$ of its hyperfine interaction to the electronic spin.

Based on this observation, we propose a method to mitigate the correlated dephasing noise affecting nuclear spins that serve as data qubits, which is achieved by measuring other nuclear spins acting as spectator qubits. While the data qubits store arbitrary quantum states, the spectator qubits are initially prepared in the +1 eigenstate of the spin-1/2 operator I_x, which is maximally sensitive to random phase accumulation.

Consider a simplified scenario in which a single data qubit and a single spectator qubit are associated with an NV center, and we attempt to entangle this NV center with another located elsewhere. As a result of attempting remote entanglement, the spectator qubit and the data qubit acquire random but correlated phases. The system dynamics is described by the rotating-frame Hamiltonian in Eq (6.2), ignoring the effect of $A_\perp$.

Let us denote the phase accumulated by the data qubit as φ, and define the relative coupling constant g as the ratio of the hyperfine interaction strength of the spectator and data qubits, i.e.,

$$g = A_\parallel^{\text{spectator}} / A_\parallel^{\text{data}}. \tag{6.8}$$

As a result, the state of the spectator qubit after the phase accumulation can be expressed as follows:

$$\left| C_{\text{spec}} \right\rangle = \frac{|m_s = -1/2\rangle + e^{ig\varphi} |m_s = 1/2\rangle}{\sqrt{2}}. \tag{6.9}$$

6.4.1. NOISE MITIGATION VIA PHASE ESTIMATION

To maximize the information gained from measuring the spectator qubit, it is imperative to make a careful selection of its measurement basis, based on our knowledge of the random phase φ that has been acquired by the data qubit.

For example, if the phase distribution $P(\varphi)$ is symmetrical and localized around $\varphi = 0$, the optimal choice is to measure the spectator qubit in the Pauli Y-basis [10, 51]. The likelihood functions for the spectator measurements are then expressed as follows:

$$P(\text{m} = 0, 1 | \varphi) = \frac{1 + (-1)^m \sin(g\varphi)}{2}, \tag{6.10}$$

Spectator : $|\psi_i\rangle$ ————⊕————

Ancilla qubit : $|0\rangle$ —[H]—●—[$R_z(-\vartheta_i)$]—[H]—[measure]
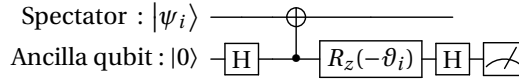
Figure 6.4: Schematic of the ith spectator qubit measurement. Before reading out the ancilla qubit in X-basis, it is first rotated around the Z-axis by an adaptive angle ϑ_i, which is chosen according to previous spectator qubit measurements according to Eq. (6.13).

where $m = 0$ and $m = 1$ represent the spectator measurement being in $m_s = -1/2$ and $m_s = +1/2$, respectively. By applying Bayes' theorem, the posterior distribution can be computed, which is proportional to the product of the likelihood function and the prior distribution $P(\varphi)$, up to normalization. This leads to a narrower posterior distribution, enabling a more accurate estimation of the phases acquired by the nuclear spins, thus mitigating the noise of the data qubit in real time.

However, caution must be exercised when using a spectator qubit with a high absolute value of its relative coupling constant g. When there is a significant probability that $g\varphi \mod 2\pi$ is not equal to $\varphi \mod 2\pi$, it becomes more challenging in obtaining information on φ by measuring the value of $g\varphi$. This is distinct from typical quantum sensing scenarios, where a more sensitive sensor qubit (i.e., larger absolute value of the relative coupling strength g in our situation) generally results in a better sensing performance. For quantum sensing applications, the target signal is usually too weak to cause concerns about the phase ambiguity.

To further decrease the phase uncertainty, it is possible to perform adaptive measurements on multiple spectator qubits, which effectively implements a phase estimation protocol. Each time a spectator qubit is measured, Bayes' theorem is applied to compute the posterior phase distribution. The updated distribution is then used to determine the optimal measurement basis for the next spectator qubit measurement. By iteratively repeating this process, we can achieve an increasingly accurate estimation of the phase acquired by the data qubit.The details for implementing the phase estimation protocol are elaborated below.

PHASE ESTIMATION PROCEDURE

Spectator qubits are first initialized in the equal superposition state, which has maximum sensitivity to a stochastic phase. They are then measured one by one in carefully chosen bases, each of which depends on previous spectator measurements.

As shown in Fig. (6.4), before measuring the ith spectator qubit in the Pauli-Y basis, it is first rotated around the Z axis by an angle ϑ_i. This measurement yields the outcome $m_i = 0, 1$ with the probability

$$P(\mathrm{m}_i|\varphi) = \frac{1 + (-1)^{m_i} \cos\left(g_i\varphi - \vartheta_i\right)}{2}, \tag{6.11}$$

where φ denotes the stochastic phase acquired by a data qubit and g_i is the relative coupling strength of the ith spectator qubit. Note that this angle ϑ_i determines the measurement basis of the ith spectator and depends on the previous $i - 1$ measurements.

Using the Bayes' theorem, reading out n spectator qubits in a row leads to the posterior distribution (up to normalization)

$$P(\varphi|\mathcal{M}_n) \propto \prod_{i=1}^{n} \frac{1 + (-1)^{m_i} \cos(g_i\varphi - \vartheta_i)}{2} P(\psi), \tag{6.12}$$

where $P(\varphi)$ denotes the prior distribution, and $\mathcal{M}_n = [m_1, m_2, \cdots, m_n]$ records the measurement outcomes of the previous n spectator qubits. The measurement basis of the $(n+1)$th spectator qubit is determined by this n-bit record $\mathcal{M}_n$, i.e.,

$$\vartheta_{n+1} = g_{n+1}\overline{\psi}_n \pm \frac{\pi}{2}, \tag{6.13}$$

where the estimator $\overline{\varphi}_n$ is given by [10, 51]

$$\overline{\varphi}_n = \arg \int e^{i\varphi} P(\varphi|\mathcal{M}_n)\, \mathrm{d}\varphi. \tag{6.14}$$

Such choices of measurement bases are argued to be optimal as they minimize the Holevo phase variance [10, 51]

$$V\big[p(\varphi)\big] = \left|\int e^{i\varphi} p(\varphi)\, \mathrm{d}\psi\right|^{-2} - 1, \tag{6.15}$$

which serves as a natural quantifier to measure the dispersion in a stochastic phase that is likely to be large. For example, when the phase distribution $p(\psi)$ is sharply peaked, the Holevo phase variance reduces to the usual definition of variance, i.e.,

$$\begin{aligned}
V\big[p(\varphi)\big] &= \left|\langle e^{i\varphi}\rangle\right|^{-2} - 1 = \left|\langle e^{i(\varphi - \langle\varphi\rangle)}\rangle\right|^{-2} - 1 \\
&\approx \left|\langle 1 - \frac{1}{2}(\varphi - \langle\varphi\rangle)^2 + i(\varphi - \langle\varphi\rangle)\rangle\right|^{-2} - 1 \\
&= \left[1 - \frac{1}{2}\langle(\varphi - \langle\varphi\rangle)^2\rangle\right]^{-2} - 1 \\
&\approx \langle(\varphi - \langle\varphi\rangle)^2\rangle.
\end{aligned} \tag{6.16}$$

The estimator in Eq. (6.15) also becomes the usual mean value, i.e.,

$$\begin{aligned}
\overline{\varphi}_i &= \arg\left[e^{i\langle\varphi\rangle}\langle e^{i(\varphi - \langle\varphi\rangle)}\rangle\right] \\
&\approx \arg\left(e^{i\langle\varphi\rangle}\right) \\
&= \langle\varphi\rangle.
\end{aligned} \tag{6.17}$$

6.4.2. NUMERICAL SIMULATION

We begin our investigation by using numerical simulations to explore the use of spectator qubits. Specifically, we consider C_6 with $A_\parallel = -36.308 \times 2\pi$ kHz as the data qubit and use seven other nuclear spins as spectator qubits, as enumerated in Table 6.1. To illustrate the concepts, we first simulate a simplified situation in which there are no imperfections other than the correlated noise caused by the electronic spin during entanglement attempts. In addition, we use the secular approximation in Eq (6.2) and ignore
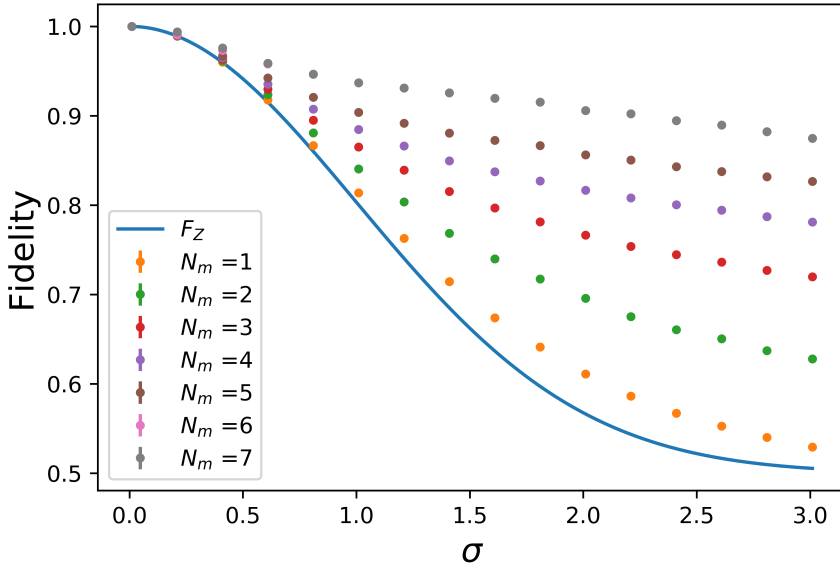
Figure 6.5: Numerical simulations of real-time noise mitigation using spectator qubits. In each simulation round, a random phase φ is assigned to the memory qubit C_6 with $A_\parallel = -36.308 \times 2\pi$ kHz, selected from a Gaussian distribution with a standard deviation of σ. The remaining seven nuclear spins, acting as spectator qubits, are also assigned phases according to their relative coupling strengths. At the beginning, all qubits are prepared in an equal superposition of the $m_s = \pm 1/2$ states. The fidelity of the memory qubit in the absence of the spectator qubits, denoted as F_z, is calculated using Eq.6.18 and represented by the blue solid line. The spectators are measured adaptively in ascending order of the absolute value of $A_\parallel$, as described in Appendix 6.4.1. The memory qubit fidelity is determined after each spectator is measured. For example, the purple dots labeled $N_m = 4$ represent the memory fidelity after measuring C_1, C_2, C_3, and C_4. The ordering of spectators is chosen so that we have more information about the random phase accumulated when measuring spectator qubits with larger $|g|$ at later times. Remarkably, measuring the spectator qubits can restore the fidelity of the memory qubit from nearly 0.5 to close to 0.9 when $\sigma = 3$. However, the enhancement due to the final spectator qubit C_8 becomes difficult to see when the accumulated phase on the data qubit is substantial, namely when σ is large. This difficulty arises primarily because the relative coupling constant of C_8 is remarkably large, facilitating its ability to accumulate a phase beyond 2π. It's worth noting that the noticeable improvement in data qubit fidelity from measuring C_8 is only apparent when $\sigma < 0.5$. It should be noted that the simulation only considers the correlated nuclear spin dephasing and does not account for other noise sources, such as the adverse effects of reading and initializing the spectator qubits.

the perpendicular ($A_\perp$) hyperfine interaction components. In this case, the only noise source for the nuclear spins is this correlated dephasing.

In each simulation round, we generate a random phase φ from a Gaussian distribution with a standard deviation of σ, and we vary the value of σ throughout the simulation. The phase φ is assigned to the data qubit, while the correlated phases $g\varphi$ are assigned to the respective spectators. For simplicity, we assume a single measurement of each spectator qubit, following the order of increasing $|g|$. Moreover, we refrain from complicating the simulation by re-initializing a spectator qubit and measuring it again after more entanglement attempts.

By postponing the measurement of a spectator qubit with a larger $|g|$ until later, we can exploit the information obtained from earlier spectator measurements to decrease the likelihood of $g\varphi \mod 2\pi$ being different from $\varphi \mod 2\pi$. The challenges associated with differentiating the large phases acquired by those spectator qubits with large $|g|$ can therefore be mitigated.

Since the goal is to investigate the effectiveness of using spectator qubits to reduce the dephasing of the data qubit, the data qubit is also initialized in the equal superposition of its $m_s = \pm 1/2$ states. Without using the information from the spectator measurements, the fidelity of the data qubit can be easily calculated as follows:

$$F_Z = \frac{1}{2} + \frac{1}{2} e^{-\sigma^2/2}, \tag{6.18}$$

which is represented by the blue solid line in Fig 6.5. Note that the prior phase standard deviation σ depends on the number of entanglement attempts implemented, that is, more attempts result in a larger σ.

In the simulation, the spectator qubits are measured adaptively according to the phase estimation protocol described in chapter 6.4.1, and we evaluate how the fidelity of the data qubit can be improved by using more spectator qubits by varying the number of spectators used. For example, the green dots with $N_m = 2$ in Fig.6.5 show the fidelity of the data qubit after measuring C_1 and C_2 and using their measurement results to mitigate the noise affecting the data qubit. It is clearly better than the fidelity of the data qubit when only the information provided by C_1 was used, which is represented by the orange dots labeled $N_m = 1$.

The enhancement in data qubit fidelity becomes especially pronounced when the preceding phase uncertainty, denoted as σ, is substantial, thereby rendering other sources of noise relatively inconsequential. , as shown in Fig 6.5. However, the last spectator qubit, C_8, has a relatively large coupling constant ($A_\parallel = 213.15(4) \times 2\pi$ kHz) and is therefore less helpful in the large σ regime than other spectator qubits. The improvement of the data qubit fidelity by measuring C_8 can only be observed at $\sigma < 0.5$.

To maximize the effectiveness of C_8 as a spectator qubit, one viable approach involves periodic measurements after certain intervals of entanglement attempts to ensure that the accumulated phase remains small enough. Conversely, another approach is to measure additional spectator qubits with smaller relative coupling constants, thereby reducing the phase uncertainty before measuring C_8.

The simulation results shown in Fig. 6.5 demonstrate the potential advantages of using spectator qubits. However, it is important to note that the error model used here is

oversimplified, i.e., it assumes that the fidelity of the nuclear spin qubits is limited only by the correlated dephasing noise induced by the entangling operations. The simulation does not consider other possible sources of noise, such as uncorrelated natural nuclear spin dephasing, or the negative effects of measurement and initialization of the spectators.

6.5. PRELIMINARY EXPERIMENTS

To elucidate the concept of spectator qubits experimentally, we initiated preliminary experiments with two nuclear spins: C_5 (acting as the memory) and C_6 (acting as the spectator), which are listed in Table 6.1. These particular spins are chosen for their high control fidelity, with the electron-nuclear maximal entangling gate fidelity expected to exceed 99% [14]. This high fidelity facilitates a clearer observation of improvements due to the use of spectator information, thereby minimizing the influence of extraneous imperfections at this preliminary stage.

We experimentally implement the pulse sequences depicted in Fig 6.6 to simulate the pulse sequence for generating remote entanglement demonstrated in Fig 6.2. It is important to note that the sequence shown in Fig 6.6(a) is implemented to simulate the scenario where the microwave echo pulses in each entangling attempt are removed. Additionally, we use only a single NV center and omit the optical pulse utilized for generating the spin-photon entangled state, i.e., the laser (in orange) after the $\pi/2$ pulse in Fig 6.2.

In the sequence shown in Fig 6.6(a), we minimize the waiting time t_e to about 1 μs. Due to the microwave π pulses in each entanglement attempt in the sequence shown in Fig 6.6(b), there are two waiting periods, each lasting about 2.316 μs, which is equivalent to the Larmor period of the nuclear spins when the electronic spin remains in the $m_s = 0$ state. In addition, the electronic spin reset takes 5 μs with a power of 1 μW for both sequences in each entanglement attempt.

To initialize the data and spectator qubit, the SWAP method shown in Fig 3.6(b) is employed, which involves two electron-nuclear entangling gates and an electronic spin reset process. The duration of each electron-nuclear entangling gate is approximately 0.5-1 ms, making the total duration for carbon initialization around 1-2 ms. Additionally, the electronic reset process takes about 100 μs, which is much longer than the 5 μs duration of the electronic spin reset in an entangling attempt.

The nuclear-spin readout is accomplished by entangling the nuclear spins with the electronic spin, which is subsequently measured, as shown in Fig 3.6(a). To measure the data and spectator qubits, the electronic spin readout takes 37 μs and 120 μs, respectively. If photon detection occurs during these processes, the laser is turned off within 1 μs to minimize the likelihood of unintended electronic spin flips.

It is noteworthy that the time durations of the electronic spin reset, the electronic spin readout, and the waiting periods, are selected for convenience and are not optimized to maintain the coherence of the nuclear spins. When optimizing pulse sequences, it is crucial to consider factors such as the finite duration of microwave pulses (e.g., a π pulse lasts around 132 ns) and microwave pulse errors. Discussions on these optimizations can be found in Refs. [32, 45].

6.5.1. MEASUREMENTS OF THE MEMORY AND SPECTATOR QUBIT

It is important to note that, in our preliminary experiments, we do not follow the phase estimation protocol described in Chap 6.4.1 for measuring the nuclear spins. This is because we want to avoid characterizing the prior distribution of the phase acquired by the nuclear spins. Moreover, we are not entirely confident that the dominant noise source is indeed correlated dephasing. In the following, we explain in detail how we measure the data and spectator qubit.

To track the decay of the coherence of the data qubit, we measure its Bloch vector length, denoted by L. The Bloch vector length is determined by calculating the expectation values of the operators $X = 2I_x$, $Y = 2I_y$, and $Z = 2I_z$, where I_x, I_y, and I_z are the spin-1/2 operators. Under the assumption that the expectation value of Z is zero, we measure the expectation values $\langle X \rangle$ and $\langle Y \rangle$ only, and calculate the Bloch vector length as following:

$$L = \sqrt{\langle X \rangle^2 + \langle Y \rangle^2}. \tag{6.19}$$

This assumption is based on the fact that the nuclear spins are initially prepared in the eigenstate of I_x and that the primary noise source is dephasing, i.e., the longitudinal relaxation time T_1 is much longer than the dephasing time T_2.

The phases acquired by nuclear spins have an average value of zero, as shown in Eq (6.7), indicating that the optimal measurement basis for the spectator qubit is the Pauli Y-basis. However, the assumption of zero mean may not hold in practice and the optimal spectator measurement basis may vary. Hence, we sweep the measurement basis of the spectator qubit to determine the optimal one in our experiment. To do this, we rotate the spectator qubit around the Z-axis by an angle before measuring it in the X-basis, and we sweep the value of this angle.

For each value of N, we determine three Bloch vector lengths of the memory qubit. Two of them are conditioned on the two spectator measurement outcomes, and the third one is unconditional. The optimal measurement basis yields the longest conditional Bloch vector lengths. In Fig 6.7, we plot the weighted average of the conditional Bloch vector lengths, which corresponds to the upper bound of the data qubit fidelity that we can recover using the information provided by the spectator measurement.

6.5.2. MEMORY DECOHERENCE WITHOUT SPECTATORS

Our experiment initiates by implementing a T_2 measurement on the nuclear spins, where we express the time in units of time one entanglement attempt take. We prepare the data qubit in the +1 eigenstate of the spin-1/2 operator I_x, and evaluate its decay by monitoring the decrease in its Bloch vector length with an increase in the number of entanglement attempts.

It is important to note that during each experimental round, a π pulse is applied to the data qubit after $N/2$ attempts to cancel quasi-static noise and extend the coherence time of the nuclear spin. Even after a total experiment time that is required to perform $N = 600$ entanglement attempts, the coherence of the data qubit is preserved to a significant extent. This suggests that natural nuclear spin dephasing, characterized by T_2 under echo, does not constitute a limiting factor in our experiments.

We then include the electronic spin reset and microwave pulses required by the entanglement generation protocols, and measure the decay of the data qubit again. As
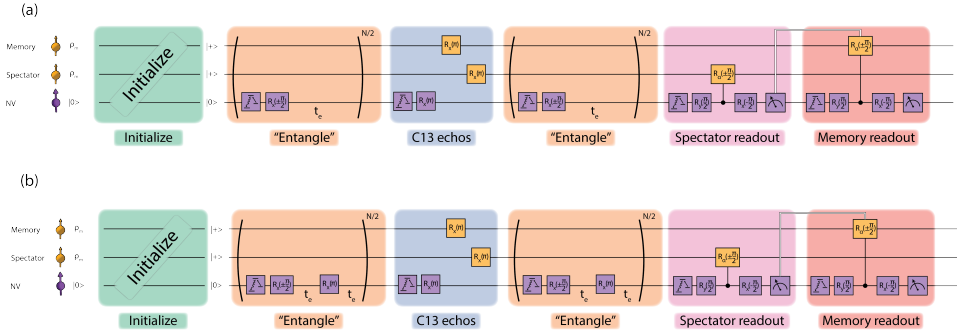
Figure 6.6: Pulse sequences for implementing remote entangling protocols with a single spectator qubit. See Appendix 6.7.1 for more details on the entangling protocols. The pulses for creating spin-photon entanglement are not implemented, as the probability of the electronic spin state being altered during this process is expected to be negligible. The spectator qubit is measured in the Pauli-Y basis, and the measurement outcome is used to compensate for the random phase acquired by the memory qubit after entanglement. Echo pulses on the carbon nuclear spins are used to cancel their quasi-static noise and the average phase due to the entangling attempts. (a) In each entangling attempt, the electronic spin is initially prepared in the $m_s = 0$ state and then a microwave pulse rotates it into a superposition of $m_s = 0$ and $m_s = -1$. (b) In each entangling attempt, an additional echo pulse is applied to the electronic spin to mitigate decoherence of nearby nuclear spins. Note that this additional echo pulse is mandatory for the double-click protocol.

6

expected, the inclusion of these entanglement operations significantly reduces the coherence time of the data qubit, as indicated by the black lines in Fig 6.7. In this case, the coherence of the data qubit is almost lost after a few hundred entanglement attempts.

However, the adverse effects of the entanglement operations can be mitigated by incorporating microwave π pulses, as shown in Fig 6.6(b). Therefore, the data qubit fidelity can withstand a larger number of entangling attempts compared to the implementation of the sequence in Fig 6.6(a), where the microwave π pulses are removed from each entangling attempt. We expect that this is mainly because these π pulses effectively reduce the uncertainty of the correlated phases accumulated by the nuclear spins during the waiting periods, as discussed in chapter 6.3.1.

6.5.3. Mitigating decoherence using a spectator qubit

To investigate whether incorporating a spectator qubit can mitigate the issue of entangling operations limiting data qubit coherence, we initialize both the data and spectator qubit in the +1 eigenstate of the spin-1/2 spin operator I_x and implement pulse sequences in Fig 6.6 with varying numbers of entangling attempts N.

In Fig 6.7(a) the memory decay becomes slower when the spectator information is used. This indicates that correlated dephasing noise is important and is mitigated. The initial loss of fidelity ($N = 0$) is probably mostly due to the imperfect initialization/measurement of the spectator qubit and the corresponding disturbance on the data qubit. However, in Fig 6.7(b), the use of spectator information does not show an improvement over not using the spectator qubit when an echo pulse is implemented on the electronic spin in each entanglement attempt.
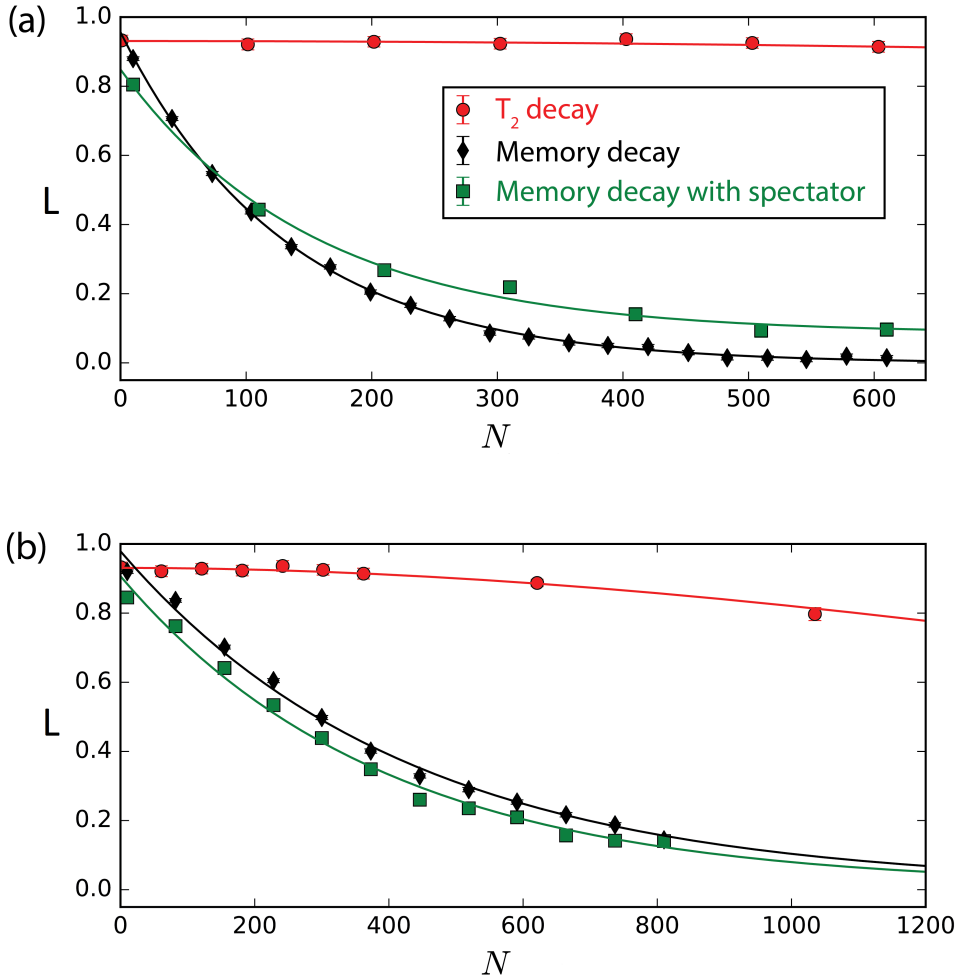
Figure 6.7: Preliminary experimental results examining the use of a single spectator qubit for improving the memory qubit coherence during remote entanglement generation. The error bars indicate one standard deviation of uncertainty. The red dots show the T_2 decay of the memory qubit in the absence of entangling operations, where the electronic spin remains in the $m_s = 0$ state and is not manipulated during each entangling attempt. The black rhombus labeled as "memory decay" represents the decay of the memory qubit under entangling operations, which involve resetting the electronic spin and applying microwave pulses. Both decays involve only the memory qubit, which is initialized in an equal superposition of its $m_s = \pm 1/2$ states. The green squares represent measurements of memory decay when the information provided by a spectator qubit measurement is incorporated. The X-axis shows the number of entangling attempts N, and the Y-axis shows the Bloch vector length L of the memory qubit given in Eq (6.19). Note that when the spectator information is used, the Y-axis is the average value of the Bloch vector length conditioning on the spectator measurement outcome. (a) The pulse sequence shown in Fig 6.6(a) is utilized to simulate the entangling protocol depicted in Fig 6.2 with the microwave π pulses removed in each entangling attempt. In the absence of the π pulses, the use of spectator qubits results in improved coherence of the memory qubit, particularly when the number of entangling attempts is large. However, if the number of entangling attempts is small, the spectator qubit may introduce additional noise due to its initialization and measurement processes, as discussed in Chapter 6.3.1. (b) The pulse sequence shown in Fig 6.6(b) is utilized to assess the performance of spectator qubits while emulating the entangling protocol depicted in Fig 6.2 with the microwave π pulses included. In the presence of these π pulses, the use of a spectator qubit systematically reduces the coherence of the memory qubit, regardless of the number of entangling attempts. This suggests that these π pulses may remove the correlated noise, and the use of a spectator qubit cannot mitigate the remaining independent noise.

One hypothesis for the preliminary experiments is that the echo pulse on the electronic spin removes most of the correlated dephasing noise on the nuclear spins, so that the depolarization due to $A_\perp$ becomes relatively more significant. This can be verified in future work by numerical simulations and by repeating the experiments with nuclear spins with much smaller $A_\perp$. We note that such depolarization caused by non-zero $A_\perp$ can be greatly reduced by operating at higher magnetic fields. In any case, a more quantitative analysis is needed, which would require a comparison with a theoretical simulation that takes into account other imperfections, such as initialization and measurement errors, the perturbation of the data qubit by spectator measurements, and the effect of the perpendicular hyperfine component $A_\perp$.

6.6. Discussion

We have investigated the potential of using spectator qubits to enhance memory robustness in the context of building a quantum network using NV centers in diamond. This approach is not only experimentally simpler, but also complementary to other memory enhancement techniques. Unlike quantum error correction and decoherence-protected subspaces, both of which require high-fidelity control of the involved qubits, spectator qubits operate without direct interaction with the data qubits, requiring only single-qubit initialization and readout.

The use of spectator qubits is similar to dynamic decoupling techniques in that simple operations are used to mitigate noise. Due to the experimental simplicity, even nuclear spins with relatively low control fidelity may be suitable as spectator qubits. Furthermore, the information obtained from spectator measurements can be used to protect multiple data qubits simultaneously at no additional cost. This is particularly desirable for many advanced quantum network applications, such as entanglement distillation and surface code stabilizer measurements [18, 33, 40]. However, the usefulness of spectators is somewhat limited due to the less compelling nature of spatially correlated noise. Conversely, as explained in chapter 3.3, dynamical decoupling techniques are effective against gradually evolving noise over time, which is ubiquitous across platforms.

Our numerical simulations have shown that the use of spectator qubits can offer significant advantages when spatially correlated dephasing is the dominant source of noise, i.e., by performing seven single-qubit initializations and measurements, we observe a remarkable improvement in the fidelity of the data qubit, from about 0.5 to 0.9. However, our preliminary experimental results suggest that such a significant improvement may be difficult to observe in practice due to other imperfections. Further quantitative analysis is required before any conclusions can be drawn.

6.7. Appendix

6.7.1. Remote entangling protocols

In this section, we present the theoretical description of the single-click and double-click entangling protocols that can be used to entangle multiple NV centers.

SINGLE-CLICK PROTOCOL

The first protocol, referred to as the "single-click" protocol, relies on only detecting one emitted photon [15, 24]. In this protocol, both electronic spins in the nodes A and B are first initialized in the $m_s = 0$ state using the optical spin pump. Then, a microwave pulse is applied to rotate the spins into an superposition state given by

$$|e\rangle_{A/B} = \sqrt{\alpha}\,|\downarrow_{A/B}\rangle + \sqrt{1-\alpha}\,|\uparrow_{A/B}\rangle,$$

where $|\downarrow\rangle$ ($|\uparrow\rangle$) represents the electronic spin state with $m_s = 0$ ($m_s = -1$), and the subscripts A and B label the NV centers.

Then we selectively excite the electronic spin in $|\downarrow\rangle$ to the excited states, which quickly decays with a photon being emitted. This optical process creates an entangled state between the electronic spin and the emitted photon, which is given by

$$\left|e, \text{photon}\right\rangle_{A/B} = \sqrt{\alpha}\,|\downarrow_{A/B}\rangle\,|1_{A/B}\rangle + \sqrt{1-\alpha}\,|\uparrow_{A/B}\rangle\,|0_{A/B}\rangle,$$

where $|0\rangle$ and $|1\rangle$ represent the absence and presence of a photon, respectively.

To minimize the probability of ISC-induced flipping of the electronic spin during the optical process described above, a specific optical transition with much reduced ISC-rate is selected. This transition is between the ground state $|\downarrow\rangle$ ($m_s = 0$), and the excited state $|E_x\rangle$. Additionally, to avoid inducing phonons modes that will disrupt the resulting entangled state between the electronic spin and the emitted photon, it is necessary for the photon to be emitted into the zero phonon line (ZPL). These issues have been discussed in Chap 3.1.2 and Chap 3.1.3.

The two emitted photons from two nodes then go into a 50 : 50 beam splitter, whose effect can be described as a unitary transformation:

$$\hat{a}_C^\dagger = \frac{1}{\sqrt{2}}(\hat{a}_A^\dagger + \hat{a}_B^\dagger), \qquad \hat{a}_D^\dagger = \frac{1}{\sqrt{2}}(\hat{a}_A^\dagger - \hat{a}_B^\dagger), \tag{6.20}$$

where $\hat{a}^\dagger$ is the creation operator. The subscripts A/B also denote the input ports of the beam splitter, while the subscripts C and D represent the output ports.

After the photons interfere at the beam splitter, the total state of the spin-photon system is given in the form (sorted by the number of photons),

$$\begin{aligned}
|\Psi\rangle = {}&(1-\alpha)\,|\uparrow_A\uparrow_B\rangle\,|0_A0_B\rangle \\
&+ \sqrt{\alpha(1-\alpha)/2}\,\left(|\uparrow_A\downarrow_B\rangle + |\downarrow_A\uparrow_B\rangle\right)\,|1_C0_D\rangle \\
&+ \sqrt{\alpha(1-\alpha)/2}\,\left(|\uparrow_A\downarrow_B\rangle - |\downarrow_A\uparrow_B\rangle\right)\,|0_C1_D\rangle \\
&+ \alpha/\sqrt{2}\,|\downarrow_A\downarrow_B\rangle\,\left(|2_C0_D\rangle + |0_C2_D\rangle\right).
\end{aligned} \tag{6.21}$$

The beam splitter erases the which-path information of the photons, detection of a single photon thus heralds the generation of a maximally entangled state of the electronic spins (the $\pm$ sign depends on the output port where the photon detector clicks),

$$|\phi_\pm\rangle = \frac{1}{\sqrt{2}}\left(|\uparrow_A\downarrow_B\rangle \pm |\downarrow_A\uparrow_B\rangle\right). \tag{6.22}$$

In the high photon-loss regime, the probability of detecting two emitted photons simultaneously is negligible. Therefore, when both electronic spins are in $|\downarrow\downarrow\rangle$, only one of the emitted photons can be detected and the other will be lost. In this case, a photon detection click falsely heralds the entanglement generation. As a consequence, the heralded output state is a mixed state, which is described by the density matrix,

$$\rho_\pm = (1-\alpha)\left|\phi_\pm\right\rangle\left\langle\phi_\pm\right| + \alpha\left|\downarrow_A\downarrow_B\right\rangle\left\langle\downarrow_A\downarrow_B\right|. \tag{6.23}$$

There is a trade-off between the generation rate and the state fidelity: increasing the parameter α leads to a higher probability of detecting an emitted photon, while the output state fidelity is decreased.

DOUBLE-CLICK PROTOCOL

The second protocol requires detecting two photons, which is hence called the double-click protocol [6, 24]. In this protocol, both electronic spins are first prepared in the equal superposition of the $m_s = 0, -1$ states. Then an optical pulse is first applied to excite the electronic spin in the state $|\downarrow\rangle$, which quickly decays back to $|\downarrow\rangle$ with a photon emitted. Subsequently, a microwave π pulse flips the electronic spin state. At the end, the same optical pulse is applied again so that another photon is emitted. Note that, these two photons must be emitted into the ZPL, and the selected optical transition is the same as the single-click protocol due to its reduced ISC rate.

The photon emitted before the π pulse is said to be in the early time-bin, while the other one is said to be emitted into the late time-bin. The two time-bins are labeled using the subscripts E and L, respectively. The procedure described above prepares a spin-photon entangled state in each NV center, i.e.,

$$\left|e, \text{photon}\right\rangle_{A/B} = \frac{1}{\sqrt{2}}(\left|\downarrow_{A/B}\right\rangle\left|1_{A/B, E}\right\rangle + \left|\uparrow_{A/B}\right\rangle\left|1_{A/B, L}\right\rangle),$$

For convenience, we explicitly write down the state for the two NV centers, i.e.,

$$\left|e, \text{photon}\right\rangle = \frac{1}{2}\left[\left|\downarrow_A\downarrow_B\right\rangle\left|1_{A,L}1_{B,L}\right\rangle + \left|\downarrow_A\uparrow_B\right\rangle\left|1_{A,L}1_{B,E}\right\rangle + \left|\uparrow_A\downarrow_B\right\rangle\left|1_{A,E}1_{B,L}\right\rangle + \left|\uparrow_A\uparrow_B\right\rangle\left|1_{A,E}1_{B,E}\right\rangle\right].$$

Same as the single-click protocol, the emitted photons are sent into the 50:50 beam splitter. According to Eq (6.21), we have the state transformations:

$$\left|1_{A, E/L}\right\rangle \rightarrow \frac{1}{\sqrt{2}}\left(\left|1_{C, E/L}\right\rangle + \left|1_{D, E/L}\right\rangle\right), \qquad \left|1_{B, E/L}\right\rangle \rightarrow \frac{1}{\sqrt{2}}\left(\left|1_{C, E/L}\right\rangle - \left|1_{D, E/L}\right\rangle\right). \tag{6.24}$$

If two photons are in the same time-bin, both photons can only appear in the same output port of the beam splitter, i.e.,

$$\left|1_{A, E}, 1_{B, E}\right\rangle \rightarrow \frac{1}{\sqrt{2}}\left(\left|2_{C, E}\right\rangle - \left|2_{D, E}\right\rangle\right) \qquad \left|1_{A, L}, 1_{B, L}\right\rangle \rightarrow \frac{1}{\sqrt{2}}\left(\left|2_{C, L}\right\rangle - \left|2_{D, L}\right\rangle\right), \tag{6.25}$$

which is the so-called Hong-Ou-Mandel effect. For two photons in different time-bins, the output states are given by

$$\left|1_{A, E}1_{B, L}\right\rangle \rightarrow \frac{1}{2}\left(\left|1_{C, E}1_{C, L}\right\rangle - \left|1_{C, E}1_{D, L}\right\rangle + \left|1_{D, E}1_{C, L}\right\rangle - \left|1_{D, E}1_{D, L}\right\rangle\right),$$
$$\left|1_{A, L}1_{B, E}\right\rangle \rightarrow \frac{1}{2}\left(\left|1_{C, E}1_{C, L}\right\rangle + \left|1_{C, E}1_{D, L}\right\rangle - \left|1_{D, E}, 1_{C, L}\right\rangle - \left|1_{D, E}1_{D, L}\right\rangle\right). \tag{6.26}$$

The final spin-photon state of the two nodes after the beam splitter is then given by

$$
\begin{aligned}
|\psi\rangle = \frac{\sqrt{2}}{4}\Big[& |\psi_+\rangle\Big(|1_{C,E}1_{C,L}\rangle - |1_{D,E}1_{D,L}\rangle\Big) + |\downarrow_A\downarrow_B\rangle\Big(|2_{C,L}\rangle - |2_{D,L}\rangle\Big) \\
 + & |\psi_-\rangle\Big(|1_{D,E}1_{C,L}\rangle - |1_{C,E}1_{D,L}\rangle\Big) + |\uparrow_A\uparrow_B\rangle\Big(|2_{C,E}\rangle - |2_{D,E}\rangle\Big)\Big].
\end{aligned}
\tag{6.27}
$$

The maximal entangled states $|\psi_\pm\rangle = \big(|\uparrow_A\downarrow_B\rangle \pm |\downarrow_A\uparrow_B\rangle\big)/\sqrt{2}$ are obtained when detecting two photons that are in different time-bins.

Unlike the single-click protocol, the double-click protocol does not require advanced phase stabilization techniques to minimize the uncertainty of the differences in the optical phase acquired by the emitted photons (which are neglected in this discussion) [6, 24]. However, the double-click protocol requires the detection of photons twice, resulting in a success rate as low as 10^{-8}, which presents a significant challenge for the creation of additional remotely entangled pairs while storing the quantum states [27, 29, 37, 44]

References

[1] M. H. Abobeih, J. Cramer, M. A. Bakker, N. Kalb, M. Markham, D. J. Twitchen, and T. H. Taminiau. One-second coherence for a single electron spin coupled to a multi-qubit nuclear-spin environment. *Nat. Commun.*, 9(1):2552, 2018.

[2] M. H. Abobeih, J. Randall, C. E. Bradley, H. P. Bartling, M. A. Bakker, M. J. Degen, M. Markham, D. J. Twitchen, and T. H. Taminiau. Atomic-scale imaging of a 27-nuclear-spin cluster using a quantum sensor. *Nature*, 576(7787):411–415, 2019.

[3] M. H. Abobeih, Y. Wang, J. Randall, S. J. H. Loenen, C. E. Bradley, M. Markham, D. J. Twitchen, B. M. Terhal, and T. H. Taminiau. Fault-tolerant operation of a logical qubit in a diamond quantum processor. *Nature*, 606(7916):884–889, 2022.

[4] S. Akibue and M. Murao. Network Coding for Distributed Quantum Computation Over Cluster and Butterfly Networks. *IEEE Trans. Inf. Theory*, 62(11):6620–6637, 2016.

[5] J.-D. Bancal, S. Pironio, A. Acín, Y.-C. Liang, V. Scarani, and N. Gisin. Quantum non-locality based on finite-speed causal influences leads to superluminal signalling. *Nat. Phys.*, 8(12):867–870, 2012.

[6] S. D. Barrett and P. Kok. Efficient high-fidelity quantum computation using matter qubits and linear optics. *Phys. Rev. A*, 71:060310, 2005.

[7] H. P. Bartling, M. H. Abobeih, B. Pingault, M. J. Degen, S. J. H. Loenen, C. E. Bradley, J. Randall, M. Markham, D. J. Twitchen, and T. H. Taminiau. Entanglement of spin-pair qubits with intrinsic dephasing times exceeding a minute. *Phys. Rev. X*, 12:011048, 2022.

[8] S. Barz, E. Kashefi, A. Broadbent, J. F. Fitzsimons, A. Zeilinger, and P. Walther. Demonstration of blind quantum computing. *Science*, 335(6066):303–308, 2012.

6

[9] H. Bernien, B. Hensen, W. Pfaff, G. Koolstra, M. Blok, L. Robledo, T. H. Taminiau, M. Markham, D. J. Twitchen, L. Childress, and R. Hanson. Heralded entanglement between solid-state qubits separated by three metres. *Nature*, 497(7447):86–90, 2013.

[10] D. W. Berry, H. M. Wiseman, and J. K. Breslin. Optimal input states and feedback for interferometric phase estimation. *Phys. Rev. A*, 63:053804, 2001.

[11] M. S. Blok, N. Kalb, A. Reiserer, T. H. Taminiau, and R. Hanson. Towards quantum networks of single spins: analysis of a quantum memory with an optical interface in diamond. *Faraday Discuss.*, 184:173–182, 2015.

[12] J. M. Boss, K. Chang, J. Armijo, K. Cujia, T. Rosskopf, J. R. Maze, and C. L. Degen. One- and two-dimensional nuclear magnetic resonance spectroscopy with a diamond quantum sensor. *Phys. Rev. Lett.*, 116:197601, 2016.

[13] C. E. Bradley, S. W. de Bone, P. F. W. Möller, S. Baier, M. J. Degen, S. J. H. Loenen, H. P. Bartling, M. Markham, D. J. Twitchen, R. Hanson, D. Elkouss, and T. H. Taminiau. Robust quantum-network memory based on spin qubits in isotopically engineered diamond. *NPJ Quantum Inf.*, 8(1):1–9, 2022.

[14] C. E. Bradley, J. Randall, M. H. Abobeih, R. C. Berrevoets, M. J. Degen, M. A. Bakker, M. Markham, D. J. Twitchen, and T. H. Taminiau. A ten-qubit solid-state spin register with quantum memory up to one minute. *Phys. Rev. X*, 9:031045, 2019.

[15] C. Cabrillo, J. I. Cirac, P. García-Fernández, and P. Zoller. Creation of entangled states of distant atoms by interference. *Phys. Rev. A*, 59:1025–1033, 1999.

[16] J. P. Clemens, S. Siddiqui, and J. Gea-Banacloche. Quantum error correction against correlated noise. *Phys. Rev. A*, 69:062313, 2004.

[17] S. Daiss, S. Langenfeld, S. Welte, E. Distante, P. Thomas, L. Hartung, O. Morin, and G. Rempe. A quantum-logic gate between distant quantum-network modules. *Science*, 371(6529):614–617, 2021.

[18] S. de Bone, R. Ouyang, K. Goodenough, and D. Elkouss. Protocols for Creating and Distilling Multipartite GHZ States With Bell Pairs. *IEEE trans.quantum eng.*, 1:1–10, 2020.

[19] A. Delteil, Z. Sun, W.-B. Gao, E. Togan, S. Faelt, and A. Imamoğlu. Generation of heralded entanglement between distant hole spins. *Nat. Phys.*, 12(3):218–223, 2015.

[20] B. Desef and M. B. Plenio. Optimizing quantum codes with an application to the loss channel with partial erasure information. *Quantum*, 6(667):667, 2022.

[21] M. W. Doherty, N. B. Manson, P. Delaney, F. Jelezko, J. Wrachtrup, and L. C. L. Hollenberg. The nitrogen-vacancy colour centre in diamond. *Phys. Rep.*, 528(1):1–45, 2013.

[22] L.-M. Duan and C. Monroe. Colloquium: Quantum networks with trapped ions. *Rev Mod Phys*, 82:1209–1224, 2010.

[23] A. Ekert and R. Renner. The ultimate physical limits of privacy. *Nature*, 507(7493):443–447, 2014.

[24] K. Goodenough, D. Elkouss, and S. Wehner. Optimizing repeater schemes for the quantum internet. *Phys. Rev. A*, 103:032610, 2021.

[25] D. Gottesman, T. Jennewein, and S. Croke. Longer-baseline telescopes using quantum repeaters. *Phys. Rev. Lett.*, 109:070503, 2012.

[26] R. S. Gupta, L. C. G. Govia, and M. J. Biercuk. Integration of spectator qubits into quantum computer architectures for hardware tune-up and calibration. *Phys. Rev. A*, 102:042611, 2020.

[27] B. Hensen, H. Bernien, A. E. Dréau, A. Reiserer, N. Kalb, M. S. Blok, J. Ruitenberg, R. F. L. Vermeulen, R. N. Schouten, C. Abellán, W. Amaya, V. Pruneri, M. W. Mitchell, M. Markham, D. J. Twitchen, D. Elkouss, S. Wehner, T. H. Taminiau, and R. Hanson. Loophole-free Bell inequality violation using electron spins separated by 1.3 kilometres. *Nature*, 526(7575):682–686, 2015.

[28] S. Hermans. *Quantum Networks using Spins in Diamond*. PhD thesis, QuTech, Delft University of Technology, 2022.

[29] S. L. N. Hermans, M. Pompili, H. K. C. Beukers, S. Baier, J. Borregaard, and R. Hanson. Qubit teleportation between non-neighbouring nodes in a quantum network. *Nature*, 605(7911):663–668, 2022.

[30] J. Hofmann, M. Krug, N. Ortegel, L. Gérard, M. Weber, W. Rosenfeld, and H. Weinfurter. Heralded entanglement between widely separated atoms. *Science*, 337(6090):72–75, 2012.

[31] P. C. Humphreys, N. Kalb, J. P. J. Morits, R. N. Schouten, R. F. L. Vermeulen, D. J. Twitchen, M. Markham, and R. Hanson. Deterministic delivery of remote entanglement on a quantum network. *Nature*, 558(7709):268–273, 2018.

[32] N. Kalb, P. C. Humphreys, J. J. Slim, and R. Hanson. Dephasing mechanisms of diamond-based nuclear-spin memories for quantum networks. *Phys. Rev. A*, 97:062330, 2018.

[33] N. Kalb, A. A. Reiserer, P. C. Humphreys, J. J. W. Bakermans, S. J. Kamerling, N. H. Nickerson, S. C. Benjamin, D. J. Twitchen, M. Markham, and R. Hanson. Entanglement distillation between solid-state quantum network nodes. *Science*, 356(6341):928–932, 2017.

[34] P. Kómár, E. M. Kessler, M. Bishof, L. Jiang, A. S. Sørensen, J. Ye, and M. D. Lukin. A quantum network of clocks. *Nat. Phys.*, 10(8):582–587, 2014.

6

[35] D. Layden, M. Chen, and P. Cappellaro. Efficient quantum error correction of dephasing induced by a common fluctuator. *Phys. Rev. Lett.*, 124:020504, 2020.

[36] D. A. Lidar, I. L. Chuang, and K. B. Whaley. Decoherence-free subspaces for quantum computation. *Phys. Rev. Lett.*, 81:2594–2597, 1998.

[37] M. Lucamarini, Z. L. Yuan, J. F. Dynes, and A. J. Shields. Overcoming the rate-distance limit of quantum key distribution without quantum repeaters. *Nature*, 557(7705):400–403, 2018.

[38] S. Majumder, L. Andreta de Castro, and K. R. Brown. Real-time calibration with spectator qubits. *NPJ Quantum Inf.*, 6(1):1–9, 2020.

[39] D. L. Moehring, P. Maunz, S. Olmschenk, K. C. Younge, D. N. Matsukevich, L.-M. Duan, and C. Monroe. Entanglement of single-atom quantum bits at a distance. *Nature*, 449(7158):68–71, 2007.

[40] N. H. Nickerson, J. F. Fitzsimons, and S. C. Benjamin. Freely scalable quantum technologies using cells of 5-to-50 qubits with very lossy and noisy photonic links. *Phys. Rev. X*, 4:041041, 2014.

[41] J. L. Orrell and B. Loer. Sensor-assisted fault mitigation in quantum computation. *Phys. Rev. Applied*, 16:024025, 2021.

[42] Y. Ouyang. Avoiding coherent errors with rotated concatenated stabilizer codes. *NPJ Quantum Inf.*, 7(1):1–7, 2021.

[43] M. Pompili, C. Delle Donne, I. te Raa, B. van der Vecht, M. Skrzypczyk, G. Ferreira, L. de Kluijver, A. J. Stolk, S. L. N. Hermans, P. Pawełczak, W. Kozlowski, R. Hanson, and S. Wehner. Experimental demonstration of entanglement delivery using a quantum network stack. *NPJ Quantum Inf.*, 8(1):1–10, 2022.

[44] M. Pompili, S. L. N. Hermans, S. Baier, H. K. C. Beukers, P. C. Humphreys, R. N. Schouten, R. F. L. Vermeulen, M. J. Tiggelman, L. Dos Santos Martins, B. Dirkse, S. Wehner, and R. Hanson. Realization of a multinode quantum network of remote solid-state qubits. *Science*, 372(6539):259–264, 2021.

[45] A. Reiserer, N. Kalb, M. S. Blok, K. J. M. van Bemmelen, T. H. Taminiau, R. Hanson, D. J. Twitchen, and M. Markham. Robust quantum-network memory using decoherence-protected subspaces of nuclear spins. *Phys. Rev. X*, 6:021040, 2016.

[46] S. Ritter, C. Nölleke, C. Hahn, A. Reiserer, A. Neuzner, M. Uphoff, M. Mücke, E. Figueroa, J. Bochmann, and G. Rempe. An elementary quantum network of single atoms in optical cavities. *Nature*, 484(7393):195–200, 2012.

[47] J. Rubio, P. A. Knott, T. J. Proctor, and J. A. Dunningham. Quantum sensing networks for the estimation of linear functions. *J. Phys. A: Math. Theor.*, 53(34):344001, 2020.

[48] L. J. Stephenson, D. P. Nadlinger, B. C. Nichol, S. An, P. Drmota, T. G. Ballance, K. Thirumalai, J. F. Goodwin, D. M. Lucas, and C. J. Ballance. High-rate, high-fidelity entanglement of qubits across an elementary quantum network. *Phys. Rev. Lett.*, 124:110501, 2020.

[49] R. Stockill, M. J. Stanley, L. Huthmacher, E. Clarke, M. Hugues, A. J. Miller, C. Matthiesen, C. Le Gall, and M. Atatüre. Phase-tuned entangled state generation between distant spin qubits. *Phys. Rev. Lett.*, 119:010503, 2017.

[50] T. H. Taminiau, J. J. T. Wagenaar, T. van der Sar, F. Jelezko, V. V. Dobrovitski, and R. Hanson. Detection and control of individual nuclear spins using a weakly coupled electron spin. *Phys. Rev. Lett.*, 109:137602, 2012.

[51] B. M. Terhal and D. Weigand. Encoding a qubit into a cavity mode in circuit qed using phase estimation. *Phys. Rev. A*, 93:012315, 2016.

[52] B. Tonekaboni, A. Chantasri, H. Song, Y. Liu, and H. M. Wiseman. Greedy versus map-based optimized adaptive algorithms for random-telegraph-noise mitigation by spectator qubits. *Phys. Rev. A*, 107:032401, 2023.

[53] A. Youssry, G. A. Paz-Silva, and C. Ferrie. Noise detection with spectator qubits and quantum feature engineering. *New J. Phys.*, 25(7):073004, 2023.

6

7

PREPARING DICKE STATES IN A SPIN ENSEMBLE USING PHASE ESTIMATION

We present a Dicke state preparation scheme which uses global control of N spin qubits: our scheme is based on the standard phase estimation algorithm, which estimates the eigenvalue of a unitary operator. The scheme prepares a Dicke state non-deterministically by collectively coupling the spins to an ancilla qubit via a ZZ-interaction, using $\lceil \log_2 N \rceil + 1$ ancilla qubit measurements. The preparation of such Dicke states can be useful if the spins in the ensemble are used for magnetic sensing: we discuss a possible realization using an ensemble of electronic spins located at diamond nitrogen-vacancy centers coupled to a single superconducting flux qubit. We also analyze the effect of noise and limitations in our scheme.

7.1. Introduction

A promising application of the emerging quantum technology is quantum-enhanced sensing, sometimes referred to as quantum metrology [15, 56]. Using entangled states, one can, in principle, improve the measurement sensitivity from the standard quantum limit ($1/\sqrt{N}$) to the Heisenberg limit ($1/N$) [15, 21, 22], where N is the number of probes or repetitions. However, preserving this quantum advantage is difficult in the presence of decoherence [16]. For instance, a single-qubit Pauli Z-error can totally dephase a N-qubit GHZ-state, which would obtain Heisenberg-limited sensitivity in the noiseless case [55].

N-qubit Dicke states form a class of entangled states which are interesting for metrology [3, 23, 48, 55, 65]. Compared to other states used in quantum sensing, Dicke states have been argued to be more robust to various noise sources such as spin dephasing, spin damping, and spin number fluctuations [65]. Recent work has demonstrated a scheme to use Dicke states for detecting the magnetic field induced by a single spin [23]. Another distinctive feature of the use of Dicke states is that the optimal sensitivity can be obtained through only global control on the set of spins [3, 65]. This is relevant for realizing practical quantum sensing using entangled states, as precise individual spin qubit control can be difficult. Furthermore, superpositions of Dicke states can be used for quantum error correction [43, 47].

Dicke state preparation has been experimentally realized using photons [30, 60] and trapped-ion qubits [25, 40], and there also exist many theoretical preparation proposals suitable for a few qubits, see Ref. [19, 26, 33, 61] for example. However, it remains a challenge for large spin ensembles like $N > O(100)$ diamond Nitrogen-Vacancy centers (negatively-charged NV [1]), each hosting an electronic spin $S = 1$. Since these NV center spins are rather isolated from each other, it is costly to perform entangling gates between the electronic spins [17, 18, 38]. This limitation excludes quantum algorithms for preparing Dicke states which are based on the full addressability of the qubits [8, 37]. To address this issue, some work has been dedicated to schemes which require only a global control of the spin ensemble, such as using steady state evolution [36], repeated energy transfer [23], continuous weak measurements [51], and the use of geometric phase gates [29]. Unfortunately, these methods are still demanding currently when N is large, as they often need complicated measurement-based feedback, high fidelity control and long preparation times. For example, the optimized scheme in Ref. [23] uses $O(N)$ rounds of initialization and evolution of an ancilla qubit. Our goal is to improve the scaling with N so that one could possibly handle a larger error rate on the ancilla qubit.

In this chapter, we present a Dicke state preparation scheme that uses standard phase estimation [39], which prepares an eigenstate of a unitary operator by estimating its eigenvalue. This algorithm is based on executing projective measurements on the spin ensemble using an ancilla qubit, and it will prepare a random Dicke state. The scheme requires a ZZ-coupling between each spin in the ensemble to a single ancilla qubit. In Section 7.3 we detail how this coupling could be realized between an ensemble of NV electronic spins and a superconducting flux qubit as ancilla.

Our scheme is efficient with respect to the number of operations. It uses only $\lceil \log_2 N \rceil + 1$ rounds of phase estimation for preparing a random N-spin Dicke state. Each round of phase estimation measures a global operator of the spins, i.e., it applies an ancilla-qubit

controlled global $J_z = \frac{1}{2} \sum_{i=1}^{N} Z_i$ rotation followed by ancilla qubit readout. The total time for performing the controlled rotations is upper-bounded by a constant and the preparation time thus scales as $O(\log_2 N)$. With a probability $\sim O(1/\sqrt{N})$, the prepared Dicke state would obtain Heisenberg-limited sensitivity using only global control.

Besides the efficiency, our scheme also has some noise-resilience: phase estimation can be realized with integrated dynamical decoupling, which provides robustness to the dephasing of the ancilla qubit as well as the dephasing of the spins in the ensemble. Furthermore, by repeating the projective measurements and performing a simple majority vote, the effects of ancilla qubit decay and flipped measurements (due to ancilla qubit dephasing or imperfect measurement) can be mitigated.

This chapter is organized as follows. In Sec. 7.1.1, we briefly review Dicke states and Heisenberg-limited sensing. In Sec. 7.2 we present the idea of using phase estimation to prepare Dicke states. In Sec. 7.3 we discuss the Hamiltonian and a possible experimental setup with multiple NV centers coupled to a flux qubit. In Sec. 7.4 we numerically consider the performance of the scheme given the dominant noise sources. Finally, we discuss the results in Sec. 7.5.

7.1.1. DICKE STATES
For simplicity, we assume even spin number N throughout this chapter (odd spin-number N can be treated similarly). The N-spin (or qubit) Dicke state $|N, m_z\rangle$ with $m_z \in \{-\frac{N}{2}, \ldots, \frac{N}{2}\}$ is a uniform, permutation-symmetric, superposition of N-bit strings $|x\rangle$ where all bit-strings have $N/2 + m_z$ spins in $|0\rangle$, i.e., their Hamming weight is $N/2 - m_z$. For example, $|N = 4, m_z = 0\rangle = \frac{1}{\sqrt{6}}(|0011\rangle + |0101\rangle + |0110\rangle + |1001\rangle + |1010\rangle + |1100\rangle)$. A Dicke state $|N, m_z\rangle$ is an eigenstate of the collective spin operator

$$J_z = \frac{1}{2} \sum_{i=1}^{N} Z_i, \tag{7.1}$$

with eigenvalue m_z. Here Z_i is the Pauli Z operator on the spin labeled i. In addition, we have $J_x = \frac{1}{2} \sum_{i=1}^{N} X_i$ and $J_y = \frac{1}{2} \sum_{i=1}^{N} Y_i$.

To use such states for metrology, one imagines that the prepared quantum state is transformed by $e^{-i\theta J_y}$ and the goal is to estimate the rotation angle θ which is assumed to be small. A standard metrological method (for NV centers, limited by T_2 and optical measurement accuracy) is Ramsey spectroscopy [6] using a single qubit state repeatedly (or, equivalently, using a product state of multiple qubits). In this context, the Ramsey method corresponds to preparing a simple product state $e^{i\frac{\pi}{2} J_y} |00\ldots0\rangle$ and letting it thus evolve to $e^{-i(\theta - \frac{\pi}{2}) J_y} |00\ldots0\rangle = (\frac{1}{\sqrt{2}}(|+\rangle_Y + e^{i(\theta - \frac{\pi}{2})} |-\rangle_Y)^{\otimes N}$. The rotation angle θ can then be estimated by measuring each spin in Z-basis. The measurements give the expectation value $\langle J_z(\theta) \rangle = \frac{N}{2} \sin(\theta)$, which is most sensitive to small perturbations of θ around $\theta = 0$ [15]. The sensitivity of a product state is limited by the standard quantum limit, i.e., the variance in θ scales as $(\Delta\theta)^2 \sim 1/N$. It has been argued that Dicke states for $m_z = O(1)$ can reach the Heisenberg-limited sensitivity (i.e., $(\Delta\theta)^2 \sim 1/N^2$), as follows.

In general, one will measure some operator $\mathcal{M}$ on the final state $\exp(-i\theta J_y)|N, m_z\rangle$ to estimate the value of θ. The variance of θ can be calculated by the error propagation

formula

$$(\Delta\theta)^2 = \frac{(\Delta\mathcal{M}(\theta))^2}{|\partial_\theta \langle\mathcal{M}(\theta)|\mathcal{M}(\theta)\rangle|^2}, \tag{7.2}$$

where the expectation value is with respect to the initial state $|N, m_z\rangle$ and $\mathcal{M}(\theta)$ is the Heisenberg-evolved operator. If we were to measure $\mathcal{M} = \alpha J_x + \beta J_z$, then

$$\begin{aligned}\langle\mathcal{M}(\theta)|\mathcal{M}(\theta)\rangle &= \langle J_z|J_z\rangle\,(\beta\cos(\theta) + \alpha\sin(\theta))\\ &\approx m_z(\beta + \theta\alpha),\end{aligned} \tag{7.3}$$

for small θ (note that $\langle N, m_z| J_x |N, m_z\rangle = 0$). We measure J_x by choosing $\beta = 0, \alpha = 1$, its expectation value $\langle J_x(\theta)|J_x(\theta)\rangle$ has an optimal dependence on θ when m_z is large. However, the variance $(\Delta J_x(\theta))^2$ will be large in a rotated Dicke state, precluding any Heisenberg gains.

The proposal is instead to measure $\mathcal{M} = J_z^2$, so that the variance is given by (see details in Ref. [3]):

$$\begin{aligned}(\Delta\theta)^2 = [(\Delta J_x^2)^2 f(\theta) + 4\langle J_x^2\rangle - 3\langle J_y^2\rangle\\ - 2\langle J_z^2\rangle \times (1 + \langle J_x^2\rangle) + 6\langle J_z J_x^2 J_z\rangle] / [4(\langle J_x^2\rangle - \langle J_z^2\rangle)^2]\end{aligned} \tag{7.4}$$

with $f(\theta) = \frac{(\Delta J_z^2)^2}{(\Delta J_x^2)^2 \tan^2(\theta)} + \tan^2(\theta)$. The minimal variance is obtained when $\tan^2(\theta) = \sqrt{(\Delta J_z^2)^2/(\Delta J_x^2)^2}$. For Dicke state $|N, m_z\rangle$ the minimal variance (obtained at $\theta \approx 0$) is

$$(\Delta\theta_{\min})^2 = \frac{2m_z^2 + 2}{N^2 + 2N - 12m_z^2} + \frac{64m_z^4 - 16m_z^2}{(N^2 + 2N - 12m_z^2)^2}. \tag{7.5}$$

Note that the sensitivity can surpass the standard quantum limit when $m_z \sim O(\sqrt{N})$ and is Heisenberg-limited when $m_z \sim O(1)$. In addition, when $m_z = 0$, $(\Delta\theta_{\min})^2 = \frac{2}{N(N+2)}$ saturates the quantum Cramér-Rao bound [55]. The expectation value $\langle J_z^2|J_z^2\rangle$ can in principle be obtained by measuring J_z, squaring its outcome and gathering sufficient statistics by repeating the measurements. We are thus especially interested in Dicke states close to $|N, 0\rangle$, i.e., $|N, m_z\rangle$ with $m_z \sim O(1)$. Other than this motivation, we do not focus on aspects of using a (noisy) Dicke state for metrology in this chapter.

7.2. Phase estimation preparation for Dicke states

In this section, we will show how to prepare a Dicke state using a phase estimation algorithm.

Phase estimation of a unitary operator is the process of measuring its eigenvalue and simultaneously projecting the input state to the corresponding eigenstate. This idea has for example been proposed to prepare Gottesman-Kitaev-Preskill states in a bosonic system, realized by determining the eigenvalues of two unitary operators approximately [20, 54].

For preparing Dicke states, we will start from a product state, e.g. Eq. (7.8), where all spins in the ensemble are in the same state. Such a product state is clearly already permutation-symmetric but not yet an eigenstate of J_z. Since the Dicke state $|N, m_z\rangle$
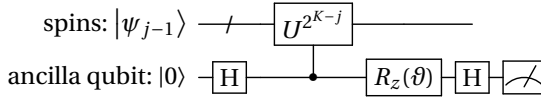
Figure 7.1: The jth round phase estimation for the unitary operator $U = e^{i2\pi J_z/2^K}$ in Eq. (7.7). This circuit projectively measures the eigenvalues of the unitary operator $U_j = e^{i\pi 2^{1-j}(J_z - A_{j-1})}$ on the input state $\left|\psi_{j-1}\right\rangle$ in Eq. (7.10). Before the measurement, the ancilla qubit is rotated around the Z-axis by the angle $\vartheta = \pi A_{j-1} 2^{1-j}$, with $A_j = \sum_{l=1}^{j} 2^{l-1} b_l$. Here $b_l = 0, 1$ is the measurement outcome of the previous measurement of U_l.

is the unique N-qubit permutation-symmetric eigenstate of the operator J_z with eigenvalue m_z, we can then prepare a Dicke state via phase estimation. This is realized by measuring the eigenvalues of a unitary operator U whose eigenvalues are in 1-1 correspondence to the eigenvalues m_z. Note that it is important to start the phase estimation scheme in the permutation-symmetric subspace, as J_z has eigenstates outside of this permutation-symmetric subspace on which we do not want to project.

Since the eigenvalue $m_z \in [-N/2, N/2]$, the integer $m_z + 2^K$ with $K = \lceil \log_2 N \rceil + 1$ is positive. To find the unitary operator for phase estimation, we write down the binary representation

$$m_z + 2^K = \sum_{l=1}^{K+1} b_l 2^{l-1}. \tag{7.6}$$

Note that the value of m_z can be unambiguously determined using the first K of $K + 1$ bits (i.e. $b_l = 0, 1$ with $l = 1, 2, \dots K$). Then the unitary operator for phase estimation is

$$U = e^{i2\pi(J_z + 2^K)/2^K} = e^{i2\pi J_z/2^K}. \tag{7.7}$$

This gives $U|N, m_z\rangle = e^{i\phi(m_z)}|N, m_z\rangle$, where $\phi(m_z) = \pi \sum_{l=1}^{K} b_l 2^{l-K}$ is indeed an 1-1 function of the first K bits in Eq. (7.6). Therefore, the preparation of a Dicke state is transformed to the task of performing phase estimation for this unitary operator U.

Using phase estimation, one cannot prepare a specific Dicke state $|N, m_z\rangle$ deterministically, as there is in general no easy operation that could transform $|N, m_z\rangle$ to $\left|N, m_z' \neq m_z\right\rangle$ [32]. However, we can easily maximize the probability of obtaining a Dicke state whose sensitivity is Heisenberg-limited. This requires starting from the product state

$$|\psi_0\rangle = \left(\frac{|0\rangle + |1\rangle}{\sqrt{2}}\right)^{\otimes N} = \sum_{m_z = -N/2}^{N/2} \sqrt{p(m_z)}|N, m_z\rangle, \tag{7.8}$$

where $p(m_z)$ is a binomial distribution with average $\langle m_z \rangle = 0$ and standard deviation $\sqrt{N}/2$ (i.e., $p(m_z) = \binom{N}{m_z + N/2}/2^N$). This distribution reaches its maximum at $m_z = 0$ and $p(m_z = 0) \approx \sqrt{2/(\pi N)}$ (using Stirling's approximation). Dicke states $|N, m_z\rangle$ with $m_z \sim O(1)$ can thus be obtained with a probability $O(1/\sqrt{N})$. To prepare these states, one would thus need to repeat the preparation $O(\sqrt{N})$ times on average.

Among many other variants [41, 54], we choose standard or 'textbook' phase estimation: standard phase estimation uses only K measurements to determine the eigenvalue

of J_z by determining the first K bits in Eq. (7.6). Furthermore, these measurements can be executed in a sequential manner, where only one ancilla qubit is required. The ancilla qubit is used as the control to apply controlled-$U^{2^{K-j}}$ gates with $j = 1, 2 \dots, K$ starting at $j = 1$, for which $U^{2^{K-1}} = \exp(i\pi J_z)$.

The circuit of the jth round phase estimation is shown in Fig. 7.1, where the ancilla qubit is measured in a basis determined by previous measurement outcomes $m_i = 0, 1$ with $i = 1, 2, \dots j - 1$. Before readout, the ancilla qubit is rotated around the Z-axis by the angle $\vartheta = \pi A_{j-1} 2^{1-j}$, where $A_j = \sum_{l=1}^{j} 2^{l-1} b_l$ (and $A_0 = 0$). The jth round phase estimation is described by the projector

$$P(b_j) = \frac{1 + (-1)^{b_j} U_j}{2},$$

$$U_j = e^{i\pi 2^{1-j}(J_z - A_{j-1})},$$

(7.9)

We note that $P(b_j = 0)P(b_j = 1) = 0$ as U_j has eigenvalues ± 1 on the space of states with given value for A_{j-1}. After j rounds of phase estimation, the spins in the ensemble are projected into a superposition of Dicke states, i.e.,

$$\begin{aligned} |\psi_j\rangle &= \frac{1}{\sqrt{\mathcal{N}_j}} P(b_j) \cdots P(b_2) P(b_1) |\psi_0\rangle \\ &= \frac{1}{\sqrt{\mathcal{N}_j}} \sum_{n \in \mathbb{Z}} \sqrt{p(2^j n + A_j)} |N, 2^j n + A_j\rangle, \end{aligned}$$

(7.10)

where $\mathcal{N}_j$ is the normalization factor. Since $|2^j n + A_j| \leq N/2$, either $n = 0$ or $n = -1$ when $j = K$. The eigenvalue of J_z is therefore unambiguously determined, i.e., for $j = K$:

$$|\psi_j\rangle = \begin{cases} |N, A_j\rangle & A_j < 2^{j-1}, \\ |N, A_j - 2^j\rangle & A_j > 2^{j-1}. \end{cases}$$

(7.11)

As the standard deviation of $p(m_z)$ is $\sqrt{N}/2$, the equality in Eq. (7.11) approximately holds when $2^j \sim O(\sqrt{N})$. This means that in fact determining only the first $\lceil K/2 \rceil$ bits in Eq. (7.6) can produce the target state with high fidelity, that is, the number of required ancilla qubit measurements can be further reduced in practice.

The controlled-$U^{2^{K-j}}$ gate is realized through the Hamiltonian in Eq. (7.13) below. The coupling strength γ between the spins and the ancilla qubit determines how fast the gate is performed. Due to the exponentially decreasing rotation angles, the total evolution time T of these controlled rotations is bounded, i.e.,

$$T = \sum_{j=1}^{K} t_j = \frac{\pi}{\gamma}(2 - \frac{1}{2^K}) < \frac{2\pi}{\gamma},$$

$$t_j = \frac{\pi}{2^{j-1}\gamma}.$$

(7.12)

Note that the preparation scheme requires initializing all qubits in $|+\rangle$ state, which can consume a considerable amount of time by itself, see Section 7.3.1 for the experimental setup with NV electronic spins.

An important comment on the use of standard phase estimation in Fig. 7.1 is the following. Any gate will be implemented with some constant (small) error in practice, hence it is impossible to realize the rotation U in Eq. (7.7) when K (and thus N) is too large. This error limits the maximum spin number N that we can handle, as the rotation angle $2\pi/2^K$ scales as $O(1/N)$. For example, for $N = 500$, we have $K = 9$ and $2\pi/2^K \approx$ 0.012, see also a further discussion in Section 7.4.2.

One can also prepare a specific Dicke state by performing post-selection on the measurement outcomes, preparing $|N, m_z \neq 0\rangle$ in this way would require less operations than $|N, m_z = 0\rangle$ (see the details in Appendix 7.6.1). In addition, the idea of phase estimation can be used to prepare specific superpositions of Dicke states, which are potentially useful for metrology under noise [47] (see the details in Appendix 7.6.2).

7.3. System Hamiltonian and experimental realization

In this section, we will sketch an experimental realization using a superconducting flux qubit coupled to an ensemble of NV centers.

We consider a hybrid system where a set of N two-level spins is collectively coupled to an ancilla qubit. To implement our scheme, we need the system Hamiltonian to be of the following form

$$H = H_0 + H_{\text{coupl}},$$

$$H_0 = \omega_0 J_z - \frac{1}{2}\omega Z, \quad H_{\text{coupl}} = \frac{\gamma}{2} Z \otimes J_z \tag{7.13}$$

with J_z in Eq. (7.1). Here, $\hbar = 1$ and γ is the coupling strength between the ancilla qubit and the spins, ω is the angular frequency of the ancilla qubit. The spins in the ensemble are assumed to have the same energy splitting, denoted by angular frequency ω_0.

In this system, we assume the ability to (i) implement single-qubit rotations and projective measurements on the ancilla qubit, (ii) implement global rotations of the spins (generated by J_x, J_y and J_z), (iii) initialize the ancilla qubit and the spins in $|0\rangle$.

The phase estimation scheme involves qubit-controlled rotations around J_z, which are realized through the interaction H_I. The evolution operator of H_I is

$$e^{-iH_I t} = e^{-i\frac{\gamma}{2}tJ_z}\left(|0\rangle\langle 0| \otimes I + |1\rangle\langle 1| \otimes e^{i\gamma tJ_z}\right), \tag{7.14}$$

where the unconditional rotation $e^{-i\frac{\gamma}{2}tJ_z}$ can be neglected. Since the free Hamiltonian H_0 commutes with H_I, we can also neglect the effect of H_0.

7.3.1. Sketch of experimental implementation

One possible experimental setup of the proposed protocol is an ensemble of NV centers coupled to a superconducting flux qubit. Each NV center hosts a single (electronic) $S = 1$ spin. Sensing a magnetic field or spin by means of this electronic spin has been of high interest in the last decade, see e.g., Ref. [6, 11] and references therein. Sensing using an ensemble of NV centers, without preparing them in a particular entangled state, has been used at ambient temperatures in, e.g., Ref. [7, 31].

In addition, proposals exist to use the ^{13}C nuclear spins which surround a NV center to enhance the sensing performance [57, 58]. Direct magnetic sensing using nuclear

spins however would be inefficient, as their gyromagnetic ratio is about a factor 1000 less than that of the electronic spin.

The proposal in Ref. [34] envisions coupling a flux qubit to NV center electronic spins for the transfer and storage of quantum information. This has been experimentally realized in Ref. [66], where a flux qubit was coupled to $O(10^7)$ NV centers to resonantly transfer a flux qubit excitation to a collective spin excitation and back [1]. In Ref. [23] the preparation of Dicke states using a coupled flux qubit was considered for sensing, using this energy-transferring flip-flop interaction (of the form $\sigma_+ J_- + \sigma_- J_+$ where $\sigma_\pm$ acts on flux qubit and $J_\pm = \frac{1}{2}(J_x + iJ_y)$ on the ensemble). The basic idea for the Dicke state preparation in Ref. [23] is then to repeat an excitation transfer from the flux qubit to the spins: (i) the flux qubit is first flipped to $|1\rangle$, (ii) the hybrid system evolves for some chosen time during which the ancilla qubit goes back to $|0\rangle$ and the spins in $|N, m_z = j\rangle$ evolve to $|N, m_z = j - 1\rangle$. Repeating this process $O(N)$ times, one obtains the state $|N, m_z = 0\rangle$ from an arbitrary Dicke state, say the product state $|N, m_z = N/2\rangle = |00\ldots0\rangle$.

In earlier work [52], the preparation of other sensing states, such as spin-cat and spin-squeezed states, was considered using a flux qubit coupled to a collection of NV-center electronic spins.

ZZ Coupling between Flux Qubit and NV center Electronic Spins

The coupling between the flux qubit and the NV center is magnetic, i.e. the two persistent current states of the flux qubit generate opposite magnetic fields which enter the Zeeman term in the NV center electronic spin Hamiltonian. As in Ref. [34, 66] one can imagine that the flux qubit is sitting on a diamond substrate with implanted NV centers, and say the loop of the flux qubit is about $1\mu m \times 1\mu m$. If the NV-centers are in a cubic volume 1×10^{-18} m^3 below the loop, a NV-center density of 10^{21} m^{-3} [5] would lead to already having about 1000 NV centers in this cube.

The Hamiltonian of a general flux qubit itself is given by

$$H_{\text{flux}} = \frac{\lambda}{2} X_f - \frac{\epsilon}{2} Z_f, \tag{7.15}$$

where the Z-basis is given by two persistent current states ($|0\rangle, |1\rangle$), –eigenbasis states of flux–, inducing opposite magnetic fields [10, 12, 42]. Here we include a label f to denote that these are Pauli operators on the flux qubit. The Pauli X_f term is due to the kinetic charging energy. The case $\epsilon = 0$ corresponds to a symmetric double-well potential in flux. Since the required interaction in Eq. (7.13) is $Z_f \otimes J_z$, we could envision that the current states are flux-qubit eigenstates. This implies an asymmetric double-well flux potential with $\epsilon > 0$ and $\epsilon \gg |\lambda|$ (requiring a large shunting capacitance). This is unlike some of the previous work mentioned above in which one works at $\epsilon = 0$.

Recent experiments demonstrate a long coherence time of the flux qubit at the flux sweet spot $\epsilon = 0$. The energy relaxation time T_1 is about 40μs and the dephasing time T_2 is about 10 μs with dynamical decoupling [64]. Single-qubit gates with duration about 2ns and fidelity about 99.92% are also realized [64]. However, tuning a flux qubit away from $\epsilon = 0$ decreases the dephasing time substantially. This is due to flux noise, i.e., the

---

[1]In [66] no external magnetic field was applied on the NV-electronic spins so that the states $|m_z = \pm 1\rangle$ are (nearly) degenerate and the excitation is to the level $|m_z = \pm 1\rangle$ and back.

flux qubit becomes much more sensitive to fluctuations of ϵ, which can be somewhat improved by dynamical decoupling [10]. For this reason we discuss an alternative way of using the flux qubit at $\epsilon = 0$ and the flip-flop interaction to realize a Dicke state preparation in Appendix 7.6.3.

There are four types of NV centers, each aligned with a different NV-axis of the carbon lattice (i.e. the direction from the vacancy to the nitrogen) [31], and one does not control the orientation of these NV-axes. We choose one type of NV center and call its NV-axis the z-axis so that its associated electronic spin ($S = 1$) has Hamiltonian [13]

$$H_{NV} = \Delta S_z^2 + W_z^{\text{ext}} S_z,\tag{7.16}$$

where W_z^{ext} represents the effect of an externally applied magnetic field and Δ is the zero-field splitting ($\Delta \approx 2.88$ GHz). Here we neglect components of the magnetic field which are not aligned with the NV-axis.

With $W_z^{\text{ext}} \neq 0$, the states $|S_z = m = \pm 1\rangle$ are made non-degenerate and we imagine, as is fairly standard, using the lowest two energy eigenstates $|S_z = m = 0\rangle$ and $|S_z = m = -1\rangle$ as the qubit. The externally applied magnetic field (O(100) Gauss) [1] which splits off the $m = \pm 1$ level should lie in the plane of the flux qubit loop, avoiding any stray effects on the flux qubit itself.

For a collection of N NV centers, we thus restrict ourselves to the electronic $\{|m = 0\rangle$, $|m = -1\rangle\}$ qubit subspace per NV center, and use the collective spin operators J_x, J_y, J_z acting on these qubits.

An additional magnetic field in the y-direction or x-direction, assuming it is uniformly experienced by all NV centers oriented along the z-axis, would induce additional Zeeman terms in the NV center Hamiltonian. This leads to global rotations, $\exp(-i\theta J_y)$, which we want to sense.

By applying microwave ($O(1)$GHz) pulses with a frequency which is resonant with the NV-center electronic spins, rotations generated by the collective spin operators J_x, J_y can be performed [9, 13]. To obtain the initial state $|\psi_0\rangle$ in Eq. (7.8), we first initialize all NV-center electronic spins in $|0\rangle$ through resonant optical excitations (the initialization duration is of the order of $O(100)\,\mu s$ [49] and is executed simultaneously for all NV-center electronic spins), then one performs the global rotation $e^{i\frac{\pi}{2} J_y}$ [13]. In addition, the NV-center electronic spins can be collectively measured optically to measure J_z, but the limited photon collection efficiency limits the readout contrast [6, 53, 63].

The Hamiltonian of a single NV-center and a flux qubit is

$$H = H_{\text{flux}} + H_{NV} + H_{\text{coupl}}.\tag{7.17}$$

The coupling term H_{coupl} models the NV-electronic spin experiencing a magnetic field due to the different persistent current flux qubit states: it can be written in the form

$$H_{\text{coupl}} = -\gamma_e \vec{B}_{\text{flux}} \cdot \vec{S}\tag{7.18}$$

with spin $S = 1$ operators $\vec{S} = (S_x, S_y, S_z)$ and gyromagnetic ratio γ_e (~ 2.8MHz/Gauss). Let's call the axis perpendicular to the flux qubit loop $\hat{r}$, so that $\vec{B}_{\text{flux}} \approx B\hat{r} Z_f$, where Z_f is the flux qubit Pauli Z operator and B is the magnetic field strength at the NV center.
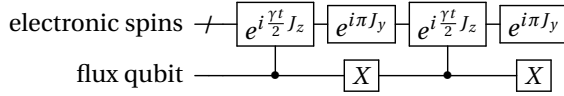
Figure 7.2: The controlled-$e^{i\gamma t J_z}$ gate with integrated dynamical decoupling, up to the unconditional rotation $e^{-i\frac{\gamma t}{2} J_z}$. Echo pulses are simultaneously applied to the NV-center electronic spins and the flux qubit. The pulses are at a frequency resonant with those NV-center electronic spins which should remain coupled to the flux qubit, while the coupling to the other NV-centers is echoed away.

Here we assume that the NV centers are centrally placed below the flux qubit, so that magnetic field components in directions other than $\hat{r}$ are negligible.

Since the coupling is much weaker than the electronic spin qubit frequency, we neglect the change of the precession axis induced by this coupling term. The coupling is thus approximated as

$$H_{\text{coupl}} \approx \frac{\gamma}{2} Z_f \otimes S_z. \tag{7.19}$$

Ref. [34] estimates that the coupling strength can be about 12kHz, depending on the strength of the magnetic field B and the proximity to the NV-center. We assume that we can use an orientation $\hat{r}$, so that the (projected) coupling strength $\gamma/2 = -\gamma_e B r_z$ is also of the order of $O(10)$kHz.

The four types of NV centers are simultaneously coupled to the flux qubit, each having a different coupling strength as their NV-axes are different and having a different resonance frequency [31]. In principle all types of NV centers could be used for sensing different components of the magnetic field [7]. However, since we have only a single controlling flux-qubit to create an entangled state, it is preferred to dynamically decouple the interaction with the other NV centers away.

For example, to cancel the coupling to 3 of the 4 NV center types, one could perform phase estimation with integrated dynamical decoupling. The circuit in Fig. 7.2 realizes the controlled-$e^{i\gamma t J_z}$ gate up to the unconditional rotation $e^{-i\frac{\gamma t}{2} J_z}$. The echo pulse $e^{i\pi J_y}$ is implemented using resonant microwaves with NV centers whose NV axis is the z-axis. These other NV centers are thus decoupled from the flux qubit.

The integrated echo pulses also provide resilience to the dephasing of the flux qubit and NV-center electronic spins. Note that we can split the controlled rotations to controlled $e^{i\gamma t J_z/n}$ with $n = 4, 6, 8, \ldots$, so that we obtain a further suppression of the dephasing. For simplicity, we will consider $n = 2$ in numerics in Section 7.4.

The coherence time of NV-center electronic spins is not a limiting factor for realizing our preparation scheme. The energy relaxation time T_1 of NV-center electronic spins exceeds 8 hours at 25mK [4]. For a NV ensemble with a NV-density about 10^{21} m^{-3}, the dephasing time T_2 (with dynamical decoupling) can be about 50ms at 77 K [5]. Because the dephasing of a NV electronic spin mainly comes from its surrounding spin bath environment [14], we may expect a longer dephasing time at the operating temperature of the flux qubit (tens of mK).

The weak point of this sketched proposal is the strength of the coupling γ versus the (short) dephasing time of the flux qubit $T_2 < O(1)\mu$s if it is operated away from its flux sweet spot. Even though the flux qubit only needs to stay coherent during each

round of phase estimation individually, i.e. during a circuit as in Fig. 7.1, a $O(10)$ kHz coupling γ requires an interaction time much longer than the flux qubit coherence time in particular for small j.

As an alternative, it may be possible to use the three levels ($S = 1$) of the NV-center electronic spins to apply controlled rotations adiabatically while operating the flux qubit in a more phase-coherent regime with $T_2 = O(10)\mu$s. In this scenario we work at $\epsilon = 0$ for the flux qubit in Eq. (7.15) and adiabatically change the flux qubit frequency through flux-control while staying at $\epsilon = 0$. Remember that the states $|m = 0\rangle_{\mathrm{NV}}$ and $|m = -1\rangle_{\mathrm{NV}}$ form the NV-center qubit subspace and $|m = +1\rangle_{\mathrm{NV}}$ is a third level.

If we apply a Hadamard transformation to make the flux qubit Hamiltonian diagonal in Z_f, the coupling term will read $H_{\mathrm{coupl}} = -\gamma_e B X_f \otimes \vec{S} \cdot \hat{r}$. Neglecting non-secular terms, one is left with an interaction which removes a flux-qubit excitation while exciting the NV center electronic state $m = 0$ to $m = \pm 1$ and vice-versa. We imagine adiabatically flux-tuning the flux qubit frequency to the avoided crossing between $|1\rangle_{\mathrm{flux}} \otimes |m = 0\rangle_{\mathrm{NV}}$ and $|0\rangle_{\mathrm{flux}} \otimes |m = +1\rangle_{\mathrm{NV}}$ and back so as to get an effective ZZ-interaction in the $|m = 0\rangle_{\mathrm{NV}}$ and $|m = -1\rangle_{\mathrm{NV}}$ and flux-qubit subspace. This way of obtaining a ZZ-interaction using a third level is commonly done for superconducting transmon qubits [35, 50]. Here we would need to generate this interaction between a single ancilla qubit and N NV electonic qubits, each with a third level. Note that this idea is different from flux-tuning the frequency of the flux qubit to be resonant with the NV-center electronic spin qubit frequency to activate the flip-flop interaction [23, 66]. We discuss the details about adiabatically applying controlled rotations in Appendix 7.6.3.

In this alternative scenario, one is also limited by the strength of the magnetic coupling. The coupling can only be enhanced by increasing the proximity of the NV-centers to the flux-qubit loop and having a higher current associated with the flux qubit states (leading to a stronger magnetic field), but the Josephson critical current density puts limits on this.

	Typical value
NV electronic spin T_1	> 1h
NV electronic spin T_2	$> O(50)$ ms
NV electronic spin initialization time	$O(100)\mu s$
Flux qubit T_1	$O(50)\mu s$
Flux qubit T_2	$< O(1)\mu s$
Flux qubit single-qubit gate time	$O(1)\,ns$
Magnetic coupling γ	$O(10)$ kHz

Table 7.1: Parameters that are relevant for realizing the preparation scheme using the sketched experimental setup, where an ensemble of NV electronic spins is collectively coupled to a single superconducting flux qubit. The main challenge is the weak magnetic coupling γ versus the short dephasing time T_2 of the flux qubit.

For realizing the preparation scheme using the sketched experimental setup, relevant parameters with their typical values are listed in Table 7.1.

7.4. PREPARATION WITH NOISE

In this section, we look at the performance of the phase estimation scheme for stronger coupling strength γ than what has been stated in the previous section, and some limited decoherence of the flux qubit. The spins in the ensemble are assumed to be perfect, as their coherence time is not a limiting factor for our scheme.

7.4.1. LIMITED COHERENCE TIME OF THE FLUX QUBIT

The flux qubit has energy relaxation time T_1 and limited pure dephasing time T_ϕ with $\frac{1}{T_2} = \frac{1}{2T_1} + \frac{1}{T_\phi}$. A simple model for the effect of T_ϕ is that of a phase flip channel. That is, during the controlled-$e^{i\gamma t J_z}$ gate, the flux qubit obtains a Pauli Z error with an error rate [39]

$$P_{T_\phi}(t) = \frac{1 - e^{-t/T_\phi}}{2}. \tag{7.20}$$

Such Pauli Z error can flip the ancilla qubit readout in the phase estimation circuit. Fortunately, we can suppress this error to some extent by repeating each circuit in Fig. 7.1 and taking a majority vote of the answers.

Flux qubit decay to zero temperature with rate $\kappa = 1/T_1$ can be described by a Lindblad master equation

$$\frac{d\rho}{dt} = -i[H,\rho] + \kappa \mathscr{D}[\sigma_- \otimes I]\rho. \tag{7.21}$$

Here $\sigma_- = |0\rangle\langle 1|$ is the annihilation operator on the ancilla qubit, ρ is the density matrix of the total system, and $\mathscr{D}[c]$ is defined as $\mathscr{D}[c]\rho = c\rho c^\dagger - \frac{1}{2}\{c^\dagger c, \rho\}$. The Kraus operators for a short time dt are

$$\delta M_0 = |0\rangle\langle 0| \otimes I + e^{-\frac{1}{2}\kappa dt}|1\rangle\langle 1| \otimes e^{i\gamma dt J_z},$$
$$\delta M_1 = \sqrt{\kappa dt}|0\rangle\langle 1| \otimes I. \tag{7.22}$$

Here the free evolution $e^{-iH_0 dt}$ and the unconditional rotation $e^{-i\frac{\gamma}{2}tJ_z}$ in Eq. (7.14) are omitted. Note that the Kraus operator δM_1 does not commute with H_I.

For a finite evolution time t, the action of the controlled-$e^{i\gamma t J_z}$ gate is given by a continuous set of Kraus operators

$$M_0(t) = |0\rangle\langle 0| \otimes I + |1\rangle\langle 1| \otimes e^{-\frac{1}{2}\kappa t} e^{i\gamma t J_z},$$
$$M_1(t') = \sqrt{\kappa e^{-\kappa t'}}|0\rangle\langle 1| \otimes e^{i\gamma t' J_z} \quad \text{for } t' < t. \tag{7.23}$$

The controlled rotation in the presence of ancilla qubit decay is then described by the quantum channel

$$\rho_{out} = M_0(t)\rho_{in}M_0^\dagger(t) + \int_0^t dt' M_1(t')\rho_{in}M_1^\dagger(t'). \tag{7.24}$$

where ρ_{in} and ρ_{out} are the input and output states of the controlled gate.

Now we consider implementing the controlled-$e^{i\gamma t J_z}$ gate with integrated echo pulses as in Fig. 7.2. If the ancilla qubit does not decay, the circuit applies the Kraus operator

$$(X \otimes e^{i\pi J_y}) M_0(t/2) (X \otimes e^{i\pi J_y}) M_0(t/2)$$
$$= \sqrt{e^{-\frac{1}{2}\kappa t}} e^{-i\frac{\gamma t}{2}J_z} \left(|0\rangle\langle 0| \otimes I + |1\rangle\langle 1| \otimes e^{i\gamma t J_z}\right). \tag{7.25}$$
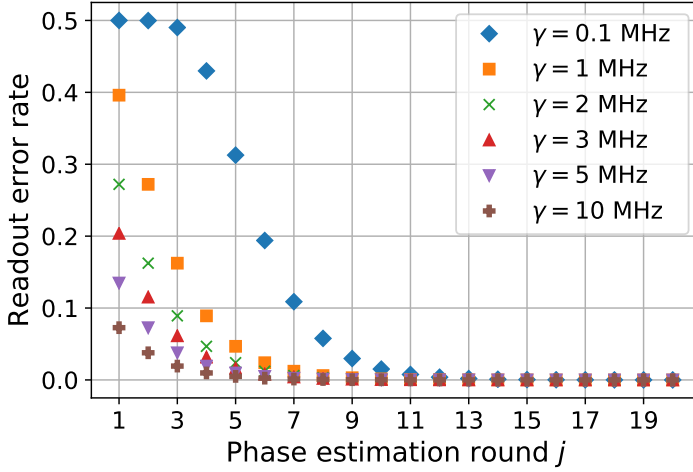
Figure 7.3: (Color online) The flux qubit readout error rate induced by flux qubit dephasing. Here we fix the pure dephasing time of the flux qubit as $T_\phi = 2\mu s$. In the jth round phase estimation, the evolution time is $t_j = \pi 2^{1-j}/\gamma$ which leads to the readout error rate $P_{T_\phi}(t_j)$ in Eq. (7.20).

This is the desired gate up to the unconditional rotation $e^{-i\frac{\gamma t}{2}J_z}$, which happens with the probability $e^{-\frac{1}{2}\kappa t}$. Otherwise, the ancilla qubit decays and an unconditional rotation around J_z is applied to the spins. In phase estimation, no projector is implemented and the ancilla qubit readout gives the outcome $0, 1$ with equal probability.

The flux qubit decay probability during the controlled-$e^{i\gamma t J_z}$ gate (with integrated echo pulses) is given by

$$P_{T_1}(t) = 1 - e^{-\frac{t}{2T_1}}. \tag{7.26}$$

7.4.2. INACCURATE CONTROL OF THE FLUX QUBIT

Each time we perform the controlled-$e^{i\gamma t J_z}$ gate, there may be a random small deviation δt of the evolution time t which becomes important when t is small. This means we actually perform the controlled-$\beta e^{i\gamma t J_z}$ gate with $\beta = e^{i\delta\theta J_z}$ and $\delta\theta = \gamma\delta t$.

Preparing an N-spin Dicke state means determining the eigenvalue of the unitary rotation U in Eq. (7.7), whose rotation angle $2\pi/2^K$ scales as $O(1/N)$. As we have discussed, determining the first $\lceil K/2 \rceil$ bits in Eq. (7.6) produces the target state with high fidelity. That is, we only need to determine the eigenvalue of a unitary rotation whose rotation angle scales as $O(1/\sqrt{N})$. This scaling characterizes how much timing inaccuracy our scheme can tolerate and thus how large N can be.

7.4.3. NUMERICAL SIMULATIONS

In the presence of inaccurate control, ancilla qubit dephasing, or ancilla qubit decay, the spins in the ensemble stay in the subspace which is symmetric under spin permutations.

They can be treated as a large pseudo-spin of size $J = N/2$. We therefore limit ourselves to a state vector in a $N+1$-dimensional space rather than the full size 2^N. The simulation is based on the QuTip Python package [27, 28], and the code can be found in [59].

The preparation starts from the product state $|\psi_0\rangle$ in Eq. (7.8), and determines the eigenvalue m_z of J_z using standard phase estimation. Each round of phase estimation is repeated multiple times, and a simple majority vote is performed. The fidelity of the prepared state, with respect to the predicted state $|N, m_z\rangle$, is used as a measure of how good the preparation is. We compute $F = \langle N, m_z | \rho | N, m_z \rangle$ where ρ is the density matrix prepared by the noisy, imperfect protocol.

Here we assume that $T_1 = 50$ μs and $T_\phi = 2$ μs for a flux qubit far away from flux-sweet spot. To ensure P_{T_ϕ} is reasonably small in the first few rounds of phase estimation, we need the coupling strength to be a few MHz, say, $\gamma = 5$MHz, as shown in Fig. 7.3. The corresponding flux qubit decay probability $P_{T_1}(t)$ would then only be about 0.6% in the first (longest) round of phase estimation. Hence the effect of pure dephasing T_ϕ dominates.

Suppose each round of phase estimation is repeated M times with majority voting. We say that the jth round phase estimation succeeds when: (i) There is at least one measurement, during which the flux qubit does not decay, i.e., the projector $P(m_j)$ in Eq. (7.9) is implemented at least once. (ii) Majority voting of the M measurement outcomes yields the correct answer m_j.

Instead of a full simulation, we numerically calculate the probability that all rounds of phase estimation succeed, i.e., the prepared state has fidelity 100%. This probability is calculated as $P = \prod_{j=1}^{K} P_j$, with P_j the success rate of the jth round phase estimation. Clearly, the probability P sets a lower bound of the output fidelity F. The lower bound P is plotted in Fig. 7.4, where we set $K = 20$ and use a coupling strength γ much beyond current estimates. Note that 20 rounds of phase estimation correspond to about 10^6 spins. We find that P quickly approaches unity as the repeat number M grows, basically because $P_{T_\phi}(t_j)$ and $P_{T_1}(t_j)$ both decrease exponentially as j grows.

To model inaccurate timing control of the flux qubit, we run a pure state simulation. Each time we apply a controlled-rotation in the preparation, there is a randomly sampled time deviation δt. We assume that δt is distributed according to the normal distribution $\mathcal{N}(0, \sigma^2)$. Considering that single-qubit rotation on a flux qubit has a duration about 2ns [64], we set $\sigma = 0.5, 1, 3, 6, 10$ns. Additionally, we fix $\gamma = 5$MHz and $N = 500$ spins. In the simulation, we perform 6 rounds of phase estimation, and each round is repeated M times with majority voting (here $T_\phi, T_1 = \infty$). Note that in the noiseless case, 6 rounds of phase estimation gives an output fidelity $F \approx 99.65\%$ for $N = 500$.

As shown in Fig. 7.5, our scheme is resilient to inaccurate flux qubit control. Even with $\sigma = 10$ns and $\gamma = 5$MHz, the output fidelity still surpasses 90% when we repeat each projective measurement only $M = 5$ times. Considering that $\gamma = 5$MHz is much larger than an estimated 12kHz, the expected effect of inaccurate timing in flux qubit control would thus be much smaller in practice. Hence, we would not expect this timing inaccuracy to be a main experimental challenge in the near future.
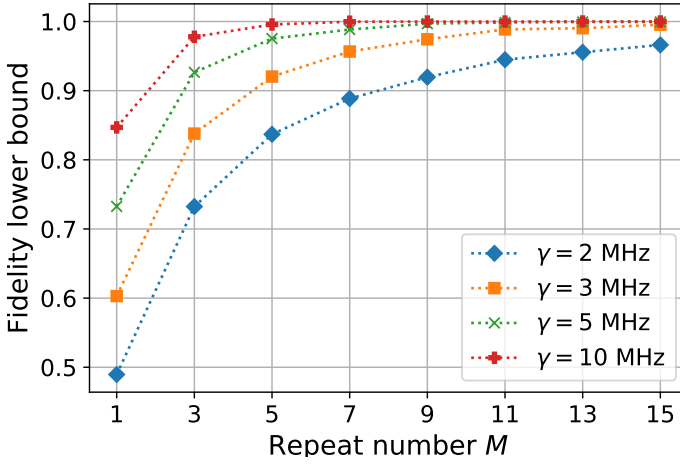
Figure 7.4: (Color online) Lower bound on the output fidelity for the preparation scheme with limited flux qubit coherence time but strong coupling. There are $K = 20$ rounds of phase estimation, each is repeated M times with majority voting. The fidelity lower bound P is the probability that all rounds of phase estimation succeed, so that the prepared state has fidelity 100%. Here we set $T_1 = 50\mu s$ and $T_\phi = 2\mu s$.
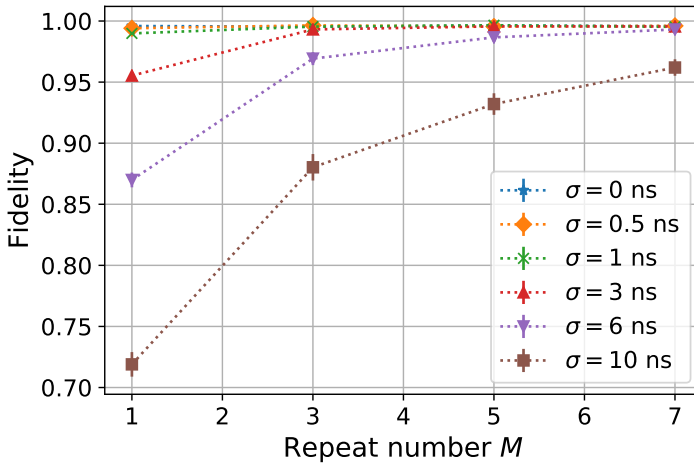

Figure 7.5: (Color online) The output fidelity of the preparation scheme with inaccurate control of the flux qubit. Here we fix the spin number $N = 500$, and the coupling strength $\gamma = 5$MHz. There are only 6 rounds of phase estimation, each is repeated M times with majority voting. When a controlled-rotation is applied, there is a time deviation δt, which is sampled according to normal distribution $\mathcal{N}(0, \sigma^2)$. The error bar is the 95% confidence interval.

7.5. Conclusion

To summarize, we have presented the idea of using phase estimation to prepare highly entangled Dicke states. Phase estimation can be realized through a global control, and only requires $O(\log_2 N)$ ancilla qubit measurements. Dicke states $|N, m_z\rangle$ with $m_z \sim O(1)$ are especially interesting for metrology as they can give Heisenberg-limited sensitivity via global control. Phase estimation can prepare such Dicke states with a probability $O(1/\sqrt{N})$, implying the need for $O(\sqrt{N})$ attempts on average.

With numerical simulations, we show that our scheme has some robustness to noise on the ancilla qubit. However, our scheme is still demanding for a spin ensemble coupled to a flux qubit as it requires a larger coupling strength or a longer flux qubit coherence time than what seems currently feasible.

One aspect of our analysis is that we assume a uniform coupling strength γ of the ancilla qubit to the spin ensemble, while in practice not all NV centers will be equidistant. Thus each spin in the ensemble will have a slightly different coupling strength $\gamma_i = \gamma + \delta\gamma_i$. The deviation $\delta\gamma_i$ results in local over-rotations leading to $U = \exp(i2\pi H_z/2^K)$ instead of Eq. (7.7), where $H_z = J_z + \frac{1}{2}\sum_i \frac{\delta\gamma_i}{\gamma} Z_i$. Phase estimation will estimate the eigenvalues of H_z to a precision set by K and approximately project the state onto an eigenstate of H_z. Product states $|x\rangle$ with the same Hamming weight are no longer degenerate with respect to H_z, which implies that a perfect eigenstate projection would lead to preparing a product state. For small enough N, when this eigenvalue-breaking contribution is small, i.e. $\sum_{i=1}^{N} |\frac{\delta\gamma_i}{2\gamma}| \ll 1$, one may expect that the projected eigenstates of H_z, starting from the state $|\psi_0\rangle$ in Eq. (7.8), are still (weighted) superpositions of bitstrings and thus entangled. In addition, imperfect state initialization can break permutation symmetry. It may be of interest to numerically simulate the sensing ability of the states that one projects onto using H_z. However, such numerical simulations are much more challenging as we have to consider matrices of size $2^N \times 2^N$.

To prepare $|N, m_z = 0\rangle$ more efficiently, we can combine our scheme with the proposal in Ref. [23] (see Sec 7.3.1), as both can be realized using the same experimental setup, i.e., a spin ensemble (e.g., diamond NV centers) coupled to a superconducting flux qubit. The difference is that the proposal in Ref. [23] requires the flux qubit to operate at $\epsilon = 0$, leading to the flip-flop interaction [34, 66]. Note that our phase estimation scheme (starting from the product state) prepares a Dicke state $|N, m_z < O(\sqrt{N})\rangle$ with a probability approaching unity. If we could tune the flux qubit to the $\epsilon = 0$ point after phase estimation (or use the scheme in Appendix 7.6.3), then we can perform the scheme in Ref. [23] to obtain $|N, m_z = 0\rangle$, which uses another $O(\sqrt{N})$ flux qubit flips.

7.6. Appendix

7.6.1. Optimizing the preparation of a specific Dicke state

Standard phase estimation can also prepare a specific Dicke state $|N, m_z = m\rangle$ when post-selection is used. To maximize the success rate, we rotate each spin initialized in $|+\rangle$ around the Y-axis by an angle 2χ. The value of χ is chosen so that $p = \frac{1}{2}\left[\cos(\chi) - \sin(\chi)\right]^2$

$= \frac{m+N/2}{N} = \frac{m}{N} + \frac{1}{2}$. The preparation of $|N, m_z = m\rangle$ then starts from

$$e^{-i2\chi J_y} |+\rangle^{\otimes N} = (\sqrt{p}\,|0\rangle + \sqrt{1-p}\,|1\rangle)^{\otimes N}$$

$$= \sum_{m_z=-N/2}^{N/2} \sqrt{\tilde{P}(m_z)} |N, m_z\rangle, \tag{7.27}$$

$$\tilde{P}(m_z) = \binom{N}{m_z + N/2} p^{m_z+N/2}(1-p)^{N/2-m_z}.$$

Here, the distribution $\tilde{P}(m_z)$ reaches its maximum at $m_z = m$, as it is most likely that we draw $pN = m + \frac{N}{2}$ 1s in this Bernoulli process, corresponding to $m_z = m$. Standard deviation of the distribution is $\sqrt{\frac{N^2-4m^2}{4N}}$. Note that $\tilde{P}(m)$ upper bounds the probability of obtaining $|N, m\rangle$.

The target state is obtained by measuring the operator $e^{i\pi 2^{1-l}(J_z-m)}$ with l integer via phase estimation as before i.e.,

$$|N, m\rangle = \frac{1}{\sqrt{\tilde{P}(m)}} \prod_{l=1}^{K} \frac{1 + e^{i\pi 2^{1-l}(J_z-m)}}{2} e^{-i2\chi J_y} |+\rangle^{\otimes N}. \tag{7.28}$$

The $K = \lceil \log_2 N \rceil + 1$ measurements are realized through the circuit in Fig. 7.1. The equality in Eq. (7.28) approximately holds when the number of measurements K satisfies that $2^K \sim O(\sqrt{\frac{N^2-4m^2}{4N}})$.

7.6.2. Quantum code: superposition of Dicke states
In Ref. [43, 46], a so-called permutation-invariant code is proposed for quantum error correction. The logical code words of this code are specific superpositions of Dicke states, namely

$$|0_L\rangle = \frac{1}{\sqrt{2^{n-1}}} \sum_{\substack{0 \le j \le n \\ j \text{ even}}} \sqrt{\binom{n}{j}} \left| N = gnu, m_z = gj - \frac{N}{2} \right\rangle.$$

$$|1_L\rangle = \frac{1}{\sqrt{2^{n-1}}} \sum_{\substack{0 \le j \le n \\ j \text{ odd}}} \sqrt{\binom{n}{j}} \left| N = gnu, m_z = gj - \frac{N}{2} \right\rangle. \tag{7.29}$$

The code can correct arbitrary t-qubit Pauli errors with $g, n > 2t + 1$, where g, n are both integers. The rational number $u \ge 1$ is a scaling parameter which controls the total qubit number $N = gnu$ [43, 46]. Note that the construction of such permutation-invariant codes has been generalized in Ref.[44], where the logical states are encoded into multiple qudits.

In Ref. [47], it was suggested to use the logical state $|+_L\rangle = \frac{|0_L\rangle + |1_L\rangle}{\sqrt{2}}$ as a probe state in metrology. It is claimed that the suggested probe state can give Heisenberg-limited sensitivity, even in the presence of a non-trivial number of errors [47]. For simplicity, we

write $|+_L\rangle$ with parameters g, n, u as

$$\left|\varphi_{g,n,u}\right\rangle = \frac{1}{\sqrt{2^n}} \sum_{0 \le j \le n} \sqrt{\binom{n}{j}} \left| N = gnu, m_z = gj - \frac{N}{2} \right\rangle. \tag{7.30}$$

Here we show how this probe state $\left|\varphi_{g,n,u}\right\rangle$ can be prepared using phase estimation. Note that the preparation of this code has been studied in Ref. [29, 45, 62].

We first look at the simplest 9-qubit code with $g = n = 3$ and $u = 1$, which corrects an arbitrary single-qubit Pauli error. The corresponding probe state is

$$\left|\varphi_{3,3,1}\right\rangle = \frac{\left|9, -\frac{9}{2}\right\rangle + \sqrt{3}\left|9, -\frac{3}{2}\right\rangle + \sqrt{3}\left|9, \frac{3}{2}\right\rangle + \left|9, \frac{9}{2}\right\rangle}{\sqrt{8}}. \tag{7.31}$$

One can find that $\left|\varphi_{3,3,1}\right\rangle$ is an eigenstate of the operator $e^{i\frac{2\pi}{3}J_z}$ with eigenvalue -1. The basic idea is to project a permutation-invariant state into an -1 eigenstate of $e^{i\frac{2\pi}{3}J_z}$, i.e., a superposition of $|N = 9, m_z\rangle$ with $m_z = \pm\frac{3}{2}, \pm\frac{9}{2}$. That is to say, we can prepare the target state by determining the eigenvalue of the unitary operator $e^{i\frac{2\pi}{3}J_z}$. This can be realized by measuring the operator multiple times with post-selection, which can effectively project out Dicke states $|N, m_z\rangle$ with $m_z \ne \pm\frac{3}{2}, \pm\frac{9}{2}$.

However, the obtained superposition is not necessarily the target state $\left|\varphi_{3,3,1}\right\rangle$, as the amplitudes are carefully chosen. To fix this problem, we will start from the initial state $\left|\overline{\varphi}_{3,3,1}\right\rangle$ which satisfies

$$
\begin{aligned}
\left\langle 9, \frac{9}{2} \middle| \overline{\varphi}_{3,3,1} \middle| 9, \frac{9}{2} \middle| \overline{\varphi}_{3,3,1} \right\rangle &= \left\langle 9, -\frac{9}{2} \middle| \overline{\varphi}_{3,3,1} \middle| 9, -\frac{9}{2} \middle| \overline{\varphi}_{3,3,1} \right\rangle, \\
\left\langle 9, \frac{3}{2} \middle| \overline{\varphi}_{3,3,1} \middle| 9, \frac{3}{2} \middle| \overline{\varphi}_{3,3,1} \right\rangle &= \left\langle 9, -\frac{3}{2} \middle| \overline{\varphi}_{3,3,1} \middle| 9, -\frac{3}{2} \middle| \overline{\varphi}_{3,3,1} \right\rangle, \\
\left\langle 9, \frac{3}{2} \middle| \overline{\varphi}_{3,3,1} \middle| 9, \frac{3}{2} \middle| \overline{\varphi}_{3,3,1} \right\rangle &= \sqrt{3} \left\langle 9, \frac{9}{2} \middle| \overline{\varphi}_{3,3,1} \middle| 9, \frac{9}{2} \middle| \overline{\varphi}_{3,3,1} \right\rangle.
\end{aligned} \tag{7.32}
$$

For a superposition of Dicke states, we observe that a rotation $e^{i\theta J_y}$ changes the distribution of m_z, which can be seen from Eq. (7.27). The desired initial state $\left|\overline{\varphi}_{3,3,1}\right\rangle$ can be approximately constructed as

$$\left|\overline{\varphi}_{3,3,1}\right\rangle = \frac{1}{\sqrt{\mathcal{N}}} \frac{e^{-i\theta J_y} + e^{i\theta J_y}}{2} |+\rangle^{\otimes 9}, \quad \theta = 0.57056 \tag{7.33}$$

with $\mathcal{N}$ the normalization factor. Here the value of θ is obtained numerically. The application of the operator $(e^{-i\theta J_y} + e^{i\theta J_y})/2$ can be realized by measuring $e^{i2\theta J_y}$ with postselection, followed by the unitary rotation $e^{-i\theta J_y}$. The target state $\left|\varphi_{3,3,1}\right\rangle$ is then approximately obtained:

$$\left|\varphi_{3,3,1}\right\rangle \approx \frac{1}{\sqrt{P_{succ}}} \left[\frac{1 - e^{i\frac{2\pi}{3}J_z}}{2}\right]^M \frac{e^{-i\theta J_y} + e^{i\theta J_y}}{2} |+\rangle^{\otimes 9}. \tag{7.34}$$

In the noiseless case, setting the number of times you apply the measurement to $M = 5$, gives a fidelity about 99.9%. The probability for obtaining the targeted state $|\varphi_{3,3,1}\rangle$ is $P_{succ} \approx 19.2\%$.

The preparation described here can be easily generalized for preparing $|\varphi_{g,n,u}\rangle$ with arbitrary g, n, u. The corresponding initial state $|\overline{\varphi}_{g,n,u}\rangle$ now satisfies ($j = 0, 1, \ldots, n$)

$$\frac{\left\langle N = gnu, m_z = gj - \frac{N}{2} | \overline{\varphi}_{g,n,u} | N = gnu, m_z = gj - \frac{N}{2} | \overline{\varphi}_{g,n,u} \right\rangle}{\left\langle N = gnu, m_z = -\frac{N}{2} | \overline{\varphi}_{g,n,u} | N = gnu, m_z = -\frac{N}{2} | \overline{\varphi}_{g,n,u} \right\rangle} = \sqrt{\binom{n}{j}}. \tag{7.35}$$

Note that $|\overline{\varphi}_{g,n,u}\rangle$ can be constructed in the same way as the 9-qubit case in Eq. (7.33), but now we need multiple projectors in the form $\prod_l (e^{-i\theta_l J_y} + e^{i\theta_l J_y})/2$ with different angles θ_l. These angles can also be obtained numerically.

Similarly, we find that $|\varphi_{g,n,u}\rangle$ is a simultaneous $+1$ eigenstate of the operators

$$S_{g,n,u}(a) = e^{i\frac{2a\pi}{g}(J_z + \frac{gnu}{2})} \tag{7.36}$$

with a integer. Measuring these operators multiple times with post-selection, qubits in the initial state $|\overline{\varphi}_{g,n,u}\rangle$ can be effectively projected into the target state $|\varphi_{g,n,u}\rangle$.

7.6.3. ADIABATIC CONTROLLED ROTATION

Here we explain how to apply controlled global rotations to a NV ensemble by adiabatically tuning the flux qubit frequency and using the third level of the electronic spin at each NV center. Starting from an appropriate product state, such controlled-rotation can also be used to prepare a highly entangled Dicke state via phase estimation.

For a collection of N identical NV electronic spins which are coupled to a flux qubit, the Hamiltonian can be written in the form

$$H_{\text{sys}} = H_0 + H_{\text{coupl}},$$
$$H_0 = -\frac{\omega(t)}{2} Z_f + \Delta \sum_{i=1}^{N} S_{z_i}^2 + W^{\text{ext}} \sum_{i=1}^{N} S_{z_i}, \tag{7.37}$$
$$H_{\text{coupl}} = -\gamma_e B X_f \otimes \sum_i^{N} \vec{S}_i \cdot \hat{r},$$

where $\vec{S}_i = (S_{x_i}, S_{y_i}, S_{z_i})$ is the spin $S = 1$ operator for the NV-electronic spin labeled i, Z_f and X_f are the Pauli operators of the flux qubit. As we will adiabatically tune the flux qubit frequency $\omega(t)$, it is a function of time t. Here the flux qubit is operating at $\epsilon = 0$ in Eq. (7.15) and the X_f-basis is given by two different persistent current states, inducing opposite magnetic fields [10, 12, 42].

For simplicity, we relabel the three qubit states of the NV electronic spin as

$$|S = 1, m_z = +1\rangle = |2\rangle,$$
$$|S = 1, m_z = 0\rangle = |0\rangle, \tag{7.38}$$
$$|S = 1, m_z = -1\rangle = |1\rangle.$$

so that state $|2\rangle$ is outside the computational subspace. Here we assume that $\hat{r}$, the direction orthogonal to the flux loop, is along the $\hat{x}$-direction of the NV-centers. This means that the NV-axis lies in the plane of the flux qubit loop, so that the coupling term equals $H_{\text{coupl}} = -\gamma_e B X_f \otimes \sum_i^N S_{x_i}$. Using the definition $\hat{S}_x = (|2\rangle\langle 0| + |0\rangle\langle 2| + |1\rangle\langle 0| + |0\rangle\langle 1|)/\sqrt{2}$, the coupling Hamiltonian can be written as (here we only keep the flip-flop terms)

$$H_{\text{coupl}} \approx g |0\rangle\langle 1|_f \otimes \sum_{i=1}^N (|2\rangle\langle 0|_i + |1\rangle\langle 0|_i) + h.c., \tag{7.39}$$

where $g = -\gamma_e B/\sqrt{2}$. The free Hamiltonian H_0 can be written as

$$H_0 = -\frac{\omega(t)}{2} |0\rangle\langle 0|_f + \frac{\omega(t)}{2} |1\rangle\langle 1|_f$$
$$+ \omega_1 \sum_{i=1}^N |1\rangle\langle 1|_i + \omega_2 \sum_{i=1}^N |2\rangle\langle 2|_i, \tag{7.40}$$
$$\omega_1 = \Delta - W^{ext}, \quad \omega_2 = \Delta + W^{ext}.$$

With an external magnetic field of $O(100)$ Gauss along the NV axis ($W^{ext} > 0$), the frequency difference $\omega_2 - \omega_1$ can be as large as $O(1)$GHz [2]. To implement the controlled rotation, we will start from $\omega_1 < \omega(t) < \omega_2$, adiabatically tuning $\omega(t)$ up to ω_2 and then tuning it back. Such adiabatic control can be done by applying a flux through the loop which sets the tunnel barrier of the flux qubit, see, e.g., Ref. [24]. If one moves away from the sweet-spot point of this controlling loop, some additional flux noise can be incurred.

We can set $\omega(t)$ to stay far away from ω_1 during the adiabatic path so that we are not activating any flip-flop interactions inside the computational space. Hence, we further neglect the off-resonant flip-flop terms between $|1\rangle_f \otimes |0\rangle_i$ and $|0\rangle_f \otimes |1\rangle_i$ and obtain an approximate interaction Hamiltonian

$$\tilde{H}_{\text{coupl}} = g \sum_{i=1}^N \left[|0\rangle\langle 1|_f \otimes |2\rangle\langle 0|_i + |1\rangle\langle 0|_f \otimes |0\rangle\langle 2|_i \right]. \tag{7.41}$$

For each Dicke state $|N, m_z\rangle$ (except when $m_z = -N/2$ and all spins are in state $|1\rangle$), we can define a two-dimensional subspace spanned by orthogonal states to which the dynamics is confined:

$$\left|\phi_0(m_z)\right\rangle = |1\rangle_f \otimes |N, m_z\rangle,$$
$$\left|\phi_1(m_z)\right\rangle = \frac{\tilde{H}_{\text{coupl}} \left|\phi_0(m_z)\right\rangle}{\sqrt{\left\langle\phi_0(m_z)\right| \tilde{H}_{\text{coupl}}^\dagger \tilde{H}_{\text{coupl}} \left|\phi_0(m_z)\right\rangle}}. \tag{7.42}$$

Note that the states $\left|\phi_1(m_z)\right\rangle$ differ from $\left|\phi_0(m_z)\right\rangle$ in that one of the NV center qubits in $|0\rangle$ has been flipped to $|2\rangle$, while the flux qubit has been flipped from $|1\rangle$ to $|0\rangle$. We assume that we start from a product state where the probability of $|m_z| < O(\sqrt{N})$ approaches unity for large N, we can neglect the zero effect of the interaction on the state $\left|N, m_z = -\frac{N}{2}\right\rangle$.

In the subspace spanned by $\{|\phi_0(m_z)\rangle, |\phi_1(m_z)\rangle\}$, we write the system Hamiltonian as

$$
\begin{aligned}
\tilde{H}_{\text{sys}} &= H_0 + \tilde{H}_{\text{coupl}} \\
&= \begin{pmatrix} (\frac{N}{2} - m_z)\omega_1 + \frac{\omega(t)}{2} & G(m_z) \\ G(m_z) & (\frac{N}{2} - m_z)\omega_1 + \omega_2 - \frac{\omega(t)}{2} \end{pmatrix}
\end{aligned}
\tag{7.43}
$$

with effective coupling strength

$$
\begin{aligned}
G(m_z) &= \sqrt{\langle\phi_0(m_z)| \tilde{H}_{\text{coupl}}^\dagger \tilde{H}_{\text{coupl}} |\phi_0(m_z)\rangle} \\
&= g\sqrt{\frac{N}{2}(\frac{N}{2} + 1) - m_z(m_z - 1)}.
\end{aligned}
\tag{7.44}
$$

Note that for the product state $|0\dots0\rangle$ with $m_z = N/2$, $G(N/2) = g\sqrt{N}$. The eigenvalues of $\tilde{H}_{\text{sys}}$ in this subspace are

$$
E(t) = \frac{\omega_2}{2} \pm \sqrt{G(m_z)^2 + \left(\frac{\omega_2 - \omega(t)}{2}\right)^2} + \left(\frac{N}{2} - m_z\right)\omega_1.
\tag{7.45}
$$

On the adiabatic trajectory lasting for time T, the following phases can be neglected (or trivially compensated): (i) NV centers qubits in the state $|1\rangle$ which together pick up a total phase $\exp\left(-i\int_{t=0}^{T} dt\left(\frac{N}{2} - m_z\right)\omega_1\right)$; (ii) the phase $\frac{1}{2}\omega_2 T$ obtained by the flux qubit being in $|1\rangle_f$; (iii) the phase $\exp\left(i\int_{t=0}^{T} \frac{\omega(t)}{2} dt\right)$ obtained by the flux qubit being in $|0\rangle_f$.

The coupling strength $G(m_z)$ is minimum when $m_z = N/2$, and scales as $O(N)$ for $m_z = O(1)$. Thus, initially when we don't want any interaction, we need to choose $|\omega_2 - \omega| \gg G(m_z)$ for all $|m_z| \leq O(\sqrt{N})$, that is, ω_2 and ω should be sufficiently detuned. With this weak coupling the states $|\phi_0(m_z)\rangle, |\phi_1(m_z)\rangle$ are approximate eigenstates (besides states such as $|0\rangle_f |N, m_z\rangle$ which do not couple).

The gap on the adiabatic trajectory in the m_z-labeled subspace is

$$
\Delta(m_z) = 2\sqrt{G(m_z)^2 + \left(\frac{\omega_2 - \omega(t)}{2}\right)^2}
\tag{7.46}
$$

, which is minimized at the avoided crossing $\omega(t) = \omega_2$. As we seek to apply this interaction on a state for which $|m_z| \sim O(\sqrt{N})$ and N is large, $\Delta(m_z) \approx gN/2$ at the avoided crossing. We thus assume the path is fully adiabatic. One could possibly choose a trajectory such as in Ref. [35].

If we assume that a negligible phase is picked up during a relatively-fast trajectory, followed by a waiting time δt at the avoided crossing and a fast switch back, we can see that the state $|\phi_0(m_z)\rangle \to e^{i\varphi(\delta t)}|\phi_0(m_z)\rangle$ where

$$
\begin{aligned}
\varphi(\delta t) &= -G(m_z)\delta t \\
&\approx g\delta t\left(\frac{m_z^2 - m_z}{\sqrt{N(N+2)}} - \frac{\sqrt{N(N+2)}}{2}\right).
\end{aligned}
\tag{7.47}
$$

Here we have assumed that $|m_z| \ll N$ to Taylor expand $G(m_z)$ and neglected higher order terms. The m_z-independent phase $-g\delta t \frac{\sqrt{N(N+2)}}{2}$ can be further compensated by a single-qubit rotation of the flux qubit after the adiabatic trajectory.

Thus in the limit of large spin number N, the adiabatic procedure approximately applies the unitary

$$V(\delta t) = |0\rangle \langle 0|_f \otimes I + |1\rangle \langle 1|_f \otimes \exp\left\{\left(\frac{ig\delta t}{N}(J_z^2 - J_z)\right)\right\}. \tag{7.48}$$

Now we will start the preparation from a product state $e^{-i2\chi J_y} |+\rangle^{\otimes N}$ with an appropriate value of χ as in Eq. (7.27). Here we consider a specific example: we choose the value of χ so that the product state $e^{-i2\chi J_y} |+\rangle^{\otimes N}$ is a superposition of Dicke states, which are localized around $|N, m_z = 2\sqrt{N}\rangle$. When N is large, the probability for $0 \leq m_z \leq 4\sqrt{N}$ approaches unity. For this product state, we can make an approximation that the eigenvalues of J_z and $J_z^2 - J_z$ are in 1-1 correspondence. We can use this form of controlled rotation in Eq. (7.48) to perform phase estimation and then prepare $|N, m_z \sim O(\sqrt{N})\rangle$.

However, this adiabatic form of applying a controlled rotation makes it hard to get a strong interaction, as the rotation angle scales as $O(1/N)$.

REFERENCES

[1] M. Abobeih. *From atomic-scale imaging to quantum fault-tolerance with spins in diamond*. PhD thesis, TU Delft, the Netherlands, 2021.

[2] M. H. Abobeih, J. Randall, C. E. Bradley, H. P. Bartling, M. A. Bakker, M. J. Degen, M. Markham, D. J. Twitchen, and T. H. Taminiau. Atomic-scale imaging of a 27-nuclear-spin cluster using a quantum sensor. *Nature*, 576(7787):411–415, 2019.

[3] I. Apellaniz, B. Lücke, J. Peise, C. Klempt, and G. Tóth. Detecting metrologically useful entanglement in the vicinity of Dicke states. *New J. Phys.*, 17(8):083027, 2015.

[4] T. Astner, J. Gugler, A. Angerer, S. Wald, S. Putz, N. J. Mauser, M. Trupke, H. Sumiya, S. Onoda, J. Isoya, et al. Solid-state electron spin lifetime limited by phononic vacuum modes. *Nat. Mater.*, 17(4):313–317, 2018.

[5] N. Bar-Gill, L. M. Pham, A. Jarmola, D. Budker, and R. L. Walsworth. Solid-state electronic spin coherence time approaching one second. *Nat. Commun.*, 4(1):1–6, 2013.

[6] J. F. Barry, J. M. Schloss, E. Bauch, M. J. Turner, C. A. Hart, L. M. Pham, and R. L. Walsworth. Sensitivity optimization for NV-diamond magnetometry. *Rev. Mod. Phys.*, 92(1):015004, 2020.

[7] J. F. Barry, M. J. Turner, J. M. Schloss, D. R. Glenn, Y. Song, M. D. Lukin, H. Park, and R. L. Walsworth. Optical magnetic detection of single-neuron action potentials using quantum defects in diamond. *Proc. Natl. Acad. Sci.*, 113(49):14133–14138, 2016.

[8] A. Bärtschi and S. Eidenbenz. Deterministic Preparation of Dicke States. In *Fundamentals of Computation Theory*, pages 126–139. Springer International Publishing, 2019.

[9] C. Bradley, J. Randall, M. Abobeih, R. Berrevoets, M. Degen, M. Bakker, M. Markham, D. Twitchen, and T. Taminiau. A ten-qubit solid-state spin register with quantum memory up to one minute. *Phys. Rev. X*, 9(3):031045, 2019.

[10] J. Bylander, S. Gustavsson, F. Yan, F. Yoshihara, K. Harrabi, G. Fitch, D. G. Cory, Y. Nakamura, J.-S. Tsai, and W. D. Oliver. Noise spectroscopy through dynamical decoupling with a superconducting flux qubit. *Nat. Phys.*, 7(7):565–570, 2011.

[11] F. Casola, T. van der Sar, and A. Yacoby. Probing condensed matter physics with magnetometry based on nitrogen-vacancy centres in diamond. *Nat. Rev. Mater.*, 3(1):1–13, 2018.

[12] J. Clarke and F. K. Wilhelm. Superconducting quantum bits. *Nature*, 453(7198):1031–1042, 2008.

[13] J. Cramer. *Quantum error correction with spins in diamond.* PhD thesis, TU Delft, the Netherlands, 2016.

[14] G. De Lange, Z. Wang, D. Riste, V. Dobrovitski, and R. Hanson. Universal dynamical decoupling of a single solid-state spin from a spin bath. *Science*, 330(6000):60–63, 2010.

[15] C. L. Degen, F. Reinhard, and P. Cappellaro. Quantum sensing. *Rev. Mod. Phys.*, 89(3):035002, 2017.

[16] R. Demkowicz-Dobrzański, J. Kołodyński, and M. Guţă. The elusive Heisenberg limit in quantum-enhanced metrology. *Nat. Commun.*, 3(1):1–8, 2012.

[17] F. Dolde, V. Bergholm, Y. Wang, I. Jakobi, B. Naydenov, S. Pezzagna, J. Meijer, F. Jelezko, P. Neumann, T. Schulte-Herbrüggen, et al. High-fidelity spin entanglement using optimal control. *Nat. Commun.*, 5(1):1–9, 2014.

[18] F. Dolde, I. Jakobi, B. Naydenov, N. Zhao, S. Pezzagna, C. Trautmann, J. Meijer, P. Neumann, F. Jelezko, and J. Wrachtrup. Room-temperature entanglement between single defect spins in diamond. *Nat. Phys.*, 9(3):139–143, 2013.

[19] L.-M. Duan and H. J. Kimble. Efficient engineering of multiatom entanglement through single-photon detections. *Phys. Rev. Lett.*, 90:253601, 2003.

[20] K. Duivenvoorden, B. M. Terhal, and D. Weigand. Single-mode displacement sensor. *Phys. Rev. A*, 95(1):012305, 2017.

[21] V. Giovannetti, S. Lloyd, and L. Maccone. Quantum-enhanced measurements: beating the standard quantum limit. *Science*, 306(5700):1330–1336, 2004.

[22] V. Giovannetti, S. Lloyd, and L. Maccone. Advances in quantum metrology. *Nat. Photonics*, 5(4):222, 2011.

7

[23] H. Hakoshima and Y. Matsuzaki. Efficient detection of inhomogeneous magnetic fields from a single spin with Dicke states. *Phys. Rev. A*, 102:042610, 2020.

[24] R. Harris, J. Johansson, A. J. Berkley, M. W. Johnson, T. Lanting, S. Han, P. Bunyk, E. Ladizinsky, T. Oh, I. Perminov, E. Tolkacheva, S. Uchaikin, E. M. Chapple, C. Enderud, C. Rich, M. Thom, J. Wang, B. Wilson, and G. Rose. Experimental demonstration of a robust and scalable flux qubit. *Phys. Rev. B*, 81:134510, 2010.

[25] D. B. Hume, C. W. Chou, T. Rosenband, and D. J. Wineland. Preparation of Dicke states in an ion chain. *Phys. Rev. A*, 80:052302, 2009.

[26] R. Ionicioiu, A. E. Popescu, W. J. Munro, and T. P. Spiller. Generalized parity measurements. *Phys. Rev. A*, 78:052326, 2008.

[27] J. R. Johansson, P. D. Nation, and F. Nori. Qutip: An open-source Python framework for the dynamics of open quantum systems. *Comput. Phys. Commun.*, 183(8):1760–1772, 2012.

[28] R. Johansson, P. Nation, and F. Nori. QuTiP 2: A Python framework for the dynamics of open quantum systems. *Comput. Phys. Commun.*, 184:1234–1240, 2013.

[29] M. T. Johnsson, N. R. Mukty, D. Burgarth, T. Volz, and G. K. Brennen. Geometric pathway to scalable quantum sensing. *Phys. Rev. Lett.*, 125:190403, 2020.

[30] N. Kiesel, C. Schmid, G. Tóth, E. Solano, and H. Weinfurter. Experimental observation of four-photon entangled Dicke state with high fidelity. *Phys. Rev. Lett.*, 98:063604, 2007.

[31] S. Kitazawa, Y. Matsuzaki, S. Saijo, K. Kakuyanagi, S. Saito, and J. Ishi-Hayase. Vector-magnetic-field sensing via multifrequency control of nitrogen-vacancy centers in diamond. *Phys. Rev. A*, 96(4):042115, 2017.

[32] T. Kobayashi, R. Ikuta, Ş. K. Özdemir, M. Tame, T. Yamamoto, M. Koashi, and N. Imoto. Universal gates for transforming multipartite entangled Dicke states. *New J. Phys.*, 16(2):023005, 2014.

[33] L. Lamata, C. E. López, B. P. Lanyon, T. Bastin, J. C. Retamal, and E. Solano. Deterministic generation of arbitrary symmetric states and entanglement classes. *Phys. Rev. A*, 87:032325, 2013.

[34] D. Marcos, M. Wubs, J. Taylor, R. Aguado, M. D. Lukin, and A. S. Sørensen. Coupling nitrogen-vacancy centers in diamond to superconducting flux qubits. *Phys. Rev. Lett.*, 105(21):210501, 2010.

[35] J. M. Martinis and M. R. Geller. Fast adiabatic qubit gates using only σ_z control. *Phys. Rev. A*, 90(2):022307, 2014.

[36] S. J. Masson and S. Parkins. Extreme spin squeezing in the steady state of a generalized Dicke model. *Phys. Rev. A*, 99:023822, 2019.

[37] C. S. Mukherjee, S. Maitra, V. Gaurav, and D. Roy. Preparing Dicke States on a Quantum Computer. *IEEE Transactions on Quantum Engineering*, 1:1–17, 2020.

[38] P. Neumann, R. Kolesov, B. Naydenov, J. Beck, F. Rempp, M. Steiner, V. Jacques, G. Balasubramanian, M. Markham, D. Twitchen, et al. Quantum register based on coupled electron spins in a room-temperature solid. *Nat. Phys.*, 6(4):249–253, 2010.

[39] M. A. Nielsen and I. Chuang. *Quantum computation and quantum information*. American Association of Physics Teachers, 2002.

[40] A. Noguchi, K. Toyoda, and S. Urabe. Generation of Dicke states with phonon-mediated multilevel stimulated raman adiabatic passage. *Phys. Rev. Lett.*, 109:260502, 2012.

[41] T. E. O'Brien, B. Tarasinski, and B. M. Terhal. Quantum phase estimation of multiple eigenvalues for small-scale (noisy) experiments. *New J. Phys.*, 21(2):023022, 2019.

[42] T. P. Orlando, J. E. Mooij, L. Tian, C. H. van der Wal, L. S. Levitov, S. Lloyd, and J. J. Mazo. Superconducting persistent-current qubit. *Phys. Rev. B*, 60:15398–15413, 1999.

[43] Y. Ouyang. Permutation-invariant quantum codes. *Phys. Rev. A*, 90(6):062317, 2014.

[44] Y. Ouyang. Permutation-invariant qudit codes from polynomials. *Linear algebra and its applications*, 532, 2016.

[45] Y. Ouyang. Permutation-invariant quantum coding for quantum deletion channels. In *2021 IEEE International Symposium on Information Theory (ISIT)*, pages 1499–1503, 2021.

[46] Y. Ouyang and J. Fitzsimons. Permutation-invariant codes encoding more than one qubit. *Phys. Rev. A*, 93:042340, 2016.

[47] Y. Ouyang, N. Shettell, and D. Markham. Robust Quantum Metrology With Explicit Symmetric States. *IEEE Trans. Inf. Theory*, 68(3):1809–1821, 2022.

[48] L. Pezze, A. Smerzi, M. K. Oberthaler, R. Schmied, and P. Treutlein. Quantum metrology with nonclassical states of atomic ensembles. *Rev. Mod. Phys.*, 90(3):035005, 2018.

[49] L. Robledo, L. Childress, H. Bernien, B. Hensen, P. F. A. Alkemade, and R. Hanson. High-fidelity projective read-out of a solid-state spin quantum register. *Nature*, 477(7366):574–578, 2011.

[50] M. A. Rol, F. Battistel, F. K. Malinowski, C. C. Bultink, B. M. Tarasinski, R. Vollmer, N. Haider, N. Muthusubramanian, A. Bruno, B. M. Terhal, and L. DiCarlo. Fast, high-fidelity conditional-phase gate exploiting leakage interference in weakly anharmonic superconducting qubits. *Phys. Rev. Lett.*, 123:120502, 2019.

[51] J. K. Stockton, R. van Handel, and H. Mabuchi. Deterministic Dicke-state preparation with continuous measurement and control. *Phys. Rev. A*, 70:022106, 2004.

7

[52] T. Tanaka, P. Knott, Y. Matsuzaki, S. Dooley, H. Yamaguchi, W. J. Munro, and S. Saito. Proposed robust entanglement-based magnetic field sensor beyond the standard quantum limit. *Phys. Rev. Lett.*, 115:170801, 2015.

[53] J. Taylor, P. Cappellaro, L. Childress, L. Jiang, D. Budker, P. Hemmer, A. Yacoby, R. Walsworth, and M. Lukin. High-sensitivity diamond magnetometer with nanoscale resolution. *Nat. Phys.*, 4(10):810–816, 2008.

[54] B. Terhal and D. Weigand. Encoding a qubit into a cavity mode in circuit QED using phase estimation. *Phys. Rev. A*, 93(1):012315, 2016.

[55] G. Tóth. Multipartite entanglement and high-precision metrology. *Phys. Rev. A*, 85(2):022322, 2012.

[56] G. Tóth and I. Apellaniz. Quantum metrology from a quantum information science perspective. *J. Phys. A Math. Theor.*, 47(42):424006, 2014.

[57] T. Unden, P. Balasubramanian, D. Louzon, Y. Vinkler, M. B. Plenio, M. Markham, D. Twitchen, A. Stacey, I. Lovchinsky, A. O. Sushkov, et al. Quantum metrology enhanced by repetitive quantum error correction. *Phys. Rev. Lett.*, 116(23):230502, 2016.

[58] V. Vorobyov, S. Zaiser, N. Abt, J. Meinel, D. Dasari, P. Neumann, and J. Wrachtrup. Quantum Fourier transform for nanoscale quantum sensing. *Npj Quantum Inf.*, 7(1):1–8, 2021.

[59] Y. Wang. software supplementary. `https://github.com/YWang92/DickeStatePreparation.git`.

[60] W. Wieczorek, R. Krischek, N. Kiesel, P. Michelberger, G. Tóth, and H. Weinfurter. Experimental entanglement of a six-photon symmetric Dicke state. *Phys. Rev. Lett.*, 103:020504, 2009.

[61] C. Wu, C. Guo, Y. Wang, G. Wang, X.-L. Feng, and J.-L. Chen. Generation of Dicke states in the ultrastrong-coupling regime of circuit QED systems. *Phys. Rev. A*, 95:013845, 2017.

[62] C. Wu, Y. Wang, C. Guo, Y. Ouyang, G. Wang, and X.-L. Feng. Initializing a permutation-invariant quantum error-correction code. *Phys. Rev. A*, 99(1):012335, 2019.

[63] L. Xu, H. Yuan, N. Zhang, J. Zhang, G. Bian, P. Fan, M. Li, C. Zhang, Y. Zhai, and J. Fang. High-efficiency fluorescence collection for nv-center ensembles in diamond. *Opt. Express*, 27(8):10787–10797, 2019.

[64] M. Yurtalan, J. Shi, G. Flatt, and A. Lupascu. Characterization of multilevel dynamics and decoherence in a high-anharmonicity capacitively shunted flux circuit. *Phys. Rev. Appl.*, 16:054051, 2021.

[65] Z. Zhang and L. Duan. Quantum metrology with Dicke squeezed states. *New J. Phys.*, 16(10):103037, 2014.

[66] X. Zhu, S. Saito, A. Kemp, K. Kakuyanagi, S. I. Karimoto, H. Nakano, W. J. Munro, Y. Tokura, M. S. Everitt, K. Nemoto, M. Kasu, N. Mizuochi, and K. Semba. Coherent coupling of a superconducting flux qubit to an electron spin ensemble in diamond. *Nature*, 478(7368):221–224, 2011.

7

8

CONCLUSION

Recent experimental advancements have illustrated the potential of NV centers in diamond for various quantum technologies, such as quantum sensing [1, 4], quantum networking [10, 14], quantum simulation [15], and fault-tolerant quantum computation [2]. However, for practical use of NV centers in diamond for quantum technologies, further improvements in noise reduction are needed. This thesis aims to contribute to addressing this challenge.

Chap 4 presents an 8-qubit code proposed for fault-tolerant and universal quantum computation, which is suitable for demonstrating fault-tolerant quantum computation using an NV-based network. This code can leverage the all-to-all connectivity of the NV nodes connected via optical links. A circuit for implementing the one-bit addition algorithm using this 8-qubit code is designed to illustrate its potential as an example of fault-tolerant universal quantum computation. Notably, the optimized protocol requires only 13 physical qubits and outperforms its non-fault-tolerant counterpart when the fidelity of entangling gates between remote NV nodes is below a pseudo threshold of about 2%. This pseudo threshold is relatively high, which suggests that the proposed one-bit addition experiment could be feasible for NV-based networks in the near future.

Chap 5 presents our experimental demonstration of the essential building blocks required for implementing fault-tolerant quantum error correction (QEC) using a single NV center. The primary objective of this work is to encode a logical qubit of the 5-qubit code by repeatedly measuring multi-qubit operators. The protocol is optimized to minimize the total number of gate operations and avoid costly entangling gates that are directly implemented between nuclear spins. Our experimental results demonstrate the advantages of the fault-tolerant encoding scheme over its non-fault-tolerant counterpart, representing a significant advancement towards realizing fault-tolerant quantum computation using NV centers.

Despite extensive efforts in circuit optimization, the manipulation of spin qubits within NV nodes remains too noisy, and compromises the effectiveness of QEC protocols. To illustrate, the current level of fidelity for connecting two NV nodes in NV-based networks is only on the order of 80-90% [9, 11], far below the required 2% pseudo-

threshold essential for our proposed implementation of one-bit addition in Chapter 4. Furthermore, while our fault-tolerant encoding scheme for the 5-qubit code outperforms its non-fault-tolerant counterpart, the prepared logical qubit continues to exhibit a significantly higher error rate compared to its constituent nuclear spin qubits. This elevated logical error rate is largely due to the limited fidelity of the electron-nuclear entanglement gates, which ranges from 93% to 99% [5]. These results highlight the current impracticality of relying on QEC protocols to manage noise, especially when NV centers are used for tasks such as quantum network construction and quantum simulation.

A prominent source of noise in the construction of such networks arises from nuclear spin dephasing induced by uncontrolled electronic spin dynamics during the execution of entanglement protocols [16]. Despite the theoretically proven efficacy of the phase-flip QEC code in dealing with dephasing noise, practical benefits continue to elude realization even with the most rudimentary 3-qubit configuration, mainly due to control fidelity constraints [6, 19].

In chapter 6, we present a direct methodology for assessing the impact of noise on nuclear spins acting as data qubits. This approach makes use of information obtained from the direct measurement of other nuclear spins acting as spectator qubits. This technique exploits the key insight that dephasing noise, which affects different nuclear spins, exhibits spatial correlations during the entanglement generation process. The experimental implementation of spectator qubits is comparatively straightforward, requiring only the individual measurement and initialization of these spectators, thereby minimizing adverse effects on the data qubits.

While this strategy shares similarities with dynamic decoupling, a method that uses simple operations to significantly suppress temporally correlated dephasing noise, its effectiveness is limited by the fact that spatially correlated dephasing noise is typically not the dominant noise source. Consequently, the use of spectator qubits underscores the importance of a comprehensive understanding of the underlying physical platforms, thereby facilitating the development of error mitigation techniques carefully tailored to specific hardware constraints.

An alternative approach to the use of NV centers is to exploit their extended coherence time and use them as memory for other systems with better control fidelity [12, 20]. This exclusive use of NV cores as memory can simplify the manipulation of spin qubits and eliminate the need for complex gate sequences required for direct implementation of fault-tolerant protocols on NV centers. In addition, hybridized devices offer new possibilities for controlling defect centers [8, 13, 17]. For example, coupling an ensemble of NV centers with a superconducting flux qubit allows global control of the NV centers [13, 21]. Based on such global control, the chapter 7 demonstrates an exponentially more efficient preparation scheme for highly entangled Dicke states.

It is worth highlighting that the weak coupling between NV centers and other systems poses a significant challenge for effectively utilizing hybridized systems, which may not necessarily be less complex than achieving the high gate fidelity required to directly implement fault-tolerant QEC protocols on NV centers. Nevertheless, the potential to combine the strengths of different systems is an area of active research and worth further investigation [3, 7, 8, 12, 18, 20].

References

[1] M. H. Abobeih, J. Randall, C. E. Bradley, H. P. Bartling, M. A. Bakker, M. J. Degen, M. Markham, D. J. Twitchen, and T. H. Taminiau. Atomic-scale imaging of a 27-nuclear-spin cluster using a quantum sensor. *Nature*, 576(7787):411–415, 2019.

[2] M. H. Abobeih, Y. Wang, J. Randall, S. J. H. Loenen, C. E. Bradley, M. Markham, D. J. Twitchen, B. M. Terhal, and T. H. Taminiau. Fault-tolerant operation of a logical qubit in a diamond quantum processor. *Nature*, 606(7916):884–889, 2022.

[3] A. Albrecht, A. Retzker, F. Jelezko, and M. B. Plenio. Coupling of nitrogen vacancy centres in nanodiamonds by means of phonons. *New J. Phys.*, 15(8):083014, 2013.

[4] N. Aslam, M. Pfender, P. Neumann, R. Reuter, A. Zappe, F. F. de Oliveira, A. Denisenko, H. Sumiya, S. Onoda, J. Isoya, and J. Wrachtrup. Nanoscale nuclear magnetic resonance with chemical resolution. *Science*, 357(6346):67–71, 2017.

[5] C. E. Bradley, J. Randall, M. H. Abobeih, R. C. Berrevoets, M. J. Degen, M. A. Bakker, M. Markham, D. J. Twitchen, and T. H. Taminiau. A Ten-Qubit Solid-State spin register with quantum memory up to one minute. *Phys. Rev. X*, 9(3):031045, 2019.

[6] J. Cramer, N. Kalb, M. A. Rol, B. Hensen, M. S. Blok, M. Markham, D. J. Twitchen, R. Hanson, and T. H. Taminiau. Repeated quantum error correction on a continuously encoded qubit by real-time feedback. *Nat. Commun.*, 7:11526, 2016.

[7] M. Fukami, D. R. Candido, D. D. Awschalom, and M. E. Flatté. Opportunities for long-range magnon-mediated entanglement of spin qubits via on- and off-resonant coupling. *PRX Quantum*, 2:040314, 2021.

[8] D. A. Golter, T. Oo, M. Amezcua, I. Lekavicius, K. A. Stewart, and H. Wang. Coupling a surface acoustic wave to an electron spin in diamond via a dark state. *Phys. Rev. X*, 6(4):041060, 2016.

[9] B. Hensen, H. Bernien, A. E. Dréau, A. Reiserer, N. Kalb, M. S. Blok, J. Ruitenberg, R. F. L. Vermeulen, R. N. Schouten, C. Abellán, W. Amaya, V. Pruneri, M. W. Mitchell, M. Markham, D. J. Twitchen, D. Elkouss, S. Wehner, T. H. Taminiau, and R. Hanson. Loophole-free bell inequality violation using electron spins separated by 1.3 kilometres. *Nature*, 526(7575):682–686, 2015.

[10] S. L. N. Hermans, M. Pompili, H. K. C. Beukers, S. Baier, J. Borregaard, and R. Hanson. Qubit teleportation between non-neighbouring nodes in a quantum network. *Nature*, 605(7911):663–668, 2022.

[11] S. L. N. Hermans, M. Pompili, H. K. C. Beukers, S. Baier, J. Borregaard, and R. Hanson. Qubit teleportation between non-neighbouring nodes in a quantum network. *Nature*, 605(7911):663–668, 2022.

[12] G. Kurizki, P. Bertet, Y. Kubo, K. Mølmer, D. Petrosyan, P. Rabl, and J. Schmiedmayer. Quantum technologies with hybrid systems. *Proc. Natl. Acad. Sci. U. S. A.*, 112(13):3866–3873, 2015.

8

[13] D. Marcos, M. Wubs, J. M. Taylor, R. Aguado, M. D. Lukin, and A. S. Sørensen. Coupling nitrogen-vacancy centers in diamond to superconducting flux qubits. *Phys. Rev. Lett.*, 105:210501, 2010.

[14] M. Pompili, S. L. N. Hermans, S. Baier, H. K. C. Beukers, P. C. Humphreys, R. N. Schouten, R. F. L. Vermeulen, M. J. Tiggelman, L. Dos Santos Martins, B. Dirkse, S. Wehner, and R. Hanson. Realization of a multinode quantum network of remote solid-state qubits. *Science*, 372(6539):259–264, 2021.

[15] J. Randall, C. E. Bradley, F. V. van der Gronden, A. Galicia, M. H. Abobeih, M. Markham, D. J. Twitchen, F. Machado, N. Y. Yao, and T. H. Taminiau. Many-body-localized discrete time crystal with a programmable spin-based quantum simulator. *Science*, 374(6574):1474–1478, 2021.

[16] A. Reiserer, N. Kalb, M. S. Blok, and et al. Robust quantum-network memory using decoherence-protected subspaces of nuclear spins. *Phys. Rev. X*, 6:021040, 2016.

[17] P. K. Shandilya, D. P. Lake, M. J. Mitchell, D. D. Sukachev, and P. E. Barclay. Optomechanical interface between telecom photons and spin quantum memory. *Nat. Phys.*, 17(12):1420–1425, 2021.

[18] L. Trifunovic, F. L. Pedrocchi, and D. Loss. Long-distance entanglement of spin qubits via ferromagnet. *Phys. Rev. X*, 3:041023, 2013.

[19] G. Waldherr, Y. Wang, S. Zaiser, M. Jamali, T. Schulte-Herbrüggen, H. Abe, T. Ohshima, J. Isoya, J. F. Du, P. Neumann, and J. Wrachtrup. Quantum error correction in a solid-state hybrid spin register. *Nature*, 506(7487):204–207, 2014.

[20] Z.-L. Xiang, S. Ashhab, J. Q. You, and F. Nori. Hybrid quantum circuits: Superconducting circuits interacting with other quantum systems. *Rev. Mod. Phys.*, 85:623–653, 2013.

[21] X. Zhu, S. Saito, A. Kemp, K. Kakuyanagi, S. I. Karimoto, H. Nakano, W. J. Munro, Y. Tokura, M. S. Everitt, K. Nemoto, M. Kasu, N. Mizuochi, and K. Semba. Coherent coupling of a superconducting flux qubit to an electron spin ensemble in diamond. *Nature*, 478(7368):221–224, 2011.

8

CURRICULUM VITÆ

Yang WANG

10/09/1992	Born in Wanzhou, Chongqing, China
09/2011–07/2015	B.Sc. in Physics, Sichuan University, China
10/2015–10/2017	M.Sc. in Physics, RWTH Aachen University, Germany
	Thesis: Quantum error correction with the GKP code and concatenation with stabilizer codes
	Supervisor: Prof. dr. B. M. Terhal
03/2018–03/2023	PhD, QuTech, Delft University of Technology, the Netherlands
	Thesis: Using spins in diamond for quantum technologies
	Promotor: Prof. dr. B. M. Terhal
	Co-promotor: Dr. ir. T. H. Taminiau
03/2023– Present	Postdoc, 3rd Physical Institute, University of Stuttgart, Germany
	Supervisor: Prof. dr. J. Wrachtrup

LIST OF PUBLICATIONS

5. Fault-tolerant one-bit addition with an 8-qubit error detecting code.
   Y. Wang, Selwyn Simsek, Ben Criger
   In preparation, tentative title. Author order does not reflect the contribution.

4. Robust quantum-network nodes through real-time noise mitigation using spectator qubits.
   Y. Wang*, S. J. H. Loenen*, C. E. Bradley, M. Markham, D. J. Twitchen, B. M. Terhal,
   and T. H. Taminiau,
   In preparation, tentative title.

3. Fault-tolerant operation of a logical qubit in a diamond quantum processor.
   M. H. Abobeih, **Y. Wang**, J. Randall, S. J. H. Loenen, C. E. Bradley, M. Markham, D. J. Twitchen,
   B. M. Terhal, and T. H. Taminiau.
   Nature 606, 884-889 (2022).

2. Preparing Dicke states in a spin ensemble using phase estimation.
   Y. Wang, B.M. Terhal.
   Phys. Rev. A 104, 032407 (2021)

1. Quantum error correction with the toric Gottesman-Kitaev-Preskill code.
   C. Vuillot, H. Asasi, **Y. Wang**, L.P. Pryadko, B.M. Terhal
   Phys. Rev. A 99, 032344 (2019)

 * *First authorship.*